Ricerca di Sistema elettrico

Validazione e analisi dei gas di fissione in combustibili MOX ad elevato burnup

D. Rozzia, N. Forgione, A. Ardizzone, A. Del Nevo

VALIDAZIONE E ANALISI DEI GAS DI FISSIONE IN COMBUSTIBILI MOX AD ELEVATO BURNUP

D. Rozzia, N. Forgione (UNIPI), A. Ardizzone (POLITO), A. Del Nevo (ENEA)

Settembre 2013

Titolo

Validazione e analisi dei gas di fissione in combustibili MOX ad elevato burnup

Descrittori

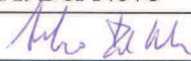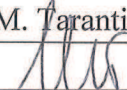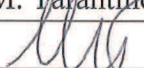|	
Tipologia del documento:	**Rapporto Tecnico**
Collocazione contrattuale:	Accordo di programma ENEA-MSE su sicurezza nucleare e reattori di IV generazione
Argomenti trattati:	Sicurezza nucleare
	Generation IV reactors
	Combustibile nucleare

Sommario

Il documento costituisce il contributo alla task A.3 dell'Accordo Di Programma 2012. L'obiettivo dell'attività è la validazione del codice TRANSURANUS versione 2012 nel simulare il comportamento di combustibili tipo MOX assoggettato sia a "normal conditions" che "power ramps". Particolare enfasi è data alle principali variabili che influenzano il fenomeno del "Fission Gas Release (FGR). Due database sperimentali nel range di "burn-up" 25 - 30MWd/kgHM sono stati selezionati, modellati e analizzati: l'esperimento PRIMO (1 barretta) e l'esperimento IFA-597 (2 barrette). Questi databases sono stati rilasciati a scopo "benchmarking" e appartengono al database pubblico "International Fuel Pin performance Experimental database (IFPE)". Tale banca dati è stata create ed è mantenuta da OECD/NEA appositamente per raccogliere dati necessari allo sviluppo e validazione di codici principalmente di tipo "fuel pin mechanics" (es. TRANSURANUS).

Note

* Autori:

D. Rozzia (UNIPI), N. Forgione (UNIPI), A. Ardizzone (POLITO), A. Del Nevo (ENEA)

Copia n.			In carico a:			
1			NOME			
			FIRMA			
0	EMISSIONE	18/09/13	NOME	A. Del Nevo *	M. Tarantino	M. Tarantino
			FIRMA			
REV.	DESCRIZIONE	DATA		REDAZIONE	CONVALIDA	APPROVAZIONE

(This page has been intentionally left blank)

Abstract

The present document constitutes the contribution LP2.a.3_b to the task A.3 of ADP-2012. The aim of this report is the assessment of TRANSURANUS code version 2012 in simulating MOX fuel behavior with particular reference to the FGR phenomenon. This type of fuel has been selected as fuel for both GEN-IV systems as ALFRED or ASTRID and advanced thermal reactors as EPR. Since fuel pin mechanics codes are usually based on empirical correlations obtained from experiments, their applicability to new designs should be demonstrated by verification and validation processes. This complex task requires the large use of experimental databases. Due to the un-availability of public databases on FR fuel, the first step, is verification and validation of fuel pin mechanic codes against thermal reactor public databases. The International Fuel Pin performance Experimental database (IFPE) aims to provide in the public domain, a comprehensive and well-qualified database on Zr clad UO2 – MOX fuel for model development and validation. Two experimental databases in the burn-up range from 25 - 30MWd/kgMOX have been selected from the IFPE to fulfil the objective: the PRIMO experiment (1 rod) and IFA-597 experiment (2 rods). They have been released for benchmarking purpose.

The PWR Reference Irradiation of MOX Fuels (PRIMO) program sought to investigate the MOX fuel behavior under steady-state and transient conditions. It started in 1986. The aims were to investigate the capability of MOX to sustain normal operation conditions typical of commercial PWR, to study thermal and irradiation induced phenomena occurring in fuel and to obtain thermo-mechanical data under power ramp conditions. The PRIMO program included sixteen MOX fuel rods manufactured through different fabrication processes and ramp-tested at different burn-up levels between 20 and 60 MWd/kgHM. The irradiation history and the experimental data of one fuel rod named BD8 from the PRIMO program was included in the International Fuel Performance Experimental Database and released for benchmarking purpose. It was base-irradiated in the BR2 Pressurized Water cooled Reactor (PWR) at an average linear power of 18.5 kW/m up to a burn-up of about 30 MWd/kgHM. The fuel rod then underwent a ramp test in the Osiris PWR up to a peak linear power of 39.5 kW/m. Post irradiation examinations were carried out to investigate rod behavior such as fission gas release (FGR), clad creep, clad and fuel elongations.

The Instrumented Fuel Assembly 597 (IFA-597) experiment was carried out in the Halden Boiling Heavy water Reactor under the auspices of the Halden Reactor Project. The experiment aimed to study the thermal and fission gas release behavior of MOX fuel, and to explore differences in performance between solid and hollow pellets. Two MOX rods (labeled 10 and 11) were instrumented with a fuel center thermocouple and a pressure bellow transducer and irradiated in the Halden Reactor. The experiment consisted of four power cycles up to 33 MWd/kgMOX. The linear power was in the range 15-35 kW/m. Details of the fabrication data as well as irradiation data up to a burn-up of 26 MWd/kgMOX (reached at the end of the third cycle) were released with the aim of code benchmarking. The in-pile data on fuel temperature, rod inner pressure and results of the gas puncturing and mass spectrometry of the extracted gas were also released. The datasets of this experiment are included in the International Fuel Performance Experimental database.

This document consists of eight main sections and two attached appendixes. Section one points out the objective and the framework of the activity. In the second section, the MOX fuel is described and the main differences between MOX and UO₂ are briefly discussed giving emphasis on modeling issues. PRIMO and IFA-597 experiments are described in section three. Section four includes the procedure adopted to develop the TRANSURANUS reference input decks. The main capabilities of TRANSURANUS in treating the FGR phenomenon and its connected parameters and processes are described in section five. Sections sis and seven constitute the core of this report. They aim to validate TRANSURANUS code against PRIMO and IFA-597 experiments exploring its capabilities by systematic comparison between simulated and measured trends and by extensive sensitivity analysis. The section includes the comparison with the related benchmarks. Conclusions are finally given in section eight. Appendix A and B report detailed figures in support to the sensitivity analyses.

CONTENTS

Abbreviations

ADS	Accelerator Driven System
ADP	Accordo Di Programma
ALFRED	Advanced Lead cooled Fast Reactor
Am	Americium
AR	After Ramp
ASTRID	Advanced Sodium Test Reactor for Industrial Demostration
BI	Base Irradiation
BN	Belgonucleaire
BNFL	British Nuclear Fuels plc (UK)
BOL	Beginning Of Life
CEA	Commissariat à l'Energie Atomique
CIRTEN	Consorzio Interuniversitario per la Ricerca Tecnologica Nucleare
CL	Conditioning Level
COCA	Cobroyage (co-milling) Cadarache
CRP	Coordinate Research Program
Cu	Curium
DIMNP	Dipartimento di Ingegneria Meccanica Nucleare e della Produzione
ENEA	Agenzia nazionale per le nuove tecnologie, l'energia e lo sviluppo economico sostenibile
EOL	End of Life
EPMA	Electron Probe Micro Analysis
F	Failed
FBFC	Franco Belge de Fabrication de Combustible
FBR	Fast Breeder Reactor
FGR	Fission Gas Release
FP	Fission Product
FR	Fast Reactor
FRAPCON-3	"Steady state fuel rod performance code"
FUMEX	Fuel Modeling at Extended Burn-up
Gd	Gadolinium
GEN-IV	GENeration - IV
HBS	High burn-up Structure
He	Helium
HBWR	Halden Boyling Water Reactor
HRP	Halden Reactor Project
IAEA	International Atomic Energy Agency
IFA	Instrumented Fuel Assembly
IFE	Institute For Energetik
ITU	Institute for Transuranium Elements
IFPE	International Fuel Performance
JNC	Japan Nuclear Cycle development institute
JRC	Joint Research Centre
KAERI	Korean Atomic Energy Research Institute
Kr	Kripton
LFR	Lead cooled Fast Reactor
LHR	Linear Heat Rate

LVDT	Linear Variable Differential Transducer
LWR	Light Water Reactor
MA	Minor Actinide
MHI	Mitsubishi Heavy Industries
MHYRRA	Multi-purpose HYbrid Research Reactor
MIMAS	Micronized MASter blend
MLI	Mean Linear Intercept
MOX	Mixed OXide (fuel)
MTR	Material Testing Reactor
NEA	Nuclear Energy Agency
NF	Non Failed
NFF	Neutron Fast Flux
NITROX	de-nitration process for PuO_2 production (France)
NNL	National Nuclear Laboratory (UK)
NPP	Nuclear Power Plant
NSC	Nuclear Science Committee
OECD	Organization for Economic Co-operation and Development
O/M	Oxygen to Metal ratio
PCI	Pellet-Cladding Interaction
PCMI	Pellet-Cladding Mechanical Interaction
PIE	Post Irradiation Examination
PRIMO	PWR Reference Irradiation of MOX fuels program
PTI	Prior To Irradiation
PTR	Prior To Ramp
Pu	Plutonium
PWR	Pressurized Water Reactor
SFR	Sodium cooled Fast Reactor
RTL	Ramp Terminal Level
RR	Ramp Rate
SCC	Stress Corrosion Cracking
SCK•CEN	Studiecentrumvoor Kernenergie Centre d'Études de l'Énergie Nucléaire
TD	Theoretical Density
TDN	Thermal De-Nitration
TU	TRANSURANUS
TWCA	The Wah Chang Albany
U	Uranium
UNIPI	Università di Pisa
UO_2	Uranium Oxide
Xe	Xenon
XRF	X-ray Fluorescence
Zr-4	Zircaloy-4

List of figures

List of tables

1 Introduction

1.1 Background

In the last decades two main trends have been identified in the nuclear technology. The first one deals with the continuous increase of the discharge burn-up. In this framework, new cladding materials capable to sustain higher burn-ups have been developed and new experiments have been executed to better understand high burn-ups phenomena (i.e. the HBS formation, the in cladding hydrogen pick-up, the delayed hydride cladding failure mechanism etc…), to check the new materials performance and to check the existing safety criteria (that were defined at lower burn-ups and for old materials)[1][2].

The second deals with the introduction of commercial MOX fuel. Three temporal phases in the management of plutonium arising from nuclear power generation (civil plutonium) are identified[3].

- The first phase has seen a gradual introduction of the recycling of mixed oxide fuel up to an industrial scale in light water reactors in several countries, is currently well established. MOX usage in LWRs is a well understood and mature technology and MOX can be managed in a very similar way to uranium fuel. The current inventory of separated civil plutonium is safely stored and has still to be recycled. The necessary safeguards arrangements have kept pace with these developments wherever plutonium is handled, fabricated, stored, transported and irradiated.
- The second phase (up to, say, 2030) is beginning at the time of writing. It is characterized by an ongoing but irregular expansion of MOX recycling in which other countries will acquire MOX technology and additional nuclear plants will be licensed for MOX fuel. It could then be expected that the stockpiles of separated plutonium (both civil and weapons surplus) will begin to diminish and move to significantly lower levels during this phase. As well as extending the number of power plants loading MOX fuel, the technology now needs to be developed for advanced reactors such as the GEN-IV Fast Reactor (i.e. LFR or SFR) or Accelerator Driven Systems (i.e. MHYRRA). Additionally, more environmentally friendly reprocessing methods with reduced emissions will be needed to prepare for the third and long term phase of plutonium recycle and management.
- In this preparation for the third phase of development, emphasis must be placed on both achieving greater public acceptance for plutonium fuel technology as well as making the power producing utilities more attractive economically. These same utilities will be the ultimate source of the financing needed to establish the stable development of nuclear power based on uranium and, over the longer term, plutonium fuels. A fuel that is more expensive than others or which may limit reactor operation is unacceptable for the power producers. If the economic and performance targets cannot be reached and negative public attitudes persist, there will be no third phase of plutonium recycle. However, if such a development can be realized, the third phase should see the progressive introduction of advanced thermal reactors as well as fast reactors, alongside new technologies specifically designed for MOX fuel. The aim will be to manage the production and use of plutonium effectively to avoid major stockpiling.

The fission process not only generates heat in the nuclear fuel pellets, it also produces a broad spectrum of fission products, most of which are radioactive and should not be released to the environment. In the defense in depth concept, the fuel matrix and the cladding constitute the first two barriers against the release of radio nuclides from a nuclear power plant[1]. In thermal reactors, it is generally accepted that MOX fuel behaves similar to UOx fuel and should therefore wind stand the same safety requirements. Compared to UOx, MOX fuel mainly differentiate by[4],[5]: lower conductivity, lower melting point, higher creep rate, higher FGR, lower gaseous swelling and production / release of He coming from alpha decay of heavy MA[4][5]. In general, the differences

depend on the fabrication process and on the PuO_2 content. Since the experimental databases on MOX fuel are not so extended as for UOx, there is a growing interest in understanding the MOX fuel behavior both for the application in commercial LWR fuels with high burn-ups performance and next generation FRs. The exact description of all the physical phenomena occurring in fuel rods during irradiation is a complex task since it involves a wide range of disciplines ranging from chemistry, nuclear and solid-state physics, metallurgy, thermal-hydraulics, ceramics and applied mechanics. In particular, the characterization of MOX fuel for FR application is of great importance to develop advanced fuel design since FR MOX fuel has unique features: it contains larger quantities of PuO_2 than LWR, it is operated at higher temperature and in harder neutron spectrum. Developing computer codes that allow the description of the general MOX fuel behavior is mandatory to support the development of safer and more effective fuels.

1.2 Objective of the activity

The Fission Gas Release (FGR) phenomenon is of primary interest since it is considered as one possible mechanism that limits the discharge burn-up of nuclear fuel rods. Gaseous fission products, in fact, either remain in the pellets and contribute to the swelling, or are released from the pellets to the pin free volume. The fuel swelling promotes the pellet-cladding interaction while the release of fission gases leads to two other undesirable effects: the increase of fuel rod's internal pressure and the degradation of the gap conductivity. In addition, the use of MOX fuel implies the release of a non-negligible amount of He (that can be neglected in UO_2 fuel) coming from the alpha decay of Pu^{238}, Cm^{242}, Cm^{244}, and from ternary fissions. Deeper understanding of the fission gas release phenomenon, along with better modeling capabilities is the only way to move to best estimate predictions.

The aim of this report is the assessment of TRANSURANUS[6],[7],[8] code version 2012 in simulating MOX fuel behavior with particular reference to the FGR phenomenon. This type of fuel has been selected as fuel for both GEN-IV systems as ALFRED or ASTRID and advanced thermal reactors as EPR. Since fuel pin mechanics codes are usually based on empirical correlations obtained from experiments, their applicability to new designs should be demonstrated by verification and validation processes. This complex task requires the large use of experimental databases.

Due to the un-availability of public databases on FR fuel, the first un-avoidable step, is verification and validation of fuel pin mechanic codes against thermal reactor public databases. The International Fuel Pin performance Experimental database (IFPE)[9] aims to provide in the public domain, a comprehensive and well-qualified database on Zr clad UO_2 – MOX fuel for model development and code validation. The data encompasses both normal and off-normal operation and include prototypic commercial irradiations as well as experiments performed in Material Testing Reactors. This work is carried out in close co-operation and co-ordination between the NEA, the IAEA and the IFE/OECD Halden Reactor Project. The database is restricted to thermal reactor fuel performance, principally with standard product Zircaloy clad UO_2 fuel, although the addition of advanced products with fuel and clad variants is not ruled out. Emphasis has been placed on including well-qualified data that illustrate specific aspects of fuel performance. Of particular interest to fuel modellers are data on: fuel temperatures, fission gas release (FGR), fuel swelling, clad deformation (e.g. creep-down, ridging) and mechanical interactions. Data on these issues are of great value if measured in-pile by dedicated instrumentation and, in this respect, the IFPE Database is fortunate in having access to several diverse experiments. In addition to direct in-pile measurement, every effort is made to include PIE information on clad diameters, oxide thickness, hydrogen content, fuel grain size, porosity, Electron Probe Micro Analysis (EPMA) and X-ray Fluorescence (XRF) measurements on caesium, xenon, other fission product and actinides.

Two databases on MOX fuel included in the IFPE and released for benchmarking purpose have been modeled by means of TRANSURANUS code: PRIMO[10] experiment and IFA-597[11],[12].

1.3 Validation domains

TRANSURANUS is a computer program for the thermal and mechanical analysis of fuel rods in nuclear reactors[6][7][8] developed at ITU. It consists of a clearly defined mechanical–mathematical framework into which physical models can easily be incorporated. The mechanical–mathematical concept consists of a superposition of a one-dimensional radial and axial description (the so called quasi two-dimensional or 1½-D model). The code was specifically designed for the analysis of a whole rod. Besides its flexibility for fuel rod design, the TRANSURANUS code can deal with a wide range of different situations, as given in experiments, under normal, off-normal and accident conditions. The time scale of the problems to be treated may range from milliseconds to years. The code has a comprehensive material data bank for oxide, mixed oxide, carbide and nitride fuels, Zircaloy and steel claddings and several different coolants. It can be employed in two different versions: as a deterministic and as a statistical code.

The validation of TRANSURANUS code is performed against the PRIMO Experiment (1 rod) and IFA-597 (2 rods).

The PWR Reference Irradiation of MOX fuels (PRIMO) program sought to investigate the MOX fuel behavior under steady-state and transient conditions[10]. It started in 1986. The aims were to investigate the capability of MOX to sustain normal operation conditions typical of commercial PWR, to study thermal and irradiation induced phenomena occurring in fuel and to obtain thermo-mechanical data under power ramp conditions. The PRIMO program included sixteen MOX fuel rods manufactured through different fabrication processes and ramp-tested at different burn-up levels between 20 and 60 MWd/kgHM. The irradiation history and the experimental data of one fuel rod named BD8 from the PRIMO program was included in the International Fuel Performance Experimental Database and released for benchmarking purpose. It was base-irradiated in the BR2 Pressurized Water cooled Reactor (PWR) at an average linear power of 18.5 kW/m up to a burn-up of about 30 MWd/kgHM. The fuel rod then underwent a ramp test in the Osiris PWR up to a peak linear power of 39.5 kW/m. Post irradiation examinations were carried out to investigate rod behavior such as fission gas release (FGR), clad creep, clad and fuel elongations.

The Instrumented Fuel Assembly 597 (IFA-597) experiment was carried out in the Halden Boiling heavy Water Reactor (HBWR)[11],[12]. The experiment aimed to study the thermal and FGR behavior of MOX fuel, and to explore differences in performance between solid and hollow pellets. Two MOX rods (labeled 10 and 11) were instrumented with a fuel center thermocouple and a pressure bellow transducer and irradiated in the Halden Reactor. The experiment consisted of four power cycles up to 33 MWd/kgMOX. The linear power was in the range 15-35 kW/m. Details of the fabrication data as well as irradiation data up to a burn-up of 26 MWd/kgMOX (reached at the end of the third cycle) were released with the aim of code benchmarking. The in-pile data on fuel temperature, rod inner pressure and results of the gas puncturing and mass spectrometry of the extracted gas were also released.

The validation domains are reported in *Tab. 1* and *Tab.* 2. They include:

- the version of the code used for the independent assessment;
- the main objective of the independent assessment;
- the range of parameters for which the assessment is performed;
- the parameters, part of the experimental database, which are suitable for the comparisons;

- the parameters adopted for the comparison between the experimental data and the code results.

VALIDATION DOMAIN							
Main phenomena	**Experiment**	**No. rods**	**Thermal modules**	**Mechanical modules**	**FGR modules**	**Burn-up modules**	**Notes**
PCI/SCC FGR	*PRIMO MOX ROD BD8*	*1*	*X*	*X*	*X*	*X*	*Version 2012*

Range (parameters) of validity			Parameters for validation		
Parameter	**Unit**	**Descript.**	**#**	**Rod BD8**	**TU simulation**
Pellet material	**--**	**MOX**	*Burn-up*	●	X
Cladding material	**--**	**Zr-4**	*Cladding creep down in BI[1] (avg. and max)*	●	X
EnrichmentU^{235}	%HM	**5.246**	*Cladding expansion AR[2] (avg. and max)*	●	X
Enrichment Pu	%HM	**7.630**	*Grain size AR[2] (pellet centre/periphery)*	○	X
Pellet outer diameter	mm	**8.041**			
Diametral gap size	μm	**200**	*FGR BI[1] and AR[2]*	●	X
Clad outer diameter	mm	**9.5**	*Elongation AR[2]*	●	X
Active length	mm	**1004.7**	*Ridges height (avg. and max) in BI[1]*	●	--[$]
Initial avg. grain size[§]	μm	**5**	*Ridges height (avg. and max) AR[2]*	●	--[$]
He filling pressure	MPa	**2.0**	*Clad ovality after BI[1]*	●	--[$]
Average burn-up	MWd/kgHM	**30**	*Failure / Not Failure, AR[2]*	●	X
Operative pressure	MPa	**15.0**			
Average LHR[3] (BI[1])	kW/m	**18.5**			
Average NFF[4] (BI, 4D1-4D2 cycles)	n/cm²s	**4*10¹²**			
Ramp rate	kW/mh	**462**	● suitable for code assessment ○ limited suitability ─ not suitable		
RTL[5]	kW/m	**39.5**			
LHR[3] change	kW/m	**20.6**			
Holding time at RTL[5]	hrs	**20**			
1 BI: Base Irradiation 2 AR: After Ramp 3 LHR: Linear Heat Rate 4 NFF: Neutron Fast Flux (>1 MeV)			5 RTL: Ramp Terminal Level $ Not predictable by 1½D code (outside TU code capabilities) § Mean intercept length		

Tab. 1 – PRIMO Experiment validation domain of TU v1m1j12.

VALIDATION DOMAIN							
Main phenomena	**Experiment**	**No. rods**	**Thermal modules**	**Mechanical modules**	**FGR modules**	**Burn-up modules**	**Notes**
FGR	*IFA-597*	2	X	X	X	X	

Range (parameters) of validity			Parameters for validation		
Parameter	**Unit**	**Descript.**	**#**	**rod 10, rod 11.**	**TU simulation**
Pellet material	--	**MOX**	*Burn-up*	●	X
Cladding material	--	**Zr-4**			
Enrichment U235	%HM	**0.22**	*Fuel temperature*	●	X
Enrichment Pu	%HM	**6.07**			
Pellet outer diameter	mm	**8.04**			
Diametral gap size	μm	**180**	*Rod internal pressure*	●	X
Clad outer diameter	mm	**9.5**			
Active length	mm	**220 – 224**	*FGR*	●	X
Initial avg. grain size[3]	μm	**5.45**			
He filling pressure	MPa	**0.5**			
Average burn-up	MWd/kgMOX	**27**	● suitable for code assessment ○ limited suitability ─ not suitable		
Operative pressure	MPa	**3.36**			
Average LHR[1]	kW/m	**16**			
Average NFF[2]	n/cm²s	**1.9*10¹²**			

1   LHR: Linear Heat Rate
2   NFF: Neutron Fast Flux (>1 MeV)
3   Mean intercept length

Tab. 2 – IFA-597, validation domain of TU v1m1j12.

2 The MOX fuel

In every nuclear reactor there is both fission of isotopes such as ^{235}U, and the formation of new, heavier isotopes due to neutron capture, primarily by ^{238}U. Most of the fuel mass in a thermal reactor is ^{238}U. Part of this isotope transmutes to ^{239}Pu (see reactions below) and by successive neutron capture to ^{240}Pu, ^{241}Pu and ^{242}Pu as well as other transuranic isotopes. The plutonium (and uranium) created in the fuel can be recovered through reprocessing. The plutonium could then be used to produce mixed oxide (MOX) nuclear fuel. Today there is a significant amount of separated uranium and plutonium which may be recycled, including from ex-military sources.

$$_{92}U^{238} + {_0}n^1 \rightarrow {_{92}}U^{239} + \gamma$$

$$_{92}U^{239} \underset{23m}{\overset{\beta}{\rightarrow}} {_{93}}U^{239} \underset{2.3g}{\overset{\beta}{\rightarrow}} {_{94}}Pu^{239}$$

Eq. 1
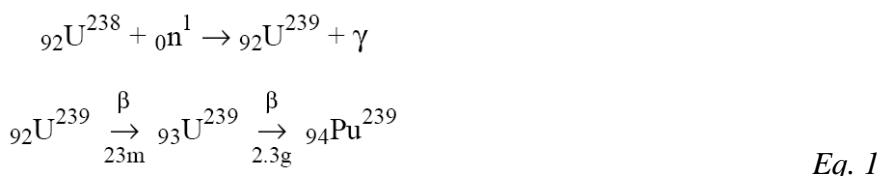
Plutonium reprocessed in LWR fuel contains five principal isotopes, namely, ^{238}Pu, ^{239}Pu, ^{240}Pu, ^{241}Pu and ^{242}Pu. These isotopes have roughly the same probability of fission in FRs, however, in LWRs only ^{239}Pu and ^{241}Pu experience fission and hence contribute to energy production[5].

2.1 Fabrication processes

2.1.1 Fabrication of oxide powder

Numerous methods have been used, and others are being developed, to obtain plutonium dioxide in a suitable form for MOX fuel fabrication. The methods deriving plutonium dioxide from the nitrate widely used followed by the processes to convert plutonium metal to oxide powder. Precipitation of plutonium oxalate and thermal de-nitration methods are briefly recalled in the following. Co-precipitation methods, gel precipitation methods and methods of conversion of plutonium metal to oxide are not discussed in this section, we recommend Ref. [3] for a more detailed description of these methods.

2.1.1.1 Precipitation of plutonium oxalate

This precipitation method is the most widely used commercial method of converting plutonium nitrate solution to dioxide. The plutonium stream is concentrated in evaporators and conditioned to Pu (IV) with hydrogen peroxide before precipitation, *Fig. 1*. An excess of oxalic acid is used to reduce the solubility of the product. The oxalate is decomposed to oxide, which is suitable for ceramic fuel fabrication. The particle size and structure of the oxide are governed by the initial precipitation and, in turn, by the temperature and by concentrations of plutonium, nitric acid and oxalic acid.

$$Pu(NO_3)_4 \cdot 6H_2O + 3H_2C_2O_4 \rightarrow Pu(C_2O_4)_2 \cdot 6H_2O + 4HNO_3$$

$$Pu(C_2O_4)_2 \cdot 6H_2O \rightarrow PuO_22CO + 2CO_2 + 6H_2O$$
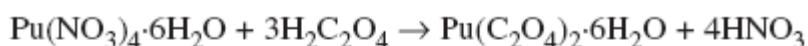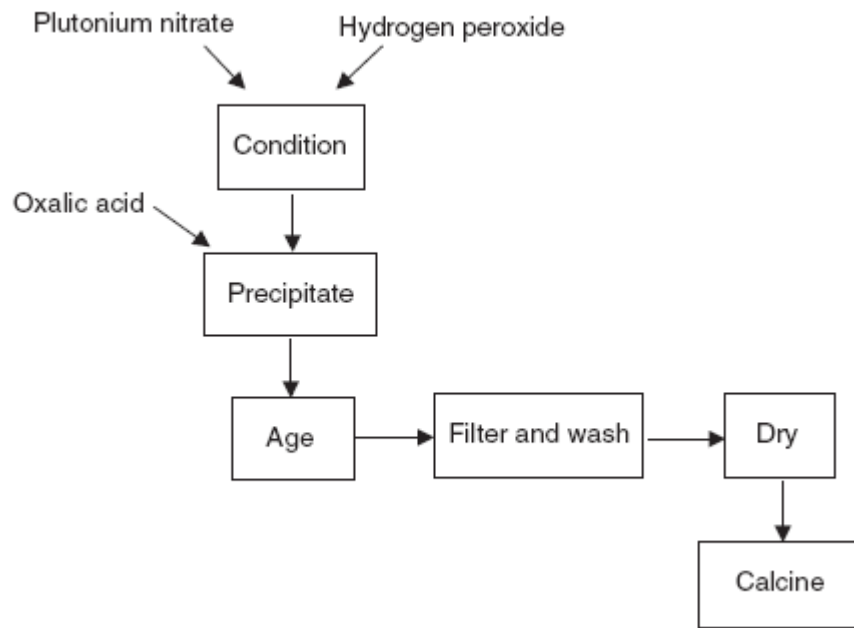
Fig. 1 – Precipitation of plutonium oxalate.

2.1.1.2 Thermal de-nitration methods

As with uranium, the most straightforward way of converting from a nitrate to an oxide is by direct thermal degradation:

$$Pu(NO_3)_4 \cdot 6H_2O \rightarrow PuO_2 + 4NO_2 + O_2 + 6H_2O$$
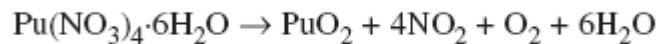
However, such methods are not presently used on a large scale in European plutonium feed production plants although wider use of them is being made in Japanese plants. Thermal de-nitration (TDN) of the oxalate has potentially the minimum number of stages and produces a low volume of liquid effluents that require further treatment. However, such benefits are outweighed by the micron particle powder quality of plutonium dioxide produced by direct TDN, rather than the free flowing powder generally desirable for subsequent processing. Different countries have investigated different de-nitration processes. I.e. the French NITROX process carries out the dehydration under reduced pressure to keep the temperature below the melting point of the hydrates.

2.1.2 MOX fuel fabrication

2.1.2.1 Conventional process

The conventional fabrication route is a direct application of the most common industrial fabrication process for uranium fuel, the enrichment of uranium being replaced by a mechanical blending of the feed powders: UO_2 and PuO_2, or $(U–Pu)O_2$ for the plutonium. *Fig. 2* reports atypical conventional process adopted by the JNC reprocessing plant. As the blended powder is not free flowing, and is therefore unsuitable for feeding to a pellet press, the powder is preconditioned by pre-compaction in a slugging press, followed by granulation, the granules being obtained by crushing the slugs. The challenge in this process is to obtain a uniform distribution of the plutonium in the product. Optimizing the ball (or attritor) mill is of paramount importance for achieving uniformity of the plutonium distribution, as well as a good dispersion of the lubricant and of the pore former, if the use of a pore former is required. The additives utilized include a binder, to improve granulation, a pore former, to achieve the low density specified for FBR fuel, and a lubricant, as universally used to optimize

pelletizing. In such processes, de-waxing of the green pellets is required prior to sintering. Excellent quality fuel can be fabricated by such a process.

Fig. 2 – Conventional MOX fuel fabrication process adopted applied by JNC in PFPF.

2.1.2.2   COCA process

A simplification of the conventional feed powder processing route (which is to MOX fuel what the enrichment operation is to uranium fuel) was developed in the1970s by CEA and applied in the Cadarache fabrication plant under the name COCA, an acronym for Cobroyage (co-milling) Cadarache. It is based on the use of an optimized ball mill acting as a blender and of a forced extrusion of the lubricated micronized powder through a sieve, resulting in free flowing granules adequate for feeding the pellet press, *Fig. 3*. This process, originally developed for FBR fuel, has been adapted for LWR fuel and used from 1989 to 1994 for manufacturing MOX fuel for EDF's PWRs.

2.1.2.3   MIMAS and OCOM processes

The MIMAS process, invented by Belgonucleaire in the early 1980s, is an adaptation of the reference fabrication process developed earlier and applied commercially in the 1970s at the Dessel plant. The reference process consisted of a single blending of PuO_2 powder with free flowing UO_2 powder, resulting in a blend of adequate flow-ability to feed the pellet press. However, when the re-processors decided that even un-irradiated MOX fuel had to be almost completely soluble in a pure nitric acid solution, the reference fuel was deemed to be no longer acceptable. To meet this new specification, the earlier single blending step was replaced by a two step blending approach: in the first step, the pure PuO_2 feed and some UO_2 are co-micronized resulting in a master mix of UO_2–(typically) 30% PuO_2, which is the fundamental principle of the MIMAS process (*Fig. 3*); in the second step, the master mix is blended down with free flowing AUC (Ammonium Uranyl Carbonate) or ADU (Ammonium Di-Uranate) UO_2 to the specified plutonium content of the MOX fuel. The very close contact between the micronized UO_2 and PuO_2 particles provides for adequate inter-diffusion during sintering and therefore the required solubility. The final product is a fuel pellet in which Pu-rich particles are distributed in a UO_2 matrix which is similar to ex-AUC UO_2 microstructure regarding grain size and pore size distribution (average grain size is 7 to 10 μm and average pore diameter 2 to 4 μm). Thus the characteristic size in the MOX fuel can be the plutonium agglomerate (particle) size. These agglomerates are nearly spherical and contain most of the plutonium isotopes. There are very few published data on the details of these agglomerates, which may influence the retention and/or release of fission product gases during irradiation, and also other properties of the fuel, which will be discussed in this report. Lippens[16] and co-workers in a paper on MIMAS fuel note that plutonium is spatially distributed homogeneously on the pellet scale (millimetres), but is heterogeneous when is observed on the micron scale. According to Lippens et al. typical Pu particle size, determined by α-autoradiography, ranges from less than 1 μm to 100 μm with a frequency distribution centred at about 15 μm and an average size around 30 μm; and a much reduced population above 50 μm.

In parallel, Alkem (subsequently part of Siemens) had developed and applied commercially the sibling Optimized Co-milling (OCOM) process, with a similar success in fabric ability and improved fuel behavior. The main differences between MIMAS and OCOM were in the ball milling and powder conditioning steps. Integral fissile Pu content is in the range of 2.0 to 3.5 wt% with a density of 10.32 to 10.45 g/cm³. However, observations using Electron Probe Micro Analyser (EPMA) indicate areas enriched in Pu of dimensions 50 to 100 μm equivalent diameters.

2.1.2.4   SBR process

The SBR (Short Binderless Route), developed and produced by British Nuclear Fuels plc (BNFL), is a way for blending and conditioning of the MOX powder before pressing and sintering, *Fig. 3*. Homogenization is attained by means of a high energy attritor mill, which blends the oxide powders and a spherodizer in order to condition the powder to granules prior to pressing and sintering. At the milling stage, lubricant and Conpore pore former are added in order to control the pellet density and obtain similar characteristics as those of the UO_2 pellets produced by BNFL from IDR (Integrated Dry Route) UO_2 powder. The MOX produced by SBR has a mean grain size of about 7.4 μm with a

standard deviation of 0.6 μm, and for pores with a diameter ≥ 5 μm the median pore size has never been observed to exceed 15.4 μm during the production. The homogeneity of the fuel with respect to plutonium agglomerates is excellent when measured by α-radiography, which is a coarse scale.
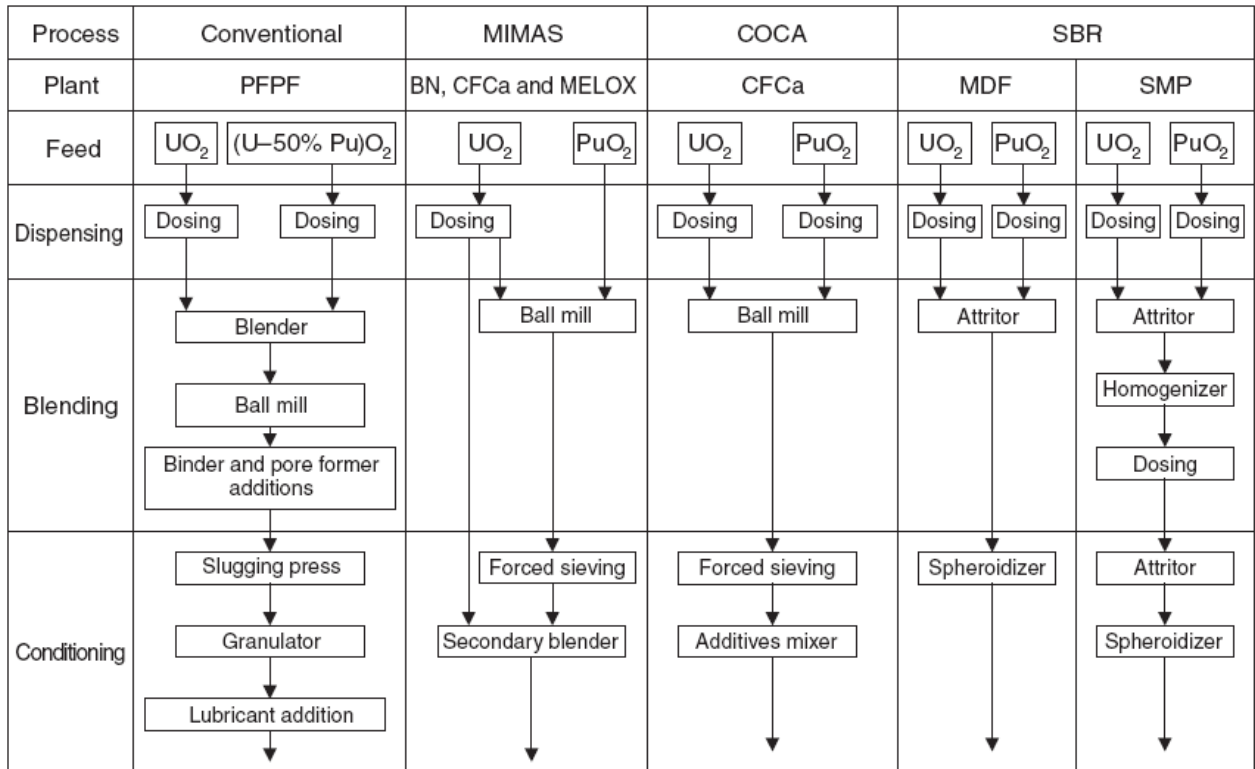
Fig. 3 –MOX fuel fabrication processes.

2.2 Current MOX use in NPP

MOX fuel was first used in a thermal reactor in 1963, but did not come into commercial use until the 1980s. So far, about 2000 t of MOX fuel has been fabricated and loaded into power reactors. In 2006 about 180 t of MOX fuel was loaded into over 30 reactors (mostly PWR) in Europe[3]. Currently, about 40 reactors in Europe (in Belgium, Switzerland, Germany and France) are licensed to use MOX, and over 30 are doing so. France aims to have all its 900 MWe series of reactors running with at least one third of the core composed by MOX. Some advanced reactor will accept up to 50% MOX assemblies. Other advanced PWR such as the EPR or AP1000 are able to accept 100% fuel loadings of MOX if required. In Japan, about ten reactors are licensed to use it and several do so. These reactors are generally loaded with a mixed core where MOX fuel content is about one third.

An advantage of MOX is that the fissile concentration of the fuel can be increased easily by adding a bit more plutonium, whereas enriching uranium to higher levels of U^{-235} is relatively expensive. As reactor operators seek to burn fuel harder and longer, increasing burn-up from around 30 MWd/kg a few years ago to over 50 MWd/kg now, makes the use of MOX more attractive[13]. MOX fuel is designed to satisfy the same operational and safety criteria as uranium fuel under equivalent conditions. This is reflected in the parallel development of design codes to accommodate the specific characteristics of MOX fuel. MOX fuel assembly design has been universally based on uranium fuel design with only minor modifications relating to the neutronic and thermo-mechanical properties of the MOX fuel itself[14].

The main concerns for MOX fuel rod behavior are as follows[3]:

- fuel center line temperature
- fission gas release
- in-pile densification and swelling
- helium gas accumulation and release
- pellet–cladding mechanical interaction (PCMI) under power ramping.

However, since the plutonium concentration of MOX fuel for LWRs is low and these differences from uranium fuel are relatively small, it is recognized that MOX fuel rod behavior is very similar to that of standard uranium fuel. No additional problems are apparent with the possible exception of higher gas release and hence an increase of rod internal pressure at high burn-up.

Because of the neutronic properties of the plutonium isotopes in MOX fuel, the reactivity decreases less rapidly with burn-up than in uranium fuel and thus MOX fuel dissipates more power later in its life, releasing more fission gas. In addition, the thermal conductivity of MOX is known to be lower than that of uranium by a few percent, which may give rise to higher fuel temperatures and thus higher fission gas release. Design changes, such as lowering the initial helium pressure and/or increasing the plenum volume in the rod, are sometimes applied to accommodate this higher gas release. With these exception, the fuel rod and assembly design are essentially unchanged from that of an equivalent uranium assembly. Generally, if a modification is applied to uranium fuel, then the same change will be incorporated in MOX fuel after, due evaluation of the experience with uranium fuel.

National and international programs to evaluate the performance of MOX fuel compared with that of uranium fuel have been carried out over a period of 35 years. These programs, which are still ongoing, are providing the data necessary to compare MOX fuel behavior with that of uranium, to develop specific MOX fuel performance models and to verify design codes. A wide range of variables has been investigated in these experiments, for example fabrication processes, cladding materials, fuel rod geometries and operating conditions. Post-irradiation examination (PIE) of commercial MOX fuel has also added a lot of data on performance and reliability. It has been concluded from both experimental and commercial irradiations that the reliability of MOX fuel remains as good as that of uranium fuel.

2.3 UO_2 – MOX fuels main differences

Because of the extremely large uranium fuel performance database and the corresponding well validated codes, it is important to define differences in structure and performance of MOX and uranium fuels. In this section, we briefly review the thermo-physical properties of MOX fuel and compare them with those of UO_2 fuel.

2.3.1   Melting temperature

Solidus and liquidus temperatures of uranium/plutonium dioxide data and correlations have been recently reviewed by Carbajo et al[4]. The Introduction of PuO_2 in UO_2 reduces the melting temperature of fuel being the melting temperature reduction an increasing function of the PuO_2 content. The burn-up and/or the deviation from stoichiometry lowers the melting temperature too. In addition, since the stoichiometry of the fuel changes/redistributes depending on the burn-up these contributions are interrelated. An empirical correlation, based on curve fitting of the data introduced by Adamson et al.[15], is recommended for applications. These curves are reported in *Fig. 4* for standard LWR fuels between 0 and 70 MWd/kgHM. The MOX melting temperature is about 50°C lower respect to the UO_2.
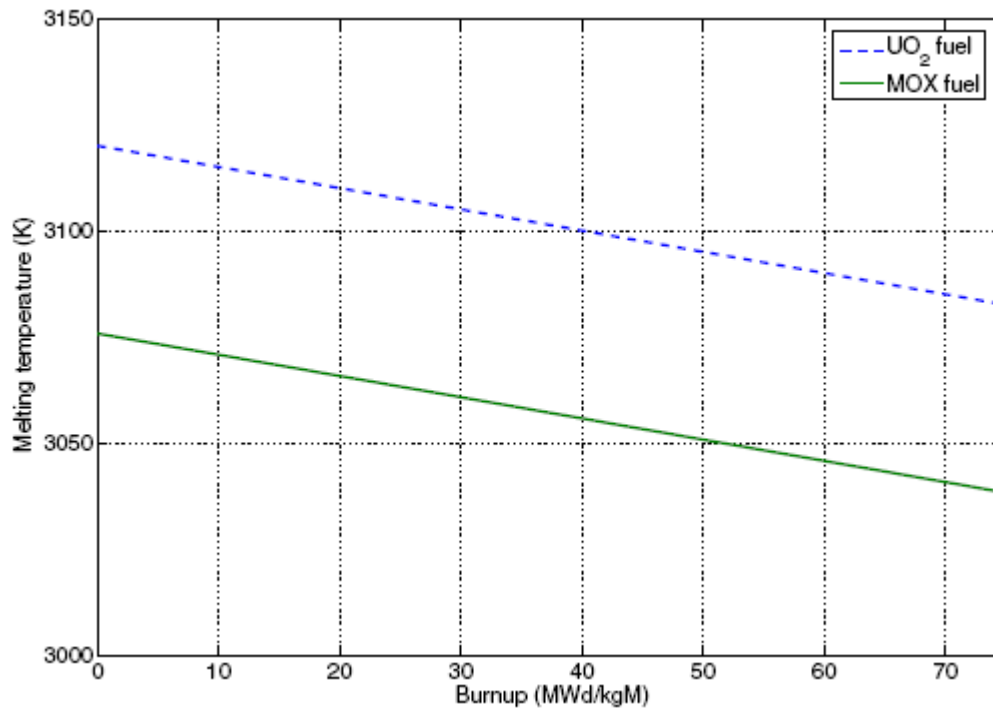
Fig. 4 – Melting temperature of UO₂ and MOX fuels as a function of burn-up according to Adamson at al.

2.3.2 Thermal Conductivity

The thermal conductivity of oxide fuels is a function of temperature, composition, density, oxygen content (oxygen-to-metal ratio, O/M) or the deviation from stoichiometry, and the fuel burn-up. The thermal conductivities of both UO_2 and MOX are reduced with temperature up to around 2000 K and then rise with temperature. The addition of PuO_2 into the UO_2 matrix reduces the thermal conductivity because of fuel heterogeneity. Moreover, the deviation of O/M from stoichiometry reduces the thermal conductivity. The fuel burn-up reduces the fuel conductivity due to the creation of FP with lower conductivity and due to the creation of new porosity. Furthermore, at high burn-ups (locally exceeding 75 MWd/kgU), the formation of the High Burn-up Structure at pellet rim locally degrades the conductivity.

There is a large amount of data and correlations for the thermal conductivity of fuel. The data are not so extensive for MOX fuel as they are for UO_2 fuel. Since 1980, theoretical research and new measurements have led to improvements in equations for thermal conductivity of un-irradiated UO_2. Recent reviews of the thermal conductivity of MOX fuel[16],[17] conclude that the presence of small quantities of PuO_2 in UO_2 slightly decreases the thermal conductivity. For example, KAERI[18] describes this degradation as a two phase material with different thermal conductivities in the matrix and in the plutonium-rich agglomerates (the reduction of thermal conductivity ranges from 7 to 10%). BNFL[19] applies a uniform degradation of 8%, while Framatome and Belgie-Nucleaire apply a linear degradation with the plutonium content[20],[21]. In-pile measurements of the centerline temperature of MOX fuel clearly indicate the slight degradation of thermal conductivity of fresh fuel[22],[23]. Measurement of the fuel center temperature of MOX irradiated to 50 MW·d/(kg HM) showed that the thermal conductivity degradation with burn-up in MOX is the approximately same as that in uranium fuel[20], *Fig. 5* and *Fig. 6*.
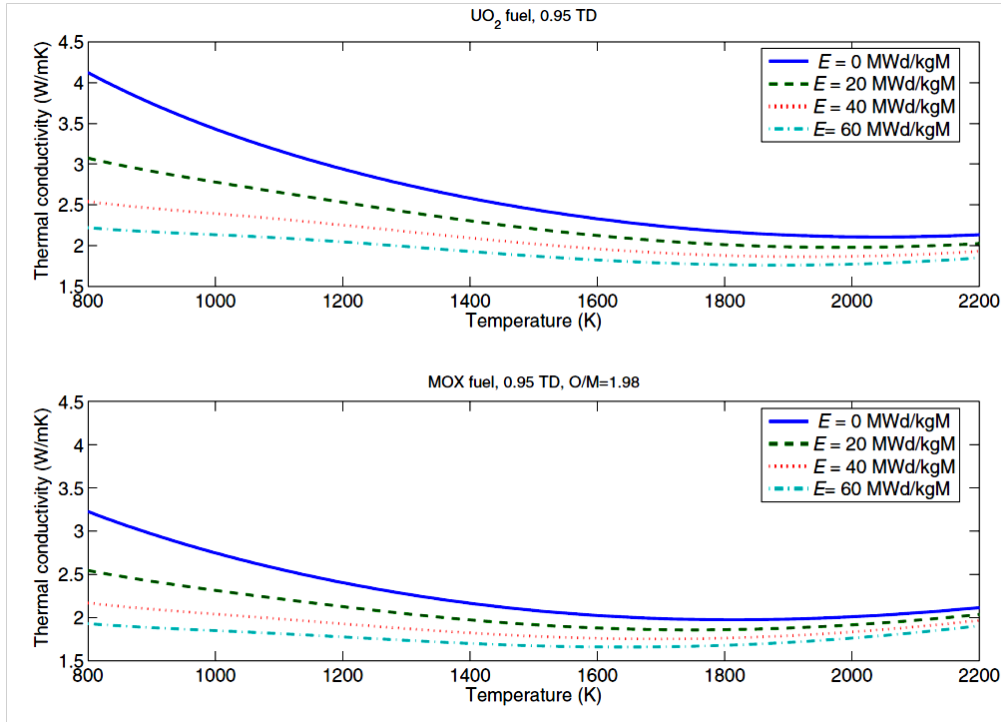
Fig. 5 – Thermal conductivity as a function of temperature at different burn-ups for UO₂ and MOX fuel according to the correlation of Lanning at al.
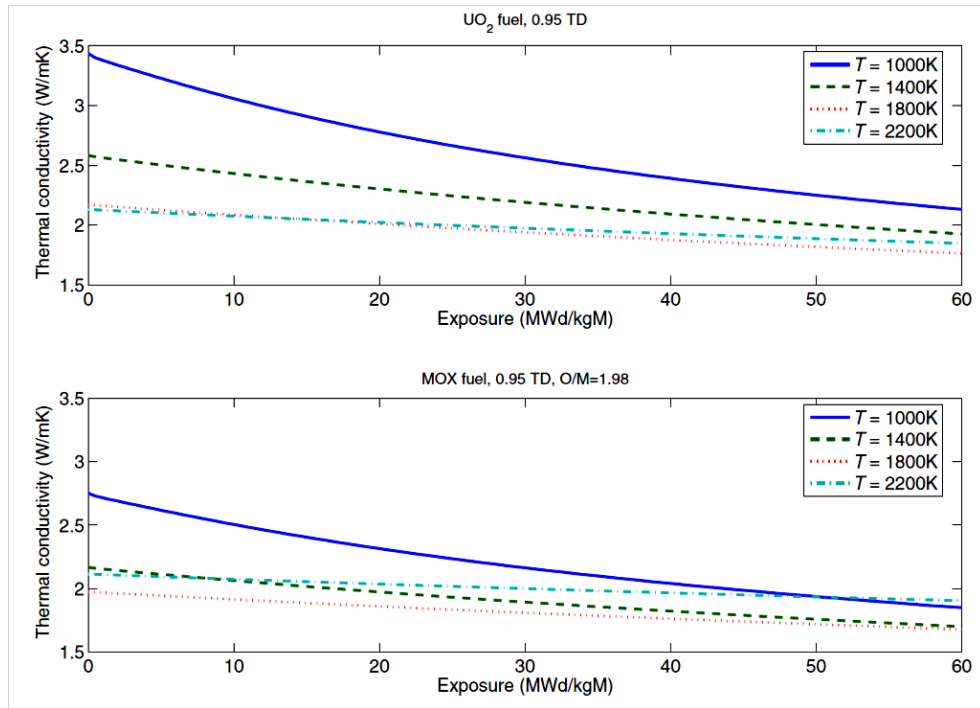
Fig. 6 – Thermal conductivity as a function of burn-up at different temperatures for UO₂ and MOX fuel according to the correlation of Lanning at al.

2.3.3 Radial power and burn-up profile

The neutronic properties of MOX fuel are responsible for a decrease in reactivity with burn-up that is markedly less pronounced than that in uranium fuel. This leads to higher power densities at higher burn-ups in comparison with uranium assemblies. Moreover, the presence of plutonium in the pellet increases the thermal flux depression towards the centre, due to the large absorption of thermal

neutrons by the plutonium isotopes. At the beginning of the MOX fuel life, the radial power profile is therefore more depressed than that in uranium fuel, whereas at end of life the higher residual plutonium content at the fuel center leads to higher local powers[20].

2.3.4 Densification

Oxide ceramic fuels like UO_2 and MOX are subjected to densification during the early stages of reactor irradiation. This phenomenon causes disappearance of submicron pores that led to a general fuel column lengthening, gap opening and pellet density increase. At a given burn-up, this process end. Furthermore, swelling and relocation oppose to its effects. Modeling fuel pellet relocation, swelling and densification is essential for the prediction of the thermal-mechanical behavior of fuel rod during irradiation.

The maximum fuel densification is reached at low burn-up (below 10 MWd/kg) and causes high fuel temperatures due to the gap thickness increase. The densification is therefore an important process to take in account for fuel safety evaluation. It is known that the irradiation induced densification of UO_2 sintered fuel pellet is dependent on a combination of grain size, mean pore size and pore size distribution[24][25]. In particular, investigation on UO_2 fuel showed that the stable fuel types (with low densifications) were characterized by grain sizes greater than 10 μm and median volume pores larger than 1 μm. The same general behavior was observed in MOX fuel, i.e., fuels with grain sizes greater than 10 μm and median pores larger than 6 μm were highly stable[24][25]. Moreover, in MOX fuel, because of the presence of Pu agglomerates one expects that Pu-rich zones give rise to high local fission rates and temperatures that affect fuel densification. In spite of the expected differences between UO_2 and MOX fuel, the comprehensive study made by Freshley et al.[24][25] on a variety of MOX fuels indicated that:

- The in-reactor densification of MOX fuel, as in UO_2, is correlated to the density changes that occur under ex-reactor isothermal re-sintering tests, for a given fabrication process.
- Generally, the densification behavior of MOX fuel is comparable with that of UO_2 fuel, i.e., the Pu-rich agglomerates have no apparent effect on the densification.
- The effects of fission rate and temperature on densification of MOX fuel are similar to those observed on UO_2 fuel.

The majority of models used to describe in-reactor densification in fuel performance codes are empirically based, correlating the change in density ρ_D to fuel burn-up by a simple relation, for example:

$$\rho_D = p_D \left(1 - exp(-bu / bu_D)\right) \qquad Eq.\ 2$$

where p_D is the maximum densification (or unstable porosity) and bu is the burn-up and bu_D is a densification-related burn-up constant (burn-up at which densification end). We observe that at lower temperatures and lower fission rates, the densification is considerably smaller for both UO_2 and MOX. These effects are taken in account changing the values of the constants in the equations. The maximum porosity reduction is related to the grain size as shown in the following equation based on experimental data of UO_2 and MOX fuels[26],[27]:

$$p_D = p_0 \left(2.23 / d\right) \qquad Eq.\ 3$$

where p_0 is the initial porosity and d is the average fuel grain size. However, *Fig. 7* shows that the deviations from this general behavior can be rather large especially in small grains fuels.
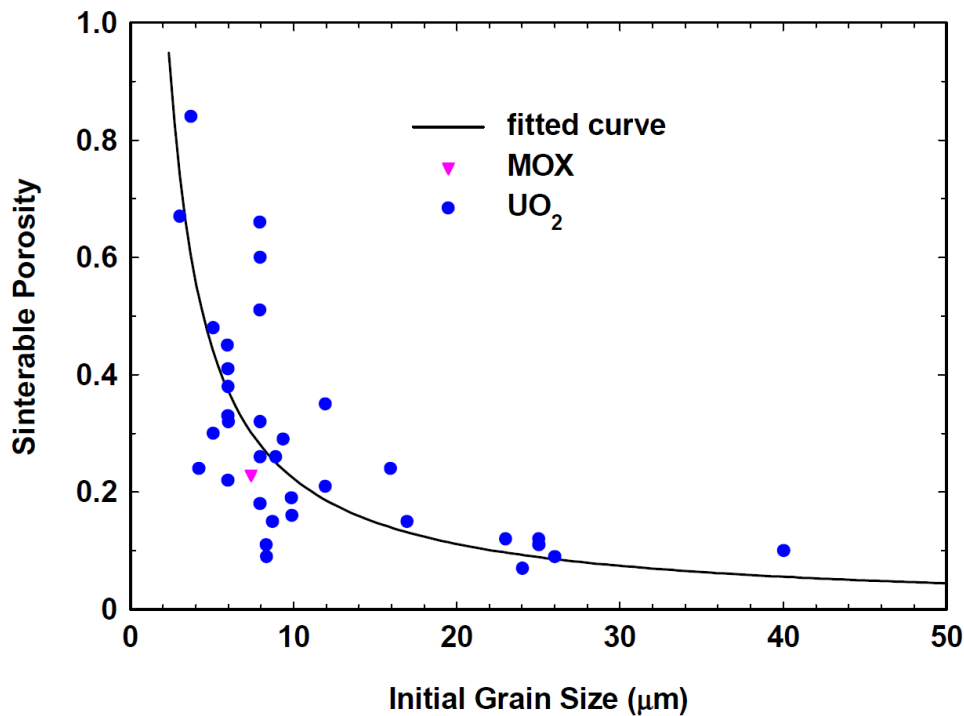
Fig. 7 – Sinter-able porosity correlation.

2.3.5 Swelling

The swelling of fuel has two components: solid fission product swelling and gaseous swelling. The former is commonly taken to be an increasing linear function of burn-up, i.e,

$$\rho_s = c\ (bu) \qquad\qquad Eq.\ 4$$

where ρ_s is the change in fuel density due to solid swelling and c is a parameter in the range 0.6 to 1.0 % / 10MWd/kgHM[5]. These considerations apply both to UO_2 and MOX.

The gaseous swelling is more complex depending on temperature and fission product gas inventory in fuel pellet. The gaseous swelling kinetics may be different in MOX fuel than in UO_2 because of the difference in fission gas release of the two fuels. A more precise kinetic model for densification and swelling should account for both fuel macrostructure (median pore size, grain size, and Pu agglomerate size) and external fields (temperature and local fission rate).

2.3.6 Fission gas release

Several physical processes contribute to FGR in UO_2 as well as in MOX fuels. They are usually separated into a-thermal and thermal release mechanisms. A-thermal release takes place by recoil and knockout of fission gas atoms by energetic fission fragments. Since these mechanisms generally result in release of less than 1%, a-thermal release alone has to date not been considered a potential problem for excessive fuel rod pressure build-up. However, there is concern that the restructuring of UO_2 at high burn-up, the so called rim zone formation (HBS), could enhance a-thermal FGR in high burn-up fuel. FGR process in MOX fuel is to a certain extent similar to that of UO_2. However, there are certain particular structural differences between the two kinds of fuel, which makes MOX fuel release different in certain conditions; notwithstanding the fact that post irradiation examinations of fuel rods irradiated in LWR indicate that gas release from MOX fuel is higher than from UO_2 fuel under similar operating conditions (*Fig. 8*).

The complexity of MOX fuel microstructure, both before and during irradiation, and the higher centerline temperature of MOX fuel in comparison with uranium fuel makes it difficult to get a simple view of FGR from these fuels for the whole range of heat rates, burn-ups and fabrication technologies. In experimental programs carried out in the Halden reactor, in-pile pressure measurements performed at different burn-ups showed that the empirical threshold for significant fission gas release (>1%) derived by Vitanza[7] for uranium fuel also applies to MOX fuel[28],[29]. However, the fission gas release of MOX fuels with can be expected to differ from that of uranium fuel because of the concentration of burn-up and fission products in the plutonium rich agglomerates. In fact, due to the limited range of fission fragments, there could be large regions of the fuel which are effectively un-irradiated. Fission gas release would then depend on the diffusion of gas through un-irradiated regions in which inter-linked micro-structures were absent. Experimental results[30] revealed examples of FGR continuing during low power/temperature holds (seepage effect). It suggests that the inter-linkage of MOX fuel occurs with the same temperature-burn-up characteristics as UO_2 fuel, suggesting that the fission gas diffusion coefficients are similar. However, there are possible indications that the post-inter-linkage release proceeds more rapidly[28],[31]. These phenomena, however, require further clarifications.

However, it should be noticed that the difference in fission gas release between MOX fuel and uranium fuel decreases when the homogeneity of the plutonium distribution is improved. This has also been confirmed by the low fission gas release from irradiated MOX fuels with good homogeneity of the plutonium distribution[3]. The use of existing uranium fuel fission gas release models for MOX fuel applications has been reported to give satisfactory results for fission gas release and rod pressure evaluations[20].
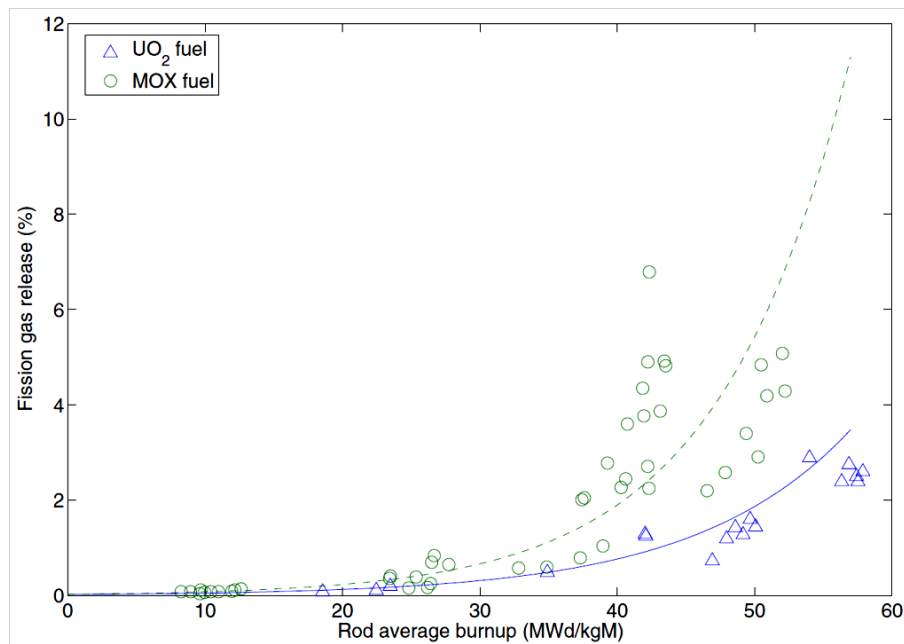
Fig. 8 – Fission gas release fraction as a function of burn-up for UO₂ and MOX fuel rods measured in PWRs (Blanpain et al., 2000 and IAEA, 2003).

2.3.7   Helium generation and release

Helium is generated in fuel matrices by alpha decay of transuranic nuclides and ternary fission, the former being the major source. Therefore, helium accumulation in the matrices, especially in MOX fuels (about four times that in uranium fuels), increases exponentially with burn-up. Studies of helium behavior showed that the helium diffusion coefficient in UO_2 is about three orders of magnitude larger than that of fission gases and also that helium is highly soluble in UO_2[3]. Helium is not released from the fuel as long as its content does not exceed the solubility limit, which depends on the helium partial pressure in the rod. Hence, no helium release is observed in pre-pressurized MOX rods (>20 bar) over a broad range of burn-ups and operating conditions. However, significant helium release is observed in low pre-pressurized BWR MOX fuel rods[32].

Since in the standard diffusion theory of fission gas release, the release fraction is proportional to the square root of diffusivity, one expects that in both MOX and UO_2 fuels the helium release rate should be about 30 times larger than that of xenon. However, the concentration of helium in fuel is small relative to the concentration of the remaining gaseous fission product, helium atoms do not form their own gas bubbles. Instead the generated helium atoms diffuse to grain boundary and get trapped into the inter-granular fission products gas bubbles. These bubbles eventually grow and interlink; and the tunnel through the fuel structure is formed and transfers gas to the free volume of the pin. The analysis conducted by Kamimura et al.'s[32] indicates that the similarity between the helium release fraction of MOX fuel and UO_2 implies that in both fuels the released helium volume is strongly proportional to their production. The proportion of helium production to the FP gas production is about 0.1 for MOX fuel and 0.025 for UO_2. This difference between MOX and UO_2 fuel justifies greater consequence of helium release in MOX fuel[32].

3 Description of the experiments

3.1 The PRIMO program

The PWR Reference Irradiation of MOX Fuels (PRIMO) program started in October 1986[10]. It was jointly organized by the Studiecentrumvoor Kernenergie Centre d'Études de l'Énergie Nucléaire (SCK•CEN) and Belgonucléaire (BN) and was co-sponsored by ten participants including fuel vendors, utilities, nuclear centers and national authorities. The PRIMO program sought to investigate MOX fuel, with the following major objectives:

- Irradiation of MOX fuel rods at different burn-up stages and following power histories representative of those of PWR power plants to determine their behavior under irradiation. The data obtained have been used for the following purposes:
  - To demonstrate the ability of the MOX fuel rods to sustain irradiation conditions comparable to uranium dioxide fuel.
  - To better understand the influence of the fabrication process on the fuel behavior.
  - To benchmark the thermo-mechanical codes for MOX fuel calculations.
- To investigate the following phenomena:
  - Mechanical behavior under steady-state operation: pellet-cladding interaction, ridging effects, fuel swelling and creep.
  - Thermal behavior: fission gas release, grain growth, fuel diffusion effects.
  - Nuclear behavior: burn-up radial profiles and U/Pu isotopic effects, versus burn-up.
- To carry out a ramp test programme, to find out the failure threshold of MOX fuel rods and to obtain mechanical and thermal data under ramp conditions. The ramp tests were carried out on selected fuel types, at various burn-up levels. The ramp conditions (ramp rate, terminal power and hold time) were chosen such that the results can be compared to existing results on UO_2 fuel.

These objectives were met through extensive post-irradiation examinations (PIE) in hot cells.

The experiment included the irradiation of sixteen PWR MOX fueled rods. They can be grouped in four main types groups, which differ in the fabrication process as follows:

- Four rods, named "R", are manufactured by BN with UO_2-PuO_2 powder mechanical blending process (reference process). Among these rods, three have been taken from the old BR3/A4 fabrication campaign (1975), (designated as "RA" rods); and, the last one, is taken from the more recent BR3/4D campaign (1983, designated as "RD" rod).
- Eight rods, named "BN", are manufactured by BN with the MIMAS process. Among these rods, six are from the first BR3/4D MIMAS fabrication campaign (1983), (named "BD" rods), and the remaining two are from a more recent BR3/4E fabrication campaign (1985, named "BE" rods).
- Three rods, named "ME" are manufactured at BN (Dessel plant) for Mitsubishi Heavy Industries (MHI), using the MIMAS process as well. They differ from BD and BE rods in the design specifications (i.e. pellet size, cladding properties, gap size).
- One rod, named "SL" is manufactured at BN (Dessel plant) for FRAGEMA, using the MIMAS process. It differs from the previous rods in the design specifications.

These rods were base-irradiated in the BR-3 reactor (Mol, Belgium) up to an average burn-up ranging between 20 - 60 MWd/tHM. Non-destructive PIE were performed after the base irradiation and then eight selected rods were delivered to the OSIRIS reactor (Saclay, France) where they experienced

power ramp tests up to a peak linear power of 35.0- 47.5 kW/m. After the power ramp, non-destructive and selective destructive PIE were executed. The non-failed rods were punctured for FGR measurement. Ceramography, density, thermal diffusivity, EPMA and SIMS measurement were carried out.

Among these rods, the data provided in this report concern the BD8 fuel rod manufactured at Belgonucleaire using the MIMAS (Micronized Master Blend) process (1983). Rod BD8 was irradiated in the BR-3 SCK•CEN reactor during cycles 4D1 and 4D2 up to a peak burn-up of 30.1 GWd/tHM prior to being transferred to the ISOBELLE 1 loop for ramping in OSIRIS. During the base irradiation, the BR-3 reactor nominal power was 40.9 MWth (11.4 MWe). The primary circuit operating pressure was 140 atm.

BN and SCK•CEN provided the data (fabrication and irradiation) of rod BD8 to the OECD-NEA Expert Group[10]. This group was established by OECD/NEA Nuclear Science Committee (NSC) with the aim to deal with the status and trends of reactor physics, nuclear fuel performance and fuel cycle issues related to the disposition of weapons-grade plutonium as mixed-oxide (MOX) fuel. Among the tasks of this group, fuel pin mechanics code benchmarking activities were performed based on rod BD-8. The datasets of this rod are also included in the International Fuel Pin performance Experimental database (IFPE[9]).

3.1.1 The BR3 reactor

BR3 was the first PWR installed in Europe with a capacity of 11 MWe (40.9 MW th), *Tab. 3*. It was operated from 1962 to 1987 at Mol, Belgium[33]. It is currently under decommissioning. Its main utilization focused on operators training for the Belgian utilities and on the testing of new fuels on behalf of research centers and nuclear fuel suppliers. The BR-3 driver fuel and test fuels were similar to PWR fuels, made of UO_2 or UO_2/PuO_2(MOX) with stainless steel and later Zircaloy cladding. The exotic character of the fuels stayed in the large variety of enrichments used (up to 8.6 % ^{235}U and 10% fissile Pu), and in the specifications of the fuel and cladding materials.

Characteristic	**Unit**	**Value**
Average reactor thermal power	MW_{th}	40.9
Coolant temperature at core inlet	°C	252-257
Coolant temperature at core outlet	°C	264-269
Mass flow rate	kg/s	9.4
Average system pressure	MPa	14
Active length of core	m	1

Tab. 3 – BR-3 Reactor, main characteristics.

3.1.2 The OSIRIS reactor

OSIRIS is an experimental reactor with a thermal power of 70 MW[34], *Tab. 4*. It is a LWR, open-core, pool type reactor located at Saclay (France). The main aim of OSIRIS is to carry out tests and irradiate fuel elements and structural materials of nuclear power stations under an high flux of neutrons, and to produce radio-isotopes for medical purposes. The open-core, pool-type reactor allows to directly access the core. The reactor core is depicted in *Fig. 9*. It is capable to house up to 16 experimental devices in 4 different positions. The fast neutron flux (E>1MeV) reaches $2.2*10^{14}$n cm^{-2}s^{-1} in the experimental position 64[35]. Structures are also provided outside the core, on 3 faces of the vessel, making it possible to install up to 27 experimental devices on the first periphery, where the maximum fast neutron flux is 10 times weaker than in the core. Many others facilities can be placed on the second and third peripheries. Among these position, power ramping can be experienced in ISABELLE

1 and ISABELLE 4 loops. ISABELLE 1 was used for the power ramp test of the rod BD8. The experimental load consists of a short fuel rod, either new or re-manufactured. The power that can be evacuated by the loop is 60 kW and the maximum linear power on the fuel element is 620 W cm^{-1} with a maximum ramp speed of 700 W.cm^{-1} min^{-1}.The design of the ISABELLE 1 loop and its positioning on the periphery of the core enable irradiation and withdrawal with the reactor in operation. The loop is placed on mobile supports, the displacement of which, in relation to the core of the reactor, is used either to adjust the power of the fuel element, or to automatically control the power ramps or the cycles at variable speeds. The power released by the experimental load during irradiation is measured in real time by a heat balance produced by means of the flux, pressure and temperature sensors, as well as by a neutron balance. The ISABELLE 1 loop is also equipped with a LVDT type elongation measurements sensor to continuously monitor the lengthening of the fuel element during variations in power.

Characteristic	**Unit**	**Value**
Thermal power	MWth	70
Moderator	--	H_2O
Reflector	--	H_2O
In core Thermal flux	n/(cm^{2}s)	$3*10^{14}$
In core Fast flux	n/(cm^{2}s); (E>0.1MeV)	$4.5*10^{12}$
Core dimensions	m	0.57x0.57x0.60
Number of fuel el.	--	38
Number of control el.	--	6
Control el. material	--	Hafnium
Fuel	--	U_3SI_2Al
Fuel enrichment	%	19.75
Core inlet temperature	°C	38
Core outlet temperature	°C	47
Pool average temperature	°C	35
Primary Core flow rate	m^3/h (upward)	5600
Pool flow rate	m^3/h (downward)	500

Tab. 4 – OSIRIS Reactor main characteristics.
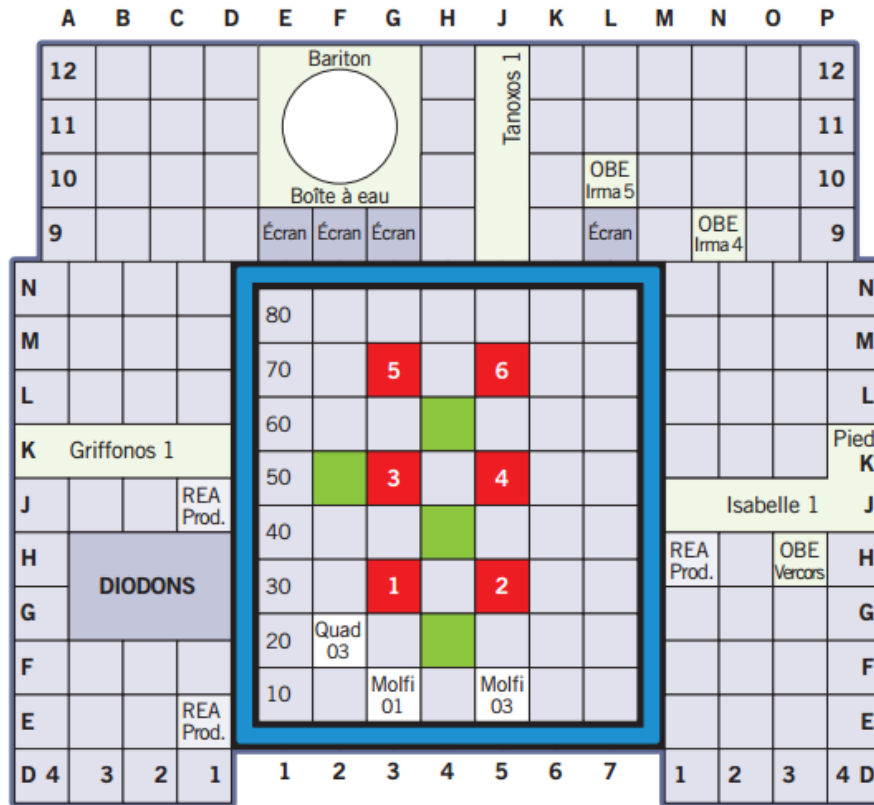
Fig. 9 – OSIRIS reactor core layout.

3.1.3 BD8 rod design

Fuel rod BD8 was manufactured at BN in 1983, the industrial process adopted was the MIMAS process (Micronized Master Blend, widely used for the fabrication of LWR MOX fuel pellets). The size of initial agglomerates and U-Pu inter diffusion phenomena during the sintering process influence the local enrichment of fissile elements. As result, the presence of Pu-rich particles, up to 30% of PuO_2, is observed in the fresh fuel[10].

The overall length of the BD8 rod is 1136mm with an active length, occupied by MOX fuel pellets, of 1005 mm, *Fig. 10* and *Fig. 11*. All the MOX fuel pellets were manufactured by BN in its Dessel plant (sintering conditions: 1700°C, 1 h under Ar+5%H_2). Three UO_2 blanket pellets were loaded at the bottom end of the mixed-oxide fuel stacks. The UO_2-depleted fuel pellets were manufactured by Franco Belge de Fabrication de Combustible (FBFC) in its Dessel plant. The summary of the fuel main data is given in *Tab. 5* and *Tab. 6*. The cladding tube is seamless Zircaloy 4 manufactured by Mannesmann Röhrenwerke (Germany) from an ingot provided by TWCA, Oregon (USA), *Tab. 7*, *Tab. 8*. The tube was stress-relieved at 460°C during 2.5 hours. A spring made of stainless steel was placed in the upper plenum free space, in order to avoid the formation of inter-pellet gaps during the rod handling. A 20 mm long spacer ring made of Zy4 was inserted in the fuel rod between the spring and the top fuel pellet.

Pellet characteristic	Unit	Value
Fabrication lot	--	BN lot IL 123
Diameter*	mm	8.034, 8.041, 8.046
Length*	mm	8.591, 9.222, 9.667
Shoulder* (side 1)	mm	0.811, 0.864, 0.903
Shoulder* (side 2)	mm	0.830, 0.883, 0.934
Dish volume* (side 1)	%	0.947, 1.011, 1.095
Dish volume* (side2)	%	0.903, 0.961, 1.051
Chamfer width* (side 1)	mm	0.274, 0.293, 0.324
Chamfer width* (side 2)	mm	0.297, 0.323, 0.344
Chamfer height* (side 1)	mm	0.102, 0.135, 0.166
Chamfer height* (side 2)	mm	0.132, 0.149, 0.170
O/M	--	1.991
^{238}U concentration**	% HM	84.68
^{235}U concentration**	% HM	5.24
^{239}Pu concentration**	% HM	7.63
^{240}Pu concentration**	% HM	2.10
^{241}Pu concentration**	% HM	0.28
^{242}Pu concentration**	% HM	0.07
Mean UO_2 grain size***	μm	5
Mean PuO_2-rich particle size	μm	21.3
Max. PuO_2-rich particle size	μm	214
Pellet surface roughness	μm	2
Density	% TD	94.64
* minimum, average, maximum value **** ** isotopic composition in October 1983 *** mean linear intercept		

Tab. 5 – PRIMO Program, rod BD8, fuel pellets characteristics.

Pellet characteristic	Unit	Value
Fabrication lot	--	BN lot 6303
Diameter	mm	8.044
Length	mm	1.994
Chamfer width (both sides)	mm	0.5
Chamfer height (both sides)	mm	0.5
O/M	--	1.994
^{238}U concentration*	% HM	99.65
^{235}U concentration*	% HM	0.35
Mean UO_2 grain size**	μm	14
Density	% TD	95.40
* isotopic composition in October 1983 ** mean linear intercept		

Tab. 6 – PRIMO Program, rod BD8, depleted uranium pellets characteristics.

Cladding characteristic	Unit	Value
Outer diameter*	mm	9.492, 9.510
Inner diameter*	mm	8.232, 8.250
Minimum wall thickness	mm	0.58
Inner surface transversal roughness	μm	3.2
Outer surface transversal roughness	μm	2.8
Tensile test temperature	°C	400
Ultimate strength	kg/mm^2	39.3
Yield strength	kg/mm^2	31.4
Elongation	%	17.8
Hydride orientation (Fn)*	--	0.04, 0.15
Grain size	μm	10
Hydrogen content	ppm	11
Oxygen content	ppm	1170
Vickers Hardness (HV200)*	--	205-214
* minimum and maximum value		

Tab. 7 – PRIMO Program, rod BD8, cladding tube characteristics.

Rod characteristic	Unit	Value
Diametric gap	μm	200
Pre-pressurization (He)	kg/cm^2	20
Uranium weight*	g	412.6
Plutonium weight	g	46.4
(U,Pu)O$_2$ weight	g	521.1
UO$_2$ weight	g	19.4
Fuel length	mm	1004.7
DU pellets length	mm	36.5
Plenum length**	mm	40.0
Total rod length	mm	1136.2
Rod free volume***	cm^3	5.7
*In MOX fuel column only.		
** Spacer tube excluded.		
*** Including: upper plenum, gap, dishes, chamfers, free volume in upper plug. Open porosity not included.		

Tab. 8 – PRIMO Program, rod BD8, fuel pin characteristics.
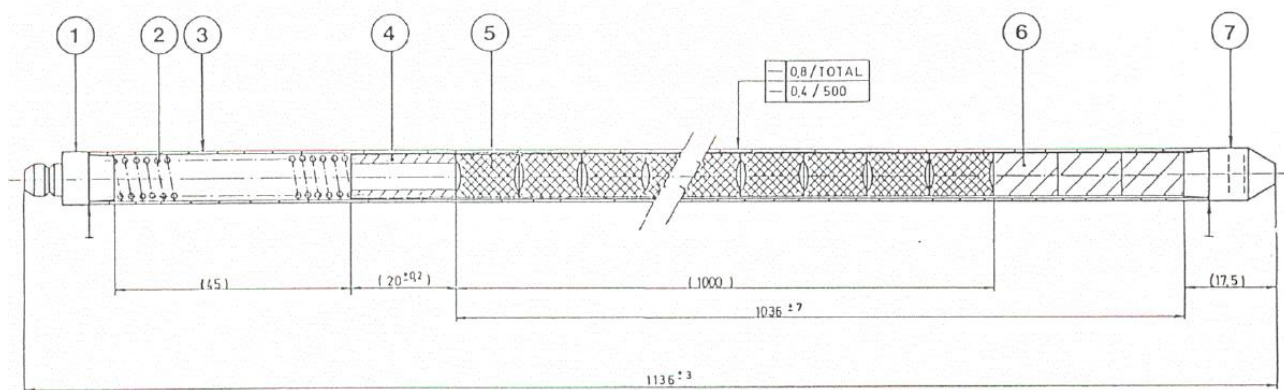
1– lower plug; 2 – lower plenum spring; 3 – cladding tube; 4 – spacer tube; 5 – MOX fuel pellets; 6 – depleted Uranium pellets; 7 – upper plug.

Fig. 10 – PRIMO Program, general layout of rod BD8.
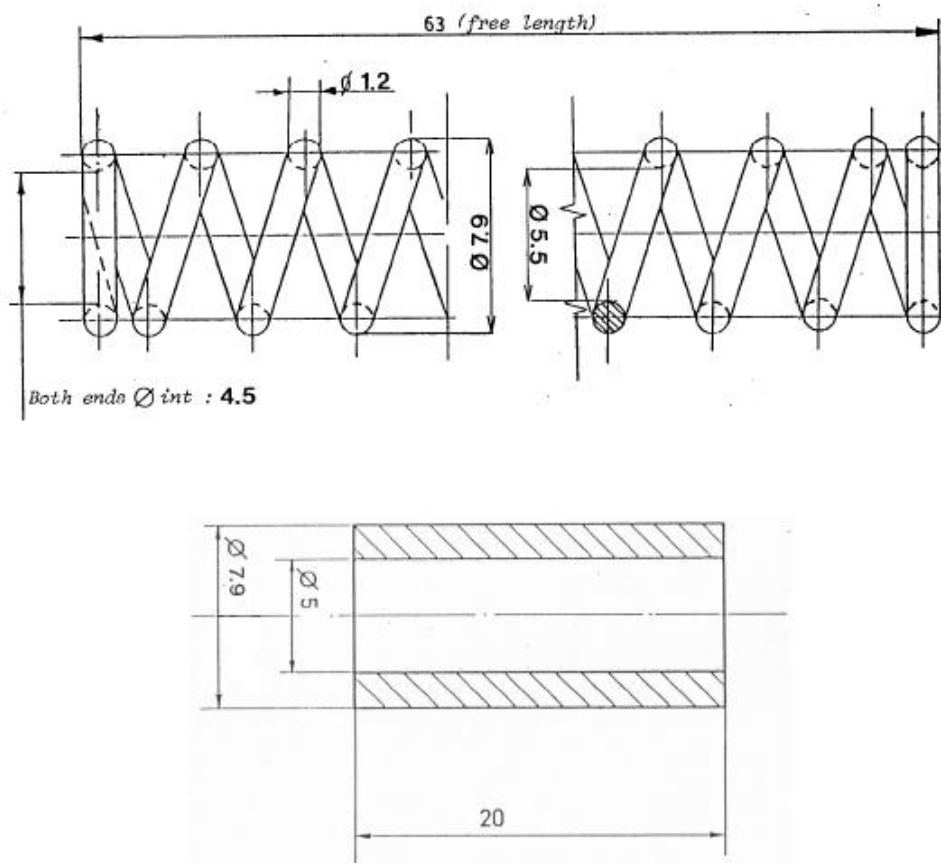
Fig. 11 – PRIMO Program, rod BD8, hold down spring and spacer tube.

3.1.4 Base irradiation

Rod BD8 was base irradiated in the BR3 reactor of SCK•CEN. During cycle 4D1 (413 days, from 13/07/1984 until 11/11/1985), the rod accumulated an average burn-up of 18.0 MWd/kgHM. During cycle 4D2 (333 days, from 03/07/1986 until 30/06/1987), the average rod burn-up reached 30.1 MWd/kgHM[10].

The average temperature of the coolant was maintained at 262.5°C; power changes were compensated by adapting the mass flow rate. Coolant inlet temperature was 255°C, and the mean outlet temperature at nominal power reached 270°C. The PRIMO MOX fuel rods were loaded in special dismountable assembly in the BR3 reactor; this assembly was designed "ad hoc" for the BR3 – core 4 with the 17x17 configuration. The mean flow area for the 17×17 assembly was 42.65 cm^2 and the mass flow rate passing through the assembly was 9.4 kg/s (specific flow rate 220 g/cm^{2}s); the hydraulic diameter in cold conditions is 14.93 m.

The linear power has been calculated by means of the 2-D diffusion code CONDOR[10]. The geometrical X-Y model covered the entire core for cycles 4D1 and 4D2. An R-Z model was used in order to obtain information on the axial behavior. Nuclear constants were obtained from the cell code PANTHER[10]. The axial effects such as variation of water density, variation of xenon density are taken into account in the results. For the rod power calculations, the actual reactor power history of each cycle has been subdivided into constant power time steps (i.e. histogram format). The step lengths have been made small enough to ensure that the power does not vary more than a few percent around the given mean values. The base irradiation power history at peak axial position and the axial power shapes in the two cycles are shown, respectively, in *Fig. 12* and *Fig. 13*.
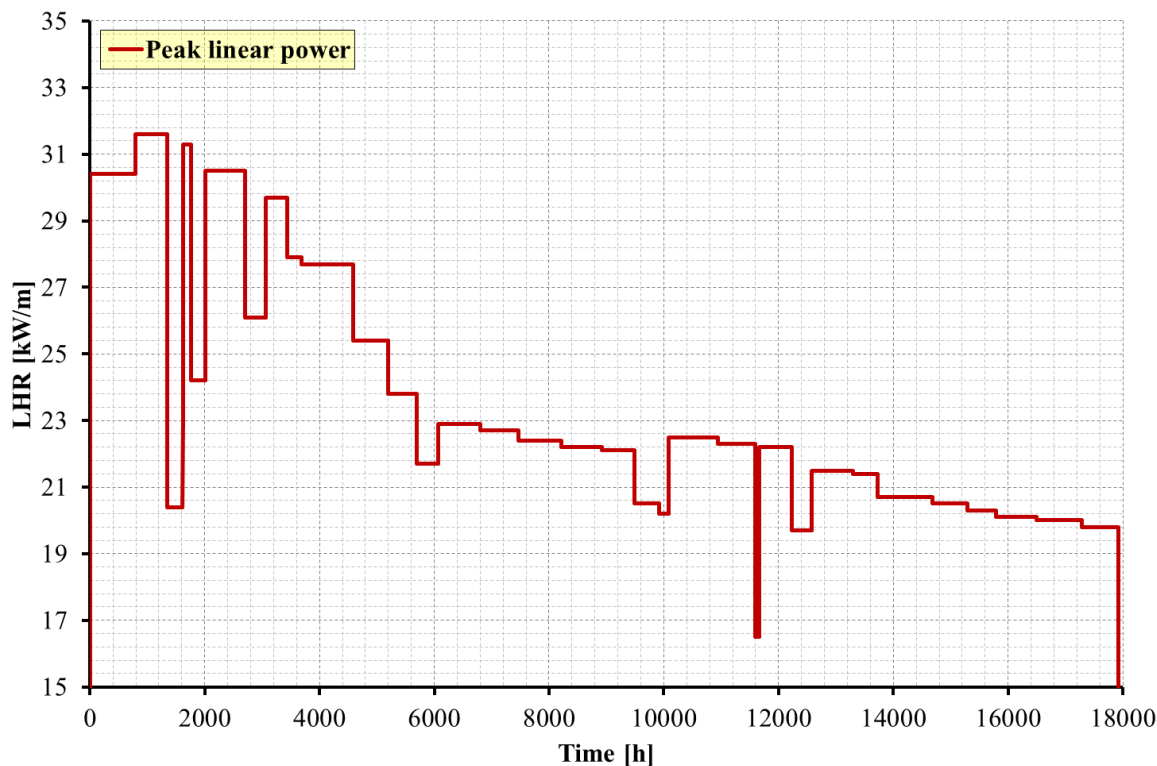
Fig. 12 – PRIMO Program, rod BD8, linear heat rate at the peak point during base irradiation.
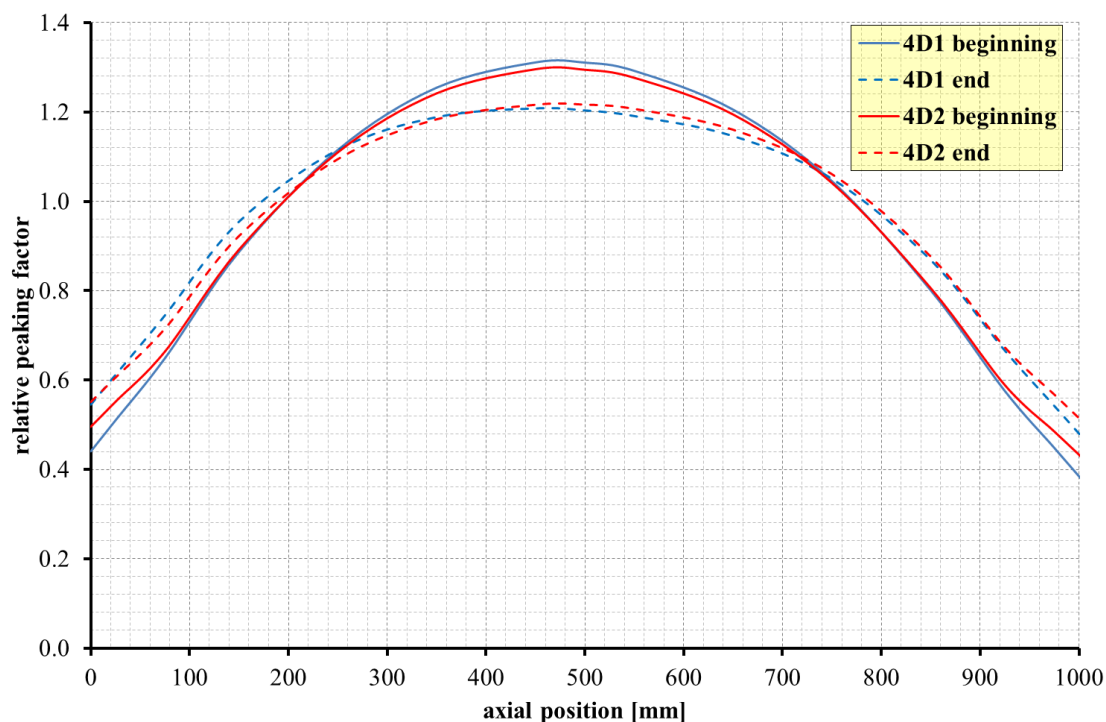
Fig. 13 – PRIMO Program, rod BD8, relative axial power profile, BR3-4D1 and BR3-4D2 cycle.

3.1.5 Power ramp irradiation

After the base irradiation, the BD8 rod was transported to CEA-Saclay for irradiation in the OSIRIS reactor. The irradiation device used for the PRIMO ramps was the ISABELLE 1 loop. The BD8 fuel rod placed in a sample holder was contained in a tube pressurized at 150 bars and cooled with light water flowing at a 200 g/s. The outer cladding temperature was kept at 342 ±5°C. The power ramp consisted of:

- Conditioning process at a peak power level of 18.9 kW/cm held for 27 hours.
- Power ramping with a Ramp Rate (RR) of 462 kW/(m-h), up to a Ramp Terminal peak power Level (RTL) of 39.5 kW/m.
- Holding at RTL for 20 hours or until the cladding failure.

The ramp test power history is shown in *Fig. 14* and *Fig. 15*.
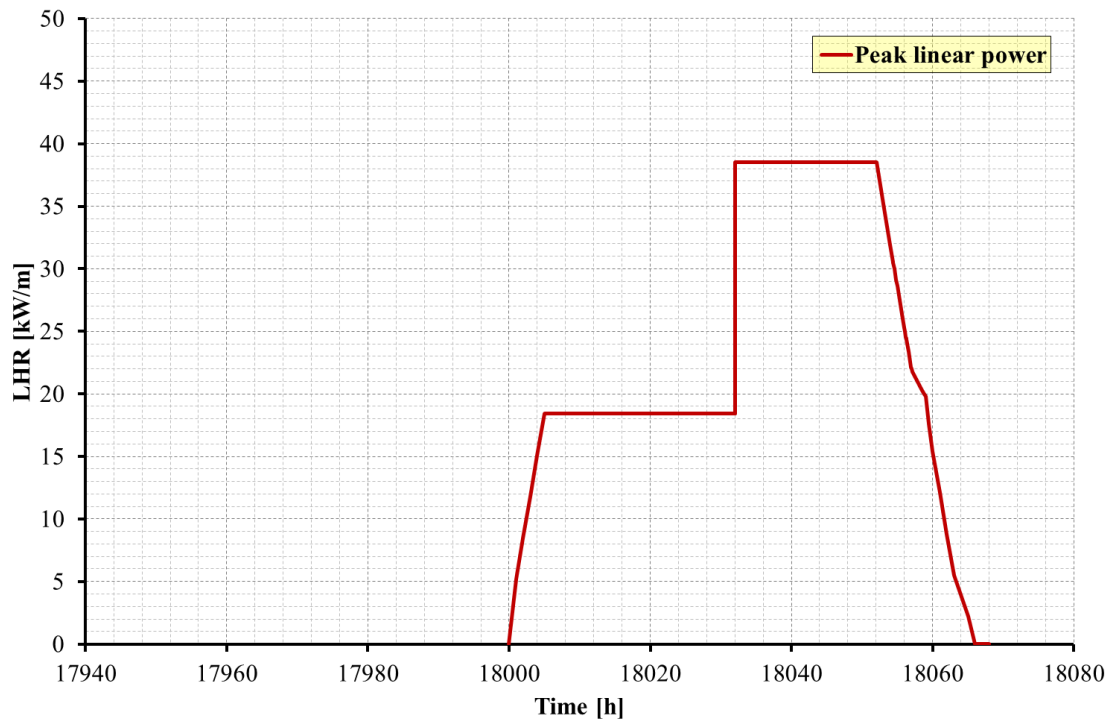
Fig. 14 – PRIMO Program, rod BD8, linear heat rate at the peak point during power ramp test.
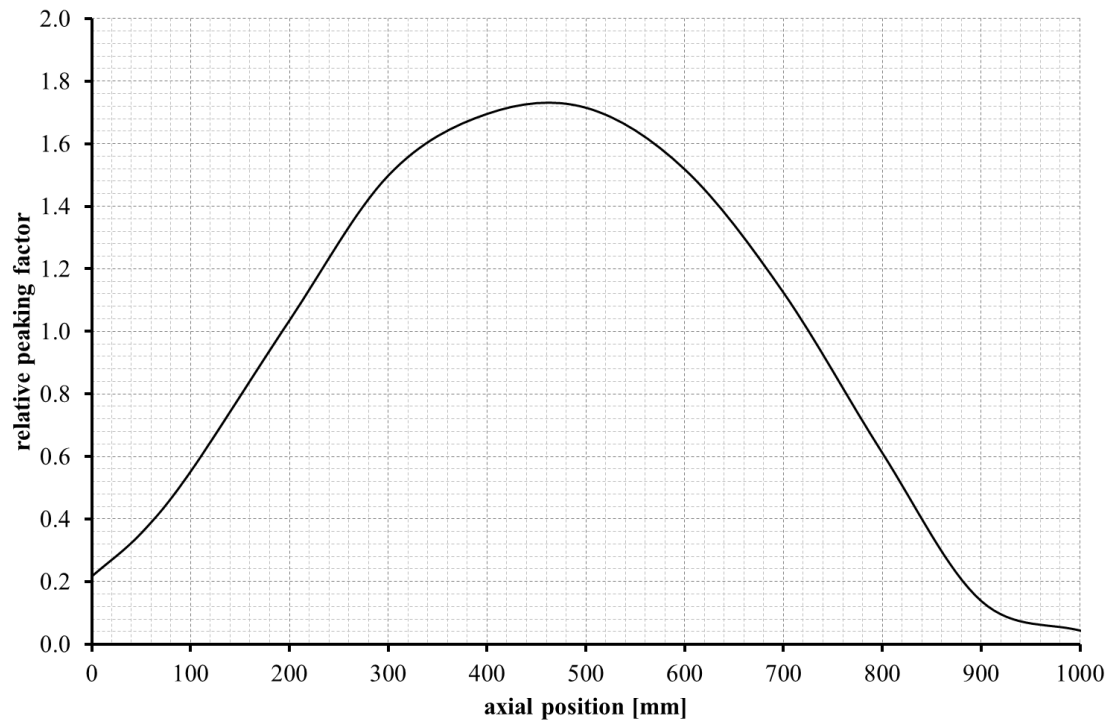
Fig. 15 – PRIMO Program, rod BD8, relative axial power profile of the OSIRIS Reactor.

3.1.6 Main Achievement from the Experiment

Post irradiation examinations were performer prior to ramping and at the end of the experiment. Both non-destructive and destructive measurements were carried out.

3.1.6.1 *Non-destructive examination*

Non-destructive data for BD8 rod were extracted from the Final Report of the PRIMO program; they were used to characterize the fuel rod evolution on three points:

- the cladding creep, irradiation growth and integrity;
- the fuel integrity;
- the pellet-cladding mechanical interaction.

Five non-destructive tests were included in the non-destructive examination programmed:

- visual examination of the cladding;
- dimensional controls (diameter and rod length measurements);
- neutron radiography;
- gamma scanning (spectrometry, burnothèque);
- eddy current test.

The cladding soundness was inspected through visual examination and eddy current test. Visual examinations showed a uniform dark-grey aspect, with scarce scratches resulting from rod manipulations. No anomaly was observed. Eddy current tests were performed in order to detect cladding abrupt defects such as incipient cracks as well as longer and more gradual defects. Neither primary defects nor ridging could be observed on rod BD8. The cladding outer diameter was measured at CEA-Saclay. Two measurements were performed on two diameters at 90° (with an accuracy of ±5 micron) with the aim to determine the diameter changes and the cladding ovality. Measurements were done at 20 axial positions along the fuel column length. The rod BD8 showed cladding creep, without any sign of pellet-cladding mechanical interaction[10]. From the diameter records, the cladding diameter change or hoop strain (ε_θ) and the ovalisation (Δ) can be computed by means of the following expressions:

$$\varepsilon_\theta\ (\%) = (D_a - D_0)/D_0 * 100 \qquad \qquad Eq.\ 5$$

$$\Delta = Dmax - Dmin \qquad \qquad Eq.\ 6$$

Where
D_{min} is the minimum-recorded diameter;
D_{max} is the maximum-recorded diameter;
D_0 is the reference diameter (mean diameter at or close to the plenum level);
$D_a = (D_{max} + D_{min}) / 2$.

In order to determine the Zircaloy irradiation growth, rod length measurements were performed using neutron radiography examination. The accuracy on the results is estimated at 1 mm. The rod elongation ε_z for rod BD8 is defined as follows:

$$\varepsilon_z(\%) = (L_1 - L_0)/L_F * 100 \qquad \qquad Eq.\ 7$$

Where
L_0 is the fuel column length before irradiation;
L_1 is the fuel column length after irradiation;
L_F is the fuel column length.

The fuel column length change was measured with the same technique (and accuracy). The main results obtained prior to ramping from geometrical PIE are summarized in *Tab. 9*. "Burnothèque" examination was performed in order to determine the maximum and mean burn-up by means of non-

destructive gamma spectrometry on ^{137}Cs. The measured rod burn-up of rod BD8 was 30.1 GWd/tHM whereas the peak pellet burn-up was 39.7 GWd/tHM. The uncertainty on the experimental burn-up values is estimated to be less than 6%. These values are in good agreement with the calculated burn-up, according to which the average rod burn-up reaches 32.2 GWd/tHM and the peak pellet burn-up 38.0 GWd/tHM. The transient test allowed the following observations:

- There was no significant cladding mean diameter change.
- There was the appearance of a ridging effect in the high power zone, ranging between 10 and 17μ (diametric).
- There was a beginning of dish filling observable on the neutron radiography as a result of gaseous swelling and fuel plasticity during ramp.
- There was Cesium migration towards the coolest zones of the pellets.
- There was a sound aspect of the cladding and the fuel column, with no anomaly.

3.1.6.2 Destructive examination

During destructive examination, the parameters related to FGR were measured, they are summarized in *Tab. 10*. The fission gas release (FGR) fraction is calculated assuming a gas (Xe + Kr) generation rate of 30 cm^{3}STP/MWd. The FGR prior to ramping has been estimated on the basis of the FGR of a sibling non-ramped rod, *i.e.* rod BD10[10]. Ceramographic examination after the ramp revealed that grain growth occurred in the central part of the pellets (until r/R pellet = 0.4). The mean grain size reached about 10 μm (mean linear intercept) in that region.

Measured quantity	Unit	Value
Mean fast fluence (E>1 MeV)	10^{21} n/cm^2	2.93
Peak fast fluence (E>1 MeV)	10^{21} n/cm^2	3.69
Mean cladding hoop strain	%	-0.24
Maximum cladding hoop strain (at fast fluence peak)	%	-0.32
Mean cladding ovalisation	μm	13.00
Maximum cladding ovalisation (at fast fluence peak)	μm	18.00
Rod elongation (Cladding irradiation growth)	%	+0.21
Fuel column length change	%	-0.13

Tab. 9 – PRIMO Program, rod BD8, experimental data obtained from PIE performed PTR.

Measured quantity	Unit	Value
Total collected gas	cm^3 at 0°C, 1 bar	171.3
Volume of Xe + Kr	cm^3 at 0°C, 1 bar	46.9
Gas composition	He (% vol.) Xe (% vol.) Kr (% vol.)	72.62 25.71 1.67
Xe/Kr volume ratio	--	15.4
Total Fission Gas Release	%	11.24
Estimated Xe + Kr release prior to ramp	%	0.47
Estimated Xe + Kr release after ramp	%	10.77

Tab. 10 – PRIMO Program, rod BD8, FGR measurements.

3.2 The IFA-597 experiment

The Instrumented Fuel Assembly 597 (IFA-597) experiment took place between July 1997[11],[12],[36] and January 2002. It was carried out in the joint program of the Halden Reactor Project. The

experimental operation of the Halden Boiling Water Reactor and the Man-Machine Systems laboratories and associated research programs are sponsored through an international agreement including fuel vendors, utilities, nuclear centers and national authorities.

The experiment aimed to study the thermal and fission gas release behavior of MOX fuel, and to explore differences in performance between solid and hollow pellets. One of the rods had mainly solid pellets while the other contained only hollow pellets. The two rods were instrumented with a fuel center thermocouple and a pressure bellow transducer and irradiated in the Halden Reactor. The experiment consisted of four power cycles labeled as IFA-597.4/.5/.6/.7. The experiment was planned to irradiate the two rods up to around 60 MWd/kgMOX but, because of excessive inner pressure build-up caused by high FGR, it was interrupted at 33 MWd/kgMOX. The rods were subjected to PIE after the end of irradiation.

The in-pile data on fuel temperature, rod inner pressure and results of the gas puncturing and mass spectrometry of the extracted gas were released with the purpose of code benchmarking. Details of the fabrication data as well as information about the provided irradiation data up to a burn-up of 26 MWd/kgMOX (for a period of 626 irradiation days) are provided by T. Tverberg in 2007.

HRP provided the data of rods 10 and 11 from IFA-597 test to the OECD-NEA Expert Group[12]. This group was established by OECD/NEA Nuclear Science Committee with the aim to deal with the status and trends of reactor physics, nuclear fuel performance and fuel cycle issues related to the disposition of weapons-grade plutonium as mixed-oxide (MOX) fuel. Among the tasks of this group, fuel pin mechanics code benchmarking activities were performed based on IFA-597 experiment. The datasets of this rod are also included in the International Fuel Pin performance Experimental database (IFPE[9]).

3.2.1 The Halden BHWR

The Halden Boiling Water Reactor[37][38] (HBWR) is currently operated at 18 to 20 MW. It is situated inconspicuously within the rock on the outskirts of the town of Halden in southern Norway. The reactor has operated since 1959 and was initiated to investigate nuclear capability as a supplier of steam to the wood pulp industry. Since that time, the reactor facilities have been updated progressively and, through a series of innovative techniques, the system has become one of the most versatile in the world. Over the course of this development, some 300 in-pile experiments have been performed. These ranged in complexity from rudimentary non-instrumented rod bundles to some of the most integrated and complex in-reactor tests ever designed.

The HBWR is a natural circulation boiling heavy water reactor, *Fig. 16*. The maximum power is 25 MW (thermal), and the water temperature is 240°C, corresponding to an operating pressure of 33.3 bar. The reactor vessel primary circuit system is inside a 30-60 m thick rock cavern with a net volume of 4500 m^3, it is cylindrical with a rounded bottom. It is made of carbon steel and the bottom and the cylindrical portion are clad with stainless steel. The flat reactor lid has individual penetrations for fuel assemblies, control stations and experimental equipment. 14 tons of heavy water act as coolant and moderator. A mixture of steam and water flows upwards by natural circulation inside the shroud tubes which surround the fuel rods. Steam is collected in the space above the water while water flows downwards through the moderator and enters the fuel assemblies through the holes in the lower ends of the shroud. The steam flows to two steam transformers where heat is transferred to the light water secondary circuit. Condensate from the steam transformers returns to the reactor by gravity. An external sub-cooler loop is installed to provide experimental variation of void fraction in the fuel assemblies and the moderator, and is also used for heating and cooling purposes. In the secondary circuit, two circulation pumps pass the water through the steam transformers, a steam drum and a steam generator where steam is produced in the tertiary circuit. The tertiary steam is normally delivered as process steam to the nearby paper mill, but may also be dumped to the river. There is

generally no access to the reactor hall when the reactor is operational, and therefore all control and supervision is carried out from the control room placed outside the excavation. Light water, high pressure loops provide facilities for testing under prototypic BWR and PWR conditions. The central position in the core is occupied by an emergency core cooling tube with nozzles.

A fuel charge consists of a combination of test fuel from organizations in member countries and driver fuel assemblies, which provide reactivity for operating the reactor. The core consists of about 110 - 120 fuel assemblies, including the test fuel, in an open hexagonal lattice with a lattice pitch of 130 mm. 30 lattice positions are occupied by control stations, *Fig. 17*. The maximum height of the fuel section is 1710 mm, and the core is reflected by heavy water. Currently, each driver fuel assembly consists of eight or nine fuel rods with 6 % fuel enrichment and standard fuel pellet diameter, the main data are summarized in *Tab. 11*.

Assembly	Unit	Quantity
Shroud material	--	Zr-2
Shroud ID	mm	71
Shroud thickness	mm	1
Number of rods per assembly	--	8
Pitch circle diameter	mm	50
Fuel column height	mm	810
Fuel material	--	UO_2
Fuel enrichment	%	6
Pellet density	g/cm^3	10.52
Pellet OD	mm	10.49
Pellet height	mm	8.6-10.8
Length of natural fuel per rod	mm	12
Active length	mm	748-811
Cladding material	--	Zr-2, Zr-4
Cladding ID	mm	10.67
Cladding wall thickness	mm	0.8
Nominal gap	mm	0.16-0.18

Tab. 11 – Summary of the driver fuel main data.

Power Level	up to 20 MW (th)
Reactor Pressure	33.3 bar
Heavy Water Saturation Temperature	240°C
Maximum Subcooling	3.0 MW
Primary Steam Flow (both circuits)	160 ton/h
Return Condensate Temperature	238°C
Subcooler Flow	160 ton/h
Plenum Inlet Temperature	237°C

1. Reactor with fuel and heavy water
2. Steam Transformer
3. D$_2$O Subcooler
4. Heavy water circ. pump
5. Steam Drum
6. Light water circ. pumps
7. Steam Generator
8. Hot Well
9. Light water subcooler
10. Feed Water Tank

Fig. 16 – HBWR, scheme and main operational data.

Legend:
- Control stations
- Subcooled water (reflector)
- Steam out
- Steam pipe drain
- Subcooled water (plenum chamber)
- Emergency core cooling nozzle tube
- Thermocouples (or press gauge IMP. tube)
- Neutron shield bolt

Number of Fuel Assembly	110
Number of Control Stations	30
Core height – usable length for placing fuel -	1710 mm
Configuration	open hexagonal lattice
Lattice Pitch	130 mm
Reflector Top: thickness	300 mm
Reflector Bottom: thickness	380 mm

Fig. 17 – HBWR, core plan view of reactor top lid and main data.

3.2.2 Rods design

The MOX fuel rods, named rod 10 and rod 11, both started their irradiation with fresh fuel pellets with initial Pu-fissile enrichment or 6.07%[12]. The fresh fuel had a Pu-total enrichment of 8.44% which was measured by potentiometric titrations. Pu isotopic composition was measured by mass spectrometry in order to determine the initial Pu-enrichment. PuO_2 spot size was determined from alpha autoradiography. The pellets were fabricated trough the MIMAS process. All the fabrication data are summarized in *Tab. 12*. Rod 10 has an active length of 224 mm and is made of 17 solid fuel pellets and 4 hollow pellets to allow for the insertion of a fuel thermocouple. In rod 11, all 21 pellets are hollow and the active length is 220 mm (the above numbers do not include end pellets). The fuel pellets had an initial outer diameter of 8.04 mm and each hollow pellet has a central hole of diameter 1.8 mm. The cladding outer diameter is 9.5 mm and the initial diametrical fuel cladding gap was 180 µm in both rods. The rods are fitted at the top with a fuel center thermocouple of the W5Re/W24Re type and at the bottom with a pressure bellows transducers[11],[12], [36]. The pressure transducers are equipped with internal bellows pressurized to 4 bar (at 20°C), while the rods themselves were pressurized to 5 bar (at 20°C) with Helium before loading into IFA-597.4. Four UO_2 fuel rods, named rods 1, 2, 3 and 5, are approximately 500 mm long and are positioned to cover the whole axial region of the MOX fuel rods. They had been irradiated up to 12.7 $MWd/kgUO_2$, in IFA-597.1 before loading into IFA-597.5. The initial U^{235} enrichment of the pellets in IFA-597.1 was 4.95%. These rods can be placed or removed from IFA-597 to achieve respectively, low or high powers (temperatures).

Pellet characteristic		Unit	Rod 10	Rod 11
Fuel type		--	MIMAS-MOX	
Active length		mm	224	220
Fuel mass		kg	0.1179	0.1106
Instrumentation, upper end		mm	TF1	TF2
Instrumentation, lower end		mm	PF1	Pf2
Fuel density		g/cm^3	10.54	
Fuel density		%TD	95.86	
Initial enrichment		Pu(f)	6.07	
Fuel pellet diameter		mm	8.04	
Initial gap width		mm	0.9	
Pellet length		mm	10.7	10.5
Pellet form		--	17 solid, 4 hollow	21 hollow
Drilled center hole diameter		mm	1.8	
Dishing		--	Both ends	
Dishing depth		mm	0.26	
Land		mm	5.30	
Chamfer		--	Both ends	
Chamfer Height		mm	0.15	
Chamfer Width		mm	0.30	
Cladding material		--	Zr-4	
Filler gas pressure		bar	5 (He)	
Cladding outer diameter		mm	9.50	
Cladding thickness		mm	0.64	
Free volume		mm^3	2600	2800
Grain size		μm	4.3 – 6.6 (m.l.i.)	
Mean - max PuO$_2$-rich particle size		μm	5.1 – 231.4	
Pellet surface roughness		μm	1.4	
Cladding surface roughness		μm	0.15	
Neutron fast flux		n/cm s	1.6E11*LHR	
Heavy metal composition	U	%	80.568	
	Pu		7.424	
	Am		0.040	
Plutonium isotopic composition	^{238}Pu	%	0.914	
	^{239}Pu		65.340	
	^{240}Pu		23.675	
	^{241}Pu		6.570	
	^{242}Pu		3.494	
	^{241}Am		0.595	
Uranium isotopic composition	^{234}U	%	0.002	
	^{235}U		0.252	
	^{236}U		0.001	
	^{238}U		99.745	
Pore size distribution		μm	1.9 to 3	
Oxygen to metal ratio		--	1.999	
Re-sintering test	Duration	h	24	
	Temperature	°C	1700	
	Avg. densification	% TD	0.455	

Tab. 12 – IFA-597, rod 10 and rod 11 design data.

3.2.3 Irradiation history

The rig operated under Halden BWR conditions. The experiment consisted of four power cycles labeled as IFA-597.4/.5/.6/.7. IFA-597.4 was originally placed in position 6-33 to keep the power level within the range of 20-35 kW/m. The rig remained in this position until it was moved outwards to

position 7.37 for the second half of IFA-597.5 (march 1999)[12]. At the beginning of IFA-597.6, the rig was moved inwards to position 5-15 in order to obtain sufficient power for FGR investigations. IFA-597.7 was moved outwards to position 6-24 to suppress the power in order to avoid significant FGR. Typical axial neutron flux profiles during operation are shown in *Fig. 18, Fig. 19*. Because the neutron detector ND1 is outside the range of the MOX rods, the real axial shape is actually defined using measurements at one axial location (ND2, 3, 4). Considering the length of the MOX rods, however, it is evident that the profile over the MOX rods has been rather flat, the difference between maximum and minimum thermal neutron flux over the rod length being within 3-5%.

The total rig power and linear heat rates (LHRs) are determined using a power conversion factor (KG) and a depletion factor (CD) relating the rod power to the neutron detector signal (ND)[12]. The KG is usually obtained from early-in-life thermal-hydraulic calibration tests. However, the calibration was not performed for this test rig, partly due to the small mass of fuel in the rig (230 g). Instead of performing a power calibration measurement, the KG was obtained from comparison of the fuel temperature versus LHR relation with another test with identical fuel, which had a KG obtained from ordinary power calibration measurement and HELIOS calculations for each loading. To correctly determine the local LHR in the hollow part of the solid MOX rod (rod 10), the loss of fissionable material as well as the changes in thermal flux depression due to the hollow pellets have been considered. The increasing rod pressure causes creep of the pressure bellows transducers. It results in a slight drift in the measurement, which has been eliminated by using a standard drift correction method utilizing data in cooling down periods (coolant temperature ramps).

The linear heat rate histories for both rods are shown in *Fig. 18* as LHR at the thermocouple positions versus the average fuel burn-up. Due to the flat axial power profile, local LHR at the thermocouples are essentially the same as the average LHRs in both rods. The plan for the test series was to operate the fuel at a relatively low power and to experience power uprating roughly every 10 MWd/kgMOX in order to study the FGR behavior. To promote FGR in IFA-567.4 and IFA-567.6, the LHRs were considerably higher than in IFA-597.5 and IFA-597.7. Which were irradiated in order to accumulate fission gas in the fuel matrix.

The first test, IFA-597.4, was operated within the range 30-35 KW/m for the first half and 27-30 kW/m for the second half of the test. In this loading, the power ramp, which can be observed as steps at about 10-11 MWd/kgMOX, was conducted successfully in order to study FGR behavior of MOX fuel. The power resulted occasionally in temperature high enough to cause gas release in both MOX rods. For IFA-597.5, four UO_2 rods were added to the rig in order to suppress the LHR in the MOX rods and to avoid FGR. Consequently, LHRs remained low (8-20 kW/m) and no significant FGR occurred during this loading. The aim of IFA-597.6 was achieve sufficiently high temperatures to cause FGR, and hence it was operated within the range 23-27 kW/m. Again, appreciable gas release was observed in both MOX rods. During IFA-597.7, three UO_2 rods were added to the rig as in IFA-567.5 and essentially no FGR was observed in this loading.

The average LHR in rod 10 (solid pellets) was lower than in rod 11 (hollow pellets) in IFA-597.4 and at the beginning of IFA-597.5. After that, both rods had almost the same power throughout the irradiation. This can be explained by the redistribution of the rig power due to the change of core position.

The axial neutron flux profile was almost flat over the MOX fuel stacks, and the maximum local LHR always occurred in the middle region of the rod. For rod 11, the LHR was almost uniform along the active length (less than 2% variation respect to average value). For rod 10, the local LHRs varied

within 7%, despite, the fact that the LHR at the top of fuel stack was lower than the average due to the presence of hollow pellets[12].

Fig. 18 – IFA-597, rod 10 and rod 11, LHR at the thermocouple position

Fig. 19 – IFA-597, power axial profile.

3.2.4 Main Achievement from the Experiment

The fuel center temperature was measured during the irradiation by means of the thermocouples accommodated in the central hole in the upper part of both MOX rods, *Fig. 20*. The results indicate that the measured temperatures change is in good agreement to the linear power change.

The estimated fuel peak temperature and the measured thermocouple temperature histories are shown in *Fig. 20* along with average linear heat rates. The peak temperature was estimated by FTEMP3 code calculations. The peak temperatures in rod 10 with solid pellets are ~100-200°C higher than measured temperature and increase with linear power. On the contrary, in rod 11 with (due to the hollow pellets), the peak temperature is similar to the thermocouple data because of the flat axial profile. in rod 10, the Vitanza threshold (shown in *Fig. 20*); is exceeded in the peak axial position (solid pellet in the rod middle); however significant gas release is observed in both rods.

The rod pressurization is measured by means of pressure bellows transducers. Inner pressure histories are provided in *Fig. 21*. The internal pressure reached 28 bar in and 24 bar respectively, in rod 10 and rod 11: this was due to significant gas release occurred in both the rods. These pressures are close to the mechanical limit pressure of the bellows[12] and caused the interruption of the experiments.

The main objective of this test series was to compare FGR behavior of MOX fuel with that of UO_2 fuels. The gas release performance in MOX fuels are different from UO_2 due to the presence of plutonium. This MA promotes the generation (and hence the release) of a considerable amount of Helium . Helium contributes to the rod pressurization and could favor the release of Xe and Kr by keeping open the bubbles tunnel network at grain boundaries. Hence, it is a significant factor that should be accounted to assess the MOX fuel performance. Furthermore, the local plutonium enrichments causes non-uniform Pu distribution in the fuel matrix which may results in local high burn-ups and fission product concentrations zones within the matrix[12].

The estimation of FGR is made under the assumption of a generation rate of 33.4 cc/MWd. The fission gas generated is mainly Xenon. Helium is generated by:

- alpha decay of Curium (Cm^{242});
- ternary fissions;
- n-α of Oxygen.

In the experiment, it is assumed that Helium contributes to 10% of the total gas generation rate. The total gas generation is therefore assumed to be 36 cc/MWd. The calculated FGR is simply based on the rod pressure data and rod free volume estimation during the irradiation.

During IFA-597.4, significant gas release is observed since 6 MWd/kgMOX in both rods[12]. Around that time the fuel temperature approaches the Vitanza gas release threshold. The FGR increases further until the end of IFA-597.4. During the low power cycle IFA-597.5, no pressure increase is observed; it suggests no FGR occurs in this phase of the experiment. At the beginning of IFA-597.6 a fast increase of gas release is observed. FGR is higher in rod 10 than in rod 11 due to the considerably higher temperature achieved in former rod. However, although fuel temperature was the lowest, at the end of IFA-597.5, the FGR resulted higher in rod 11 . During IFA-597.7 no additional gas release occurs. However, gas release rate in rod 10 decreases more than expected. It could be explained by the fact that internal pressure for this rod is close to the mechanical limit of the pressure bellow which might have measured lower values of the pressure. The estimated EOL total gas release is 33% and 24% for rod 10 and rod 11 respectively[12].

Fig. 22 shows the operating history in IFA-597.6 and the pressure dependence on the linear power and fuel temperature. During this phase, three pressure burst are observed. The first pressure burst

indicates that gas release occurs throughout the corresponding power ramps (*Fig. 22*). This behavior is not observed in UO_2 fueled rods while there is similar earlier experience in MOX fuel rods[39]. This might be caused by the Helium which is released by diffusion at lower temperature than noble gases[12]. It provides an early grain boundaries inter-linkage and enhances further gas release. The second and third bursts seen in power ramp down indicate the typical delayed FGR detection[40] (the gap is closed and the pressure transducer is not able to record data until the gap re-open again in the ramp-down).

The two MOX rods were subjected to PIE after the end of irradiation. The results of the gas puncturing and mass spectrometry of the extracted gas are summarized in *Tab. 13*. The total created gas is estimated by means of HELIOS code simulations[12].

Measured quantity	**Unit**	**Rod 10**	**Rod 11**
Total Kr released		5.66	4.55
Total Xe released		106.14	85.96
Total Kr + Xe released	mg	111.80	90.51
Total Kr generated		24.35	23.51
Total Xe generated		620.91	601.49
Total Kr + Xe generated		645.32	625
Fraction Kr + Xe released	--	0.1732	0.1448

Tab. 13 – IFA-597, rod 10 and rod 11, PIE, results of gas puncturing.
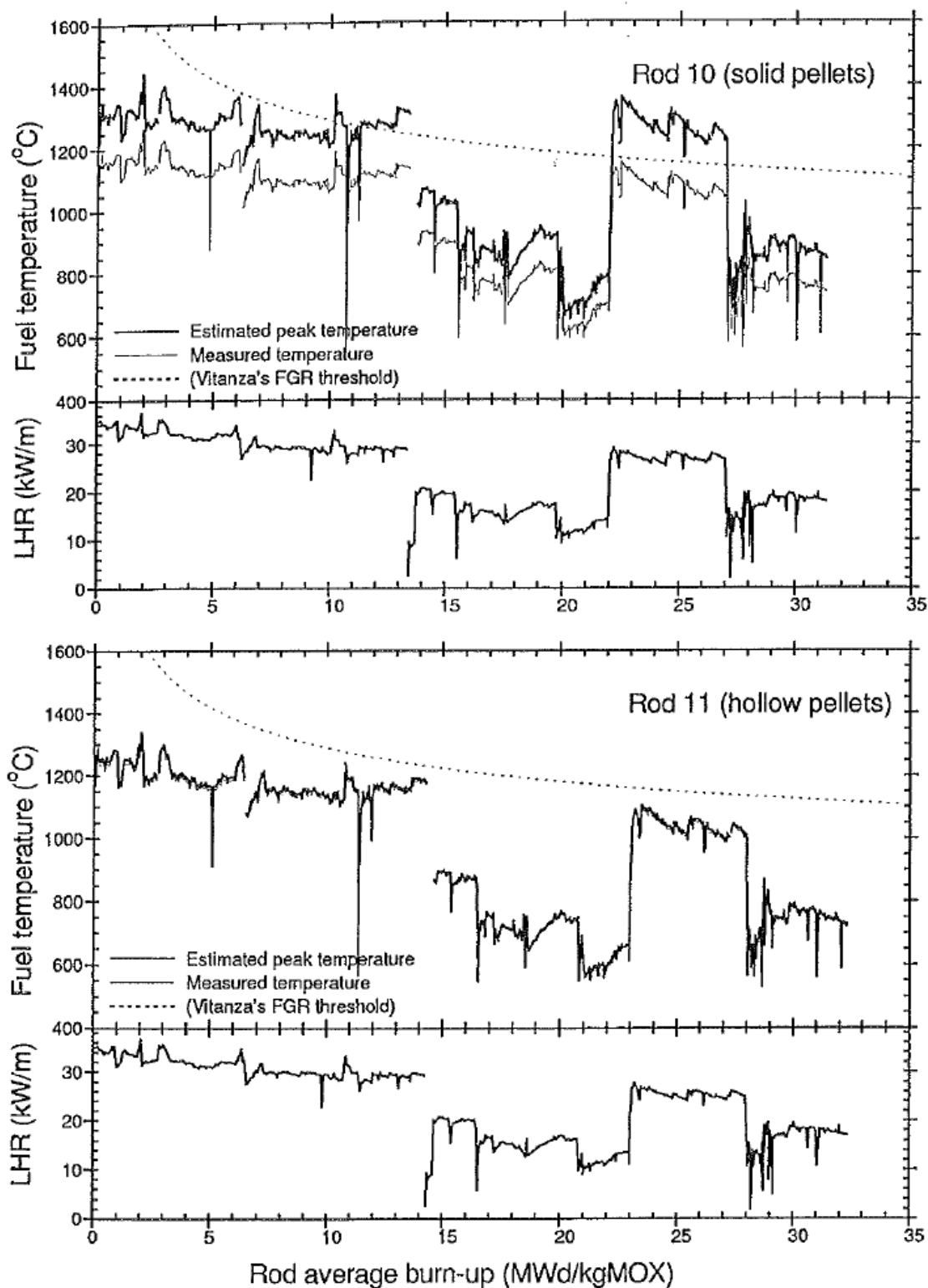
Fig. 20 – IFA-597, rod 10 and rod 11, fuel temperature and linear power history.
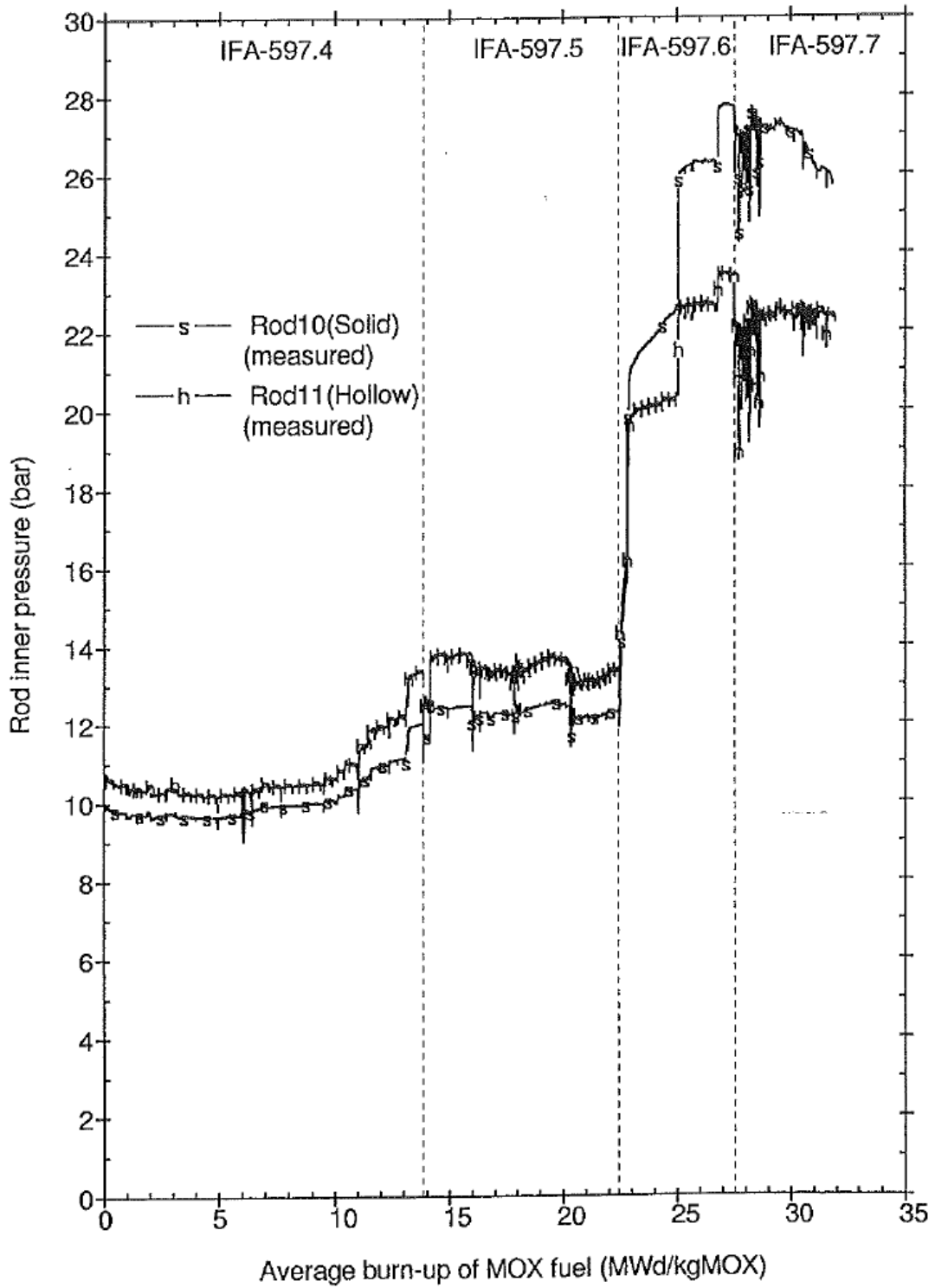
Fig. 21 – IFA-597, rod 10 and rod 11, pressure measurements.

Fig. 22 – IFA-597, rod 10 and rod 11, pressure measurements in IFA-597.6, pressure bursts.

4 Development and setup of the TRANSURANUS models

4.1 TRANSURANUS code

TRANSURANUS is a computer program for the thermal and mechanical analysis of fuel rods in nuclear reactors [6][7][8]. It was developed at the Institute for Trans-uranium Elements (ITU). The TRANSURANUS code relies on a clearly defined mechanical–mathematical framework into which physical models can easily be incorporated. The mechanical–mathematical concept consists of a superposition of a one-dimensional radial and axial description (the so called quasi two-dimensional or 1 ½ D model), the code was specifically designed for the analysis of a whole rod. TRANSURANUS code incorporates physical models of thermal and radiation densification of the fuel, models of fuel swelling, fuel cracking and relocation, a model of generation of fission gases, a model of redistribution of oxygen and plutonium, and some other physical models. Mainly research institutions, industries and license authorities exploit the code.

Besides its flexibility for fuel rod design, the TRANSURANUS code can deal with a wide range of different situations, as given in experiments, under normal, off-normal and accident conditions. The time scale of the problems to be treated may range from milliseconds up to years. The code has a comprehensive material data bank for oxide, mixed oxide, carbide and nitride fuels, Zircaloy and steel claddings and several different coolants. It can be employed in two different versions: as a deterministic and as a statistical code.

The input file of the code contains complete data needed for computation. It determines the type of reactor, cladding, coolant, fuel geometry and dimensions, surface roughness, coefficients of heat transfer, initial concentrations of uranium and plutonium isotopes, the course of power loading and the length (period) of computation. The output data are provided by subroutine that generates data files for single times, distances or locations at the fuel pin. Optionally, the output data include the pellet radius, pressure in the gap, contact pressure between the pellet and cladding, concentrations of fissionable isotopes U^{-235}, Pu^{-239} to Pu^{-242}, concentrations of fission gases, temperatures of the fuel, cladding and gases in the gap and other parameters.

The uncertainties to be considered may be grouped into three categories.

- The first category deals with the prescribed quantities. The fuel rod performance code requires on input the fuel fabrication parameters (rod geometry, composition, etc.) and irradiation parameters (reactor type, coolant conditions, irradiation history, etc.).
- The second category of uncertainties is the material properties, such as the fuel thermal conductivity or the fission gas diffusion coefficients.
- The third and last category of uncertainties is the so called model uncertainties.

The capabilities of the TRANSURANUS code can be summarized as follows:

- Analysis of all fuel rod types under normal, off-normal and accident conditions (deterministic and probabilistic) is in principle possible.
- Consistent steady-state and transient analysis.
- Clearly defined mechanical-mathematical framework into which physical models can easily be incorporated.
- Fast and reliable.
- Database, models and code extensively verified.

- Applied by different groups and different licensing authorities.

4.2 Description of the PRIMO input deck

The activity is performed using TRANSURANUS code, version "v1m1j12", with the deterministic option, steady state thermal and mechanical analysis[6]. The version of the manual is "v1m1j12". The boundary conditions are prepared using a program written in PERL language.

Suitable physical models are chosen for the simulation of MOX fuel behavior subjected to standard power ramp condition. In particular, the fission gas intra-granular diffusion equation is solved by the URGAS algorithm[41], the gas diffusion coefficient is modeled according to Matzke[42] for the thermal part and to Dowling for the a-thermal part[43]. The inter-granular behavior is modeled according to the modified Koo model[44]. The thermal conductivity is according to the standard MOX correlation developed by Van Uffelen and Schubert.

Only the active part of the fuel is accounted for the simulation. It has been divided into 12 axial slices according to the experimental data available at different elevations. The slice analysis is selected (islice = 1). The nominal design values are used if available; the measured values are considered when nominal values are not specified.

4.2.1 Selection of the boundary conditions

The boundary conditions implemented for the analysis are:

- Linear heat rate at 12 axial position;
- Cladding waterside temperature;
- Fast neutron flux (>1 MeV), *Fig. 24*;
- Coolant pressure.

The axial mesh is shown in *Fig. 25*. The linear power history is specified in form of histogram at each of the 12 axial positions. The rate of change between two constant values is fixed to 6kW/m-h according to ITU recommendations. The base irradiation implemented is reported in *Fig. 12*.

The conditioning phase and the power ramp have been modeled in agreement with the experimental specifications reported in section 3.1.5. The power rate to reach the conditioning level is assumed 6 kW/m-h, *Fig. 14*.

During the ramp test, the water-side cladding temperature is given as boundary condition whereas, in the base irradiation, only the coolant temperature at core inlet and outlet are specified. A simple method based on power balance is adopted to obtain an approximation of the temperature axial profile starting from the data available in the base irradiation. The temperature difference between two subsequent axial nodes is obtained as shown below.

$$\Delta T_{i+1} = (l_i (q_{l,i} + q_{l,i+1})/2) / (W c_p) \qquad \text{Eq. 8}$$

Where
ΔT_i is the temperature difference between node i and node i+1;
l_i is the distance between node between node i and node i+1;
$q_{l,i}$ is the linear power at node i;
$q_{l,i+1}$ is the linear power at node i+1;
W is the mass flow rate;
c_p is the water specific heat (assumed constant).

TU code is capable to model the heat exchange between the coolant and the cladding outer surface (taking the coolant temperature at each axial node and the mass flow rate as boundary conditions) or to implement the cladding water side temperature directly as boundary condition. Nevertheless, it is not able to use both the options into the same calculation. In order to develop a suitable input deck, a first simulation of the base irradiation is carried out without considering the ramp to get the coolant-side cladding temperature history in the base irradiation and to develop the reference model that includes the power ramp and assumes as boundary condition the clad waterside temperature.

The fast neutron flux is given only in the base irradiation at 12 axial positions. A peak value of $4.5*10^{12}$ n/(cm^{2}s) obtained from the OSIRIS Reactor data is assumed in the ramp simulation, its axial shape is assumed equal to the linear power shape. The error associated with this approximation is expected to be negligible since the main physical effects of fast neutron flux is associated to long time exposures.

The coolant pressure is known and matches the operational pressure of the two reactors in which the experiment took place: respectively 140 bar, 150 bar for BR-3 and OSIRIS.
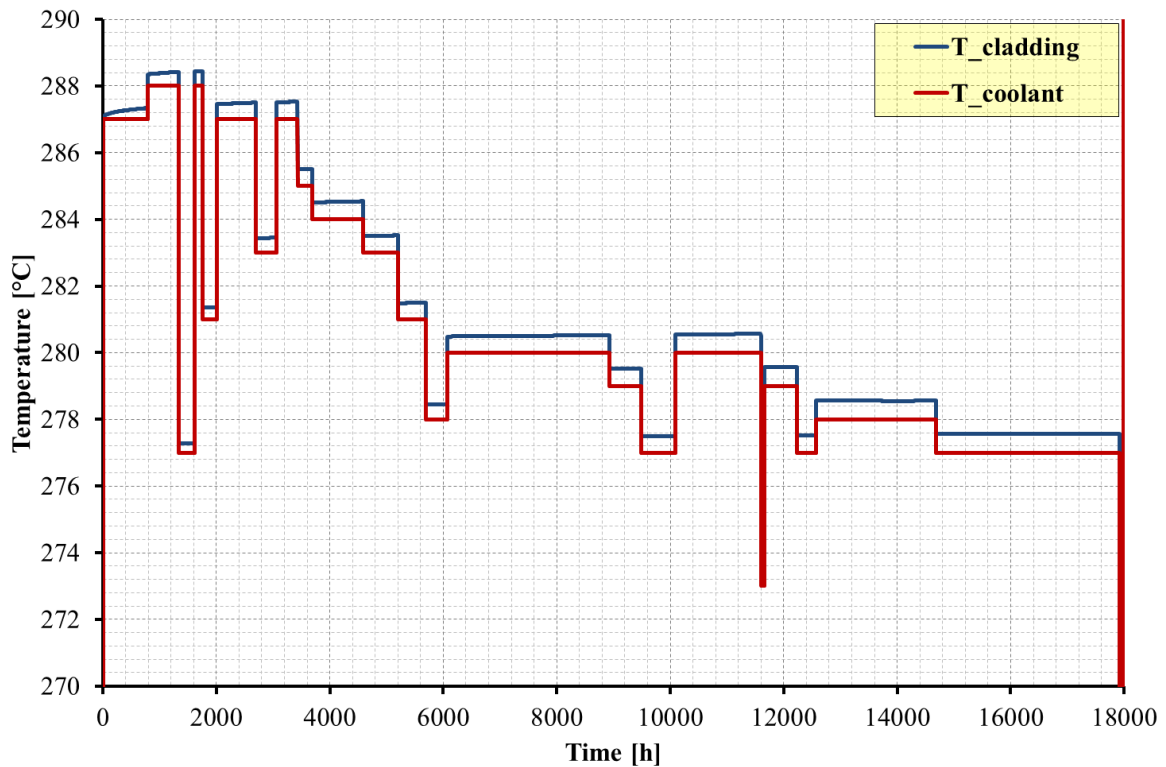
Fig. 23 – PRIMO Program, rod BD8,cladding and coolant temperatures during base irradiation.
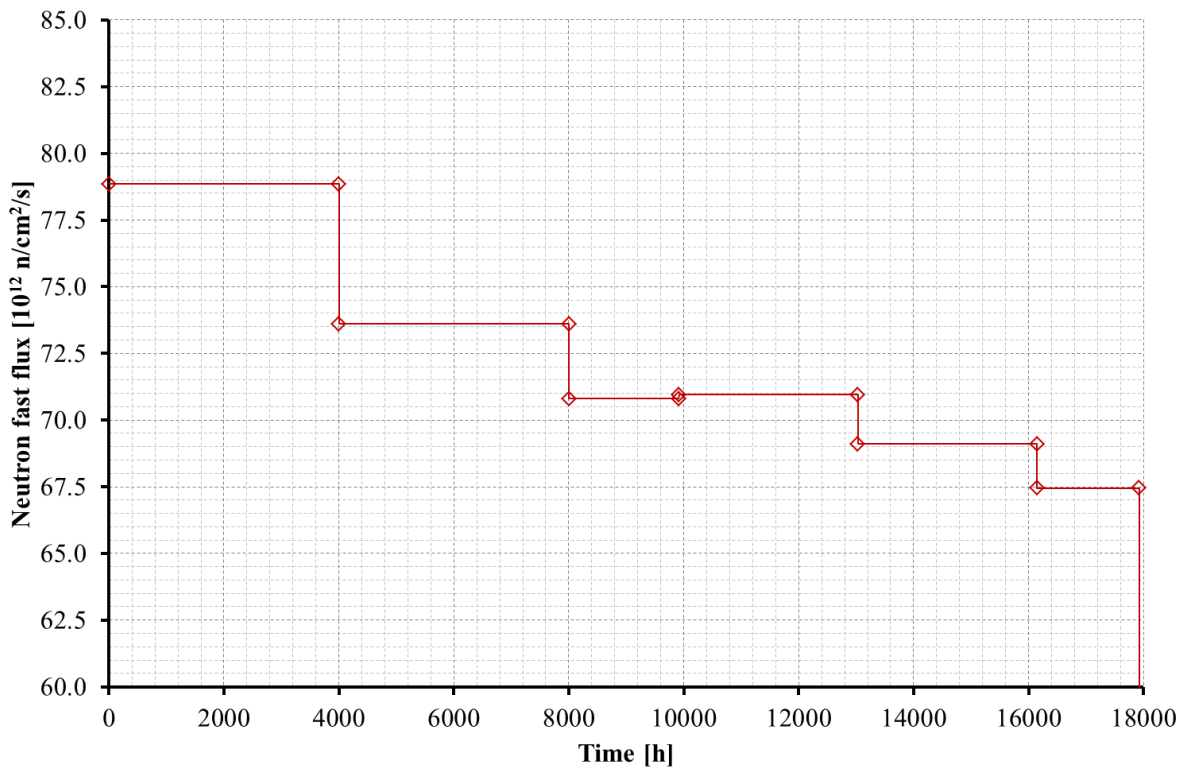
Fig. 24 – PRIMO Program, rod BD8, neutron fast flux during base irradiation.
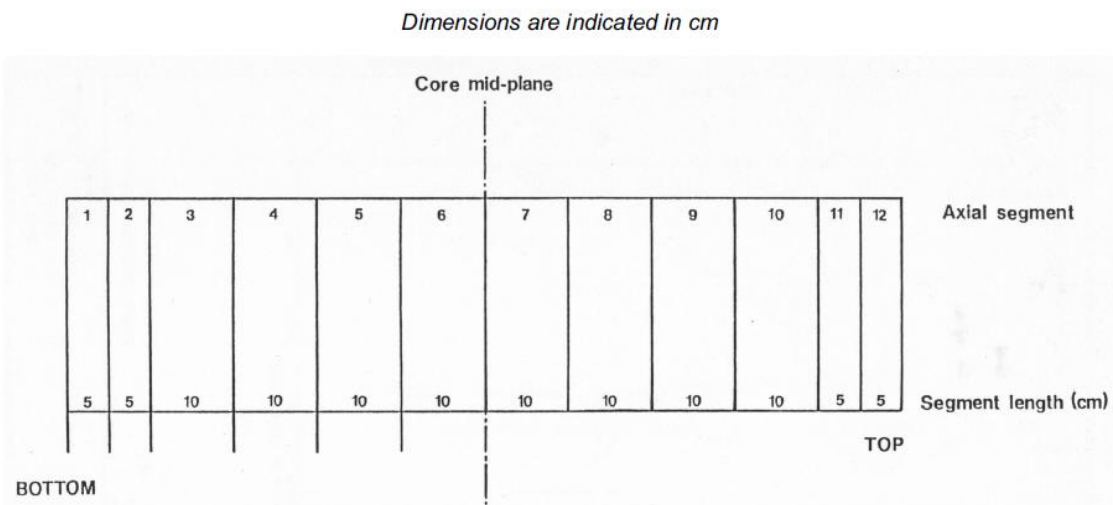
Fig. 25 – PRIMO Program, rod BD8, BD8 rod axial mesh.

4.3   Description of the IFA-597 input deck

The simulation of the two rods from the IFA-597 experiment is performed using TRANSURANUS code, version "v1m1j12", with the deterministic option, steady state thermal and mechanical analysis[6]. The version of the manual is "v1m1j12". The boundary conditions are prepared using a program written in PERL language.

Suitable physical models are chosen for the simulation of MOX fuel behavior subjected to standard power ramp condition. In particular, the fission gas intra-granular diffusion equation is solved by the URGAS algorithm[41], the gas diffusion coefficient is modeled according to Matzke[42] for the thermal part and to Dowling for the a-thermal part[43]. The inter-granular behavior is modeled according to the

modified Koo model[44]. The thermal conductivity is according to the standard MOX correlation developed by Van Uffelen and Schubert.

Only the active part of the fuel is accounted for the simulation. It has been divided into 3 axial slices according to the experimental data available at different elevations. The sectional analysis is selected (islice = 0). The nominal design values are used if available; the measured values are considered when nominal values are not specified.

4.3.1   Selection of the boundary conditions

The boundary conditions implemented for the analysis are:

- Linear heat rate at 4 axial positions (sectional analysis);
- Fast neutron flux (>1 MeV) at 4 axial positions (sectional analysis);
- Coolant pressure and temperature (axially constant).

The rate of change between two constant values is fixed to 6kW/(m h) according to ITU recommendations. The power history is modeled according to the condensed data available in the form of txt files available in "Mixed-oxide (MOX) Fuel Performance Benchmark"[11],[12]. The irradiation data (condensed data) were provided in plain text format as local rod power (in kW/m) for each rod as a function of irradiation time comprising a total of ~626 irradiation day (until the end of IFA-597.6). The linear heat rates for each fuel rod were given for three axial locations of the rod: bottom, middle and top. In addition, the local heat rate at the axial elevation of the fuel centerline thermocouple (TF) tip were provided (denoted LHRTF). The LHR histories for the two rods are shown in *Fig. 26*.

The local fast neutron flux is shown in *Fig. 27*. It is given as a function of local linear power[11],[12]:

$$NFF = 1.6 * 10^{11} * LHR \ [n/cm^2s] \qquad\qquad Eq. \ 9$$

As stated in the benchmark specifications[12], coolant pressure and temperatures are assumed constant. The coolant conditions are 33.6 bar, 240°C during the whole experiment. The heat transfer between coolant and cladding is computed by the code (ialpha = 0).
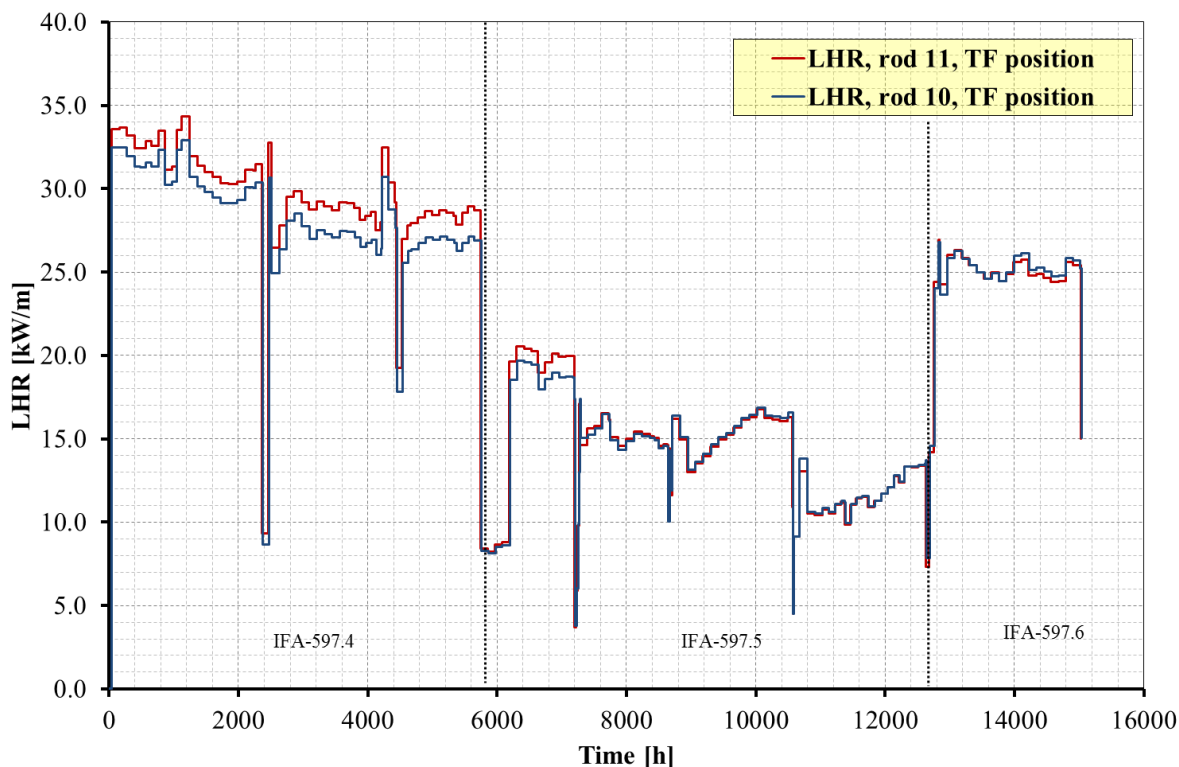
Fig. 26 – IFA-597, rod 10 and rod 11, LHR at thermocouple position.

Fig. 27 – IFA-597, rod 10 and rod 11, neutron fast flux at thermocouple position.

5 The FGR phenomenon and its modeling in TU code

5.1 The FGR phenomenon

Inert fission gas atoms have a very low solubility in the UO_2 matrix causing two important life-limiting phenomena in the fuel rod: either they remain in the pellets and contribute to the swelling, or they are released from the pellets to the pin free volume. The relevance of FGR in nuclear technology is connected with the assessment of gaseous source term in case of accident as well as the investigation of the rod performance under steady state and transient conditions. The FGR affects the rod performances as briefly recalled in the following[8].

- Xenon and Krypton (the main released species) degrade the thermal conductivity of the pin free volume (initially filled with Helium), and thus enhance the fuel temperature. Enhanced fuel temperature increases FGR and may initiate an unstable process called "thermal feedback".
- The release of fission gases increases the inner pin pressure, limiting the lifetime of a fuel rod since the inner pressure should not exceed the coolant pressure[7].
- The swelling due to gaseous fission products may lead to enhanced pellet–cladding mechanical interaction (PCMI), especially in transient conditions.
- The release of radioactive gases (and of volatile solids) from the UO_2 matrix to the free volume decreases the safety margin of a nuclear plant.

Gaseous isotopes tend to diffuse inside the grain (intra-granular processes) and to cumulate at grain boundaries in form of bubbles and structures of connected bubbles (inter-granular processes). From the grain boundaries they may reach the pin free volume basically by inter-linkage of bubbles and subsequent venting of the grain boundary inventory[6].

The first step is single gas atom diffusion in the lattice[1]. This mechanism includes different contributions that may be classified as temperature depended and a-thermal[45]. The thermal activated processes are assumed to dominate the diffusion above 1400°C being an increasing function of the temperature itself. The fission fragments contribute to the diffusion process too by means of their associated irradiation damage cascades. This last process dominates the diffusion process at temperatures below 1000°C and is practically a-thermal. In the range 1000-1400°C both the processes described above contribute to diffusion. Deviations from stoichiometry, additives (e.g. Cr, Nb), and burn-up affect the diffusion coefficient too because of their influence on the lattice structure[46]. Either natural or radiation produced imperfections in the solid matrix reduce the amount of fission products available for diffusion by trapping the migrating atoms into bubbles. A fraction of the gas atoms trapped in bubbles can be re-dissolved in the surrounding matrix through the interaction of a fission fragment with the bubble[47]. The experiments show that gas atom trapping in the grains in form of intra-granular bubbles may be a predominant effect under given conditions[48]. The trapping rate depends on the size of the intra-granular bubbles, hence on temperature, fission rate and burn-up. A second important effect of trapping occurs at grain boundaries (inter-granular process). When gas reaches grain boundaries, it precipitates on grain faces to form lenticular bubbles. Part of the gas inside these bubbles is transported back to the grain by fission spikes. When the saturation concentration is reached on the grain face, fission gas accumulates on the grain edge. If the gas at grain edges has also saturated, inter-linkage occurs forming a so-called tunnel network through which the gas can be released, especially in the case of transients[6]. In fact, during abrupt power (temperature) variations, a sudden interconnection or opening of grain face bubbles due to micro-cracking along grain boundaries takes place. Cracking causes instantaneous venting of the gas cumulated in the structure. This process

is connected to the burn-up (i.e. it occurs close to 1400 °C at 5 MWd/kgU and at 1050 °C at 60 MWd/kgU)[6].

Two additional mechanisms can affect the FGR in the high temperature range. The first one occurs above 1600°C: grains grow (that results in intra-granular trapping increase) causing grain boundary sweeping[48]. The second one occurs above 1800-2000 °C and involves diffusion of intra-granular bubbles in the grain matrix causing large columnar grain increase.

Finally, a small amount of gases may be released as consequence of a-thermal processes. Recoil and knock-out[1] are phenomena in which gas atoms that are close to the pellet outer surface are released basically by their collision with a fission fragment (recoil) or its induced irradiation cascade (knock-out).

5.1.1 FGR models

According to the Booth model[49], the intra-granular gas behavior is described by the following equations under the hypothesis of spherical grain of constant radius that contains immobile bubbles.

$$\partial Cs/\partial t = D \cdot [\partial^2 Cs/\partial r^2 + (2/r) \cdot \partial Cs/\partial r] - g*Cs + b*Cb + \beta \qquad Eq.\ 10$$

$$\partial Cb/\partial t = g*Cs - b*Cb \qquad Eq.\ 11$$

$$C_{tot} = Cs + Cb \qquad Eq.\ 12$$

Where:
D(t)   is the single gas atom diffusion coefficient;
Cs(r,t)   is the local concentrations of gas in solution in the fuel matrix;
Cb(r,t)   is the local concentrations of gas in solution in bubbles;
g   is the probability per unit time of gas atoms in solution being captured by a bubble;
b   is the probability per unit time of gas atom in bubble being re-dissolved to the matrix;
β(t)   is the rate at which gas is produced.

Under the assumption of equilibrium between trapping and resolution inside each bubble:

$$\partial Cb/\partial t = 0 \qquad Eq.\ 13$$

Assuming the effective diffusion coefficient as:

$$D_{eff} = D*b/(b+g) \qquad Eq.\ 14$$

The formulation of Speight[50] is obtained (instead of *Eqs. 6-7*):

$$\partial C_{tot}/\partial t = D_{eff}*\cdot[\partial^2 Cs/\partial r^2 + (2/r) \cdot \partial Cs/\partial r] + \beta \qquad Eq.\ 15$$

Gas that reaches the grain boundaries may precipitate on grain faces or may be transported back to the grain by fission spikes. The simplest concept to describe the inter-granular fission gas behavior is that of grain boundary saturation. It is assumed that, when a specific saturation concentration C^{sat}_{gb} (number of gas atoms per unit area) is reached, a network of interconnected bubbles has formed, which allows the release of gas atoms from the grain boundaries. Normally, it is further assumed that gas released from grain boundaries is also released from the fuel to the pin free volume. A standard model for grain boundary saturation has been developed by Dowling, White and Tucker[43]:

$$C^{sat}_{gb} = [4r*f(\theta)*f_c/(3k*Tsin2\Theta)] *(2\gamma/r + P_{ext})$$ *Eq. 16*

C^{sat}_{gb} is the number of gas atoms per unit area of grain boundary;
r   is the bubble radius;
$f(\theta)$ is a factor that considers that the bubbles are lenticular-shape and not spherical;
f_c represents the fraction of grain face area occupied by bubbles;
k   is the Boltzmann constant;
T   is temperature;
$2\cdot\Theta$ is the angle under which the lenticular bubble meets the grain boundary;
P_{ext} is the external pressure.

5.1.2   Main parameters and processes that affect the simulation of FGR

The FGR phenomenon is mainly a thermal phenomenon and, therefore, it is influenced by all the factors that influence the fuel temperature. These factors can be divided in three main groups: the first group consists of the fuel irradiation conditions and includes the reactor type, the operational conditions and the fuel burn-up (BOL or EOL). The second consists of the design parameter that affects the fuel thermal conductivity and the gap conductance (in terms of gas conductivity and gap width). In addition, the fuel grain size impacts on FGR because it influences the mean free path of fission gas atoms before being released and the grain boundaries saturation concentration. The third group, consists of all the processes that occur inside the fuel rod and cause temporary or permanent fuel and/or cladding deformations i.e. densification, swelling etc. *Tab. 14* summarizes the main parameters and phenomena.

Main parameters affecting FGR	
a) Irradiation conditions	
1. Reactor type	Power excursions caused by control system
2. Power transients	Cause fuel micro-cracking
3. Linear power	Directly affects gas intra-grains diffusion trough fuel temperature
4. Burn-up	Affects fuel thermal conductivity
b) Design parameters	
1. Gap gas mixture composition	Affects gap thermal resistance (conductance)
2. Pin total free volume	Affects gap thermal resistance (conductance)
3. Gap initial width between fuel and cladding	Affects gap thermal resistance (width)
4. Oxygen to metal ratio	Affects fuel thermal conductivity
5. Fuel additives (Gd)	Affects fuel thermal conductivity
6. Fuel porosity	Affects fuel thermal conductivity
7. Fuel grain size	Affects gas intra-grain diffusion mean free path and grain boundaries storage capability.
8. Fuel densification	Affects fuel thermal conductivity and gap width
9. High burn-up structure formation	Affects fuel microstructure at pellet periphery
c) Phenomena occurring in the fuel	
1. Cladding swelling and creep down	Affects gap thermal resistance (width)
2. Fuel swelling	Affects gap thermal resistance (width)
3. Fuel cracking and relocation	Affects gap thermal resistance (width)
4. Fuel densification	Affects fuel thermal conductivity and gap width
5. High burn-up structure formation	Affects fuel microstructure at pellet periphery

Tab. 14 – Main parameters and processes that affect the simulation of FGR.

5.2 Modeling of FGR in TU code

The following sub-sections describe the capabilities of TRANSURANUS code to exploit the FGR phenomenon and the processes that impact on its modeling.

5.2.1 FGR models

The thermal FGR is computed by solving Eq.15 coupled with an inter-granular model based on Eq.16. Two different algorithms are available: the URGAS[41] and the FORMAS[51] models. Both the models require *Deff* to solve the intra-granular gas behavior.

For each algorithm, three options are available and they differ in the effective diffusion coefficient. In general, it is given as:

$$Deff = D*b/(b+g) = D_{thermal} + D_{athermal} \qquad Eq.\ 17$$

- *Option 1, keyword FGRMOD 4.* It is according to the diffusion coefficients of Hj. Matzke[42] (thermal) and a-thermal diffusion coefficient according to R. White[52].

$$D_{thermal} = 5*10^{-8}\ e^{\ -40262/T} \qquad Eq.\ 18$$

$$D_{a\text{-}thermal} = 1.086*10^{-15}\ e^{\ -16506/T} \qquad Eq.\ 19$$

- *Option 2, keyword FGRMOD 6.* It <u>is the recommended TRANSURANUS model</u>, it is **assumed as Reference**. It is according with the diffusion coefficients of Hj. Matzke (thermal) and an a-thermal diffusion coefficient according to ITU data[8] obtained as:

$$D_{eff} \geq 1*10^{-25} \qquad Eq.\ 20$$

- *Option 3, keyword FGRMOD 9.* It is according to the diffusion coefficients of Turnbull[53]. It provides the single gas atom diffusion coefficient D as the sum of three contributors. D1(T) is the intrinsic high-temperature component, D2(R,T) is an irradiation enhanced thermal component (where R is the rating in W/gU), and D3(R) is the a-thermal term.

$$D = D_1 + D_2 + D_3 \qquad Eq.\ 21$$

$$D_1 = 7.6*10^{-10}\ e^{\ -35000/T} \qquad Eq.\ 22$$

$$D_2 = 3.22*10^{-16}\ *\sqrt{R}\ e^{\ -13800/T} \qquad Eq.\ 23$$

$$D_3 = 6*10^{-23}\ *R \qquad Eq.\ 24$$

The intra-granular model should be coupled with the inter-granular model to treat the accumulation and net release from the grains. Three options are available to simulate the inter-granular behavior of the fission gases derived from Eq.16.

- *Option 1, keyword IGRBDM 1.* It is according to a simple approximation. It assumes the saturation concentration at grain boundaries which causes the release of the surplus of gas that reaches the grain boundaries as constant[54]: $[1\text{-}4]*10^{-4} \mu mol/mm^2$ for [*FGRMOD4 or 6 – FGRMOD9*] respectively. It is the recommended option in normal operation.

- *Option 2, keyword IGRBDM 2.* It assumes that the saturation concentration at grain boundaries which causes the release of the surplus of gas takes the form[8]:

$$C^{sat}_{gb} = a/T \qquad\qquad Eq.\ 25$$

Where a is 0.1773 μmol/mm^2 or 0.7092 μmol/mm^2 depending on the intra-granular modeling, *FGRMOD4* or *6* and *FGRMOD9* respectively.

- *Option 3, keyword IGRBDM 3.* It is **assumed as Reference**. It is according to a modification of the Koo model[44] that has been developed to consider the additional release that occurs during transients like power ramps. This model consists of two contributions: micro-cracking in case of power increase or reduction, and gas transport from the grain to the grain boundaries[55]. The entire fission gas inventory stored at the grain boundaries is released if the power excursion is greater than 3.5 kW/m and the local temperature T overpasses a local burn-up (bu$_{loc}$) dependent limit (Eq.22). If the limits are not met the grain boundaries are treated according to the standard formulation (option 1). This model should be invoked in transient conditions.

$$T > 1500\ (1 - bu_{loc} / 80) \qquad\qquad Eq.\ 26$$

The a-thermal contribution to FGR due to knock-out and recoil is modeled according to Turnbull[55]:

$$g^{a\text{-}thermal} = 6.1705*10^{-8} *bu * g^{created} \qquad\qquad Eq.\ 27$$

where bu is the burn-up.

The FGR is obtained by integration in time, axis and radius of the above mentioned terms and is expressed as % of total gases released at a given time to the total amount of gas generated. The code has the capability to discriminate between the Xe and the Kr contributions.

5.2.2 Fuel conductivity correlations

The fuel conductivity affects the fuel radial temperature profile. Since this last parameter is crucial in the determination of the intra-granular thermal diffusion coefficient it is expected that the fuel conductivity influences the FGR. In general, the fuel conductivity correlations have two temperature dependent main contributions:

- Conduction through lattice vibrations (phononic term): $\lambda_{phonon}=1/(a+bT)$ where a, b are constant and T is temperature [K]. <u>It is the dominant contribute at lower temperatures.</u>
- Conduction through free electrons: $\lambda_{electronic}= c*T^3$ where c is a constant or $\lambda_{electronic}=(c_1/T^2)*e^{d/T}$ where c_1 and d are constants. <u>It contributes at high temperatures.</u>

Beside the dependence on the temperature, the thermal conductivity depends on the fuel porosity (P), the oxygen to metal ratio O/M (stoichiometry), the burn-able absorbers concentration and the burn-up.

- Porosity in a ceramic material invariably decreases the thermal conductivity. In general the effect of porosity is taken into account by a corrective factor (fp): $\lambda(P) = \lambda_{100}*fp$. In which λ_{100} is intended conductivity at 100% dense material.
- Hypo- and hyper-stoichiometric fuel has a lower thermal conductivity than stoichiometric fuel. This is generally taken into account as a corrective factor proportional to the deviation *x* to the stoichiometric value 2 in the form: $a_x x$ where a_x is a constant.
- The introduction of solid FPs and the formation of fission gas bubbles decrease the thermal conductivity λ so the burn-up effect is degradation of fuel conductivity proportional to the burn-up.

Several models are available in TRANSURANUS to account for conductivity of UO_X, MOX, UN and UC fuels. Those correlations specifically developed for MOX fuels are listed and briefly described in the following.

- *Option 1, keyword MatProp_fuel (l, 6) = 31.* It is **assumed as reference** correlation; it gives the thermal conductivity of MOX fuel (best estimate) according to Van Uffelen and Schubert. The correlation is based on experimental data obtained by Duriez et al.[56] for fresh MOX fuel and laser flash measurements of irradiated MOX fuel at ITU. It is extended by an ambipolar term recommended by Ronchi et al.[57]. The thermal conductivity λ_0 of 100 percent dense material is given by:

$$\lambda_0 = 1 / (a + a_1 bu + b T + b_1 bu T_p) + c / T^2 exp(- d / T) \qquad Eq. 28$$

$$[W/mK]$$

where:
a, a_1, b, b_1, c, d   are constants;
bu   is the local burn-up [MWd/kgU];
T   is the local absolute temperature [K];
Tp   is defined as min (1923,T).

A porosity correction is applied:

$$\lambda_p = \lambda_0 (1 - P)^{2.5} \qquad Eq. 29$$

- *Option 2, keyword MatProp_fuel (l, 6) = 32.* It computes the thermal conductivity of MOX fuel according to Carbajo et al.[58]. The thermal conductivity λ0 of 100 percent dense material is given by:

$$\lambda_0 = 1.158 \{1/[a_0+a_1x+(b_0+b_1x) t_k+ c/t_k^{2.5} exp(-d/t^k)]\} FD(bu,T) FP(bu,T) FR(T) \qquad Eq. 30$$

$$[W/mK]$$

$$\omega = 1.09 bu_{at}^{3.265} + 0.643 (T/ bu_{at})^{1/2}$$
$$FD(bu_{at},T) = \omega arctg(1/\omega)$$
$$FP(bu_{at},T) = (1 + 0.019 bu_{at}) / [(3 - 0.019 bu_{at}) (1 + exp^{-(T-1200)/*100})]$$
$$FR(T) = 1 - 0.2/(1 + exp^{-(T-900)/*80})$$

where:
a_0, a_1, b_0, b_1, c, d   are constants;
T   is the local absolute temperature [K];
x   is the stoichiometry deviation;
t_k is T/1000;
bu_{at} is the burn-up in at%
FD(bu_{at},T)   is the factor that represents the effect of dissolved fission products;
FP(bu_{at},T)   is the factor that accounts for the precipitated fission products;
FR(T)   is the factor that accounts for the radiation effect.

The porosity correction is:

$$\lambda_p = \lambda_0 \ (1\text{-}P)/(1\text{+}2P) \qquad\qquad Eq.\ 31$$

where P is the porosity.

- *Option 3, keyword MatProp_fuel (l, 6) = 33.* It computes the thermal conductivity of MOX fuel according to Lanning and Beyer[59]. The thermal conductivity λ_{95} of 95% dense material, based on the model of Duriez[56], is given by:

$$\lambda_{95} = 1/[A(x)+B(x)\ T+f(BU)+(1\text{-}0.9\ e^{-0.004BU})+g(BU)+h(T)]+ C/T^2\ exp(\text{-}D/T) \qquad Eq.\ 32$$

where:

C, D   are constants;
T   is the local absolute temperature [K];
x   is the stoichiometry deviation;
A, B, f, g, h   are simple functions depending on the parameters in brackets.

The porosity correction is according to Lucuta [60]:

$$\lambda_p = 1.079\ \lambda_{95}\ \{d\ /\ [1\text{+}0.5\ (1\text{-}d)]\} \qquad\qquad Eq.\ 33$$

where d is the fractional density.

- *Option 4, keyword MatProp_fuel (l, 6) = 34.* It computes the heat conductivity according to the Wiesenack[61] correlation for UO_2, reduced by a factor of 0.92[62]. The thermal conductivity λ_{95} of 95% dense material is given by:

$$\lambda o = 0.92\ [1/(Ao+A_1bu +B_1\ min(1650,\ \theta)+ B_2*\ min\{1650,\ \theta\ \}) + (C)\ e^{D\theta}] \qquad Eq.\ 34$$

$$\lambda p = \lambda o(1\text{-}P)^{2.5} \qquad\qquad Eq.\ 35$$

where:

Ao, A_1, B_1, B_2, C and D   are constants;
θ   is the temperature in °C;
bu   is the local burn-up [MWd/kgUO_2].

In this correlation no recommendation for the porosity correction is given. Since the correlation is based upon the MATPRO-11 correlation.

$$\lambda_p = \lambda_{95}\ (1\text{-}\beta\ P)/(1\text{-}\ 0.05\ \beta) \qquad\qquad Eq.\ 36$$

where β is a constant and P is the porosity.

- *Option 5, keyword MatProp_fuel (l, 6) = 35.* It gives the thermal conductivity of MOX fuel according to Van Uffelen and Schubert (conservative). This correlation is identical with the 'best estimate' described by eq.24. The only difference is the value of the constant a_1. This correlation is more conservative because gives a more important conductivity degradation with increasing burn-up.

5.2.3 Modeling of fuel relocation

Pellet cracking and relocation can be separated into two mechanisms [8][63]:

- Mechanism1: the elastic strain prior to cracking is redistributed, i.e. the pellet volume increases and the stress level in the pellet are reduced.
- Mechanism2: depending on the geometrical details of the rod, e.g. the gap size, relocation (i.e. a gross movement of fuel fragments), occurs.

Detailed models based on first principles in mechanics are available for mechanism1, whereas the mechanism2 by its nature can be treated only empirically. Unfortunately, in most situations, the second mechanism is by far the most important and this is the reason of the big uncertainties encountered in simulating relocation. The most important models correlate the radial relocation with the as fabricated gap size g_o and the linear power q. In some cases, burn-up dependence is also considered. There are six relocation models for LWRs available in TU[8]: IRELOC 2, 3, 4, 5, 6, 8. The ITU recommended models are IRELOC 8 and IRELOC 5.

- *Option 1, keyword IRELOC = 5*. It is the modified KWU-LWR model, ITU calibration 1997. This model calculates relocation increment according with the simple FEMAXI correlation[63]:

$$u^{rel} = 0.3 * g_o / r_o \qquad\qquad Eq.\ 37$$

  where:
  g_o is the as fabricated gap size normalized to the as fabricated pellet outer radius;
  r_o is the as fabricated fuel pellet outer radius;
  u^{rel} is the radial deformation at outer surface of the fuel due to radial relocation.

  This model applies once at the beginning of the calculation, the axial relocation is also considered as dependent by the ratio free volume/total pellet volume, the axial forces and the radial relocation. This option is strictly correlated with the number of cracks (NCRACK input variable); as usual, this number range between 4-6 (recommended range).

- *Option 2, keyword IRELOC = 2*. It is the original KWU-LWR model (calibration 1976) [8][63]. This model relies on the following equation:

$$u^{rel} = 0.35 * g_o/r_o \qquad\qquad Eq.\ 38$$

  The model is similar to IRELOC 5.

- *Option 3, keyword IRELOC = 3*. It is the GAPCON-THERMAL-3 model. This model calculates the radial deformation due to relocation *urel* only. It implements the GAPCON-THERMALIII[8][63] correlation:

$$u^{rel} = (42*b/(1+b) + 0.274q + 3) * g_o /100/r_o$$

$$b = e^{(-4+bu^{0.25})}$$

$$Eq.\ 39$$

  where:
  g_o is the as fabricated gap size normalized to the as fabricated pellet outer radius;
  q   is the linear power [kW/m],
  bu   is the local burn-up [MWd/kgU].

  This model applies only when gap is open and does not consider axial relocation.

- *Option 4, keyword IRELOC = 4*. This is the "Operational relocation model according to Eberle and Stackmann", (calibration 1997). It differs from the others: it takes into account the actual value of the gap without relocation according to the KWU equation [8][63]:

$$u^{rel} = a[1 - e\text{-}S/Df*a] \qquad\qquad Eq. 40$$

where:
S   is the difference between the actual cladding inner diameter dc (thermal expansion, elastic and creep strains included) and the un-cracked pellet diameter Df (allowing the thermal expansion, swelling and densification);
a   is equal to 0.0234 / 0.0164 for UO_2 and UO_2/PuO_2 respectively (constant that takes into account Pu).

Relocation is considered also in the axial direction as a factor applied to radial relocation.

- *Option 5, keyword IRELOC = 6*. It is the operational relocation model according to Eberle and Stackmann, implicit formulation of model number 4.

- *Option 6, keyword IRELOC = 8*. It is **assumed as reference**. It is the modified FRAPCON-3 model. This model considers as fabricated gap, linear power and burn-up. The model applies only if gap is open and does not consider relocation in the axial direction. It is based on these equations:

$$u^{rel} = 30+pfactor1+(10+pfactor2)*fbu \qquad\qquad Eq. 41$$

$$Pfactor1 = (q\text{-}20)*0.1$$
$$Pfactor2 = (q\text{-}20)*0.4$$
$$fbu = bu*0.2 \text{ if } bu <5MWd/kgU$$
$$fbu = 12 \text{ if } bu \geq 5MWd/kgU$$

where:
bu   is the burn-up [MWd/kgU];
q   is the linear power.

5.2.4 Modeling of fuel swelling

Swelling is defined as the fractional increase in the volume of the solid with respect to the initial volume *Vo* of the as-fabricated fuel [8], or by:

$$[\Delta V/V](t) = (V(t) – Vo)/Vo \qquad\qquad Eq. 42$$

Fuel swelling takes into account of two terms: solid swelling and gaseous swelling:

$$\Delta V/V = (\Delta V/V)^{sol} + (\Delta V/V)^{gas} \qquad\qquad Eq. 43$$

the fractional increase in the volume due to swelling is expressed via swelling strains $\varepsilon_{swe,i}$ (i = r, t, a = radial, tangential, axial):

$$\varepsilon_{swe,i}(t) = \varepsilon_{swe,i}(t0) + \Delta\varepsilon_{swe,i}tot \qquad\qquad Eq. 44$$

$$\Delta\varepsilon_{swe,i}{}^{tot} = f[\Delta(\Delta V/V)] \qquad\qquad Eq. 45$$

With f = 1/3 if the swelling rate can be considered isotropic.

TRANSURANUS code includes several correlations to considering the UO_X fuel swelling in LWRs and the MOX fuel swelling in FBR. The first are correlations 18, 19, 20 (underlined)(recommended), 21. The second are correlations 3, 11, 12 and 13. They are selected by mean of the option MODFUEL(j=4).

- *Option 1, keyword MODFUEL(j=4) = 20*. It is **assumed as reference**. It is the standard correlation for UO_X fuel swelling in LWRs developed by K. Lassmann [8] from correlation 19 in which gaseous swelling contribute was modified and integrated from this steady state equation:

$$(\Delta V/V)^{gas} = c*a(T)/k *(1-e^{-k*bu}) \qquad \text{Eq. 46}$$

where:
$(\Delta V/V)^{gas}$ fractional gaseous swelling;
$c, a(T), k$ are model parameters (c depends on stress, a from temperature).

Integration of previous equation is done in this manner:

$$\Delta(\Delta V/V)^{gas} = \Delta(\Delta V/V)^{gas}_{max} *(1-e^{\Delta t/\tau}) \qquad \text{Eq. 47}$$

where:
$\Delta(\Delta V/V)^{gas}$ increment of fractional increase in volume due to gaseous FPs in a time step with a burn-up increment Δbu;
$\Delta(\Delta V/V)^{gas}_{max}$ is defined as $\Delta(\Delta V/V)^{gas}_{max} = (\Delta V/V)^{gas}_{n+1} - (\Delta V/V)^{gas}_{n}$;
$n, n+1$ are related respectively to time t_n and time t_{n+1};
τ is the time constant = 1/D;
D   is the diffusion coefficient.

Solid swelling was considered as follow:

$$\Delta(\Delta V/V)^{sol} = B*\Delta bu \qquad \text{Eq. 48}$$

where:
Δbu is the burn-up increment during time step $\Delta t = t^{n+1} - t^n$;
$\Delta(\Delta V/V)^{sol}$ is the increment of fractional increase in volume due to solid FPs in a time step with a burn-up increment Δbu;
B   is a model parameter.

- *Option 2, keyword MODFUEL(j=4) = 18*. This simple correlation gives the total swelling rate for UO_X fuel in LWRs including matrix swelling due to solid and gaseous fission products[8]. The increment of the fractional volume increase is expressed as rate equation:

$$\Delta(\Delta V/V) = S*\Delta bu \qquad \text{Eq. 49}$$

where:
S   is equal to $7*10^{-7}$ [tonU/MWd], it is the swelling constant rate.

This equation takes into account only for solid swelling therefore it is recommended for normal operation.

- *Option 3, keyword MODFUEL(j=4) = 19.* It is the original MATPRO swelling model for UO_X fuel in LWRs[8]. The swelling due to solid fission products is simply proportional to the burn-up while the gaseous swelling correlation is more complicated and depends on burn-up, burn-up increment (burn-up during a given time step) and temperature T:

$$\Delta(\Delta V/V)^{sol} = b*\Delta bu$$

$$\Delta(\Delta V/V)^{gas} = a(T)*e^{-k*bu}*\Delta bu$$

Eq. 50

where:
a, b, k   are models parameters.

- *Option 4, keyword MODFUEL(j=4) = 21.* It is the implicit formulation of correlation 20.
- *Option 5, keyword MODFUEL(j=4) = 3.* This correlation was proposed by Dienst et al[64] specifically for FBR MOX fuel design purposes. The increment of the fractional volume increase is expressed by:

$$\Delta(\Delta V/V) = S*\Delta bu \qquad Eq.\ 51$$

where:
S   is the swelling rate related to the burn-up increase;
Bu   burn-up increment during current time step;
The total increment of the swelling strain $\Delta\varepsilon$ in radial, tangential and axial direction is computed as:

$$\Delta\varepsilon = S*\Delta bu/3 \qquad Eq.\ 52$$

$$S=0.012\ (open\ gap)$$
$$S=0.0065\ (closed\ gap)$$

The gaseous swelling is nil if gap is closed, its contribution is computed as:

$$\Delta(\Delta V/V)^{gas} = (S-0.0065) * \Delta bu \qquad Eq.\ 53$$

- *Option 6, keyword MODFUEL(j=4) = 11.* This correlation is given by Pesl et al.[65] for FBR MOX fuel. The increment of the fractional volume increase is expressed by:

$$\Delta(\Delta V/V) = S*\Delta bu \qquad Eq.\ 54$$

where:
S   is the swelling rate related to the burn-up increase;
Bu   burn-up increment during current time step.

The total increment of the swelling strain $\Delta\varepsilon$ in radial, tangential and axial direction is computed as:

$$\Delta\varepsilon = S*\Delta bu/3 \qquad Eq.\ 55$$

$$S=0.020 \text{ (open gap)}$$
$$S=0.0065 \text{ (closed gap)}$$

The gaseous swelling is nil if gap is closed, its contribution is computed as:

$$\Delta(\Delta V/V)^{gas} = (S-0.0065) * \Delta bu \qquad\qquad Eq. \ 56$$

- *Option 7, keyword MODFUEL(j=4) = 12.* This correlation is based on the work of Zimmermann[66] and of Dienst et al.[64] and was developed by K. Lassmann. The increment of the fractional volume increase in FBR MOX fuel is expressed by:

$$\Delta(\Delta V/V) = S*\Delta bu \qquad\qquad Eq. \ 57$$

where:
S   is the swelling rate related to the burn-up increase;
Bu   burn-up increment during current time step.

The total increment of the swelling strain Δε in radial, tangential and axial direction is computed as:

$$\Delta\varepsilon = S*\Delta bu/3 \qquad\qquad Eq. \ 58$$

$$S=0.0065 \textbf{ if } T<926.85°C,$$
$$S=9.67000E\text{-}04*exp(2.05727E\text{-}03) \textbf{ if } 926.85<T<1600°C,$$
$$S=9.70024E\text{-}04*exp(4.93355E\text{-}03) \textbf{ if } 1600<T<2000°C,$$
$$S=0.187 \textbf{ if } T>2000,$$

if the gap is open;

$$S=0.0065$$

if the gap is closed.

The gaseous swelling is nil if gap is closed, its contribution is computed as

$$\Delta(\Delta V/V)^{gas} = (S-0.0065) * \Delta bu \qquad\qquad Eq. \ 59$$

- *Option 8, keyword MODFUEL(j=4) = 13.* This correlation is based on the work of Dienst et al.[64] and was suggested by Preußer for FBR MOX fuel. The increment of the fractional volume increase is expressed by:

$$\Delta(\Delta V/V) = S*\Delta bu \qquad\qquad Eq. \ 60$$

where:
S   is the swelling rate related to the burn-up increase;
Bu   burn-up increment during current time step.

The total increment of the swelling strain Δε in radial, tangential and axial direction is computed as:

$$\Delta\varepsilon = S*\Delta bu/3 \qquad\qquad Eq. \ 61$$

$$S=0.020$$

if bu < 1 at.% and if the gap is open,

$$S=0.012$$

if bu > 1 at.% and if the gap is open,

$$S=0.0065$$

if the gap is closed.

The gaseous is nil if gap is closed, its swelling contribution is computed as:

$$\Delta(\Delta V/V)^{gas} = (S-0.0065) * \Delta bu \qquad\qquad Eq.\ 62$$

5.2.5 Modeling of fuel densification

There are several options available in TU to account for densification[8]. They are selected by the keyword IDENSI. The models applicable to LWR are:

- *Option 1 keyword IDENSI 2*: empirical model for LWR and FBR. This model needs:
    - the input of the minimum porosity DENPOR at the end of thermal irradiation induced densification and
    - the time constant DENBUP (burn-up in MWd/tU, at which irradiation induced densification is terminated).

- *Option 2 keyword IDENSI 3*: Assmann-Stehle model[67] for UO_2 in a LWR. This model needs several input data:
    - PFEIN (initial porosity of fine pores),
    - PGRO1 (fabrication porosity of coarse pores, Class 1),
    - PGRO2 (fabrication porosity of coarse pores, Class 2),
    - PGRO3 (fabrication porosity of coarse pores, Class 3),
    - RGRO1 (fabrication radius of the coarse pores, Class 1 [mm]),
    - RGRO2 (fabrication radius of the coarse pores, Class 2 [mm]),
    - RGRO3 (fabrication radius of the coarse pores, Class 3 [mm]) and
    - DENPOR.

- *Option 3 keyword IDENSI 7*: MATPRO LWR models FUDENS/FHOTPS. This model needs the input of the minimum porosity DENPOR at the end of thermal and irradiation induced densification. According with the TU manual this model option is not yet fully tested.

Reference model implemented

The reference model implemented is IDENSI 2 in which densification is treated according with this empirical correlation[8]:

$$P(bu) = P_\infty + (P_0 - P_\infty) * e^{-(5bu/bu0)} \qquad\qquad Eq.\ 63$$

where:

P(bu) is the sinter porosity;

P_∞ represents the minimum porosity (input data DENPOR);

P_0 is the fabrication porosity (input data POR000);

bu is the average burn-up in a section or slice;

bu_0 is the burn-up at which densification ends (input data DENBUP).

5.2.6 Modeling of fuel grain growth

In this activity grain growth is considered, the model is developed according to Ainscough equation:

$$dGR_{gr}/dt = k[(1/GR_{gr}) + (1/GR_{MAX})] \qquad\qquad Eq.\ 64$$

At fixed temperature the maximum grain size is fixed to:

$$GR_{max} = 2.23 * e^{-7620/T} \qquad\qquad Eq.\ 65$$

Grain growth between two times is treated as:

$$GR\ t_{n+1} = \{GR\ t_n + [6.192*1013*\varDelta t*e^{-min(46524/T,60)}]/(4*GR\ t_n)\} \qquad Eq.\ 66$$

where:
$\varDelta t$ time step width $(t_{n+1} - t_n)$;
GR   grain size;
T [K]   temperature;
t_n time n;
t_{n+1} time n+1.

The grain growth phenomenon affects the fission gas release in three ways. First of all, grain boundary sweeping provides another mechanism for the collection of the fission gas at these internal surfaces from which release can occur. This effect is taken into account by adding a supplementary fractional release term (f) from the matrix to the grain boundaries that is equal to the volume fraction of the fuel swept by the moving boundaries:

$$f = (r_{n+1}^3 - r_n^3)/ r_n^3 \qquad\qquad Eq.\ 67$$

Secondly, the diffusion distance for the fission gas atoms created in the grains increases. Unlike the first consequence this tends to reduce the release rate. Thirdly, the grain growth also reduces the capacity of the grain boundaries for storing fission gas as their total surface-to-volume ratio is decreasing.

5.2.7 Modeling of gap conductance

The fuel-cladding temperature difference $\Delta\theta_{f,cl}$ is defined by:

$$\varDelta\theta_{f,cl} = q''_{f,cl}/h \qquad\qquad Eq.\ 68$$

where:
$q''_{f,cl}$ is the heat flux density between fuel and cladding, it is defined as $q''_{f,cl} = = q'/2*\pi*r_{f0}$;
q' is the linear power;
r_{f0} is the outer fuel radius;
h   represents the heat transfer coefficient between fuel and cladding (gap conductance).

The heat transfer coefficient h depends on:

- gap width or contact pressure between fuel and cladding;
- gas pressure and composition;
- surface characteristics of cladding and fuel;

The gap conductance model incorporated in the TRANSURANUS code is the well-documented URGAP model. The original URGAP model from 1979 was revised and recalibrated in 1986 using an extended database consisting of approximately 1000 data. Four options are available in TU to simulate gap conductance [8] they are labeled as IHGAP:

- *Option 1 keyword IHGAP 0:* <u>standard Option</u> gas Bonding thermal conductivity of mixture according to Lindsay and Bromley. Accommodation coefficients are taken into account;
- *Option 2 keyword IHGAP 1*: gap conductance is prescribed; no call of URGAP-Model;
- *Option 3 keyword IHGAP 3*: as standard option but without considers accommodation coefficients;
- *Option 4 keyword IHGAP 4*: specific model gas bonding, thermal conductivity of mixture according to Tondon and Saxena. Accommodation coefficients are taken into account;
- *Option 5 keyword IHGAP 5*: as option 4, accommodation coefficients are not taken into account.

Reference model implemented

In 1991, the TRANSURANUS standard LWR thermal conductivities of the fuel and the cladding were modified[8]. The new correlation for Zircaloy gives approximately 10% higher values, whereas the thermal conductivity of the fuel has not changed significantly. Nevertheless, it was felt that the extremely sensitive gap conductance model, which depends on these material properties, should be refitted. All four model options, i.e. IHGAP = 0, 3, 4 and 5 were fitted individually and finally the URGAS model option <u>IHGAP = 0 was chosen as recommended</u>.

5.2.8 Modeling of cladding creep

Creep causes a radial contraction of the cladding due to the external pressure. This affects the gap size evolution and therefore the maximum fuel temperature. The standard option (no other models are available in the code) for Zircaloy cladding creep is assumed in the reference calculations. This correlation calculates the effective creep rate according to the Lassmann-Moreno model[8]. It considers two components of steady state creep as thermal creep and dislocation climb:

$$\dot{\varepsilon}_{eff} = \dot{\varepsilon}_{th} + \dot{\varepsilon}_{climb} \qquad\qquad Eq.\ 69$$

$$\dot{\varepsilon}_{th} = 1.083 \cdot 10^5 \cdot e^{(-1700/T)}\ sinh(\sigma_{eff}/60) \qquad\qquad Eq.\ 70$$

$$\dot{\varepsilon}_{climb} = 1.0885 \cdot 10^{-28} \cdot \sigma_{eff}\ 4 \cdot \Phi + 4.2466 \cdot 10^{-23} \cdot \sigma_{eff} \cdot \Phi \qquad\qquad Eq.\ 71$$

where

$\dot{\varepsilon}_{eff}$ is the effective strain rate [1/h];

$\dot{\varepsilon}_{th}$ is the thermal strain rate [1/h];

$\dot{\varepsilon}_{climb}$ is the strain rate due to irradiation enhances dislocation climb creep [1/h];

σ_{eff} is the effective stress [MPa];

T   is the temperature [K];

Φ is the fast neutron flux [n/(cm^2·s)].

The thermal component is depending on the clad temperature and the effective stress while, the climb component, depends upon the neutron fast flux and the effective stress.

5.2.9 Modeling of Helium release

In order to simulate the behavior of He in the fuel, both an intra-granular and an inter-granular transport model have been implemented in TU-code. Three different models can be selected to compute the Helium diffusion inside grains. The option iHe = 1 should be used standard, it is based on the fit of the diffusion coefficients reported in the review of Federici et al.[68]. The option iHe = 2 is a

lower limit of the data of Federici et al., while iHe = 3 is the correlation proposed by Ronchi and Hiernaut[69].

The inter-granular He model depends on the inter-granular behavior of fission gases and has thus been included in the fission gas grain boundary models (Grbdm1, Grbdm2 and Grbdm3). The model considers that if the temperature is higher than 800°C, Helium reaching the grain boundary is instantaneously released. If the temperature is lower than 800°C, He is trapped at the grain boundary until the saturation concentration of fission gases is reached.

The main assumption of the intra-granular module is the treatment of the trapping and resolution in equilibrium (i.e., adopting an effective diffusion coefficient) and the grain boundary as a perfect sink (i.e., same assumptions of Federici et al. (2007) and TU fission gas release model). The intra-granular behavior is then modeled by a diffusion equation inside a spherical grain and considering an effective diffusion coefficient (Deff, m^2/s). The approach is the same of ordinary fission gas diffusion.

$$\partial C_{He}/\partial t = D_{eff}[\partial^2 C_{He}/\partial r^2 + (2/r)\cdot\partial C_{He}/\partial r] + He \qquad \text{Eq. 72}$$

$$C_{He}(t_s, r=a) = 0 \qquad \text{Eq. 73}$$

where r is the radial coordinate, C_{He} (mol/m^3), the concentration of helium inside the grain, He (mol/m^3s) the helium production rate and t_s (s) the time.

The three options available provide different values of D_{eff} that are reported below:

$$iHe = 1: D_{eff} = 8.887*10^{-14}* exp(-17505.9/T) \qquad \text{Eq. 74}$$

$$iHe = 2: D_{eff} = 1.405*10^{-12}* exp(-17505.9/T) \qquad \text{Eq. 75}$$

$$iHe = 3: D_{eff} = 8.000*10^{-7}* exp(-23163.5/T) \qquad \text{Eq. 76}$$

However, the last one is an atomic diffusion coefficient derived from the interpretation of the experimental data by means of a more complex model, which takes into account trapping and resolution separately. Furthermore it is representative of a [238]Pu MOX doped fuel, where the self-irradiation is expected to have a role in the enhancement of the diffusion coefficient. For these reasons it should be used only as a conservative test case.

5.3 Summary of the reference models

The main models and correlations that may impact on the simulation of the FGR assumed to develop the reference input deck are reported in *Tab. 15* distinguishing among the correlation model related to fuel pellet, gap, cladding and fission gas release. The criteria adopted in devolving the reference input decks are:

- choice of models or correlations recommended in the TU handbook version 2012 (when indicated);
- choice of models or correlations implemented as usual (if no recommendation are given in the handbook).

PRIMO & IFA-597 Reference input decks			
Parameter	**Reference Option**	**Description**	**Other options**
Fuel conductivity	Correlation 31 (recommended)	Van Uffelen and Schubert best estimate, it takes into account the fuel temperature, burn-up, the High Burn-up Structure (HBS) and the porosity.	32, 33, 34, 35.
Fuel swelling	Correlation 20 (recommended)	Developed by K. Lassmann from correlation 19. The gaseous swelling contribute was modified and integrated from this steady state equation considering the local contribute of the burn-up, the temperature, the stress and	18, 19, 21, 3, 11, 12, 13
Pellet fragment relocation	Model ireloc 8	Modified FRAPCON-3 model. It considers the as fabricated gap size, the burn-up and the linear heat rate.	2, 3, 4, 5, 6
Fuel grain growth	Model igrnsz 1 (recommended)	Grain growth model of Ainscough and Olsen. It computes the grain radius increase as function of the fuel local temperature assuming a maximum grain radius for each temperature.	--
Fuel densification	Model idensi 2 (recommended)	Empirical model for LWR and FBR. This model needs the input of the minimum porosity DENPOR at the end of thermal and irradiation induced densification and the time constant DENBUP (burn-up in MWd/tU, at which irradiation induced densification is terminated).	3, 7
Gap conductivity	Model ihgap 0 (recommended)	Standard Option: gas Bonding thermal conductivity of mixture according to Lindsay and Bromley. Accommodation coefficients are taken into account	1, 3, 4, 5
Cladding creep	Correlation 20 (recommended)	Effective creep rate according to the Lassmann-Moreno	--
Fission gas release	Models: fgrmod6 (recommended), igrbdm3,Idifsolv0	*FGRMOD 6:* URGAS algorithm with the diffusion coefficients of Hj. Matzke (thermal) and a constant athermal diffusion coefficient. *IGRBDM 3:* New model developed according to modified Koo model for ramps simulations *IDIFSOLV 0:* Diffusion equation is solved by the URGAS-algorithm	Fgrmod: 4,9 Igrbdm: 0, 1, 2 Idifsov: 1, 2, 3 4,5,6
Helium release	iHe = 0	Helium release not computed.	iHe: 1, 2, 3

Tab. 15 – PRIMO Program & IFA-597, summary of models and correlations assumed in the reference that may impact on the FGR simulation.

6 Validation of TU code against PRIMO experiment

6.1 Reference results

The assessment of TU code in simulating rod BD8 is discussed in the following subsections. The analysis deals with the comparison between measured and predicted trends (burn-up, FGR, grain size, dimensional changes and clad integrity). The main results are presented from *Fig.28* to *Fig.36* and are summarized in *Tab. 16*.

6.1.1 Burn-up analysis

In order to demonstrate the consistency of any calculation, it is essential to predict the burn-up in a correct way. In fact, this first step implies to demonstrate that the fuel rod is analyzed under conditions that represent its state at the end of the experiment. In addition, part of the models of any fuel pin mechanic code are dependent upon the burn-up and therefore it should be verified that those models are taking into account the burn-up effects according to the experimental conditions achieved.

The measured burn-up at the end of the experiment is available in the database[10] including its uncertainty (±6%). TU code models the burn-up according to the "TRANSURANUS-LWR burn-up model"[70]. *Fig.28* and Tab. 16 summarize the results. The final value of the burn-up is well captured.

6.1.2 FGR analysis

The experimental FGR after the power ramp is estimated assuming a gas (Xe + Kr) generation rate of 30 cm^3(STP)/MWd. The fraction of the gas released after the base irradiation is estimated on the basis of the FGR of the sibling rod BD10. The measurement uncertainty is assumed 2% after base irradiation and 10% after the power ramp.

The reference calculation solves the intra-granular diffusion equation by means of the URGAS algorithm with the diffusion coefficient modeled according to Matzke plus a constant to simulate it's a-thermal part. For the inter-granular fission gas behavior, the modified Koo model developed for power ramps is applied; all these models are described in detail in section 5.1.

The simulated trends are depicted in *Fig.29* and *Fig.31* for the base irradiation and the power ramp, respectively. Each figure reports:

- The simulated FGR trend,
- The measured FGR at the end of the BI or AR with their uncertainties,
- The simulated fuel centerline temperature in the peak axial position,
- The Vitanza threshold[71] for 1% of gas release,
- The thresholds above which equiaxed and columnar grain growth are effective,
- The thresholds for a-thermal and thermal intra-granular gas diffusion.

Fig. 30 and *Fig.32* highlight the linear heat rate and the fuel-cladding gap size. Both these parameters are strictly related to the fuel temperature and therefore are essential asses the fission gas release.
The base irradiation can be divided into two main phases. In the first phase (0 - 6000 h), the fuel rod experiences the highest linear power (see *Fig. 30*). In addition, due to the influence of densification phenomena and relatively low contribution of relocation and swelling, the pellet to cladding gap remains large leading to the highest fuel central temperature experienced in the base irradiation (see *Fig.29* and *Fig. 30*). Nevertheless, even in the power peak, it remains below or close to the Vitanza temperature threshold causing a relatively low fractional fission gas release up to 0.51 %, *Fig.29*. In

the second phase, the linear heat rate tends to decrease and the gap tends to reduce (because of the end of densification and the increase of relocation and swelling contributes). Due to these facts, the fuel temperature decreases and the rod undergoes steady-state operation for about 12000 h. The FGR value slightly increases and stabilizes around its final value of 0.57 %. Even if the simulated FGR results overestimated (0.47% was measured in the experiment), the Vitanza threshold is never exceeded and the contribution to fission gas diffusion is mainly due to a-thermal processes (that dominates around and below 1000°C). In conclusion, the steady state operation can be considered as well captured, *Tab. 16*.

The ramping phase can be divided into two phases: the preconditioning and the power ramp. In the preconditioning phase a peak LHR of 18.9 kW/m is achieved and kept constant for 20 hours. In this phase, the fission gas release does not occur and the gap is opened, *Fig.31* and *Fig.32*. When the ramp starts, the peak linear power reaches 39.5 kW/m with a fast rate of increase (462 kW/m h) and the fuel central temperature grows rapidly above the Vitanza threshold, up to 1800°C. According to the modified Koo inter-granular model, during this last phase, the conditions for the complete "venting" of the fission gas trapped at the grain boundaries are met (fast power transient and high fuel temperature, as explained in section *5.2*). Furthermore, the high temperature enhances the thermal intra-granular diffusion mechanism, which is more effective than a-thermal diffusion and causes fast growth of the gas fraction that reaches the grain boundaries. The experimental value measured during PIE was 11.24 %. The final value provided by the simulation is 7.64 %. Although the result is underestimated it can be considered acceptable. *Tab. 16* summarizes the results.

6.1.3 Grain size analysis

The grain dimension is subjected to increase with the fuel temperature. In particular, the recrystallization temperature represents the limit between equal-axial grain increase and columnar grain increase. This last phenomenon produces large deformation within the pellet center (restructuring). The assessment of this parameter is connected with the simulation of the fuel centerline temperature during the ramping phase.

No precise experimental data on metallographic examinations were included in the database. Only the radius at which the grain growth phenomenon is observed during PIE (40% of fuel pellets radius) and the mean grain size in that region (axial and radial average value) is given.

TU code models the grain growth according to Ainscough and Olsen[8] (see section 5.2.6). As shown in *Fig.31,* during the power ramp, the fuel central temperature exceeds the first of these thresholds. Thus, grain growth in the central fuel region is observed (*Fig.33*), the simulations qualitatively fit the experimental trends, Tab. 16.

6.1.4 Deformation analysis at the end of the BI

Cladding and fuel column length change and cladding diameter creep down were measured after base irradiation.

The fuel elongation depends upon the burn-up, the fuel densification, the swelling, and the relocation. During the initial phase, the fuel pellets are predicted to shrink because of densification that occurs between 0 and 5000 hours, *Fig.34* and Tab. 16. Beyond 5000 hours the length of the fuel column grows because of solid and gaseous swelling. The overall effect at the end of base irradiation is a fuel column shrinkage. As shown in *Fig.34*, TU code over-predicts the fuel shortening (-2.58 mm whereas the experimental value is -1.34 mm).

Cladding irradiation growth occurs because of cladding swelling and creep under a given neutron fast fluence. TRANSURANUS code calculates the contribution to axial swelling due to fast neutrons according to the Duncombe model (1970). The Duncombe model calculates the strain due to swelling in three direction on the basis of an exponential function with different fitting constant (depending on the direction). The measured axial growth is 2.10 mm; the code underestimates this phenomenon and predicts a cladding lengthening of 1.39 mm. The comparison between simulated and experimental data is shown in *Fig.34* and Tab. 16.

Creep is defined as a time dependent change in dimension of any material (in this case, of the cladding component) under a prolonged stress that is below the yield stress. Thermal and irradiation creep lead to cladding diametric shrinkage (due to coolant pressure that exceeds inner rod pressure). The cladding diameter decrease (referred as "creep-down") provides a partial geometrical characterization of the gap status during the base irradiation (for the complete characterization, the pellet expansion is necessary). Cladding diametric shrinkage due to creep down is computed according to the Lassmann-Moreno model[72]. The experimental cladding diameter reduction at the linear power peak after BI is 30.3 μm while the code predicts 37.1. The axially averaged cladding creep down was 15.2μm according to the experimental measurement while the code predicted 17.7μm. Both the results obtained through the simulation are consistent with the experimental data and their value fall within the measurement uncertainty. The comparison between simulated and experimental data is shown in and *Tab. 16*
According to the code simulation, the pellet-cladding gap remains open during the base irradiation. This result is in accordance with the observation of the BD8 rod after base irradiation. In fact no pellet-cladding mechanical interaction was observed.

6.1.5 Parametrical determination of the failure threshold

In LWR with self standing cladding, the compressive stress experienced by the cladding due to the primary fluid pressure, is reversed to a tensile stress induced by continuing fuel thermal expansion, relocation and swelling, when the fuel cladding gap has closed. The increase of the cladding stress, especially in the region of the pellet ridges, and in presence of aggressive fission products (e.g. cesium-iodine), may lead to stress corrosion induced cladding failure in the case of power ramps. The cladding failure due to crack propagation, so-called PCI/SCC phenomena, leads to an unwanted contamination of the primary water. The PCI is thus a complex phenomenon, which depends on many parameters and mechanisms connected with the design of the fuel rod and the operative conditions experienced during the irradiation, including the power ramp occurrence[73][74].

1. The design parameters involve: the rod geometry, the oxygen to metal ratio, the pellet and cladding fabrication processes, the pellet mechanical treatments (i.e. chamfering), the gas plenum geometry, the fuel grain size, the cladding heat treatment and inner coating.
2. The effects of the irradiation on the fuel rod can be distinguished as following:
    a. the fuel pin behavior is affected by the gaseous and solid fission products formation and swelling, the evolution of the fuel thermal conductivity, the pellet cracking and fragment relocation, the grain growth, the pellet creep, the thermal expansion and hot-pressing, the densification, the burn-up and the fission gas release (FGR).
    b. the cladding behavior is influenced by: the swelling due to neutron fluence in the high-energy spectrum, the creep parameters, the oxidation, the hydridation and the susceptibility to change its thermo-mechanical properties under prolonged irradiation.
    c. the fuel pin-cladding gap is dependent, besides the modifications above, by the actual size and conductance, the pressurization, and the gas composition (OECD/CSNI).
3. Finally, the transient perturbation induced by ramps mainly affects the rod integrity. The power terminal level and excursion as well as the power rate of increase, the coolant temperature at

which the transient occurs and its duration determine the rod mechanical performance of a given type of rod (design) subjected to a given irradiation history.

According to the PRIMO experiment final report[10] the rod BD8 remained intact at a RTL of 39.5 kW/m; nor it is predicted to fail in the simulations. In this analysis the failure threshold is obtained by fictitious change of the ramp terminal level. This value is progressively increased until the code detects the fuel rod rupture: 47.4 kW/m. The results are reported in *Tab. 17*. The failure threshold seems consistent with similar ramp test experiments conducted on LWR UO$_2$ and MOX fueled rods, *Fig.36*.

PRIMO MOX					
Design data					
Parameter	**Unit**		**Quantity**		
Rod Id	--		BD8		
Fuel – clad material	--		MOX – Zr-4		
U^{235} enrichment	%HM		5.246		
Pu^{239} enrichment	%HM		7.630		
Fuel average grain size	μm (3D)		7.8		
Rod outer diameter	mm		9.500		
Gap width	mm		0.100		
Pellet outer diameter	mm		8.041		
Active length	mm		1004.7		
He filling pressure	bar		20		
Ramp test data					
Parameter	**Unit**		**Quantity**		
Conditioning level	kW/m		18.9		
Ramp terminal level	kW/m		39.5		
Ramp rate	kW/m-h		462		
Holding time	hrs		20		
Reference analysis					
Parameter	**Uncertainty**	**Exp**	**TU calc**	**Error %**	**Acceptability range**
Burn-up (MWd/kgHM)	±6%	30.1	29.81	-0.1	±10%
FGR after BI	±2%	0.47%	0.51%	+8.5	+100% / -50%
Fuel elongation after BI	±0.5 mm	-1.34 mm	-1.39 mm	-3.6	±0.5 mm
Clad elongation after BI	±0.5 mm	2.10 mm	2.59 mm	+18.9	±0.5 mm
Clad creep down after BI at axial peak (radial)	±5 μm	30.3 μm	37.4 μm	+25.8	±5 μm
Clad creep down after BI,average (radial)	±5 μm	15.5 μm	17.7 μm	+14.2	±5 μm
FGR after ramp	±10%	11.24%	7.64%	-4.6	+100% / -50%
Grain size analysis AR	--	--	--	--	--
Clad integrity AR	--	NF	NF	--	--

Tab. 16 – PRIMO Program, summary of reference analysis.

RUN	RTL	F/NF	End of PR	
			FGR %	**Error %**
Ref. RTL	39.5	NF	7.64	-31.8
RTL +5%	41.5	NF	11.16	-3.6
RTL +10%	43.5	NF	13.49	+20.4
RTL +15%	45.4	NF	15.53	+38.7
RTL +20%	47.4	F	17.53	+56.5

Tab. 17 – PRIMO Program, rod BD8, sensitivity analysis on RTL and failure threshold, results and relative errors.
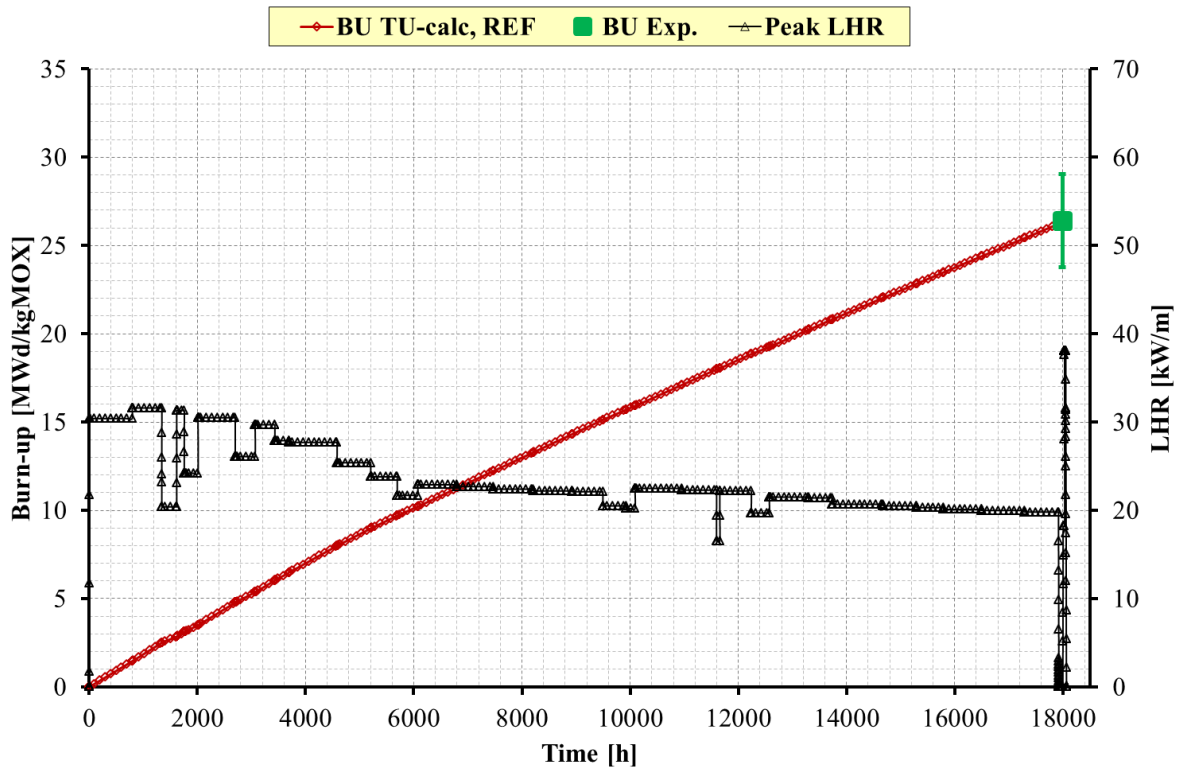
Fig.28 – PRIMO Program, rod BD8, burn-up analysis.
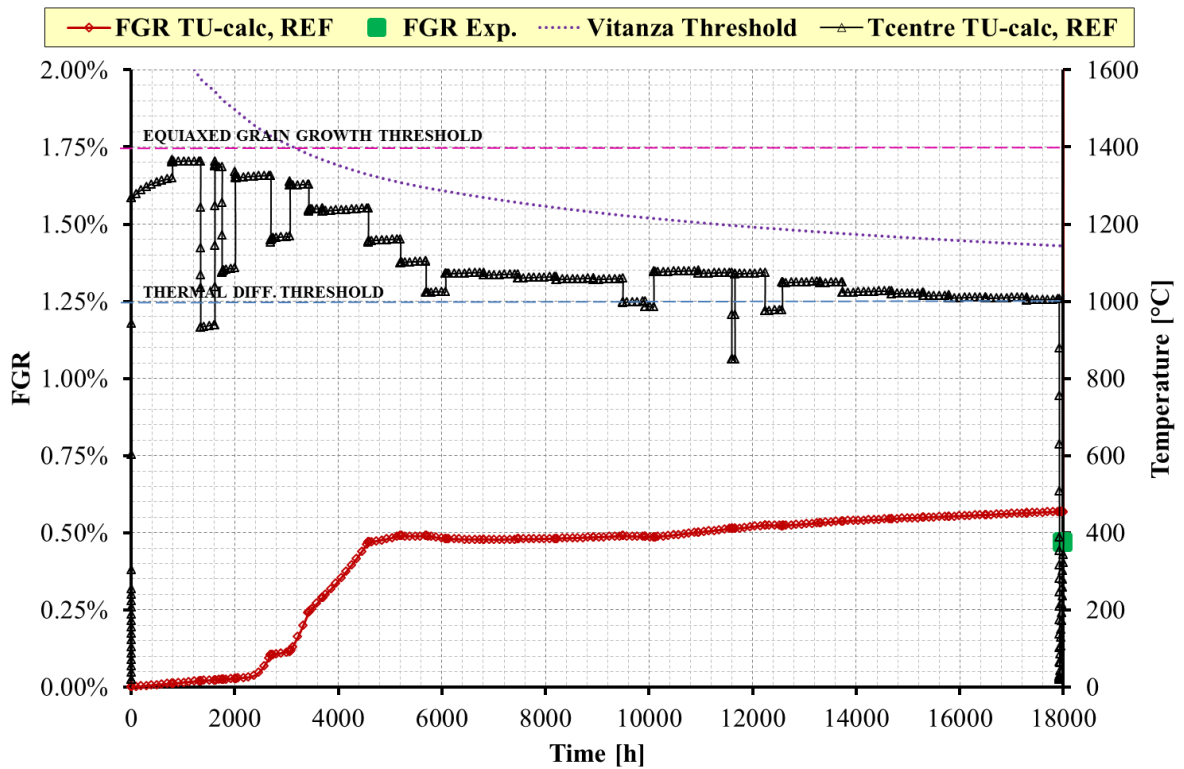
Fig.29 – PRIMO Program, rod BD8, fission gas release analysis, base irradiation.
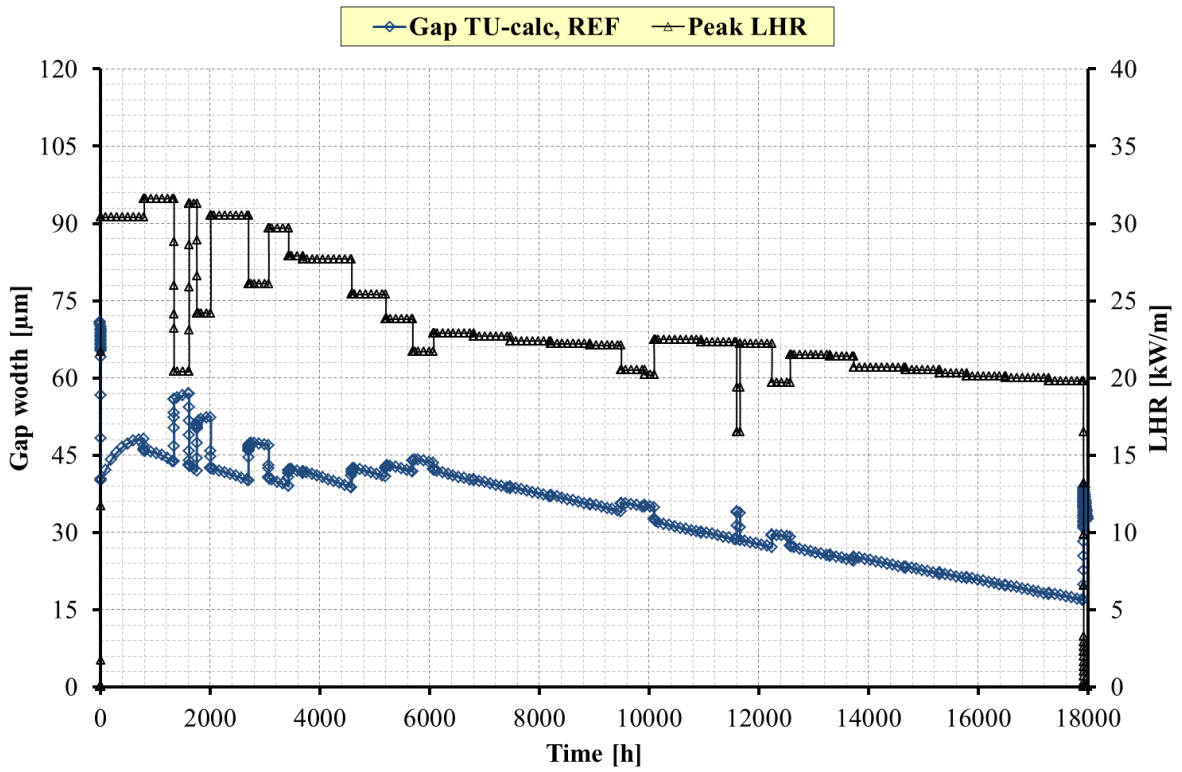
Fig. 30 – PRIMO Program, rod BD8, linear power and gap width in peak axial position, base irradiation.
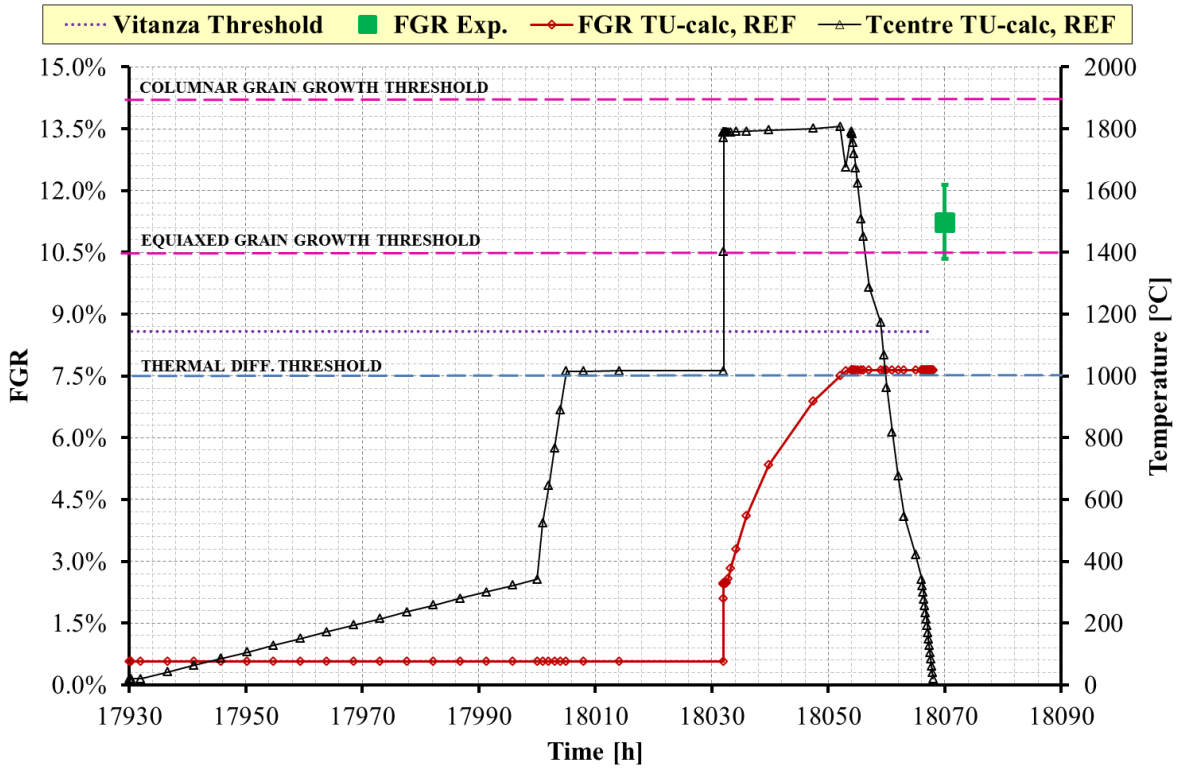
Fig.31 – PRIMO Program, rod BD8, fission gas release analysis, power ramp.

Fig.32 – PRIMO Program, rod BD8, linear power and gap width in peak axial position, power ramp.

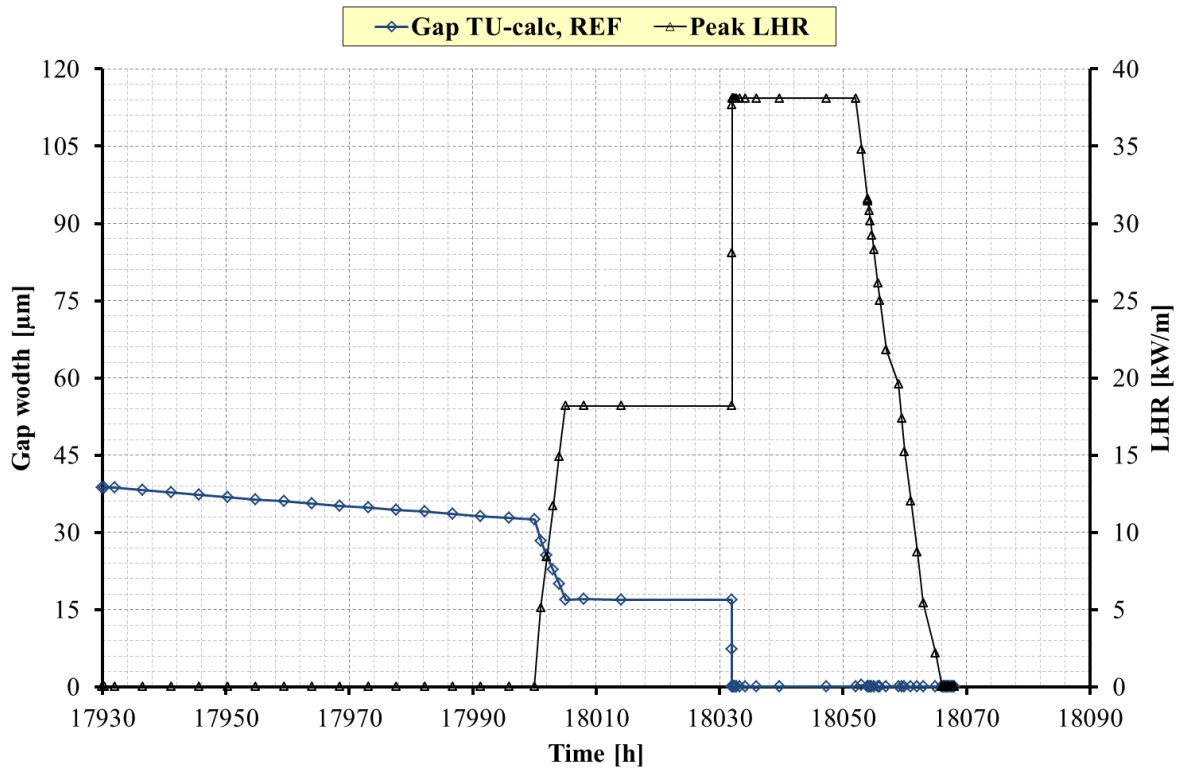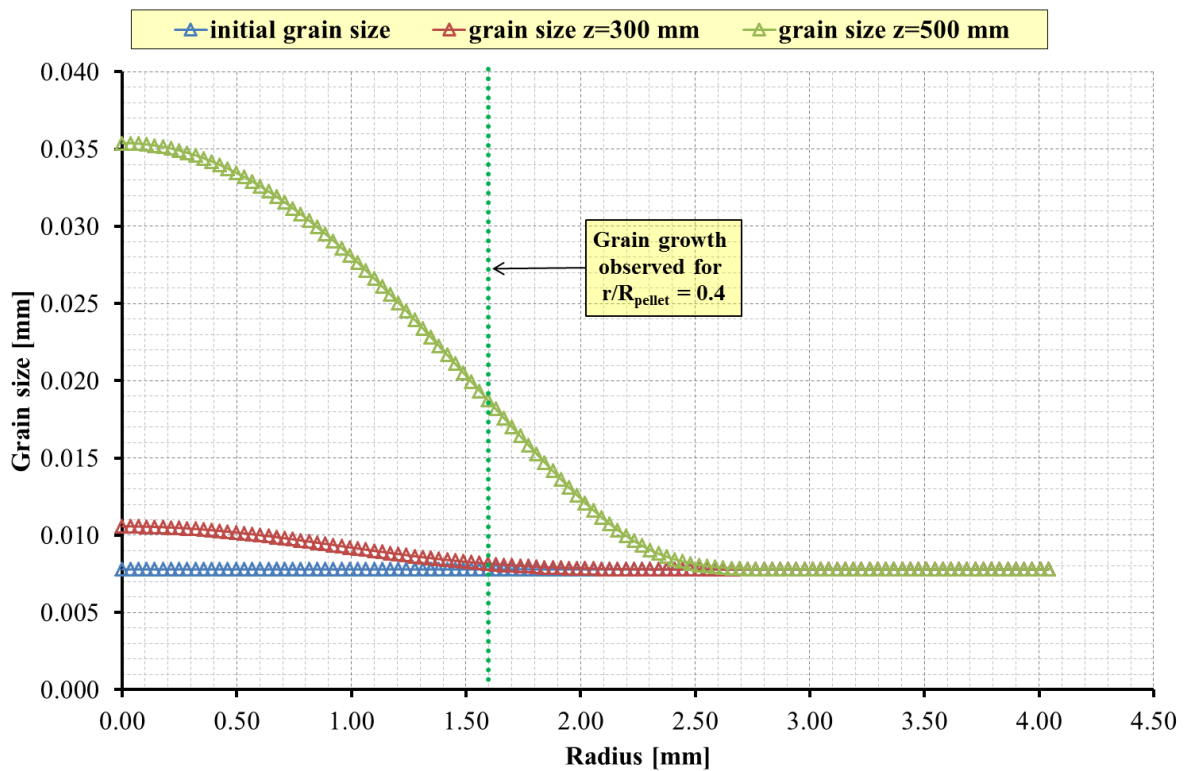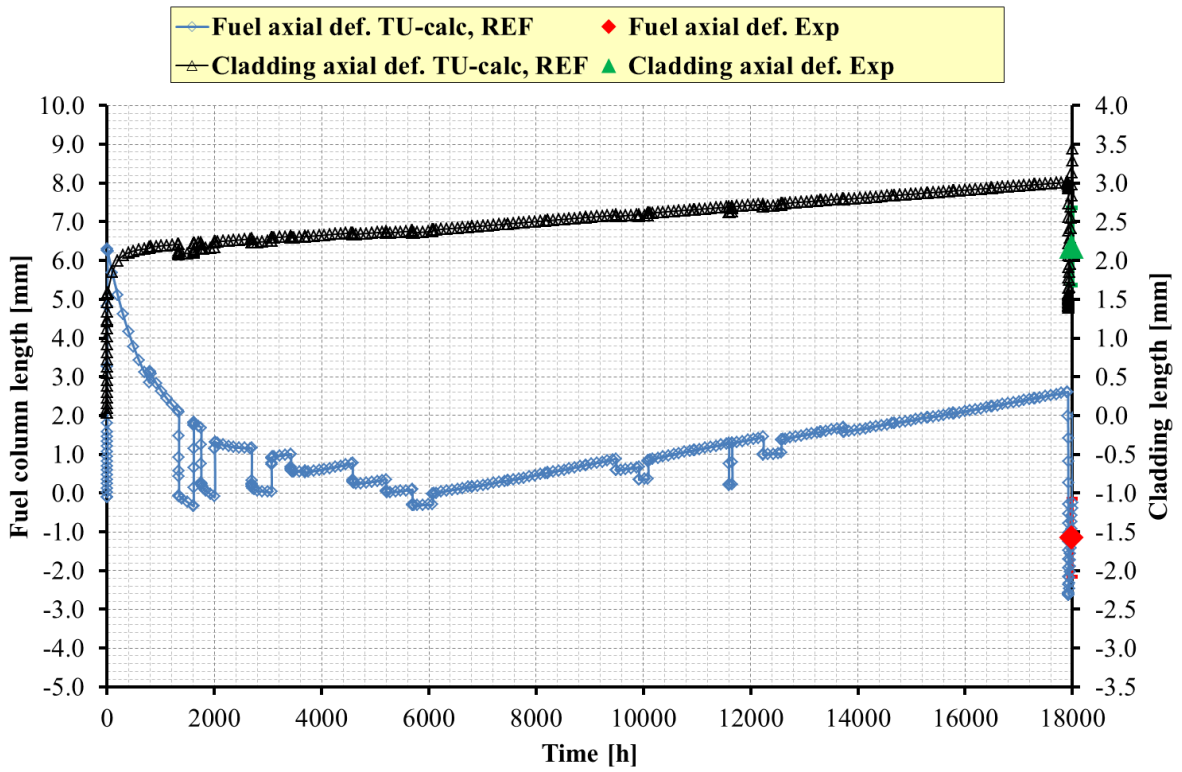*Fig.33 – PRIMO Program, rod BD8, grain growth analysis.*

Fig.34 – PRIMO Program, rod BD8, fuel and cladding axial deformation (before ramp) analysis.
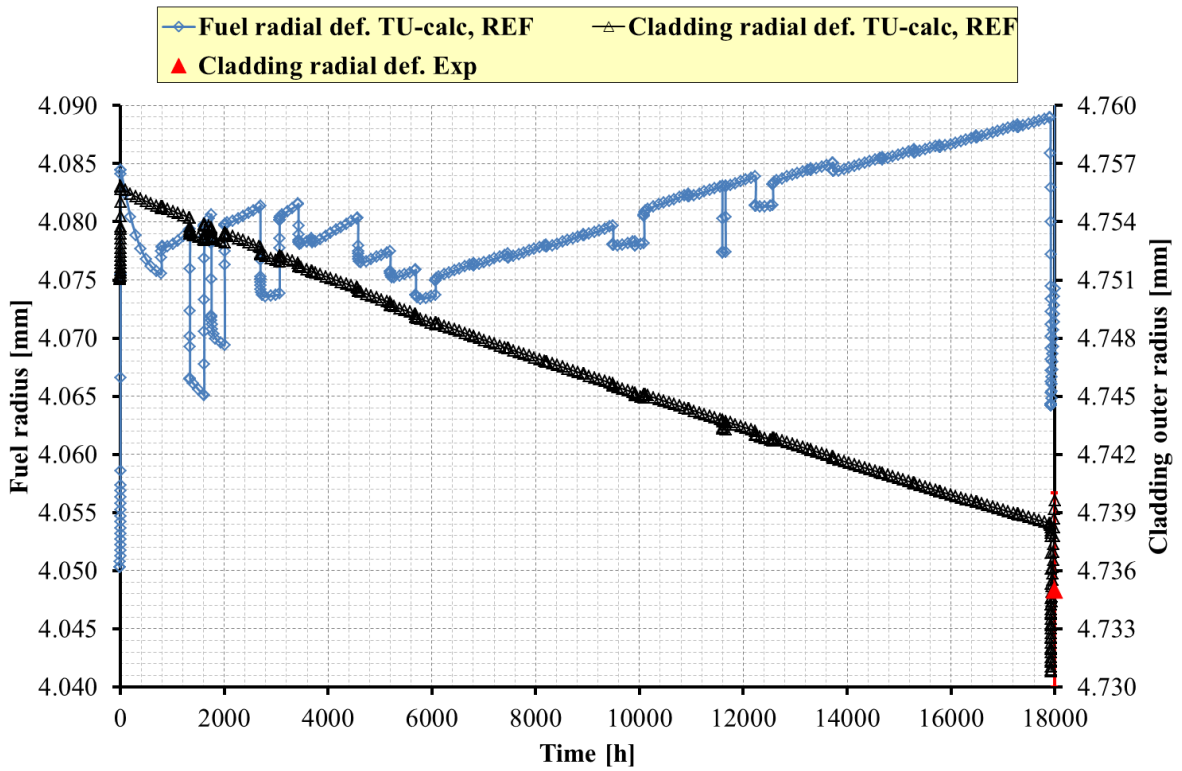

Fig.35 – PRIMO Program, rod BD8, fuel and cladding radial deformation (before ramp) analysis.

Fig.36 –PCI-SCC failure threshold, comparison with similar ramp tests.

6.2 Sensitivity analysis

The sensitivity analysis is a fundamental step for the assessment of the code capabilities. Different objectives shall be fulfilled such as to demonstrate the robustness of the calculation, to characterize the reasons for possible discrepancies between measured and calculated trends or values observed in the reference calculation, to optimize code results and user option choices, to improve the knowledge of the code by the user.

The investigation of the effect of the parameters, models and processes identified in section 5.1.2 on the code result is carried out in this section. *Tab. 18* lists the sensitivity analyses and their objectives. They are divided into three groups: the investigations on models (labeled as M), the investigation on correlations (labeled as C), and the investigation on the initial design conditions (labeled as D). This list is not exhaustive since other model options might affect the code results (i.e. the gap conductance model), as well as the uncertainties on the boundary conditions (i.e. the linear heat rate during the base irradiation and the power ramp phase, the ramp rate, the extension of holding time of ramp terminal level, the O/M etc..).

The development of the different sensitivities is hereafter reported in separate subsections distinguishing between the different groups of homogeneous selections.

Case	Run	Modification	Objective
Fission gas release	**M1.1**	Igrbdm 1	Investigate the impact of inter-granular models on fuel temperature and FGR. *Correlation according to the standard model*
	M1.2	Igrbdm 2	Investigate the impact of intergranular models on fuel temperature and FGR. *Correlation according to the temperature dependent model*
	M1.3	Igrbdm 1 FGRmod 4	Investigate the impact of intra-granular and inter-granular models on fuel temperature and FGR. *Inter-granular model according to the standard model and intra-granular model of Matzke and White Tucker.*
	M1.4	Igrbdm 2 FGRmod 4	Investigate the impact of intra-granular and inter-granular models on fuel temperature and FGR. *Inter-granular model according to the temperature dependent model and intra-granular model of Matzke and White Tucker.*
	M1.5	Igrbdm 3 FGRmod 4	Investigate the impact of intra-granular and inter-granular models on fuel temperature and FGR. *Inter-granular model according to the modified Koo model and intra-granular model of Matzke and White Tucker.*
	M1.6	Igrbdm 1 FGRmod 9	Investigate the impact of intra-granular and inter-granular models on fuel temperature and FGR. *Inter-granular model according to the standard model and intra-granular model of Turnbull.*
	M1.7	Igrbdm 2 FGRmod 9	Investigate the impact of intra-granular and inter-granular models on fuel temperature and FGR. *Inter-granular model according to the temperature dependent model and intra-granular model of Turnbull.*
	M1.8	Igrbdm 3 FGRmod 9	Investigate the impact of intra-granular and inter-granular models on fuel temperature and FGR. *Inter-granular model according to the modified Koo model and intra-granular model of Turnbull.*
Fuel conductivity	**C1.1**	Modfuel(j=6)=32	Investigate the impact of fuel conductivity on fuel temperature and FGR considering O/M effects. *Correlation according to Carbajo et al..*
	C1.2	Modfuel(j=6)=33	Investigate the impact of fuel conductivity on fuel temperature and FGR considering O/M effects . *Correlation according to Lanning and Beyer.*
	C1.3	Modfuel(j=6)=34	Investigate the impact of fuel conductivity on fuel temperature and FGR. *Correlation according to Wiesenack.*
	C1.4	Modfuel(j=6)=35	Investigate the impact of fuel conductivity on fuel temperature and FGR. *Correlation according to Van Uffelen and Schubert (conservative).*
Pellet fragment relocation	**M2.1**	Ireloc 2	Investigate the impact of fuel relocation on fuel temperature, dimensional changes, gap size and FGR. *Original KWU-LWR model based on initial gap size only.*
	M2.2	Ireloc 3	Investigate the impact of fuel relocation on fuel temperature, dimensional changes, gap size and FGR. *GAPCON-THERMAL-3 based on initial gap size, LHR and burn-up.*
	M2.3	Ireloc 5	Investigate the impact of fuel relocation on fuel temperature, dimensional changes, gap size and FGR. *Modified KWU-LWR model based on initial gap size only.*
Fuel swelling	**C2.1**	Modfuel(j4)=18	Investigate the impact of fuel swelling on fuel temperature, gap size, fuel elongation and FGR. *Simple correlation applied: swelling proportional to burn-up.*
	C2.2	Modfuel(j4)=19	Investigate the impact of fuel swelling on fuel temperature, fuel elongation and FGR. *Original MATPRO swelling model considering separate contributions of the solid and gaseous fission products*
	C2.3	Modfuel(j4)=21	Investigate the impact of fuel swelling on fuel temperature, fuel elongation, gap size and FGR. *Implicit formulation of the reference correlation.*
Fuel densification	**M3.1**	Idensi 7	Investigate the impact on FGR, fuel temperature, fuel elongation and gap width. *Original MATPRO densification model.*
Fuel density	**D1.1**	Density +1% TD	Assess the impact on FGR and fuel centerline temperature of lower initial fuel porosity corresponding to an increase of 1% TD of the initial fuel density.
	D1.2	Density -1% TD	Assess the impact on FGR and fuel centerline temperature of higher initial fuel porosity corresponding to a decrease of 1% TD of the initial fuel density.
Grain size	**D2.1**	1.25 Grain$_{design}$	Assess the impact of 25% increased grains on FGR and fuel centerline temperature
	D2.2	0.75 Grain$_{design}$	Assess the impact of 25% decreased grains on FGR and fuel centerline temperature
Gap size	**D3.1**	Gap size 108μm	Test the impact of increased gap width at the beginning of irradiation on fuel temperature and FGR. Initial value obtained assuming maximum cladding and minimum fuel radii according to design uncertainties.
	D3.2	Gap size 93μm	Test the impact of decreased gap width at the beginning of irradiation on fuel temperature and FGR. Initial value obtained assuming minimum cladding and maximum fuel radii according to design uncertainties

Tab. 18 – PRIMO Program, rod BD8, list of sensitivity analysis.

6.2.1 Assessment of FGR models (runs M1)

This sensitivity analysis aims to assess the FGR models described in 5.2.1. Each intra-granular model is associated with the inter-granular models to assess all the combinations[75]. The results are summarized in *Tab. 19*.

As explained in section 5.2.1, and *Tab. 18*, the intra-granular thermal diffusion model according to Matzke and a-thermal diffusion according to White and Tucker is referred as FGRMOD4. The reference thermal intra-granular diffusion model according to Matzke and a-thermal diffusion according to ITU data is labeled as FGRMOD6 and; the thermal and a-thermal intra-granular diffusion model according to Turnbull is referred as FGRMOD9.

The inter-granular models according to the standard model, the temperature dependent model and the reference power ramp model derived from the Koo model are labeled, respectively, IGRBDM 1, 2 and 3.

It should be mentioned that, below 1200°C, the reference intra-granular diffusion coefficient (FGRMOD6) is lower than FGRMOD4 and FGRMOD9 while above 1200°C, it becomes equal to FGRMOD4. Assuming a power rating of 35W/g, above 1320°C, FGRMOD6 overpasses FGRMOD9. This last coefficient is the highest up to 1320°C, *Fig. 37*.

Whatever is the model (both intra-granular and inter-granular), the simulations highlight no major differences among the fuel centerline temperatures in the peak axial position. In particular, during the main part of the base irradiation, the fuel maximum temperature remains below 1200°C (see *Fig.29*) and therefore: FGRMOD6 < FGRMOD4 < FGRMOD 9, *Fig. 37*. Minor parts of the base irradiation (at the beginning) experience 1200°C < T < 1320 °C (FGRMOD 4 = FGRMOD 6 < FGRMOD9) or T > 1320 °C (FGRMOD 4 = FGRMOD 6 > FGRMOD 9). In conclusion, during the base irradiation, FGRMOD9 predicts the maximum diffusion coefficient while FGRMOD 6 predicts the minimum diffusion coefficient. On the other hands (see *Fig.31*), excepts for the conditioning phase and the initial phase of the ramp test (in which FGRMOD6 ≤ FGRMOD4 < FGRMOD 9), the intra-granular diffusion coefficient FGRMOD9 is the lowest one and FGRMOD6 = FGRMOD4, (*Fig. 37*).

The inter-granular models are presented in *Fig. 38*. During the base irradiation, the saturation concentrations at grain boundaries to achieve FGR are: IGRBDM1 (FGRMOD 4-6) < IGRBDM2 (FGRMOD 4-6) < IGRBDM1 (FGRMOD 9) < IGRBDM2 (FGRMOD 9). Therefore, IGRBDM2 (FGRMOD 9) highlights the maximum grain boundaries concentration to achieve FGR while IGRBDM1 (FGRMOD 4-6) highlight the minimum. The models IGRBDM 3 is equal to IGRBDM 1 since ramp conditions does not activates. Grain boundaries venting occurs in the ramp phase since ramp conditions are achieved. IGRBDM 1 tends to overpass IGRBDM 2 because the fuel temperature reaches 1800 °C.

FGRMOD4 is analyzed in *Tab. 19* and in APPENDIX A (*Fig. A. 1* and *Fig. A. 2* base irradiation and power ramp respectively). The inter-granular models IGRBDM1, 2 and 3 are compared to the reference simulation. During the base irradiation there is no activation of the grain boundary venting model, *Fig. A. 1*. This implies that IGRBDM1 (standard model) and IGRBDM3 (modified Koo model) are coincident and they over-predict the FGR. Both the models apply constant saturation concentration ($1*10^{-4}$ μmol/mm^2) to estimate the surplus of gas that reaches the grain boundaries. IGRBDM2 model simulates lower FGR. This is because of the highest saturation concentration, *Fig. 38*. During the power ramp, the Koo model (IGRBDM3) activates and FGR tends to increase with respect to the other models, *Fig. A. 2*. IGRBDM1 and IGRBDM2 are not specifically developed for power transient conditions and they under-predict the release due to the ramp. Should be noted that, compared to the

base irradiation, the difference between IGRBDM1 and IGRBDM 2 reduces (it means that IGRBDM 2 releases more gas than IGRBDM 1 during the power ramp), because of inverted saturation concentration, *Fig. 38*. In general, compared to the reference simulation, the intra-granular diffusion coefficient FGRMOD4 is higher than FGRMOD6 (*Fig. 37*), and causes additional FGR, *Tab. 19*.

The reference model FGRMOD6 is assessed in *Fig. A. 3* (base irradiation), *Fig. A. 4* (power ramp) and *Tab. 19*. The general considerations reported for FGRMOD4 applies to FGRMOD6 too excepts the absolute values of the FGR that tends to reduce compared to FGRMOD4 because of lower intra-granular diffusion coefficient, *Tab. 19*.

FGRMOD9 is analyzed in *Fig. A. 5* and *Fig. A. 6* (reported in APPENDIX A), and *Tab. 19*. During the base irradiation, this model predicts the lowest FGR. This is connected to the highest saturation limits that reduces the FGR ($4*10^{-4}$ and 0.7092 mol/m^2 respectively), *Fig. 38*. However, it should be noted that the FGR evolution along the BI is different from the ones obtained with FGRMOD4 and FGRMOD6. In particular, the trend is monotonically increasing while, in previous cases, it was related to the LHR and the fuel temperature. The simulation of the power ramp highlights two different trends: IGRBDM1 and IGRBDM2 still predict the lowest FGR while, on the other hand, IGRBDM3 (Koo ramps model) predicts the highest fraction of fission gas released among the simulations, *Tab. 19*. This is due to the irradiation enhanced thermal component of the diffusion coefficient that promotes large accumulation of FG at the grain boundaries during the base irradiation and the initial part of the power ramp test coupled with the cyclic deactivation of the saturation concentration limit (see section 5.2.1). In the second part of the ramp, the diffusion coefficient of Turnbull becomes lower than that of Matzke and the trend of FGR increases slower, *Fig. A. 6*. It can be concluded that FGRMOD9 intra-granular model is not suitable for the simulation of power ramps.

The values at the end of the base irradiation and at the end of the power ramp predicted by the nine different combinations of diffusion models are shown in *Fig. 39* and *Fig. 40* respectively.

PRIMO MOX				
Sensitivity analysis M1: FGR models				
RUN	**End of BI FGR %**	**Error %**	**End of PR FGR %**	**Error %**
Exp. FGR	0.47	--	11.23	--
Ref. FGRMOD6, IGRBDM3	0.51	+7.84	7.64	-31.97
FGRMOD4, IGRBDM1	1.04	+54.59	7.46	-33.57
FGRMOD4, IGRBDM2	0.57	+16.96	7.24	-35.53
FGRMOD4, IGRBDM3	1.04	+54.59	9.86	-12.20
FGRMOD6, IGRBDM1	0.57	+17.40	6.99	-37.76
FGRMOD6, IGRBDM2	0.34	-36.63	6.83	-39.18
FGRMOD9, IGRBDM1	0.31	-50.16	4.04	-64.02
FGRMOD9, IGRBDM2	0.20	-57.44	3.99	-64.47
FGRMOD9, IGRBDM3	0.31	-50.16	15.98	+42.30

Tab. 19 – PRIMO Program, rod BD8, sensitivity analysis on FGR models ,results and relative errors.
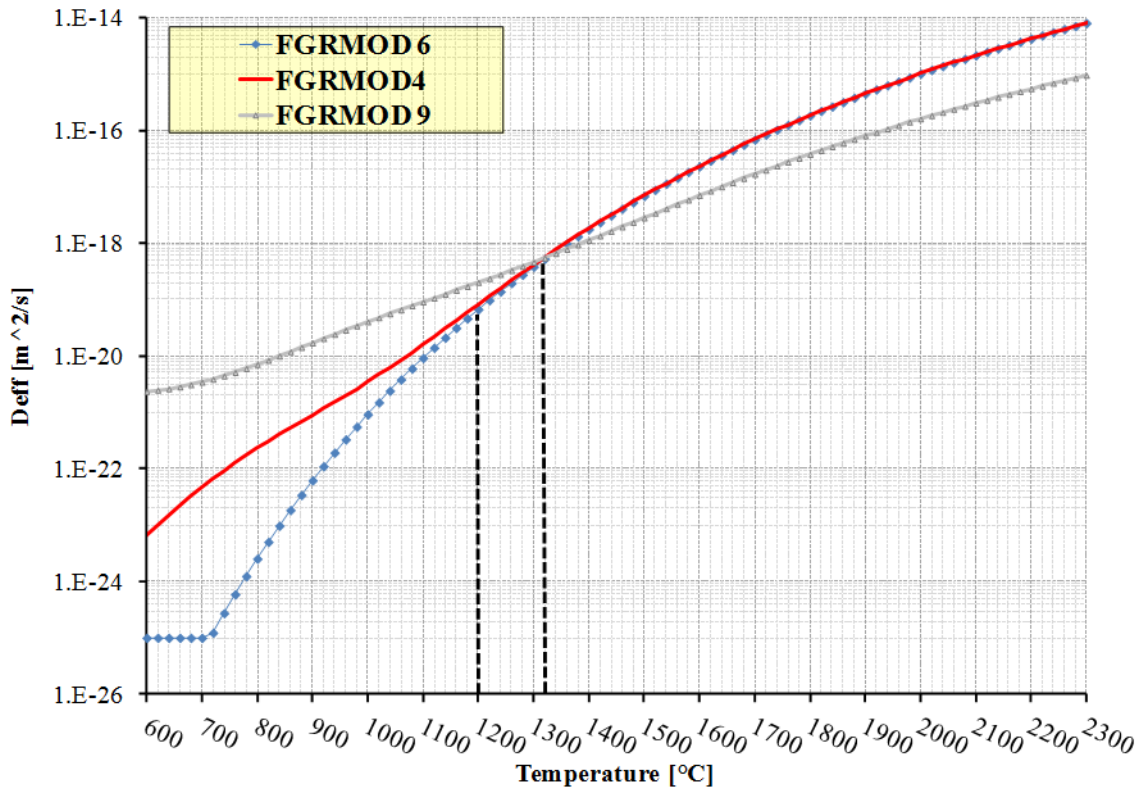
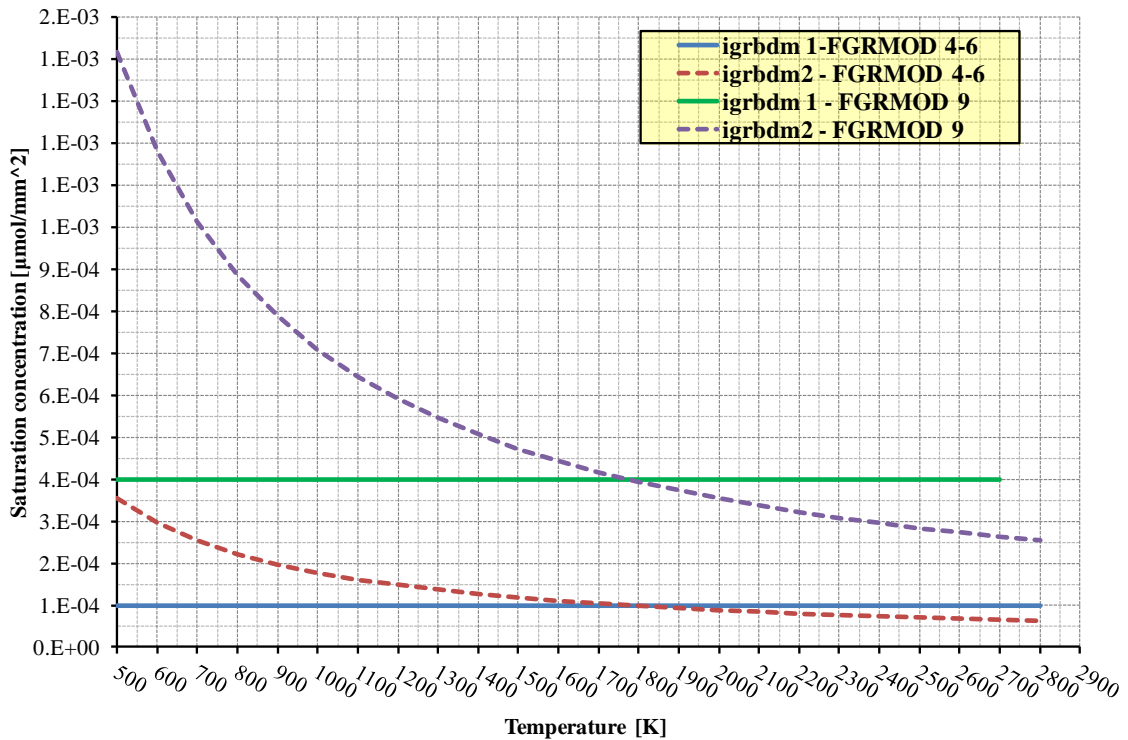*Fig. 37 – PRIMO Program, intra-granular diffusion coefficients as function of temperature.*

Fig. 38 – PRIMO Program, rod BD8, sensitivity analysis on FGR models, gas saturation concentration to release gas from grain boundaries as function of temperature.
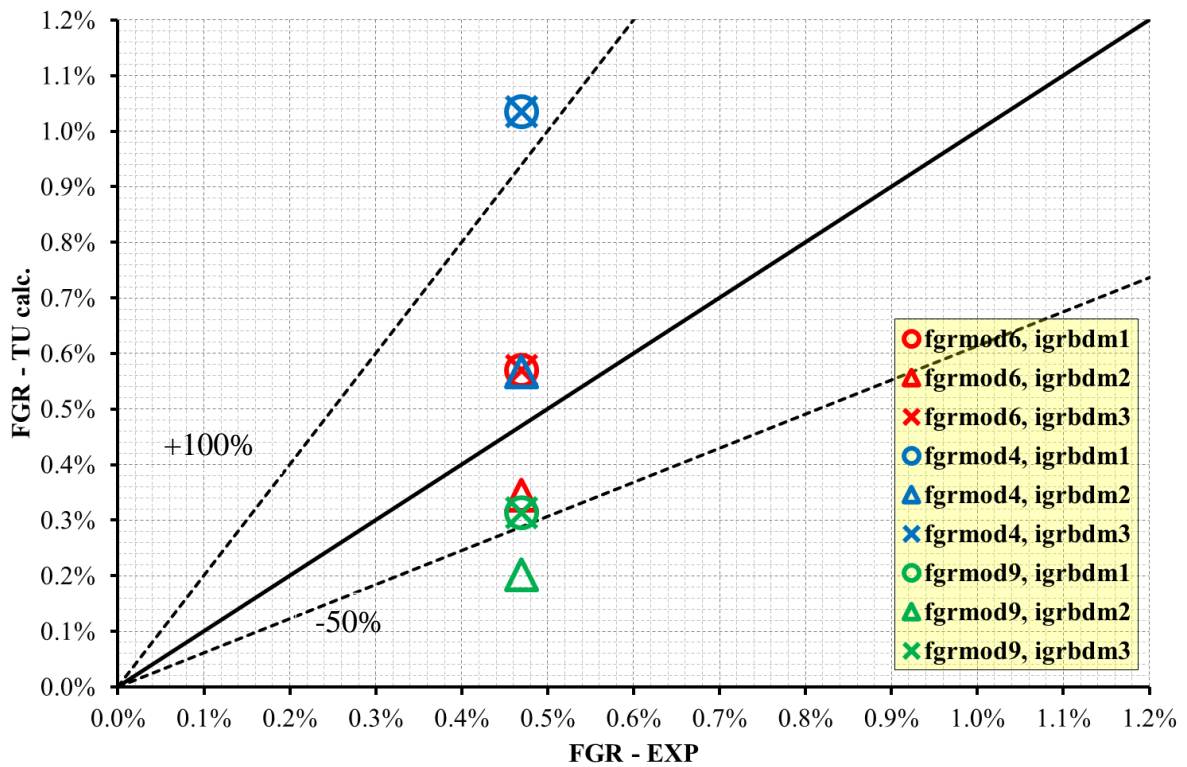
Fig. 39 – PRIMO Program, rod BD8, sensitivity analysis on FGR models, FGR, base irradiation.
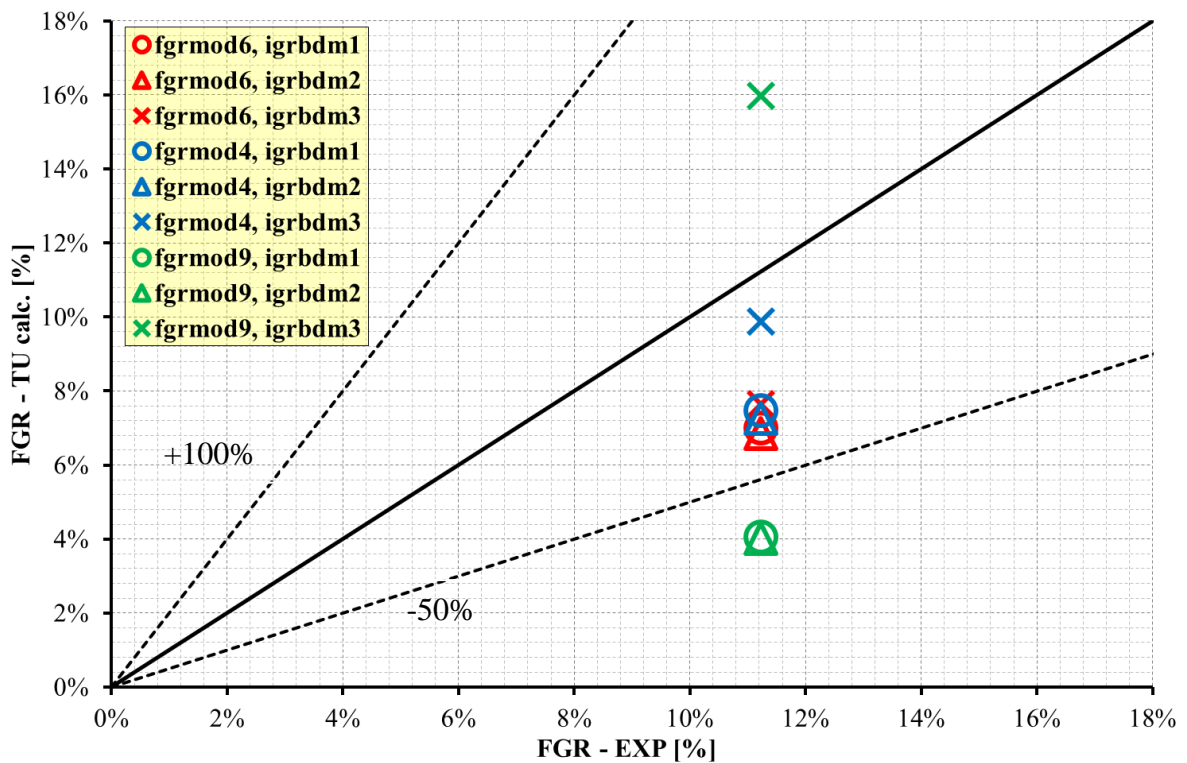

Fig. 40 – PRIMO Program, rod BD8, sensitivity analysis on FGR models, FGR, power ramp.

6.2.2 Assessment on fuel conductivity correlations (runs C1)

The thermal conductivity correlations addressed in this sensitivity analysis are described in section *5.2.2*. The reference correlation assumed in the simulation is the Van Uffelen and Schubert (best

estimate), LAMBDA 31 that accounts for the influence of the local temperature, the local burn-up, the local porosity and the HBS formation. According to section *5.2.2* and *Tab. 18*, it is assumed that:

- The correlation according to Carbajo et al is labeled as LAMBDA 32 (it accounts for the local temperature, the local burn-up, the local porosity and the HBS formation, the O/M, the dissolved and precipitated FPs and the radiation effects).
- The correlation of Lanning and Beyer is named LAMBDA 33 (it accounts for the local temperature, the local burn-up, the local porosity and the O/M).
- The correlation according to Wiesenack is labeled as LAMBDA 34 and (it was developed for UOx fuel and was reduced by a constant factor of 0.92 to accounts MA and FP effects in quasi spent fuel).
- The correlation of Van Uffelen and Schubert (conservative) is named LAMBDA 35 (it is identical to the reference correlation excepts for one fitting constant).

These correlations have been developed specifically for MOX fuel. The analysis of the results highlight that they impact on the fuel temperature at the axial peak up to 100°C during base irradiation and up to 200°C during power ramp, as shown in *Fig. A. 7* and *Fig. A. 8* (APPENDIX A). This is reflected in the calculated fission gas release. In general, the results are similar to the reference simulation except for LAMBDA 34, and LAMBDA 35. This last correlations predict the lowest and the highest fuel temperature respectively. LAMBDA 34 was developed for UO_2 and corrected with a constant factor to account for high burn-up MA and FP effects in quasi-spent fuel. This is the cause of the low FGR. Van Uffelen and Schubert correlation (LAMBDA 35) in its conservative form gives results similar to the other correlations at the end of the base irradiation and highlights the highest FGR at the end of the power ramp while. The correlations LAMBDA 32 and 33 are similar to the Van Uffelen and Schubert "best estimate" correlation which was chosen as reference. The main results are summarized in *Tab. 20*.

PRIMO MOX				
Sensitivity analysis C1: fuel conductivity correlations				
RUN	**End of BI**		**End of PR**	
	FGR %	**Error %**	**FGR %**	**Error %**
Exp. FGR	0.47	--	11.23	--
Reference TU COND31	0.51	8.51	7.64	-31.97
COND32	0.78	+65.96	7.90	-29.65
COND33	0.79	+68.09	7.89	-29.74
COND34	0.36	-23.40	4.56	-59.39
COND35	0.75	+59.57	10.4	-7.39

Tab. 20 – PRIMO Program, rod BD8, sensitivity analysis on fuel thermal conductivity, results and relative errors.

6.2.3 Assessment on relocation models (runs M2)

The choice of the relocation model (see section 5.2.3) mainly influences the gap width between fuel pellet and cladding during the irradiation. The fuel temperature is consequently affected by the relocation model and, therefore, different FGR trends are observed. The reference model is the modified FRAPCON-3 model referred as IRELOC 8. It accounts for the tangential strain due to relocation depending on the as fabricated gap, the burn-up (two simple functions below and beyond 5 MWd/kgU), the linear heat rate (a simple function that applies in the range 20 kW/m < LHR <40kW/m). It does not consider the axial strain and it does not apply when gap is closed. According to section 5.2.3 and *Tab. 18*, it is assumed that:

- The original KWU-LWR model is labeled as IRELOC 2. It accounts only for the as fabricated gap, it accounts for axial strain and it applies also when gap is closed.
- The GAPCON-THERMAL-3 model is referred as IRELOC 3. It accounts for the tangential strain due to relocation depending on the as fabricated gap, the burn-up (exponential function that saturates at 5MWd/kgU), the linear heat rate (a simple function). It does not consider the axial strain and it applies also when gap is closed.
- The modified KWU-LWR model is labeled as IRELOC 5. It accounts only for the as fabricated gap, it accounts for tangential and axial strain and it applies also when gap is closed.

The thinnest gap is predicted by model IRELOC3 during BI, *Fig. 41*. IRELOC 2 behaves similar to the reference model. IRELOC 5 predicts a larger gap compared to the reference model. During the ramping phase (*Fig. 42)* the gap is predicted to close. IRELOC 5 predicts plastic deformation of the pellet that definitively close the gap. This is connected with its activation also when gap is closed. During the base irradiation (APPENDIX A, *Fig. A. 9*, *Fig. A. 10* and *Tab. 21*), the FGR is in agreement with the gap size predicted by the relocation model: the larger is the gap, the larger is the centerline fuel temperature. Therefore, the FGR ranks in this way: IRELOC5 > IRELOC 2 > REFERENCE > IRELOC 3.

During the ramping phase, relocation occurs only for IRELOC 2, IRELOC 3 and IRELOC 5 and it is reversed by the cladding. This interacts with the fuel transient swelling model (see section 5.2.4) that causes undue increase of gaseous porosity during the ramp down phase and, therefore, it affects the fuel conductivity causing fuel temperature increase during power decrease, *Fig. A. 10*. Nevertheless, no major differences are evidenced between the reference model and those that have been investigated, *Tab. 21*.

PRIMO MOX				
Sensitivity analysis M2: fuel relocation models				
RUN	**End of BI**		**End of PR**	
	FGR %	**Error %**	**FGR %**	**Error %**
EXP FGR	0.47	--	11.23	--
Ref. IRELOC8	0.51	+8.51	7.64	-31.97
IRELOC2	0.62	+31.91	8.62	-23.24
IRELOC3	0.54	+14.89	8.48	-24.49
IRELOC5	0.36	-23.40	7.43	-33.84

Tab. 21 – PRIMO Program, rod BD8, sensitivity analysis on relocation models, results and relative errors.
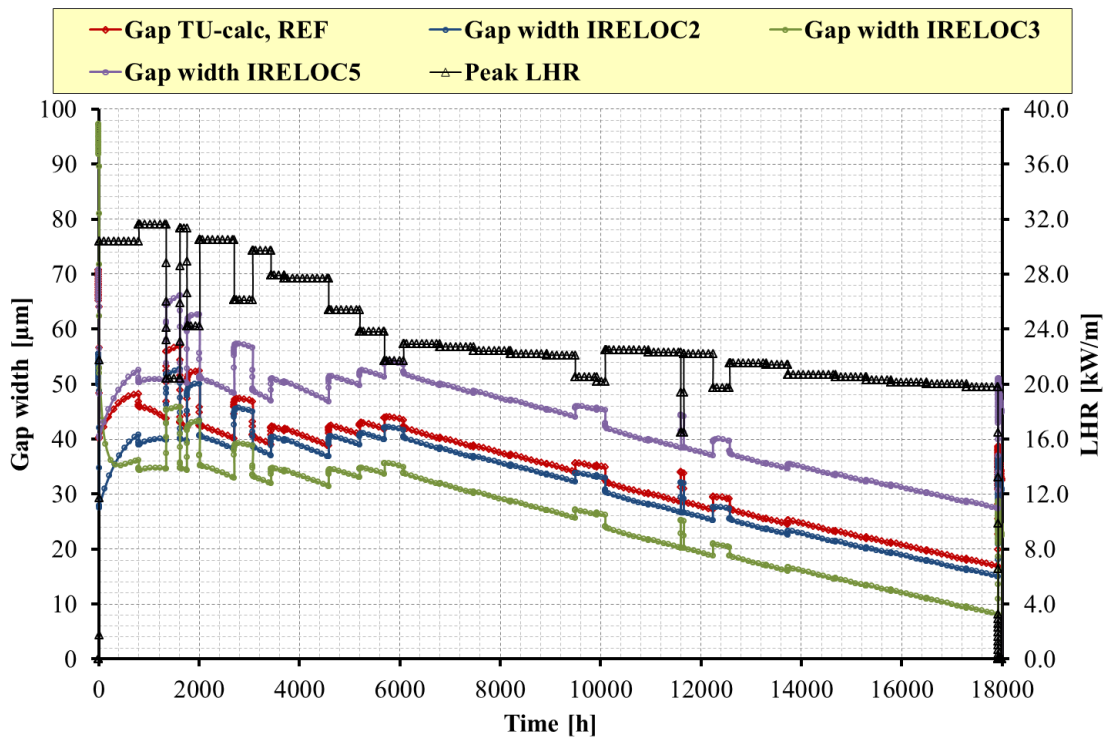
Fig. 41 – PRIMO Program, rod BD8, sensitivity analysis on relocation models, gap width in peak axial position, base irradiation.
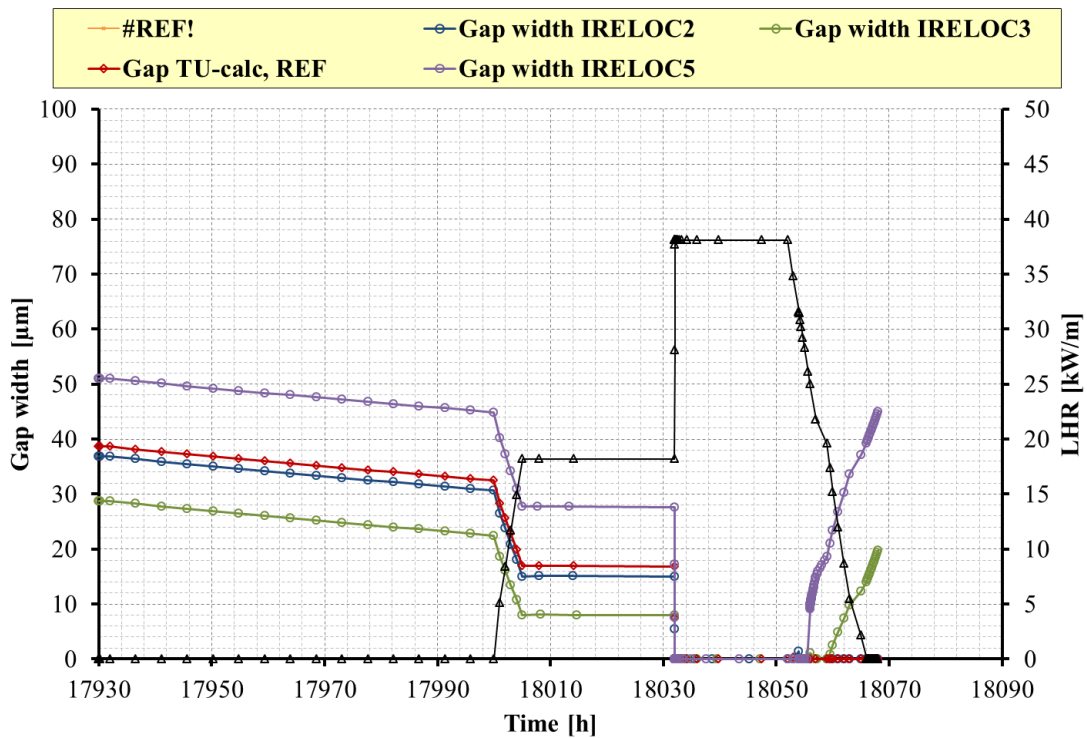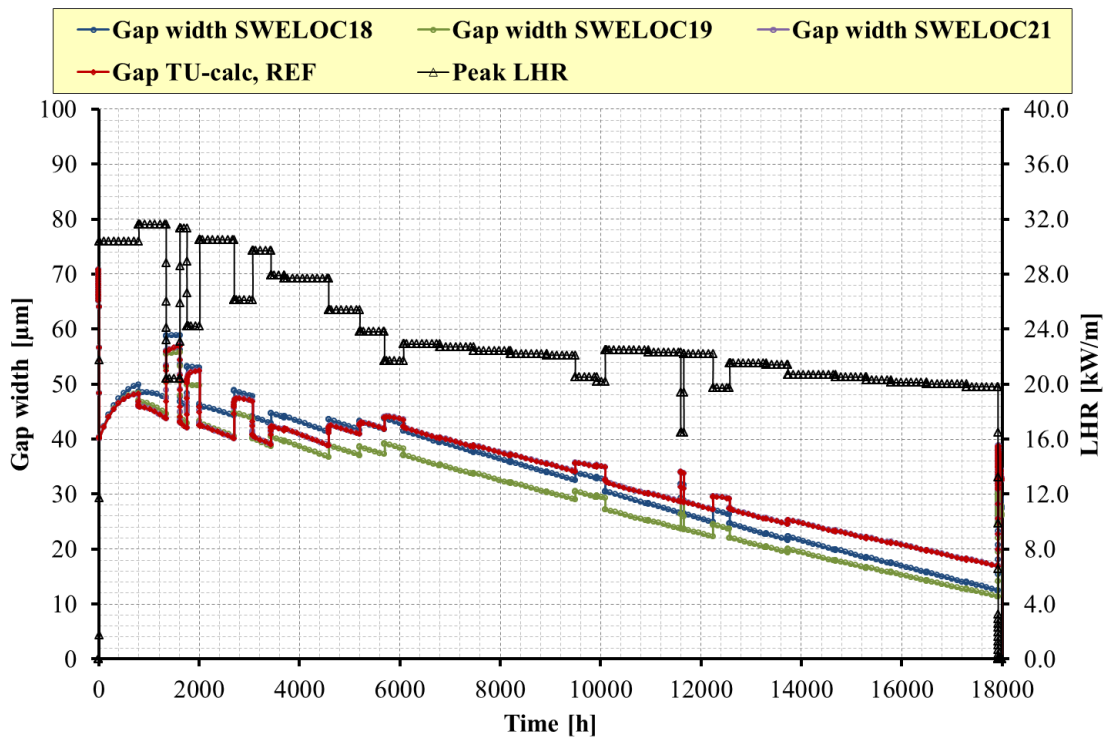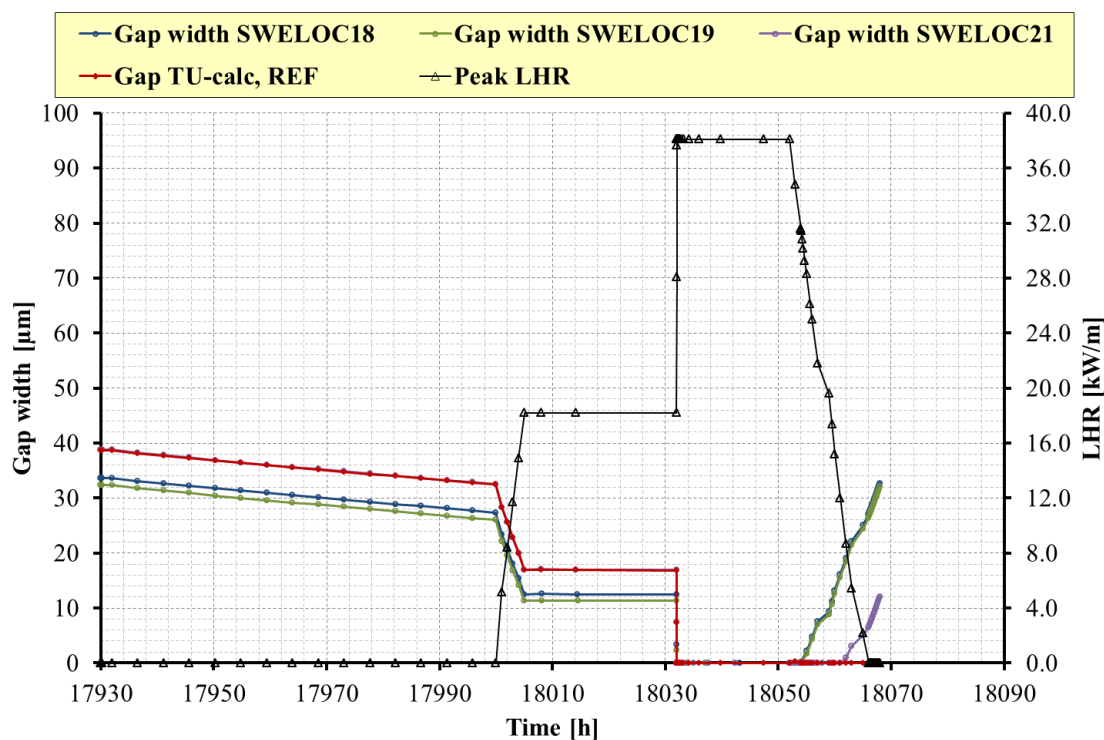

Fig. 42 – PRIMO Program, rod BD8, sensitivity analysis on relocation models, gap width in peak axial position, power ramp.

6.2.4 Assessment on fuel swelling correlations (runs C2)

The solid fission products are theoretically predicted to contribute to fuel swelling on the average by 0.032% per MWd/kgU. The contribution of gaseous fission products to fuel swelling includes rare gases such as krypton and xenon in solid solution and the volume change arising from the formation of fission gas filled bubbles. For the gases in solid solution and the small intra-granular gas bubbles, it is estimated that they furnish about 0.056% per MWd/kgU to matrix swelling rate. The inter-granular gas bubbles can make the largest contribution to volume change depending on temperature and their amount. Early studies indicated large bubbles of diameter around few microns on grain faces and also along grain edges. At high exposures and temperatures the bubbles interlink forming a tunnel network which concurrently leads to gaseous swelling and gas release.

Therefore, the choice of the swelling correlation directly affects the FGR, the fuel to cladding gap, and the fuel conductivity. The reference correlation adopted in the simulations was developed by Lassmann from the original MATPRO swelling correlation. It accounts for solid swelling as a linear function of the local burn-up and for gaseous swelling as function of local temperature, burn-up, stress and diffusion coefficient. The correlations available in TRANSURANUS are described in details in 5.2.4. According to this section and *Tab. 18*, it is assumed that:

- The simple correlation that gives the total swelling rate for UO_2 fuel due to solid FP is labeled as SWELOC 18. It is a linear function of the local burn-up.
- The original MATPRO swelling model for UO_2 fuel is referred as SWELOC 19. It accounts for solid swelling as a linear function of the local burn-up and for gaseous swelling as function of local temperature and burn-up.
- The implicit formulation of the reference correlation is labeled as SWELL 21.
- The correlation proposed by Dienst et al. for FBR MOX fuel is referred as SWELOC 3. It accounts for solid and gaseous swelling as two linear functions of the local burn-up. Gaseous swelling is zero if the gap is closed.
- The correlation proposed by by Pesl et al. for FBR MOX fuel is referred as SWELOC 11. It accounts for solid and gaseous swelling as two linear functions of the local burn-up. Gaseous swelling is zero if the gap is closed.
- The correlation by Dienst et al. recommended for FBR MOX fuel is labeled as SWELOC 13. It accounts for solid and gaseous swelling as two linear functions of the local burn-up. Gaseous swelling is zero if the gap is closed.

Only SWELOC18, SWELOC19, SWELOC21 are here discussed since SWELOC3, SWELOC11, SWELOC12 and SWELOC13 are developed to model swelling in FBR and resulted not suitable for the simulation of the PRIMO experiment over predicting the swelling contribute and causing early gap closure.

The thinnest gap is predicted by the reference correlation SWELOC20 in the first 5000 hours. SWELOC18 predicts largest gap at the beginning of the irradiation while predicts the same gap width of SWELOC19 at the end of BI, *Fig. 43*.

During the power ramp, all the fuel swelling correlations predict gap closure, therefore these correlations, mainly influence the FGR during the base irradiation.

In general the FGR at the end of the base irradiation obtained in these simulations is related to the gap width in the first 5000 hrs of the simulation, when the linear power is high and most of the gas release occurs, *Fig. A. 11* and *Fig. A. 12* (APPENDIX A). Correlation SWELOC18 predicts the highest FGR while the lowest is predicted by SWELOC19. However the difference between these models and the reference simulation is negligible (less then ±0.2 %), Tab. 22. Correlation 21 is not shown in the figures because it does not differ with the reference model 20.

PRIMO MOX				
Sensitivity analysis C2: fuel swelling correlations				
RUN	**End of BI**		**End of PR**	
	FGR %	**Error %**	**FGR %**	**Error %**
Exp. FGR	0.47	--	11.23	--
Reference SWELOC20	0.51	+8.51	7.64	-31.97
SWELOC18	0.59	+25.53	7.38	-34.28
SWELOC19	0.51	+8.51	7.74	-31.08
SWELOC21	0.51	+8.51	7.64	-31.97

Tab. 22 – PRIMO Program, rod BD8, sensitivity analysis on swelling model, results and relative errors.

Fig. 43 – PRIMO Program, rod BD8, sensitivity analysis on fuel swelling correlations, gap width in peak axial position, base irradiation.

Fig. 44 – PRIMO Program, rod BD8, sensitivity analysis on fuel swelling correlations, gap width in peak axial position, power ramp.

6.2.5   Assessment on fuel densification models (runs M3)

Densification process occurs at the beginning of the fuel irradiation; it leads to the destruction of fabricated porosity.

The IDENSI2 model is a simple empirical model suitable for both LWR and FBR; it is the standard TRANSURANUS densification model. The IDENSI7 model is the original MATPRO model and considers both densification and hot pressing phenomena[76]. However, as said in TU manual[8] the IDENSI7 model is not fully tested.

As shown in *Fig. 45*, IDENSI7 predicts a fast decrease of the gap width between fuel and cladding. It explains the lower fuel temperature and lower FGR than IDENSI2 during the base irradiation, *Fig. A. 13,* APPENDIX A.

During the power ramp, opposite behavior is observed: both fuel temperature and FGR are predicted higher by IDENSI7 respect to reference model IDENSI2, *Fig. 46,* and *Fig. A. 14* (APPENDIX A). This result can be explained considering the combination of gap width and fuel porosity. During the base irradiation, the temperature is mainly influenced by the different gap width between fuel and cladding while the fuel porosity has a minor influence because fuel temperature is relatively low. On the other hand, during the power ramp the linear power is high and only the fuel conductivity affects the fuel temperature since the gap is closed for both reference and IDENSI7 simulations. This explains the higher FGR achieved at the end of the power ramp with the option IDENSI7 *Fig. A. 14, Tab. 23*.

PRIMO MOX				
Sensitivity analysis M3: fuel densification models				
RUN	**End of BI**		**End of PR**	
	FGR %	**Error %**	**FGR %**	**Error %**
Exp. FGR	0.47	--	11.23	--
Reference IDENSI2	0.51	+8.51	7.64	-31.97
IEDNSI 7	0.34	-27.66	9.06	-19.32

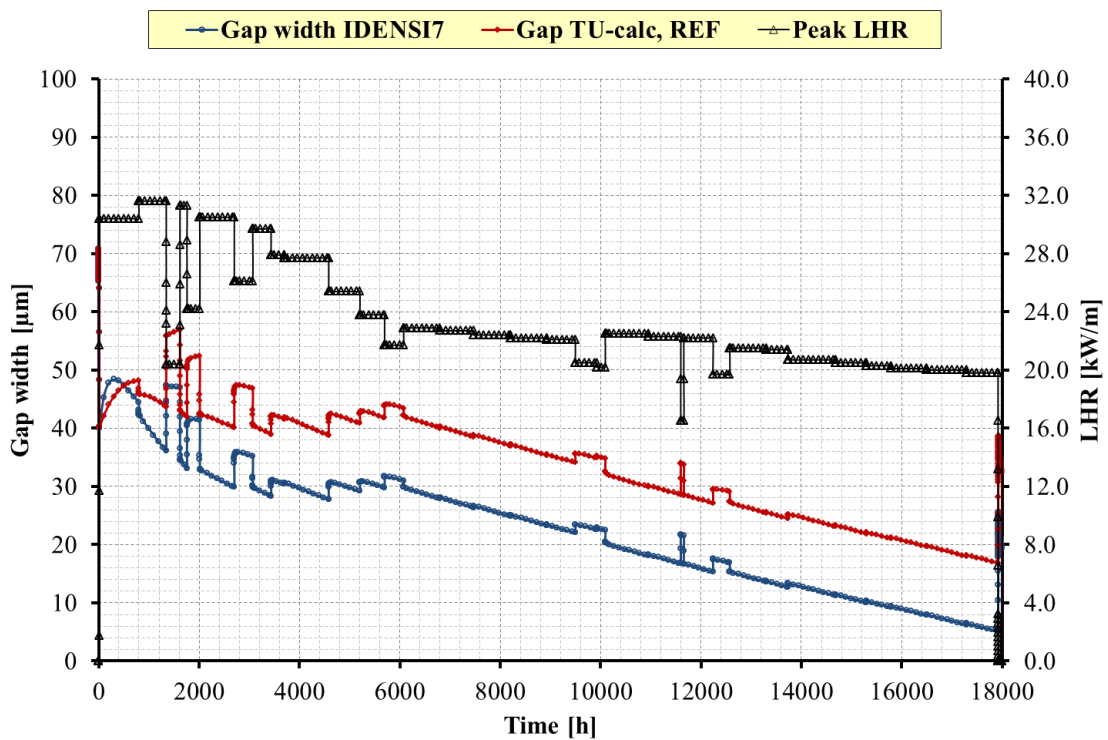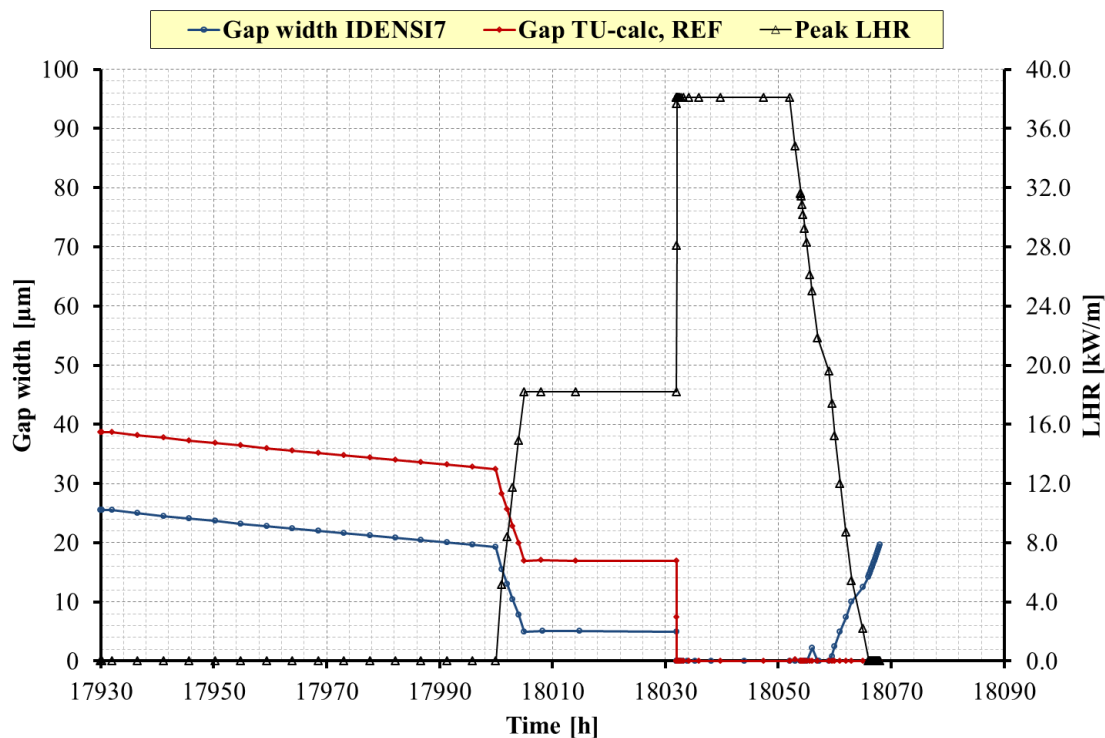*Tab. 23 – PRIMO Program, rod BD8, sensitivity analysis on densification models, results and relative errors.*

Fig. 45 – PRIMO Program, rod BD8, sensitivity analysis on densification models, gap width in peak axial position, base irradiation.

Fig. 46 – PRIMO Program, rod BD8, sensitivity analysis on densification models, gap width in peak axial position, power ramp.

6.2.6   Assessment on fabrication density (runs D1)

The fuel density indirectly affects the FGR since it influences the fuel conductivity and therefore the fuel temperature profile. The database reports the nominal density without its tolerance. It has been assumed as +/- 1% TD. Density maximization generally increases the fuel conductivity and therefore it reduces the FGR. Opposite conclusions can be drawn for density minimization. The FGR trends for maximum and minimum density are compared with the reference density in *Fig. A. 15* and *Fig. A. 16* (APPENDIX A). The results are summarized in *Tab. 24*. Since the temperatures remain relatively low and the densification takes place during in the first 10000 MWd/kgHM, the effect of the initial density is more pronounced in the base irradiation. In the power ramp, the effect is negligible because the densification has ended and the fuel temperature remains well beyond the threshold temperature for the activation of the Koo model.

PRIMO MOX				
Sensitivity analysis D1: fuel density				
RUN	**End of BI**		**End of PR**	
	FGR %	**Error %**	**FGR %**	**Error %**
Exp. FGR	0.47	--	11.23	--
Reference density	0.51	8.51	7.64	-31.97
TU calc. +1% TD	0.89	89.36	8.33	-25.82
TU calc. -1% TD	0.35	-25.53	7.07	-37.04

Tab. 24 – PRIMO Program, rod BD8, sensitivity analysis on fuel initial density, results and relative errors.

6.2.7 Assessment on grain size (runs D2)

As porosity at the end of the sintering, grain size is usually an uncertain parameter since it is usually given as average value. This means that the data are representative of the ideal situation in which the grain size is uniform in the pellet volume and do not account for local deviations that are dependent from the fabrication process. Grain size has two main effects. Firstly, the larger is the grain, the larger is the diffusion distance for the fission gas atoms created in the grains. This tends to reduce the release rate. Secondly, the larger is the grain, the lower is the capacity of the grain boundaries to store fission gas as their total surface-to-volume ratio is decreasing. In despite of this, for steady state conditions FGR is low (1-2%) and dominated by the process to saturate the grain boundaries, and therefore it can be concluded that FGR cannot be strongly dependent on the grain size. On the other hand, during power ramps, these opposite contributions may impact on the FGR together with micro-cracking of the grain boundaries that is more or less a stochastic phenomenon. Even after 50 years of testing the contribution of these three mechanisms to FGR during power ramp is still controversial: some of the experiments highlight largest release from small grains and some other highlight opposite results.

Rod BD8 has standard initial grain size (7.8 µm). The investigations assume that the average grain size is obtained from the contribution due to grains of dimension within +/- 25% its average value. The results are shown in *Fig. A. 17, Fig. A. 18* (APPENDIX A) and *Tab. 25*.

As expected, in base irradiation, no significant influence of the grain size on FGR is detected. Fuel temperature is, in general, low and thermal diffusion processes are not significant; most of the gas remains trapped inside grains. Similar trend is observed in the ramping phase too. In general, smaller grains lead to higher FGR and vice versa.

PRIMO MOX				
Sensitivity analysis D2: fuel grain size				
RUN	**End of BI**		**End of PR**	
	FGR %	**Error %**	**FGR %**	**Error %**
Exp. FGR	0.47	+0.00	11.23	+0.00
TU Reference GS	0.51	+8.51	7.64	-31.97
TU GS +25%	0.31	-34.04	7.24	-35.62
TU GS -25%	0.89	+89.36	7.68	-31.61

Tab. 25 – PRIMO Program, rod BD8, sensitivity analysis on grain size, results and relative errors.

6.2.8 Assessment on initial gap width (runs D3)

The gap size affects its thermal resistance and, consequently, it influences the temperature drop across the gas zone and the maximum temperature in the fuel. The higher is the gap size, the higher is the fuel temperature. High fuel temperature has two effects: it promotes FGR that further reduces the gap conductance (since Xe and Kr have lower conductivity that He) and it promotes gap closure because of enhanced gaseous swelling and fragment relocation.

In this analysis the effect of the gap initial size has been assessed. Since the gap tolerances are not given in the documents it has been assumed (based on *Tab. 5* and *Tab. 6*) in the range [93-108] µm.

Gap maximization generally increases the FGR and the pin pressurization. Opposite conclusions can be drawn for gap minimization. The trend are reported in APPENDIX A: *Fig. A. 19* and *Fig. A. 20* respectively. *Tab. 26* summarizes the results of the analysis. The main effects are observed during the base irradiation since during the power ramp test the gap closes.

PRIMO MOX

Sensitivity analysis D3: gap width between fuel and cladding				
RUN	**End of BI**		**End of PR**	
	FGR %	**Error %**	**FGR %**	**Error %**
Exp. FGR	0.47	--	11.23	--
TU Reference gap	0.51	+8.51	7.64	-31.97
TU calc. max gap	0.72	+53.19	7.69	-31.52
TU calc. min gap	0.46	-2.13	7.71	-31.34

Tab. 26 – PRIMO Program, rod BD8, sensitivity analysis on gap width results and relative errors.

6.3 Code to code comparison

In this section, the reference simulation (here labeled as TU-v1m1j12-ENEA) is compared to the results obtained by means of other codes employed in the benchmark[10]. The following fuel pin mechanic computer code were benchmarked:

- COSMOS, developed at KAERI, South Korea[77],
- FRED, developed at Kurchatov Institute, Russian Federation[78],
- ENIGMA, developed at NNL, UK[79],
- FRACPON-3, sponsored by the U.S. Nuclear Regulatory Commission (NRC) for evaluating light water reactor (LWR) fuel performance and maintained by Pacific Northwest National Laboratory (PNNL)[80],
- TRANSURANUS version 2004,
- FALCON, developed at ANATECH, San Diego, California[81].
- FEMAXI, developed at JAERI, Japan[82] and
- START-3, developed at JSC-VNIINM, Russian Federation[83].

As stated in the final report of the PRIMO benchmark, there is excellent agreement on the computed burn-up with all the participant simulations, the SCK-CEN experimental analyses (with CONDOR code), and the PIE results. Basically, the calculated rod average burn-ups indicate that all benchmark participants modeled the heating histories (including the axial power distribution) correctly.

The calculated fuel centerline temperatures (prior to the ramp) are illustrated in *Fig. 47*. Through 6000 h of irradiation, all the codes agree within a range of ~125°C; after that time, the Russian codes (FRED and START-3) yield results that are higher and diverge from the remaining codes (whose results are within a ~100°C). The TU-v1m1j12-ENEA simulation predicts a fuel temperature that is consistent with the most part of the codes. The older TU simulation (carried out by means of the 2004 version) predicts significantly higher temperatures; the difference between the two versions exceeds 120°C at the beginning of the simulation and progressively reduces; the fuel temperatures are almost coincident at 18000 h (end of BI). The FGR trends obtained by the benchmark participants are shown in *Fig. 48*. Most of the simulations (including TU-v1m1j12-ENEA) predict a FGR prior to ramp less than 0.8%, which is in agreement with the measured trend (0.47%). FRED, START-3 and PSI-FALCON predict higher FGR in accordance to the higher fuel temperatures.

The peak fuel temperatures during the ramp phase of the test are given in *Fig. 49*; except for the START-3 prediction (the highest one) and ENIGMA and TU-v1m1j12-ENEA prediction (lower ones), the predictions are within a range of about 200°C. The FGR trends during the power ramp are shown in *Fig. 50*. The START-3 and FALCON predict the highest values of FGR at the end of the power ramp (15.4 to 16.2% respectively); the lowest prediction is that of TU-v1m1j04 at 4.7%. ENIGMA predicts 7.2% while the other code are within the range from 9.1 to 13.7%. The TU-v1m1j12-ENEA

simulation predicts 7.7% which improves the old result. Even though the higher fuel peak temperature is predicted by TRANSURANUS older version, TU-v1m1j12-ENEA simulates higher FGR because of the selection of the ramp release model (IGRBDM 3, modified Koo model). This model was not available at the time of TU-v1m1j04 simulation; the reference inter-granular model of White and Tucker (IGRBDM 1) was selected.
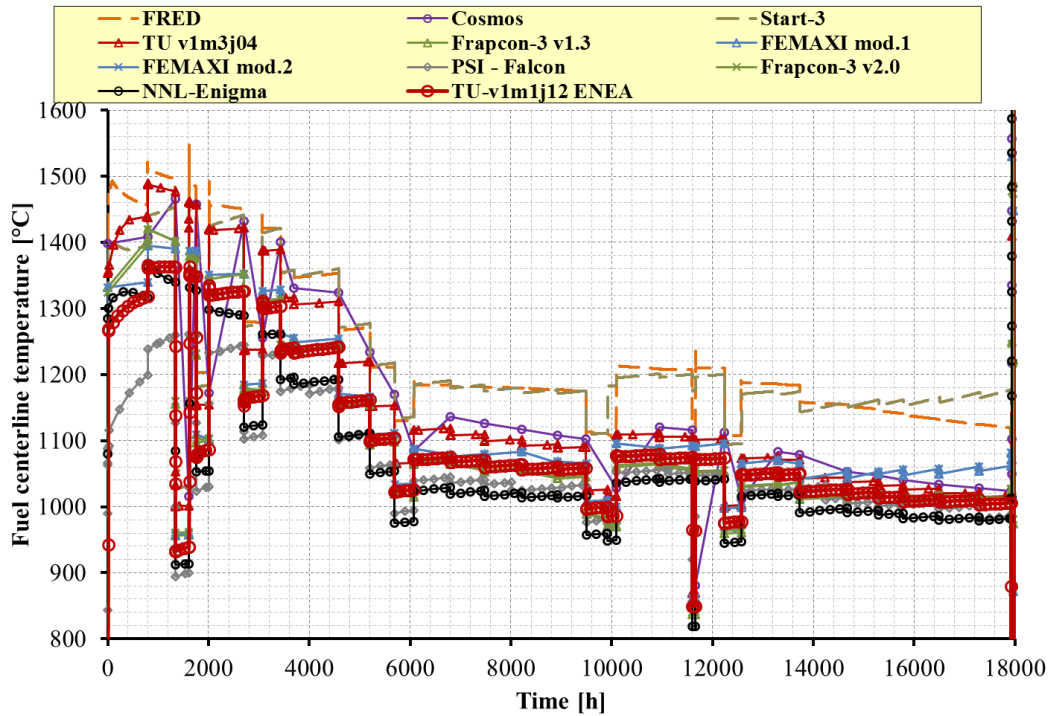

Fig. 47 – PRIMO Program, rod BD8, code-to-code comparison, fuel temperature, base irradiation.
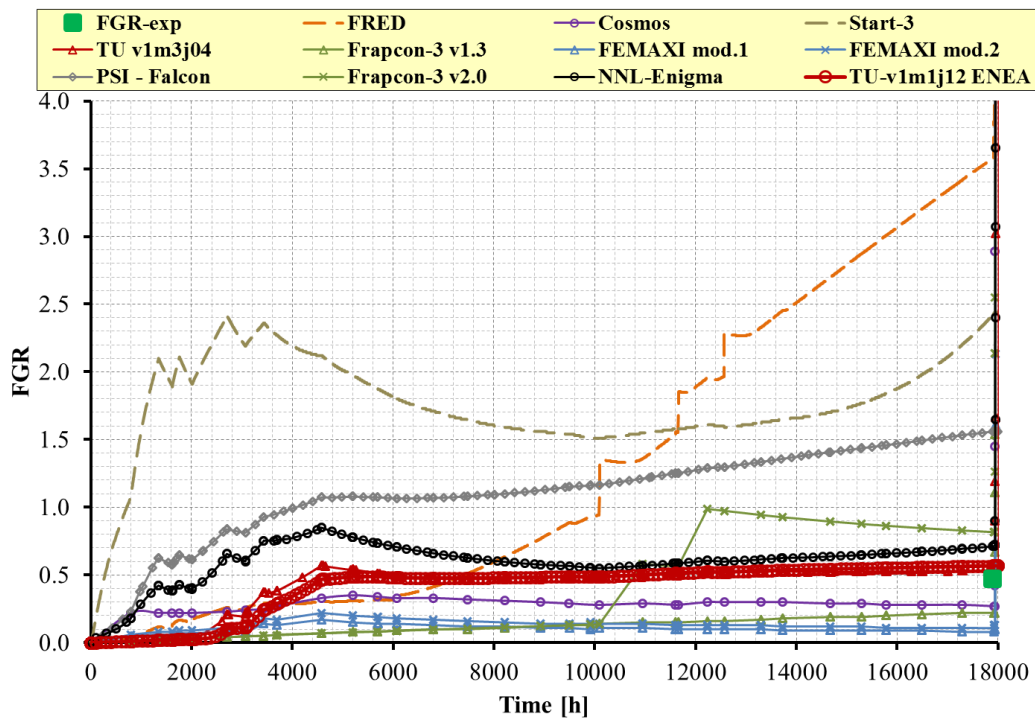
Fig. 48 – PRIMO Program, rod BD8, code-to-code comparison, FGR, base irradiation.
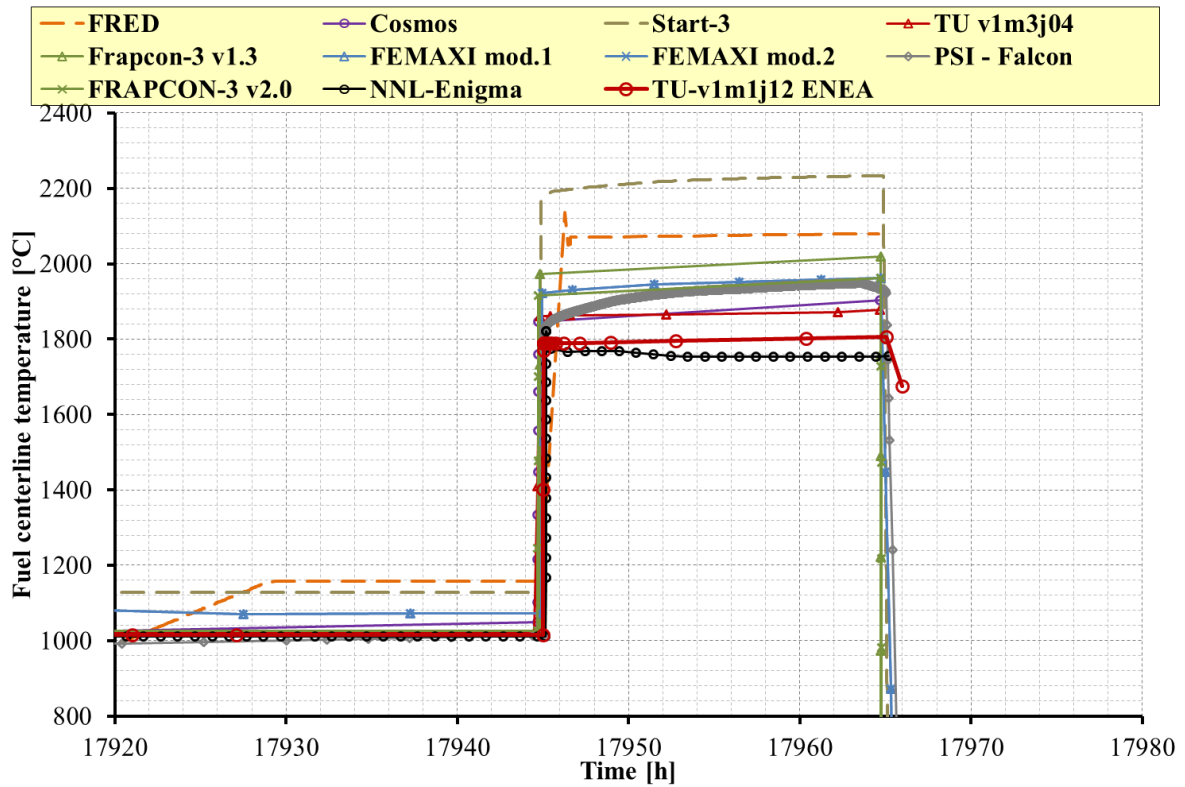
Fig. 49 – PRIMO Program, rod BD8, code-to-code comparison, fuel temperature, power ramp.

Fig. 50 – PRIMO Program, rod BD8, code-to-code comparison, FGR, power ramp.

7 Validation of TU code against IFA-597 experiment

7.1 Reference results

The assessment of TU code in simulating rods 10 and 11 from IFA-597 experiment is discussed in the following subsections. The analysis deals with the comparison between measured and predicted trends (burn-up, fuel temperature, inner pin pressure, FGR). The main results are presented from *Fig. 51* to *Fig.58* and they are summarized in *Tab. 16* and *Tab. 28*.

7.1.1 Burn-up analysis

In order to demonstrate the consistency of any calculation, it is essential to predict the burn-up in a correct way. In fact, this first step implies to demonstrate that the fuel rod is analyzed under conditions that represent its state at the end of the experiment. In addition, part of the models of any fuel pin mechanic code are dependent upon the burn-up and therefore it should be verified that those models are taking into account the burn-up effects according to the experimental conditions achieved.

The final burn-ups for the two rods are 27 MWd/kgMOX and 27.9 MWd/kgMOX respectively for rod 10 and 11. TU code models the burn-up according to the "TRANSURANUS-LWR burn-up model"[70]. As evidenced in *Fig. 51*, *Fig.52* and *Tab. 16* the burn-ups of these rods are well captured.

7.1.2 Fuel temperature analysis

The measured fuel temperatures of rods10 and rod 11 are given in the benchmark document[12] as function of time. They are shown in *Fig.53* and *Fig. 54* (rod 10 and rod 11, respectively). The graphs also provide:

- the computed fuel temperature at the thermocouple positions;
- the peak fuel temperature for rod 10 with solid pellets (it is not plotted for rod 11 with hollow pellets because it is substantially equal to the measured temperature);
- the Vitanza temperature threshold[7] for gas release onset;
- the computed gap width between fuel and cladding.

Rod 10: during IFA-597.4 and .5, the fuel temperature is in good accordance with the measured values being the error always below 40°C with a slight overestimation at the end of IFA-597.4 and at the end of IFA-597.5. During IFA-597.6, the fuel temperature is overestimated of about ~200°C. This overestimation can be explained considering the gap width trend. As stated in the benchmark document[12], the low fuel temperature and high inner pressure suggest that the gap is closed during this power cycle. On the contrary, as shown in *Fig.53*, TU code predicts the gap opened. Therefore, the fuel peak temperature in rod 10 is computed about 200°C higher than the measured temperature.

Rod 11: the comparison between measured and computed temperatures is shown in *Fig. 54*: three different trends are evidenced. The first one deals with the first high power cycle IFA-597.4 in which the fuel temperature is underestimated of about 60°C. On the other hands, during the low power period IFA-597.5, it is good accordance with measurements. Finally, during IFA-597.6, the fuel temperature is overestimated (~200°C) probably due to the same reasons provided for rod 10. As stated before, fuel peak temperature is substantially equal to the measured one; the same result is observed comparing simulated temperatures; therefore the peak temperature is not reported in *Fig. 54*.

7.1.3   Rod inner pressure analysis

The measured time dependent inner pressure histories are given in the benchmark document[12]. The comparison with the computed trends are provided in *Fig.55* and *Fig.56*. The two graphs also report the computed total free volume on the secondary axis.

Rod 10: as shown in *Fig.55*, during the first part of the experiment, the pressure is in good agreement with the experimental data . The initial value is overestimated of about 0.03 MPa; it suggests that the initial rod free volume given in the benchmark specifications[12] is slightly lower than the real one. During the first 2000 hrs of irradiation a pressure decrease is observable while the free volume is increasing of about 110 mm³ because of the effect of fuel densification. This behavior is observed both in the simulation and in the experimental data. TU code is in good accordance with the experiment up to the end of IFA-597.4 while it underestimates the next two phases mainly because of the under-prediction of FGR. In the low power cycle the underestimation is about 0.8 bar, however, the pressure main trend is qualitatively captured. In IFA-597.6, the underestimation is about 7.5 bar mainly due to the underestimation of the initial pressure spike magnitude. After this pressure increase, the code predicts a further pressure increase trend which is consistent with the experimental data. In fact, the subsequent two pressure bursts are observed because of delayed FGR detection (caused by closed gap) and should be interpreted as a continuous increase as predicted by the code.

Rod 11: the inner pressure of this hollow pellets rod is provided in *Fig.56*. The initial value of inner pressure is not consistent with the experiment. It suggests that the total pin free volume given in the benchmark document[12] is smaller than the real one. The effect of fuel densification is observed also for this rod and the computed trend is consistent with the experimental data. The measurements underlined a pressure increase during the initial high power cycle IFA-597.4 due to high FGR. TU code under-predicts this pressure increase because it does not capture the FGR during this phase. The simulated pressure results underestimated of about 2.5 bar during IFA-597.5. In IFA-597.6 behaves similar to rod 10, with an high pressure burst at the beginning of the power cycle. The simulation predicts a 3.1 bar pressure increase while the measurements underlined a 6.9 bar burst. After the burst, the computed pressure increase is still smaller respect to the experiment. The pressure underestimation is due to the FGR underestimation that occurs during the whole irradiation time. For a detailed FGR analysis, see 7.1.4.

7.1.4   FGR analysis

FGR data were provided on the HRP IFA-597 report[11],[12]. They were obtained by pressure measurements and pin free volume estimation. The comparison between experimentally estimated trends and TU code results is reported in *Fig.57* and *Fig.58* for rod 10 and rod 11 respectively. The figures include the fuel measured temperature and the Vitanza threshold.

Rod 10: the FGR reached 7% at the end of IFA-597.4, and exceeded 20% at the end of IFA-597.6 as can be seen in *Fig.57*. The code predicts correctly the onset of FGR at 2100 hrs. It suggests that the grain boundaries saturation is modeled according to the experiment. The experimental FGR increases during IFA-597.4 up to 7%. The code underestimates the FGR at the end of this period (it is predicted about 4%). The modified Koo model are activates twice: the first occurs at the power spike around 4100 hrs; the second occurs at the power down ramp at the end of IFA-597.4.
During IFA-597.5 both the experimental and computed FGR decrease due to the lower power and fuel temperature that inhibits the fission gas thermal diffusion. At the end of IFA-597.5, the experimental FGR is about 4% while the TU code predicts about 3%. FGR burst is observed during the power increase at the beginning of IFA-597.6. Large and unexpected FGR increase was evidenced in the experiment: from 4% up to 16% due to the burst. TU code under-predicts the magnitude of this phenomenon (it predicts an increase from 3% to 5.5%). affecting the simulation of the rod inner

pressure described in 7.1.3. FGR increases further after the bursts, of about 5%. A similar increase(4.5%) is highlighted also in the simulation. Therefore, the final FGR is underestimated with an error of about 50%, mainly due to the FGR burst, at the beginning of IFA-597.6.

Rod 11: the FGR analysis is provided in *Fig.58*. Even if lower peak temperatures were achieved compared to the solid pellet rod 10, during IFA-597.4, the gas release was more relevant than in rod 10 and, in particular, it exceeded 10%. This behavior can be explained by the higher linear power in the first 5000 hrs of irradiation (*Fig. 18*). After that time, the linear power was substantially equal for the two rods. As in rod 10, FGR decreases during IFA-597.5 and a big FGR burst occurred at the beginning of IFA-597.6; the final experimental FGR is about 16%. The simulation under-predicts the FGR along the whole simulation. The simulated FGR never reach 1% before the beginning of IFA-597.6 when the Koo model for power ramps activates. However, the simulated FGR step is significantly smaller than the measured one and reaches 2%. The final value predicted by TU code is slightly below 4% with an error of about 75%.

According to the simulation results, rod 10 is characterized by fuel temperatures high enough to exceed the Vitanza threshold both in the second half of IFA-597.4 and during IFA-597.6 (*Fig.53*). It explains the relevant FGR obtained in the simulations. On the other hand, rod 11 fuel temperature only approaches the Vitanza threshold during the power spike in IFA-597.4 and exceeds it for some hours during IFA-597.6; the resulting FGR is therefore lower. In addition, since the code predicts open gap in IFA-597.6, the effect of gap poisoning has to be considered. In rod 10, the high FGR (6%), causes a thermal positive feedback that contributes to further gas release. In rod 11 the thermal feedback is not relevant because of very low values of FGR (2%) at the beginning of IFA-597.6. In conclusion, the experiment evidenced high FGR for both rods. TU code under-predicts this phenomenon, particularly for rod 11.

IFA-597 rod 10

Design parameters

Parameter	Unit	Quantity
Rod Id	--	Rod 10
Fuel – clad material	--	MOX – Zr-4
U^{235} enrichment	%HM	0.22
Pu^{239} enrichment	%HM	6.07
Fuel average grain size	μm	5.45
Rod outer diameter	mm	9.50
Gap width	mm	0.09
Pellet outer diameter	mm	8.04
Pellet central hole	mm	0.00
Active length	mm	224
He filling pressure	bar	5

Reference analysis

Parameter	Uncertainty	Exp	TU calc	Error %	Acceptability band
Burn-up (MWd/kgHM)	±6%	27.0	26.8	-0.7	±10%
FGR	±10%	20.75	9.91	-52.24	+100% / -50%
Pin pressure		2.77	2.07	-25.27	

Tab. 27 – IFA-597, rod 10, summary of reference analysis.

IFA-597 rod 11

Design parameters

Parameter	Unit	Quantity
Rod Id	--	Rod 10
Fuel – clad material	--	MOX – Zr-4
U^{235} enrichment	%HM	0.22
Pu^{239} enrichment	%HM	6.07
Fuel average grain size	μm	5.45
Rod outer diameter	mm	9.50
Gap width	mm	0.09
Pellet outer diameter	mm	8.04
Pellet central hole	mm	0.90
Active length	mm	224
He filling pressure	bar	5

Reference analysis

Parameter	Uncertainty	Exp	TU calc	Error %	Acceptability band
Burn-up (MWd/kgHM)	±6%	27.5	27.4	-0.36	±10%
FGR	±10%	15.82	3.40	-78.50	+100% / -50%
Pin pressure		2.26	1.50	-33.62	

Tab. 28 – IFA-597, rod 11, summary of reference analysis.
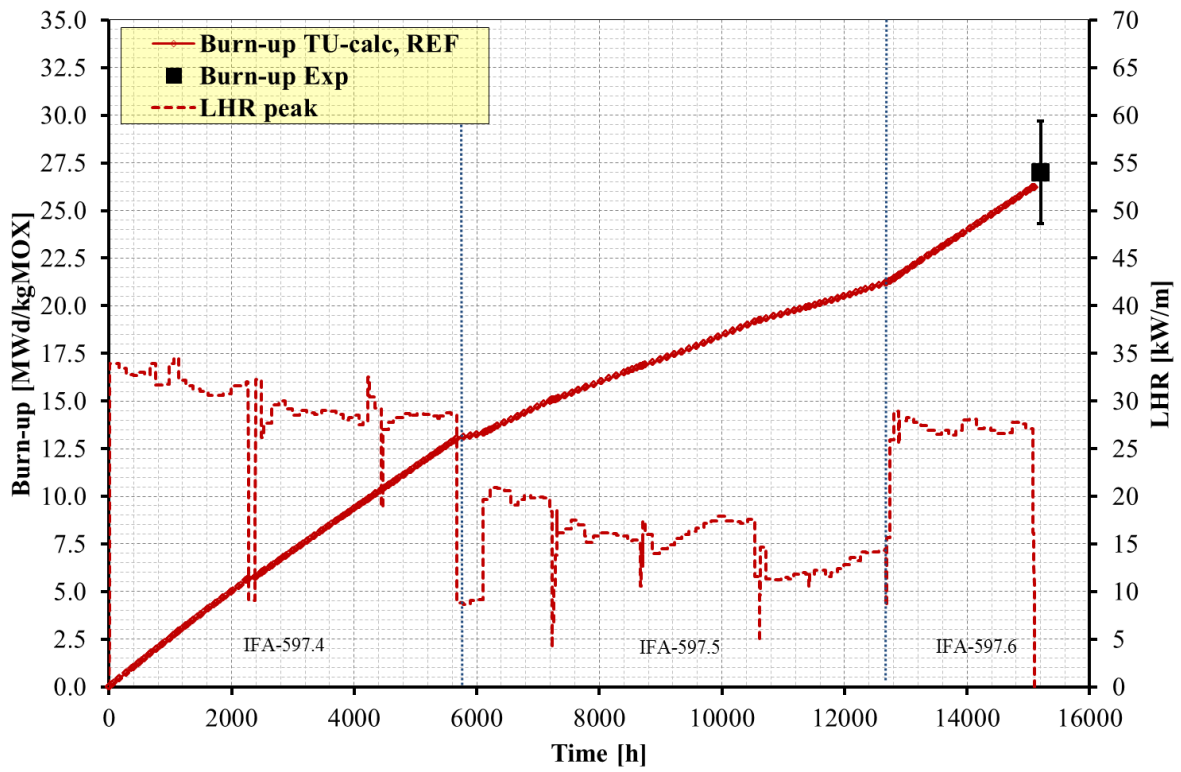
Fig. 51 – IFA-597, rod 10, burn-up analysis.
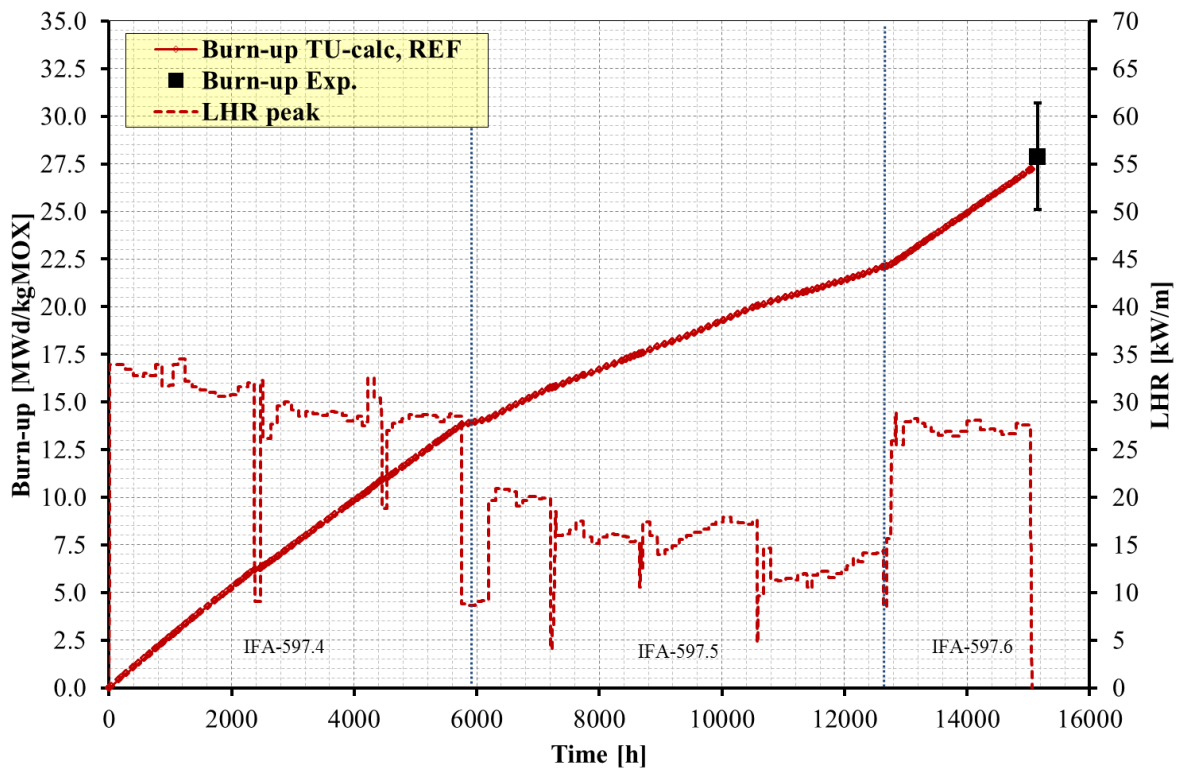
Fig.52 – IFA-597,rod 11, burn-up analysis.
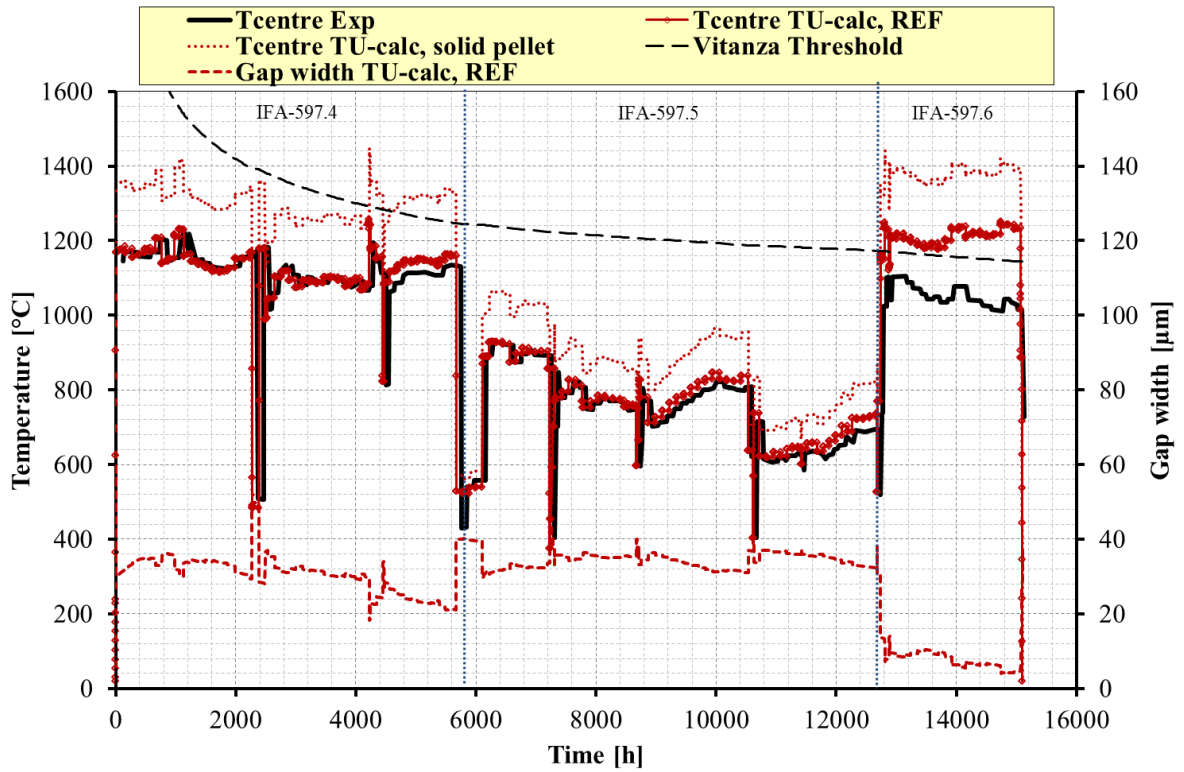
Fig.53 – IFA-597,rod 10, fuel temperature analysis
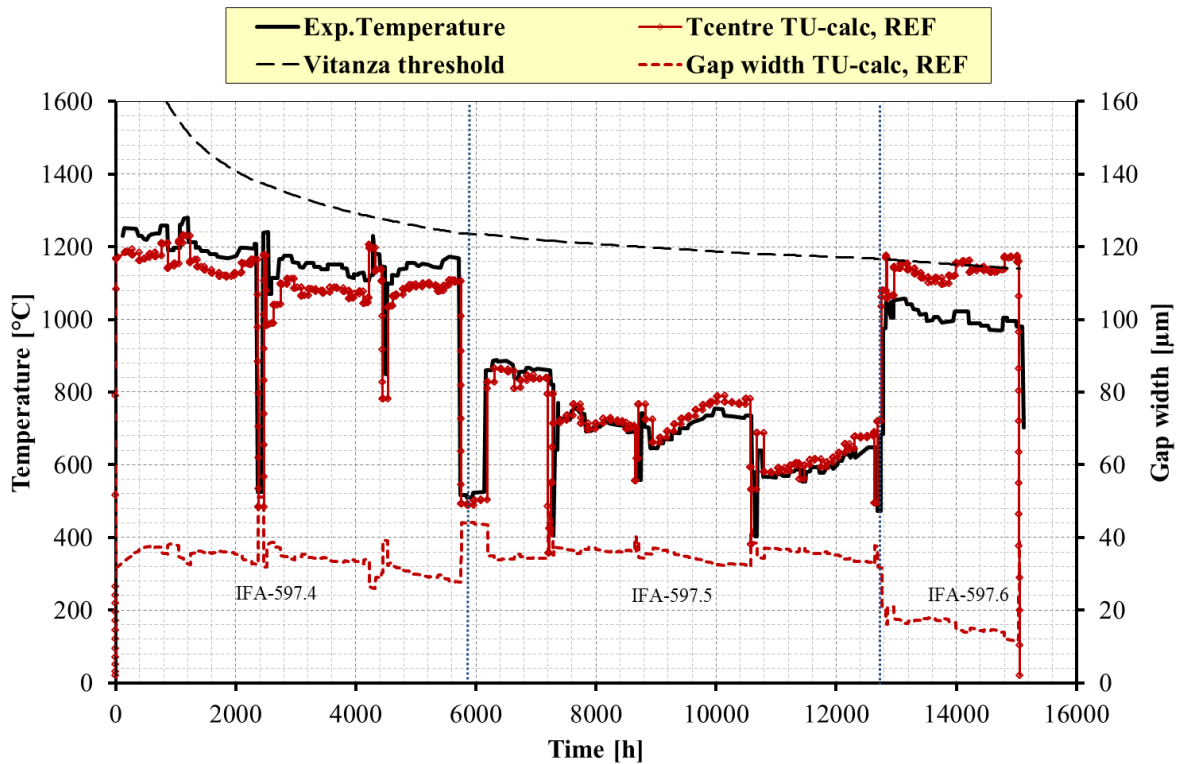
Fig. 54 – IFA-597,rod 11, fuel temperature analysis.

Ricerca Sistema Elettrico

Sigla di identificazione	Rev.	Distrib.	Pag.	di
ADPFISS – LP2 – 041	0	L	119	170
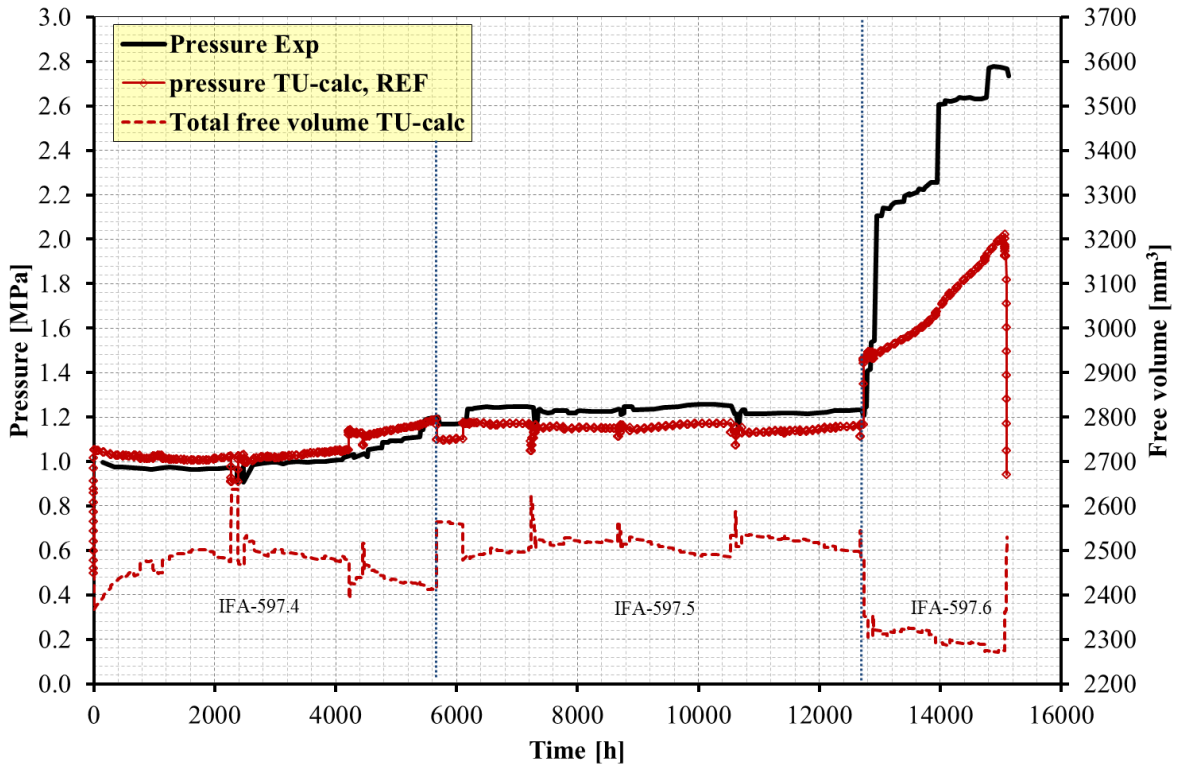
Fig.55 – IFA-597,rod 10, inner pressure analysis.
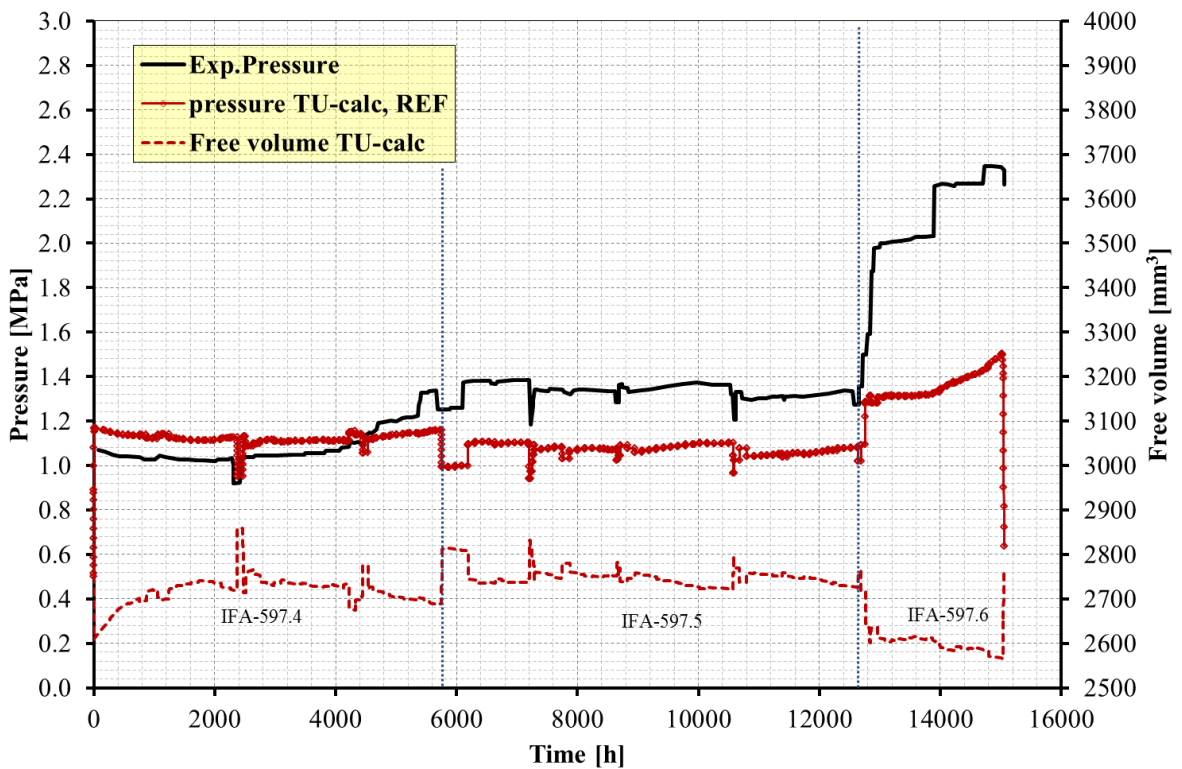
Fig.56 – IFA-597,rod 11, inner pressure analysis.
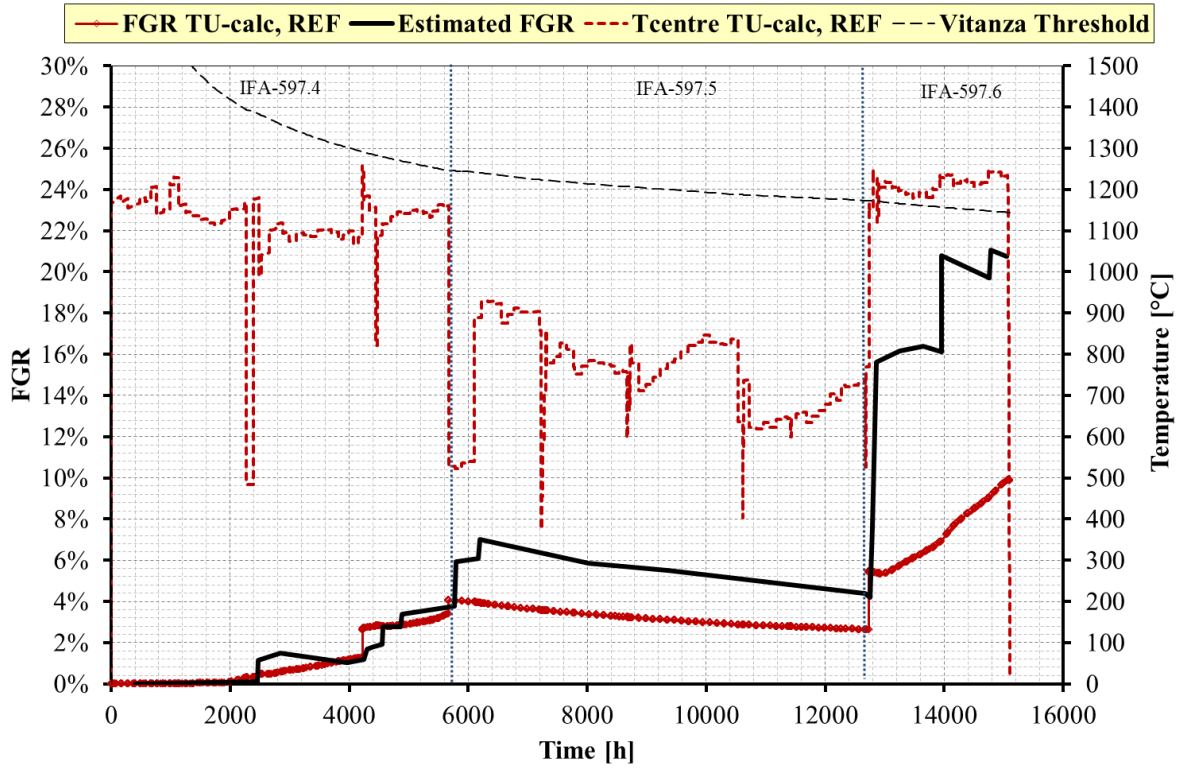
Fig.57 – IFA-597, rod 10, FGR analysis.
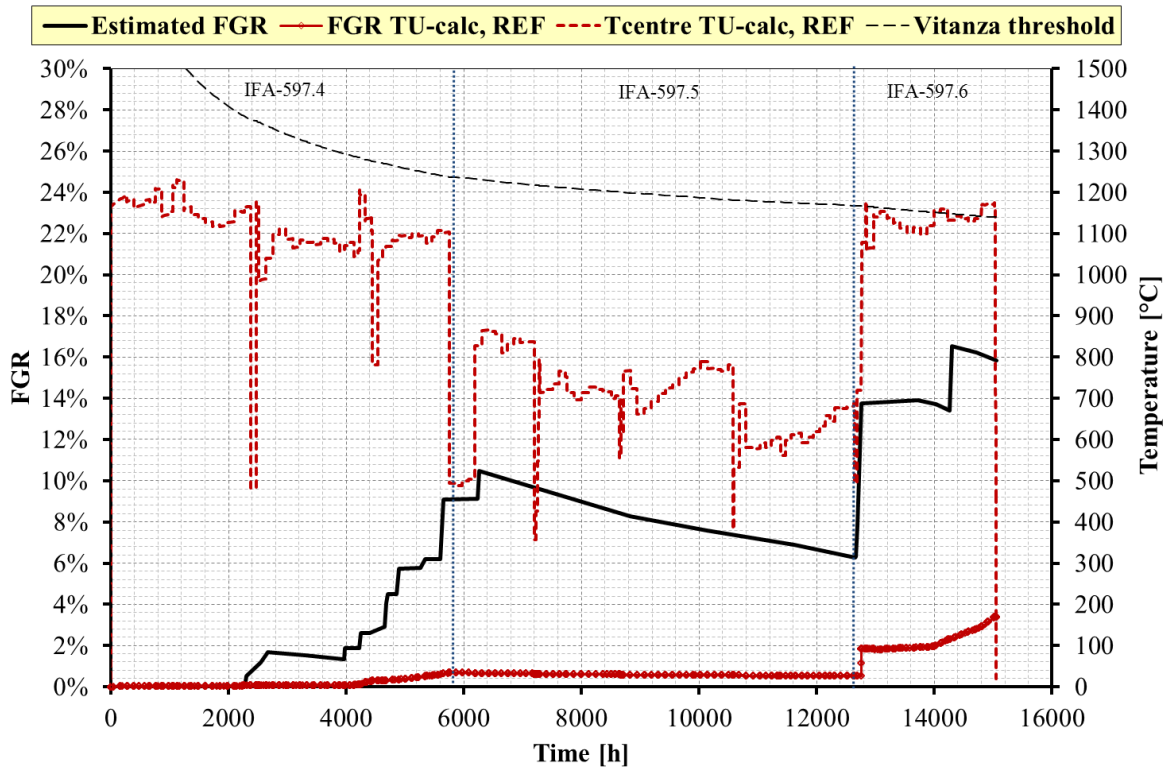
Fig.58 – IFA-597, rod 11, FGR analysis.

7.2 Sensitivity analysis

The sensitivity analysis is a fundamental step for the assessment of the code capabilities. Different objectives shall be fulfilled such as to demonstrate the robustness of the calculations, to characterize the reasons for possible discrepancies between measured and calculated trends or values observed in the reference calculation, to optimize code results and user option choices, to improve the knowledge of the code by the user.

The investigation of the effect of the parameters, models and processes identified in section 5.1.2 on the code result is carried out in this section. *Tab. 29* lists the sensitivity analyses and their objectives. They are divided into three groups: the investigations on models (labeled as M), the investigation on correlations (labeled as C), and the investigation on the initial design conditions (labeled as D). This list is not exhaustive since other model options might affect the code results, such as the uncertainties on the boundary conditions (i.e. the linear heat rate during the base irradiation and the power ramp phase, the ramp rate, the extension of holding time of ramp terminal level, etc..).

The development of the different sensitivities is hereafter reported in separate subsections distinguishing between the different groups of homogeneous selections.

Case	Run	Modification	Objective
Fission gas release	**M1.1**	Igrbdm 1	Investigate the impact of inter-granular models on fuel temperature, pin pressure and FGR. *Correlation according to the standard model*
	M1.2	Igrbdm 2	Investigate the impact of intergranular models on fuel temperature, pin pressure and FGR. *Correlation according to the temperature dependent model*
	M1.3	Igrbdm 1 FGRmod 4	Investigate the impact of intra-granular and inter-granular models on fuel temperature, pin pressure and FGR. *Inter-granular model according to the standard model and intra-granular model of Matzke and White Tucker.*
	M1.4	Igrbdm 2 FGRmod 4	Investigate the impact of intra-granular and inter-granular models on fuel temperature, pin pressure and FGR. *Inter-granular model according to the temperature dependent model and intra-granular model of Matzke and White Tucker.*
	M1.5	Igrbdm 3 FGRmod 4	Investigate the impact of intra-granular and inter-granular models on fuel temperature, pin pressure and FGR. *Inter-granular model according to the modified Koo model and intra-granular model of Matzke and White Tucker.*
	M1.6	Igrbdm 1 FGRmod 9	Investigate the impact of intra-granular and inter-granular models on fuel temperature, pin pressure and FGR. *Inter-granular model according to the standard model and intra-granular model of Turnbull.*
	M1.7	Igrbdm 2 FGRmod 9	Investigate the impact of intra-granular and inter-granular models on fuel temperature, pin pressure and FGR. *Inter-granular model according to the temperature dependent model and intra-granular model of Turnbull.*
	M1.8	Igrbdm 3 FGRmod 9	Investigate the impact of intra-granular and inter-granular models on fuel temperature, pin pressure and FGR. *Inter-granular model according to the modified Koo model and intra-granular model of Turnbull.*
Fuel conductivity	**C1.1**	Modfuel(j=6)=32	Investigate the impact of fuel conductivity on fuel temperature, pin pressure and FGR considering O/M effects. *Correlation according to Carbajo et al..*
	C1.2	Modfuel(j=6)=33	Investigate the impact of fuel conductivity on fuel temperature, pin pressure and FGR considering O/M effects . *Correlation according to Lanning and Beyer.*
	C1.3	Modfuel(j=6)=34	Investigate the impact of fuel conductivity on fuel temperature and FGR. *Correlation according to Wiesenack.*
	C1.4	Modfuel(j=6)=35	Investigate the impact of fuel conductivity on fuel temperature, pin pressure and FGR. *Correlation according to Van Uffelen and Schubert*

			(conservative).
Pellet fragment relocation	**M2.1**	Ireloc 2	Investigate the impact of fuel relocation on fuel temperature, pin pressure gap size and FGR. *Original KWU-LWR model based on initial gap size only.*
	M2.2	Ireloc 3	Investigate the impact of fuel relocation on fuel temperature, pin pressure, gap size and FGR. *GAPCON-THERMAL-3 based on initial gap size, LHR and burn-up.*
	M2.3	Ireloc 5	Investigate the impact of fuel relocation on fuel temperature, pin pressure, gap size and FGR. *Modified KWU-LWR model based on initial gap size only.*
Fuel swelling	**C2.1**	Modfuel(j4)=18	Investigate the impact of fuel swelling on fuel temperature, gap size, fuel elongation and FGR. *Simple correlation applied: swelling proportional to burn-up.*
	C2.2	Modfuel(j4)=19	Investigate the impact of fuel swelling on fuel temperature, pin pressure and FGR. *Original MATPRO swelling model considering separate contributions of the solid and gaseous fission products*
	C2.3	Modfuel(j4)=21	Investigate the impact of fuel swelling on fuel temperature, pin pressure, gap size and FGR. *Implicit formulation of the reference correlation.*
densification	**M3.1**	Idensi 7	Investigate the impact on FGR, fuel temperature, pin pressure and gap width. *Original MATPRO densification model.*
Fuel density	**D1.1**	Density +1% TD	Assess the impact on FGR and fuel centerline temperature of lower initial fuel porosity corresponding to an increase of 1% TD of the initial fuel density.
	D1.2	Density -1% TD	Assess the impact on FGR and fuel centerline temperature of higher initial fuel porosity corresponding to a decrease of 1% TD of the initial fuel density.
Grain size	**D2.1**	1.25 Grain$_{design}$	Assess the impact of 25% increased grains on FGR and fuel centerline temperature
	D2.2	0.75 Grain$_{design}$	Assess the impact of 25% decreased grains on FGR and fuel centerline temperature
Gap size	**D3.1**	Gap size 108μm	Test the impact of increased gap width at the beginning of irradiation on fuel temperature and FGR. Initial value obtained assuming maximum cladding and minimum fuel radii according to design uncertainties.
	D3.2	Gap size 93μm	Test the impact of decreased gap width at the beginning of irradiation on fuel temperature and FGR. Initial value obtained assuming minimum cladding and maximum fuel radii according to design uncertainties

Tab. 29 – IFA-597 list of sensitivity analysis.

7.2.1 Assessment of FGR models (runs M1)

This sensitivity analysis aims to assess the FGR models described in section 5.1.1. Each intra-granular model is associated with the inter-granular models to assess all the combinations[75]. *Tab. 30* and *Tab. 31* summarize the results.

According to section 5.1.1 and *Tab. 29*, the intra-granular thermal diffusion model according to Matzke and a-thermal diffusion according to White and Tucker is referred as FGRMOD 4. The reference thermal intra-granular diffusion model according to Matzke and a-thermal diffusion according to ITU data is labeled as FGRMOD 6 and; the thermal and a-thermal intra-granular diffusion model according to Turnbull is referred as FGRMOD 9.

The inter-granular models according to the standard model, the temperature dependent model and the reference power ramp model derived from the Koo model are labeled, respectively, IGRBDM 1, 2 and 3.

It should be mentioned that, below 1200°C, the reference intra-granular diffusion coefficient (FGRMOD 6) is lower than FGRMOD 4 and FGRMOD 9 while above 1200°C, it becomes equal to

FGRMOD 4. Assuming a power rating of 35W/g, above 1320°C, FGRMOD 6 overpasses FGRMOD 9. This last coefficient is the highest up to 1320°C, *Fig. 59*.

Rod 10 with solid MOX pellets: the fuel peak temperature is about 200°C higher than the measurements. Therefore, the peak fuel temperature ranges from 1300 to 1450°C during high power periods and from 800 to 1000°C during low power periods. According to *Fig. 59*, the diffusion coefficients during IFA-597.4 / .6 rank in the following manner: FGRMOD 9 < FGRMOD 4 = FGRMOD 6. During the low power cycle IFA-597.5, the they rank in a different way due to the lower fuel temperature: FGRMOD 6 < FGRMOD 4 < FGRMOD 9.

Rod 11 with hollow pellets: the fuel peak temperature is lower than rod 10. The measured temperature is close to the fuel peak temperature. During IFA-597.4 and .6 (high power) the fuel peak temperature is mainly in the range 1100-1200°C; the diffusion coefficient rank as follows: FGRMOD 4 ~ FGRMOD 6 < FGRMOD 9. During IFA-597.5, the low temperature (600-900°C) gives the following ranking: FGRMOD 4 < FGRMOD 6 < FGRMOD 9.

The inter-granular models are presented in *Fig. 60*. During the high power (and high temperature) cycle, the grain boundaries saturation concentrations for rod 10 are IGRBDM 1 (FGRMOD 4-6) < IGRBDM 2 (FGRMOD 4-6) < IGRBDM 1 (FGRMOD 9) < IGRBDM 2 (FGRMOD 9). Although hollow pellets rod highlights lower temperatures, the ranking of GB saturation concentrations remains the same of rod 10. However, at lower temperature, the distance between different models is larger. IGRBDM 3 model is not discussed because it is equal to IGRBDM 1 excepts in power ramp conditions. The results of the sensitivity analysis on FGR models are provided in section B.1 (Appendix B).

FGRMOD 4 is analyzed in *Fig. B. 1* (Appendix B) and *Tab. 30, Tab. 31*. The figures include the reference simulations and the FGRMOD 4 simulations combined with the three grain boundary models. IGRBDM 2 computes the lowest FGR during the whole experiment; the final FGR value is still lower than the reference simulation even with a higher diffusion coefficient, *Fig. B. 1 a) and b)*. IGRBDM 2 exceeds the reference FGR during IFA-597.6 mainly because of the effect of the diffusion coefficient that, at low temperature, is higher than FGRMOD 6. The gas diffusion is then more effective in the pellet periphery where temperatures are lower. FGRMOD 4 in combination with IGRBDM1 and IGRBDM 3 provide higher FGR than the reference simulation mainly because of the more effective diffusion being IGRBDM 3 associated to the highest FGR due to the activation of the power ramp conditions. Similar behavior is observed in both rods even if the values of FGR are different and remain underestimated compared to the experimental estimated FGR. The fuel temperatures highlight minor deviations from the reference calculation (only IFA-597.6 is slightly dependent upon the model due to the thermal feedback effects), *Fig. B. 1 c) and d)* while the pin pressure is driven by the FGR: *Fig. B. 1 e) and f)*.

The reference model FGRMOD6 is assessed in *Fig. B. 2 a), b), c), d), e) and f)* (Appendix B), and *Tab. 30*. The general considerations reported for FGRMOD4 applies to FGRMOD6 too excepts the absolute values of the FGR that tends to reduce compared to FGRMOD4 because of lower intra-granular diffusion coefficient. The coupling of FGRMOD6 with IGRBDM 3 (reference selection) provides highest FGR due to several activations of the modified Koo model for power ramps during IFA-597.4 and at the beginning of IFA-597.6.

FGRMOD9 is analyzed in *Fig. B. 3* (Appendix B)), and *Tab. 30, Tab. 31*. Among the intra-granular models, the model of Turnbull (FGRMOD9) associated with IGRBDM 1 or 2 compute the lowest FGR, *Fig. B. 3 a) and b)*. This is connected to the highest saturation limits that reduce the FGR ($4*10^{-4}$

and 0.7092/T mol/m^2 respectively). The simulation of the power ramp up, at the beginning of IFA-597.6, highlights two different trends: IGRBDM1 and IGRBDM2 still predict the lowest FGR while, on the other hand, IGRBDM3 (Koo ramps model) predicts the highest one. However, the combination FGRMOD 9 – IGRBDM 3 provides a final FGR that is lower than the reference simulation because, even at high temperature, grain boundaries take longer time to saturate and FGR decreases after the initial burst. Again, the same considerations apply for both rods except for the absolute values of FGR . Due to thermal feedback effects, the fuel centerline temperature is affected by the grain boundary model being those of IGRBDM3 similar to the reference one and higher than the remaining models, *Fig. B. 3 c)* and *d)*. The pin pressure is driven by the FGR: *Fig. B. 3 e)* and *f)*.

The summary of the FGR analysis is shown in *Fig. 61* and *Fig. 62* for rod 10 and rod 11 respectively. Both the rods are underestimated. Rod 10 is captured within the common acceptability band for FGR analysis while rod 11 is under-predicted.

IFA-597 rod 10				
Sensitivity analysis M1: FGR models				
RUN	FGR %	Error %	IP [MPa]	Error %
Experimental	**20.75**	**--**	**2.77**	**--**
Ref. FGRMOD6, IGRBDM3	**9.91**	**-52.24**	**2.07**	**-25.27**
FGRMOD4, IGRBDM1	10.43	-49.73	1.91	-25.27
FGRMOD4, IGRBDM2	8.73	-57.93	2.19	-31.05
FGRMOD4, IGRBDM3	11.67	-43.76	1.91	-20.94
FGRMOD6, IGRBDM1	8.72	-57.98	1.77	-31.05
FGRMOD6, IGRBDM2	7.33	-64.67	2.77	-36.10
FGRMOD9, IGRBDM1	2.46	-88.14	1.30	-53.07
FGRMOD9, IGRBDM2	1.48	-92.87	1.20	-56.68
FGRMOD9, IGRBDM3	8.51	-58.99	1.89	-31.77

Tab. 30 – IFA-597, rod 10, sensitivity analysis on FGR models ,results and relative errors.

IFA-597 rod 11				
Sensitivity analysis M1: FGR models				
RUN	**FGR %**	**Error %**	**IP [bar]**	**Error %**
Experimental	**15.82**	**--**	**2.26**	**--**
Ref. FGRMOD6, IGRBDM3	**3.40**	**-78.51**	**1.50**	**-27.44**
FGRMOD4, IGRBDM1	4.55	-71.24	1.61	-55.96
FGRMOD4, IGRBDM2	2.85	-81.98	6.16	-59.21
FGRMOD4, IGRBDM3	5.32	-66.37	7.13	-23.47
FGRMOD6, IGRBDM1	2.80	-82.30	1.44	-29.60
FGRMOD6, IGRBDM2	1.78	-88.75	1.35	-32.85
FGRMOD9, IGRBDM1	5.92	-80.91	1.23	-37.18
FGRMOD9, IGRBDM2	1.92	-87.86	1.19	-38.63
FGRMOD9, IGRBDM3	3.02	-62.58	1.47	-28.52

Tab. 31 – IFA-597, rod 11, sensitivity analysis on FGR models ,results and relative errors.
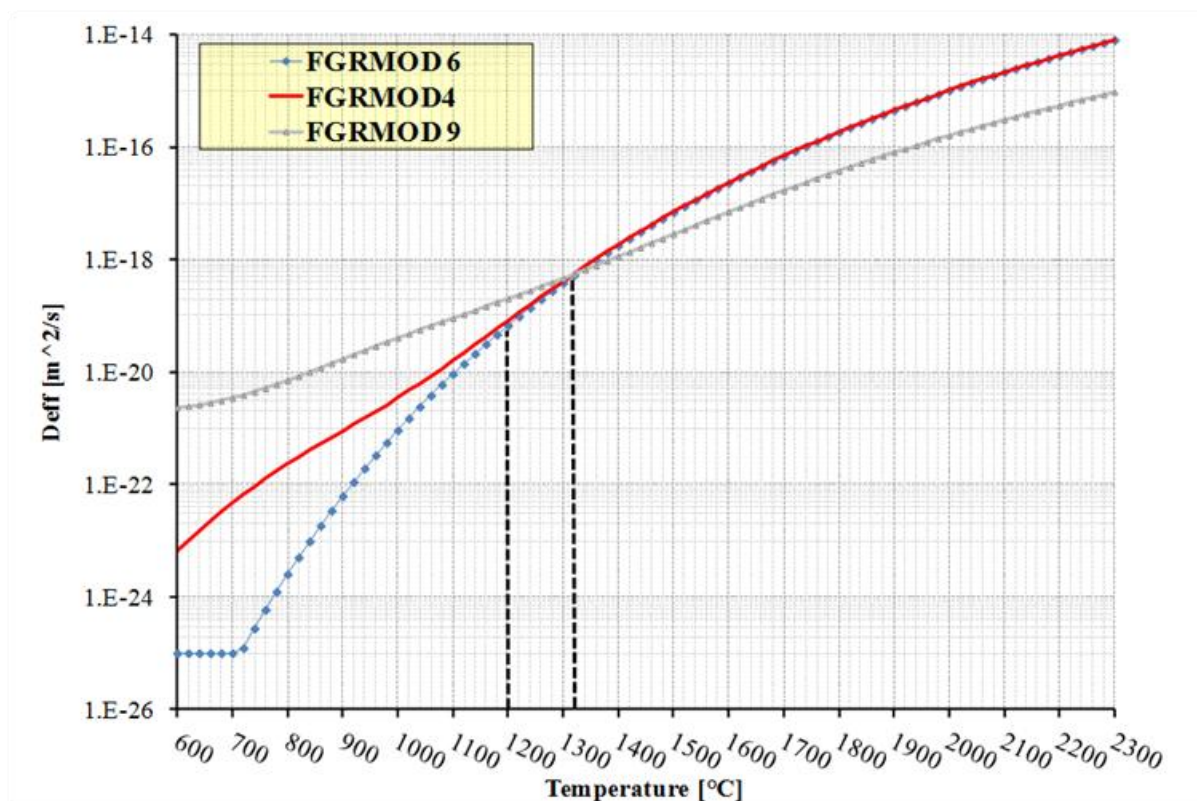
Fig. 59 – IFA-597, sensitivity analysis on FGR, intra-granular diffusion coefficients.
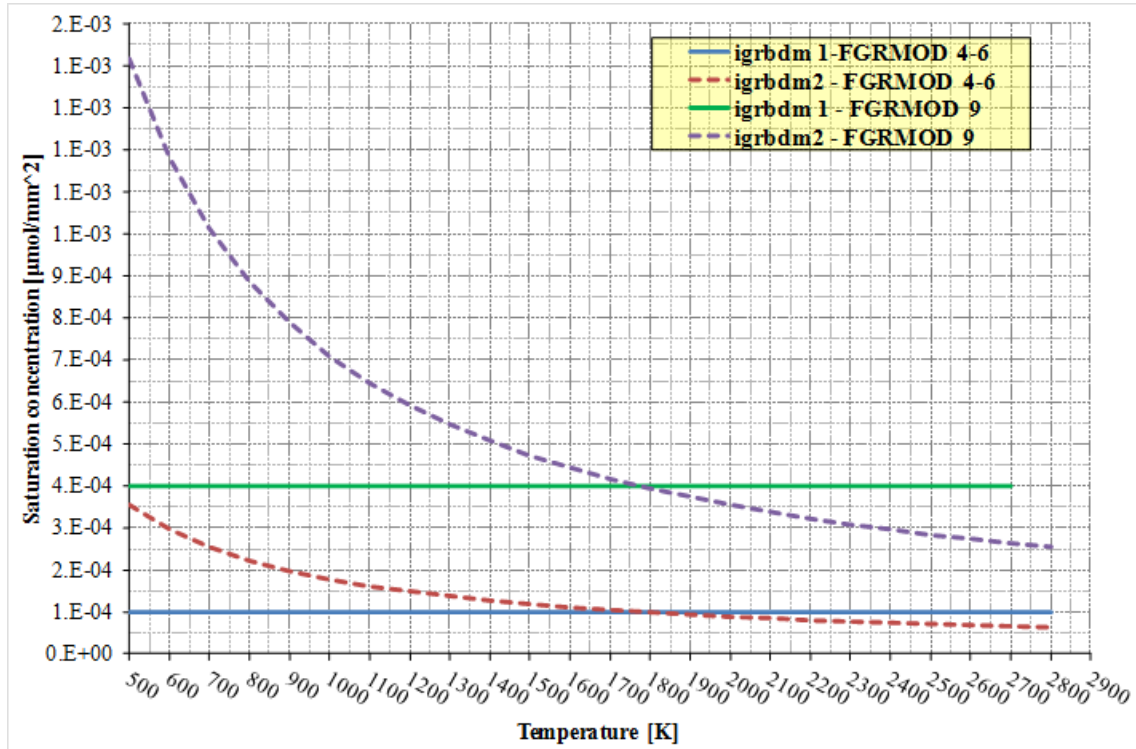
Fig. 60 – IFA-597, sensitivity analysis on FGR models, gas saturation concentration to release from grain boundaries.
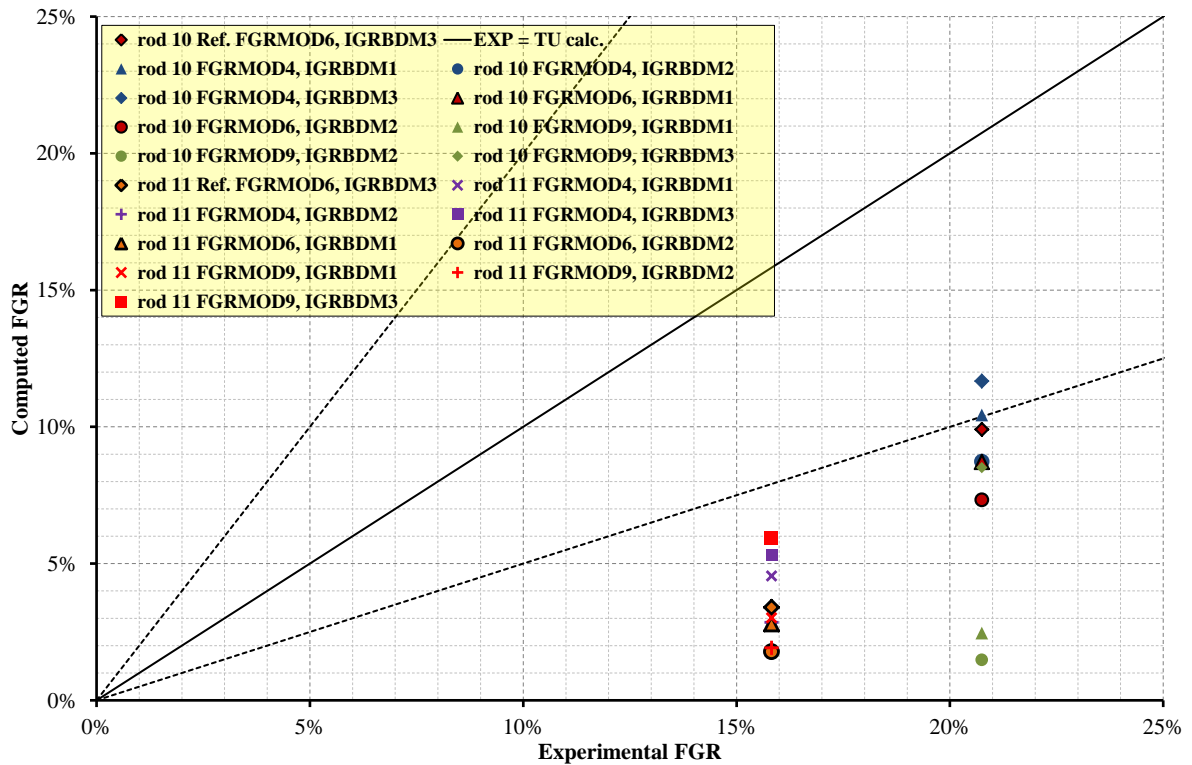
Fig. 61 – IFA-597, rod 10 and rod 11, sensitivity analysis on FGR, final results.
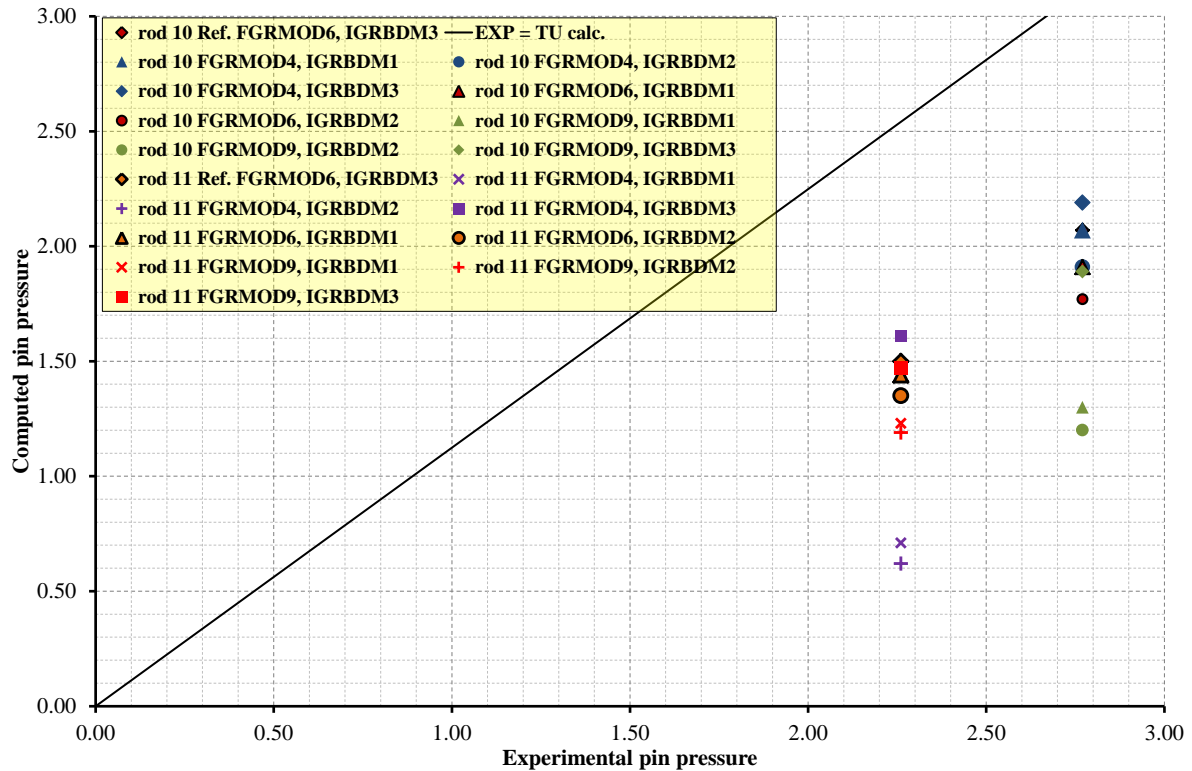
Fig. 62 – IFA-597, rod 10 and rod 11, sensitivity analysis on pin pressure, final results.

7.2.2 Assessment on fuel conductivity correlations (runs C1)

The thermal conductivity correlations addressed in this sensitivity analysis are described in section *5.2.2*. The reference correlation assumed in the simulation is the Van Uffelen and Schubert (best estimate), LAMBDA 31 that accounts for the influence of the local temperature, the local burn-up, the local porosity and the HBS formation. According to section *5.2.2* and *Tab. 29,* it is assumed that:

- The correlation according to Carbajo et al is labeled as LAMBDA 32 (it accounts for the local temperature, the local burn-up, the local porosity and the HBS formation, the O/M, the dissolved and precipitated FPs and the radiation effects).
- The correlation of Lanning and Beyer is named LAMBDA 33 (it accounts for the local temperature, the local burn-up, the local porosity and the O/M).
- The correlation according to Wiesenack is labeled as LAMBDA 34 and (it was developed for UOx fuel and was reduced by a constant factor of 0.92 to accounts MA and FP effects in quasi spent fuel).
- The correlation of Van Uffelen and Schubert (conservative) is named LAMBDA 35 (it is identical to the reference correlation except for one fitting constant).

These correlations have been developed specifically for MOX fuel.

The results are reported in *Fig. B. 4* (Appendix B) and summarized in *Tab. 32* and *Tab. 33*.

The analysis of the results highlight that the conductivity correlation impacts on the fuel temperature up to 100°C for rod 10 and 150°C for rod 11, *Fig. B. 4 c)* and *d)*. In particular, the deviations increases at higher burn-ups and the main difference is observed during IFA-597.6. The highest temperature is predicted by LAMBDA 35 correlation (conservative formulation of the reference simulation LAMBDA 31). The lowest fuel temperature is predicted by LAMBDA34 correlation that was developed for UO_2 and corrected with a constant factor. The remaining correlations are close to the

reference analysis. The difference in temperature is reflected in the computed FGR and pin inner pressure accordingly, *Fig. B. 4 a), b), e)* and *f)*. The temperature difference impacts on the FGR of about +2/-4% in rod 10, -3/+3.5% in rod 11. The gap width is influenced by the fuel temperature mainly because of different fuel thermal expansion, *Fig. B. 4 c)* and *d)*. LAMBDA 35 predicts the thinnest gap while LAMBDA 34, the thickest one.

IFA-597 rod 10				
Sensitivity analysis C1 conductivity correlations				
RUN	FGR %	Error %	IP [MPa]	Error %
Experimental	**20.75**	**--**	**2.77**	**--**
Ref. LAMBDA 31	**9.91**	**-52.24**	**2.07**	**-25.27**
LAMBDA 32	8.32	-59.90	1.87	-32.49
LAMBDA 33	10.01	-51.76	2.03	-26.71
LAMBDA 34	5.71	-72.48	1.60	-42.24
LAMBDA 35	12.9	-37.83	2.28	-17.69

Tab. 32 – IFA-597, rod 10, sensitivity analysis on fuel conductivity correlations ,results and relative errors.

IFA-597 rod 11				
Sensitivity analysis C1 conductivity correlations				
RUN	FGR %	Error %	IP [bar]	Error %
Experimental	**15.82**	**--**	**2.26**	**--**
Ref. LAMBDA 31	**3.40**	**-78.51**	**1.50**	**-27.44**
LAMBDA 32	2.59	-83.82	1.42	-37.17
LAMBDA 33	3.68	-76.93	1.53	-32.30
LAMBDA 34	8.65	-45.51	1.24	-45.13
LAMBDA 35	7.51	-52.72	1.92	-15.04

Tab. 33 – IFA-597, rod 11 sensitivity analysis on fuel conductivity correlations ,results and relative errors.

7.2.3 Assessment on relocation models (runs M2)

The choice of the relocation model (see section 5.2.3) mainly influences the gap width between fuel pellet and cladding during the irradiation. The fuel temperature is consequently affected by the relocation model and, therefore, different FGR trends are observed. The reference model is the modified FRAPCON-3 model referred as IRELOC 8. It accounts for the tangential strain due to relocation depending on the as fabricated gap, the burn-up (two simple functions below and beyond 5 MWd/kgU), the linear heat rate (a simple function that applies in the range 20 kW/m < LHR <40kW/m). It does not consider the axial strain and it does not apply when gap is closed. According to section 5.2.3 and *Tab. 29*, it is assumed that:

- The model according to the original KWU-LWR is labeled as IRELOC 2. It accounts only for the as fabricated gap, it accounts for axial strain and it applies also when gap is closed.
- The model according to GAPCON-THERMAL-3 is referred as IRELOC 3. It accounts for the tangential strain due to relocation depending on the as fabricated gap, the burn-up (exponential function that saturates at 5MWd/kgU), the linear heat rate (a simple function). It does not consider the axial strain and it applies also when gap is closed.

- The modified KWU-LWR is labeled as IRELOC 5. It accounts only for the as fabricated gap, it accounts for tangential and axial strain and it applies also when gap is closed.

The results are reported in *Fig. B. 5* (Appendix B) and summarized in *Tab. 34* and *Tab. 35*.
The thinnest gap is predicted by model IRELOC3, *Fig. B. 5 b)* and *c)*. IRELOC 2 behaves similar to the reference model while IRELOC 5 predicts the largest gap. Not any model predicts the gap closure occurred during IFA-597.6. The predicted FGR is in agreement with the gap size: the larger is the gap, the larger is the centerline fuel temperature. Therefore, the FGR ranks in this way: IRELOC5 > IRELOC 2 > IRELOC 8 (ref.) > IRELOC 3 being IRELOC 5 close to the experimental FGR. On the other hands, this last model over-predicts the fuel temperature.

IFA-597 rod 10				
Sensitivity analysis M2: fuel relocation models				
RUN	**FGR %**	**Error %**	**IP [MPa]**	**Error %**
Experimental	**20.75**	**--**	**2.77**	**--**
Ref. IRELOC 8	**9.91**	**-52.24**	**2.07**	**-25.27**
IRELOC 2	11.10	-46.51	2.14	-22.74
IRELOC 3	5.13	-75.28	1.54	-44.40
IRELOC 5	15.71	-24.29	2.59	-6.50

Tab. 34 – IFA-597, rod 10, sensitivity analysis on relocation models, results and relative errors.

IFA-597 rod 11				
Sensitivity analysis M2: fuel relocation models				
RUN	**FGR %**	**Error %**	**IP [bar]**	**Error %**
Experimental	**15.82**	**--**	**2.26**	**--**
Ref. IRELOC 8	**3.40**	**-78.51**	**1.50**	**-27.44**
IRELOC 2	4.57	-71.30	1.65	-26.99
IRELOC 3	1.51	-90.64	1.27	-43.81
IRELOC 5	11.11	-29.96	2.33	3.10

Tab. 35 – IFA-597, rod 1, sensitivity analysis on relocation models, results and relative errors.

7.2.4 Assessment on fuel swelling correlations (runs C2)

The solid fission products are theoretically predicted to contribute to fuel swelling on the average by 0.032% per MWd/kgU. The contribution of gaseous fission products to fuel swelling includes rare gases such as krypton and xenon in solid solution and the volume change arising from the formation of fission gas filled bubbles. For the gases in solid solution and the small intra-granular gas bubbles, it is estimated that they furnish about 0.056% per MWd/kgU to matrix swelling rate. The inter-granular gas bubbles can make the largest contribution to volume change depending on temperature and their amount. Early studies indicated large bubbles of diameter around few microns on grain faces and also along grain edges. At high exposures and temperatures the bubbles interlink forming a tunnel network which concurrently leads to gaseous swelling and gas release.

Therefore, the choice of the swelling correlation directly affects the FGR, the fuel to cladding gap, and the fuel conductivity. The reference correlation adopted in the simulations was developed by Lassmann from the original MATPRO swelling correlation. It accounts for solid swelling as a linear function of the local burn-up and for gaseous swelling as function of local temperature, burn-up, pellet

local stress and diffusion coefficient. The correlations available in TRANSURANUS are described in details in 5.2.4. According to this section and *Tab. 29*, it is assumed that:

- The simple correlation gives the total swelling rate for UO$_2$ fuel including matrix swelling due to solid FP is labeled as SWELOC 18. It is a linear function of the local burn-up.
- The original MATPRO swelling model for UO$_2$ fuel is referred as SWELOC 19. It accounts for solid swelling as a linear function of the local burn-up and for gaseous swelling as function of local temperature and burn-up.
- The correlation proposed by Dienst et al. for FBR MOX fuel is referred as SWELOC 3. It accounts for solid and gaseous swelling as two linear functions of the local burn-up. Gaseous swelling is zero if the gap is closed.
- The correlation proposed by by Pesl et al. for FBR MOX fuel is referred as SWELOC 11. It accounts for solid and gaseous swelling as two linear functions of the local burn-up. Gaseous swelling is zero if the gap is closed.
- The correlation by Dienst et al. recommended for FBR MOX fuel is labeled as SWELOC 13. It accounts for solid and gaseous swelling as two linear functions of the local burn-up. Gaseous swelling is zero if the gap is closed.
- SWELOC 21 is the implicit formulation of the reference correlation.

Only SWELOC18, SWELOC19, SWELOC21 are here discussed; SWELOC3, SWELOC11, SWELOC12 and SWELOC13 are developed to model swelling in FBR and are not suitable for this simulation. The results are reported in *Fig. B. 6* (Appendix B) and summarized in *Tab. 36* and *Tab. 37*.

In the simulation of rod 10, SWELOC 19 predicts the thinnest gap during IFA-597.4 and IFA-597.5, *Fig. B. 6 c)* and *d)*. During IFA-597.6, the thinnest gap is predicted by the reference correlation SWELOC20. SWELOC 18 the largest gap size, it is close to SWELOC 19. SWELOC 18 overestimates the fuel temperature due to the large gap computed in the first 6000 hrs causing high FGR. After that time, the larger FGR achieved influences the rest of the simulation through a thermal positive feedback process. At the end of the simulation, the FGR predicted by this model is the highest and it is close the experimental value, *Fig. B. 6 a)* and *b)*. SWELOC 19 predicts fuel temperatures very close to the reference case for most of the simulation while predicts higher temperature during IFA-597.6. It results in high FGR; the final value is similar to the experimental FGR. The pressure varies according to FGR; highest pin inner pressurization is predicted by SWELOC 18 and SWELOC 19, *Fig. B. 6 e)* and *f)*. SWELOC 21 is equal to the reference correlation.

The selection of the fuel swelling correlation has negligible impact on the simulation of rod 11.

IFA-597 rod 10				
Sensitivity analysis C2: fuel swelling correlations				
RUN	FGR %	Error %	IP [MPa]	Error %
Experimental	**20.75**	**--**	**2.77**	**--**
Ref. SWELOC 20	**9.91**	**-52.24**	**2.07**	**-25.27**
SWELOC18	20.91	+0.72	3.06	+10.47
SWELOC19	16.32	-21.35	2.60	-6.14
SWELOC21	9.42	-54.60	1.97	-28.88

Tab. 36 – IFA-597, rod 10, sensitivity analysis on swelling model, results and relative errors.

IFA-597 rod 11				
Sensitivity analysis C2: fuel swelling correlations				
RUN	FGR %	Error %	IP [bar]	Error %
Experimental	**15.82**	**--**	**2.26**	**--**
Ref. SWELOC 20	**3.40**	**-78.51**	**1.50**	**-27.44**
SWELOC18	3.43	-78.32	1.50	-33.63
SWELOC19	3.21	-79.71	1.48	-34.51
SWELOC21	3.39	-78.57	1.50	-33.63

Tab. 37 – IFA-597, rod 11, sensitivity analysis on swelling model, results and relative errors.

7.2.5 Assessment on fuel densification models (runs M3)

Densification process occurs at the beginning of the fuel irradiation; it leads to the destruction of fabricated porosity.

The IDENSI2 model is a simple empirical model suitable for both LWR and FBR; it is the standard TRANSURANUS densification model. The IDENSI7 model is the original MATPRO model and considers both densification and hot pressing phenomena[76]. However, as said in the TU manual[8] IDENSI7 is not fully tested and its results should be taken with care.

The results are reported in *Fig. B. 7* (Appendix B), and summarized in *Tab. 38* and *Tab. 39*. As shown in *Fig. B. 7* c) and d) IDENSI7 predicts the thinnest gap width between fuel and cladding during the whole simulations. It explains the lower fuel temperature and lower FGR / pin pressurization, *Fig. B. 7* a), b), e) and f). In the sensitivity analysis, rod 10 experiences gap closure during IFA-597.6. Therefore, the fuel temperature is well captured during IFA-597.6 (even if it is underestimated in the other phases and the associated FGR is further underestimated).

IFA-597 rod 10				
Sensitivity analysis M3: densification models				
RUN	FGR %	Error %	IP [MPa]	Error %
Experimental	**20.75**	**--**	**2.77**	**--**
Ref. IDENSI 2	**9.91**	**-52.24**	**2.07**	**-25.27**
IDENSI 7	2.60	-87.47	1.28	-53.79

Tab. 38 – IFA-597, rod 10, sensitivity analysis on densification model, results and relative errors.

IFA-597 rod 11				
Sensitivity analysis M3: densification models				
RUN	**FGR %**	**Error %**	**IP [bar]**	**Error %**
Experimental	**15.82**	**--**	**2.26**	**--**
Ref. IDENSI 2	**3.40**	**-78.51**	**1.50**	**-27.44**
IDENSI 7	0.5	-96.84	1.23	-45.58

Tab. 39 – IFA-597, rod 11, sensitivity analysis on densification model, results and relative errors.

7.2.6 Assessment on Helium release model (runs M4)

Helium generation and release from the fuel matrix is a peculiar characteristic of the MOX fuel. It contributes to inner pin pressurization but, on the other hand, mitigates the effect of gap poisoning. TU-code can compute the Helium diffusion and release similarly to ordinary FGR. Three different diffusion coefficients are available: iHe = 1 and iHe = 2 according to Federici et al. (data fit and lower limit respectively) and iHe = 3 according to Ronchi at al. A detailed description of Helium diffusion and release models in TU-code is reported in chapter 5.2.9.

This analysis aims to assess the impact of Helium release models on fuel temperature, inner pin pressure and FGR. The results are reported in *Fig. B. 8*, (Appendix B) and *Tab. 40* and *Tab. 41*. The selection of the Helium release models doesn't affect pin pressurization and FGR in both rods. This is due to the state of development of the Helium release model which is still not connected to pin pressurization and total gas release. The Ronchi et al. model (iHe = 3) predicts the highest Helium release (~55%). The Federici standard model (iHe = 1) predicts similar release (~50%). The lowest release (~30%) is computed by the Federici lower limit model (iHe = 2).

IFA-597 rod 10				
Sensitivity analysis M4: Helium release model				
RUN	**FGR %**	**Error %**	**IP [MPa]**	**Error %**
Experimental	**20.75**	**--**	**2.77**	**--**
Ref. iHe = 0	**9.91**	**-52.24**	**2.07**	**-25.27**
iHe = 1	9.91	-52.24	2.07	-25.27
iHe = 2	9.90	-52.35	2.07	-25.27
iHe = 3	9.90	-52.35	2.07	-25.27

Tab. 40 – IFA-597, rod 10, sensitivity analysis on Helium release model, results and relative errors.

IFA-597 rod 11				
Sensitivity analysis M4: Helium release model				
RUN	**FGR %**	**Error %**	**IP [bar]**	**Error %**
Experimental	**15.82**	**--**	**2.26**	**--**
Ref. iHe = 0	**3.40**	**-78.51**	**1.50**	**-27.44**
iHe = 1	3.40	-78.51	1.50	-27.44
iHe = 2	3.40	-78.51	1.50	-27.44
iHe = 3	3.40	-78.51	1.50	-27.44

Tab. 41 – IFA-597, rod 11, sensitivity analysis on Helium release model, results and relative errors.

7.2.7 Assessment on fabricated density (runs D1)

The fuel density indirectly affects the FGR since it influences the fuel conductivity and, therefore, the fuel temperature profile. The database reports the nominal density without its tolerance. It has been assumed as +/- 1% TD.

Density maximization generally increases the fuel conductivity and therefore it reduces the FGR. Opposite conclusions can be drawn for density minimization. The FGR trends for maximum and minimum density are compared with the reference density in *Fig. B. 9* (Appendix B). FGR and inner pin pressure are summarized in *Tab. 42* and *Tab. 43*.

Significant effect of the porosity is observable in the fuel temperature trends, *Fig. B. 9 c)* and *d)*. The high porosity at the beginning of the simulation favors high fuel temperature causing FGR. At the end of the densification process, even if the fabrication porosity is reduced, the thermal feedback induced by FGR in combination with relocation and swelling (that affects the gap width) influence the fuel temperature increasing or decreasing the amount of gas released. This considerations apply both for rod 10 and rod 11.

IFA-597 rod 10				
Sensitivity analysis D1: fabrication density				
RUN	**FGR %**	**Error %**	**IP [MPa]**	**Error %**
Experimental	**20.75**	**--**	**2.77**	**--**
Ref. POR000 = 0.0414	**9.91**	**-52.24**	**2.07**	**-25.27**
POR000 = 0.0314	4.90	-76.39	1.49	-46.21
POR000 = 0.0514	14.23	-30.99	2.46	-11.19

Tab. 42 – IFA-597, rod 10, sensitivity analysis on initial porosity, results and relative errors.

IFA-597 rod 11				
Sensitivity analysis D1: fabrication density				
RUN	**FGR %**	**Error %**	**IP [bar]**	**Error %**
Experimental	**15.82**	**--**	**2.26**	**--**
Ref. POR000 = 0.0414	**3.40**	**-78.51**	**1.50**	**-27.44**
POR000 = 0.0314	0.96	-93.99	1.28	-43.36
POR000 = 0.0514	9.69	-38.57	2.11	-6.64

Tab. 43 – IFA-597, rod 11, sensitivity analysis on initial porosity, results and relative errors.

7.2.8 Assessment on grain size (runs D2)

As porosity at the end of the sintering, grain size is usually an uncertain parameter since it is usually given as average value. This means that the data are representative of the ideal situation in which the grain size is uniform in the pellet volume and do not account for local deviations that are dependent from the fabrication process. Grain size has two main effects. Firstly, the larger is the grain, the larger is the diffusion distance for the fission gas atoms created in the grains. This tends to reduce the release rate. Secondly, the larger is the grain, the lower is the capacity of the grain boundaries to store fission gas as their total surface-to-volume ratio is decreasing. In despite of this, for steady state conditions FGR is low (1-2%) and dominated by the process to saturate the grain boundaries, and therefore, it can be concluded that FGR cannot be strongly dependent on the grain size. On the other hand, during power ramps, these opposite contributions may affect the FGR together with micro-cracking of the grain boundaries that is more or less a stochastic phenomenon. Even after 50 years of testing the contribution of these three mechanisms to FGR during power ramp is still controversial: some of the experiments highlight largest release from small grains and some other highlight opposite results.

Rods 10 and 11 have small initial grain size (5.5 µm m.l.i.). According to the benchmark specifications, it has been assumed a maximum grain size is of 6.6 µm and a minimum of 4.3 µm. The results are shown in *Fig. B. 10* (Appendix B) and summarized in *Tab. 44* and *Tab. 45*. Smaller grains lead to higher FGR and vice versa; this behavior is observed in both rods *Fig. B. 10 a), b), e) and f)*. While grain size minimization has a big impact on FGR and inner pin pressure, grain maximization provides results close to the reference analysis. Minimizing the grain size, the fuel temperature is over predicted, *Fig. B. 10 c), d)*.

IFA-597 rod 10				
Sensitivity analysis D2: grain size				
RUN	FGR %	Error %	IP [MPa]	Error %
Experimental	**20.75**	**--**	**2.77**	**--**
Ref. DKORN = 5.5	**9.91**	**-52.24**	**2.07**	**-25.27**
DKORN = 6.6	6.31	-69.59	1.67	-39.71
DKORN = 4.3	16.02	-22.80	2.58	-6.86

Tab. 44 – IFA-597, rod 10, sensitivity analysis on average grain size, results and relative errors.

IFA-597 rod 11				
Sensitivity analysis D2: grain size				
RUN	FGR %	Error %	IP [bar]	Error %
Experimental	**15.82**	**--**	**2.26**	**--**
Ref. DKORN = 5.5	**3.40**	**-78.51**	**1.50**	**-27.44**
DKORN = 6.6	1.50	-90.52	1.31	-42.04
DKORN = 4.3	10.31	-34.83	2.23	-1.33

Tab. 45 – IFA-597, rod 11, sensitivity analysis on average grain size, results and relative errors.

7.2.9 Assessment on initial gap width (runs D3)

The gap size affects its conductance and, consequently, it influences the temperature drop across the gas zone and the maximum temperature in the fuel. The higher is the gap size, the higher is the fuel temperature. High fuel temperature has two effects: it promotes FGR that further reduces the gap conductance (since Xe and Kr have lower conductivity that He) and it promotes gap closure because of enhanced gaseous swelling and fragment relocation.

In this analysis the effect of the gap initial size has been assessed. The gap tolerances are not given in the benchmark specifications; it has been assumed a ±0.01 mm; the gap initial width is varied in the range [0.08-0.10 mm].

Gap maximization generally increases the FGR and the pin pressurization. Opposite conclusions can be drawn for gap minimization. The computed trends are reported in *Fig. B. 11* (Appendix B) and *Tab. 46*, *Tab. 47*. In rod 10 the initial gap width impacts the FGR for about ±3% respect to the reference simulation. In rod 11, if thinner gap is assumed, FGR is predicted below 1% while if larger gap is assumed, the FGR is significant during IFA-597.6; the thermal feedback due to gas poisoning causes high fuel temperatures and the gap reduces even below the simulation with minimum initial gap because of differential thermal expansion between fuel pellets and cladding.

IFA-597 rod 10				
Sensitivity analysis D3: gap width				
RUN	FGR %	Error %	IP [MPa]	Error %
Experimental	**20.75**	**--**	**2.77**	**--**
Ref. gap = 0.09 mm	**9.91**	**-52.24**	**2.07**	**-25.27**
gap = 0.08 mm	6.26	-69.83	2.34	-15.52
gap = 0.10 mm	13.05	-37.11	1.65	-40.43

Tab. 46 – IFA-597, rod 10, sensitivity analysis on gap width, results and relative errors.

IFA-597 rod 11				
Sensitivity analysis D3: gap width				
RUN	FGR %	Error %	IP [bar]	Error %
Experimental	**15.82**	**--**	**2.26**	**--**
Ref. gap = 0.09 mm	**3.40**	**-78.51**	**1.50**	**-27.44**
gap = 0.08 mm	1.17	-92.60	1.88	-16.81
gap = 0.10 mm	6.71	-57.59	1.28	-43.36

Tab. 47 – IFA-597, rod 10, sensitivity analysis on gap width, results and relative errors.

7.2.10 Assessment on initial free volume (runs D4)

The total pin free volume mainly affects the gas composition in the gap between fuel and cladding; large volumes mitigate the positive feedback effect of FGR. In addition, when FGR occurs, higher free volume damps the pressure increase and vice versa. The free volume maximization and minimization are obtained increasing and decreasing the upper plenum length by 10 mm. Free volume maximization generally decreases the FGR and the pin pressurization. Opposite conclusions can be drawn for its minimization. The computed trends are reported in *Fig. B. 12*. The final results are summarized in *Tab. 48* and *Tab. 49* for rod 10 and 11 respectively. The main effect is observed in rod 10 where the FGR varies of 2% respect to the reference result. In rod 11 the impact on FGR is negligible because of the presence of the central void.

IFA-597 rod 10				
Sensitivity analysis D4: free volume				
RUN	FGR %	Error %	IP [MPa]	Error %
Experimental	**20.75**	**--**	**2.77**	**--**
Ref. free volume = 2.6 ccm	**9.91**	**-52.24**	**2.07**	**-25.27**
Free volume = 2.1 ccm	12.1	-41.69	2.68	-3.25
Free volume = 3.1 ccm	8.55	-58.80	1.67	-39.71

Tab. 48 – IFA-597, rod 10, sensitivity analysis on free volume, results and relative errors.

IFA-597 rod 11				
Sensitivity analysis D4: free volume				
RUN	FGR %	Error %	IP [bar]	Error %
Experimental	**15.82**	**--**	**2.26**	**--**
Ref. free volume = 2.8 ccm	**3.40**	**-78.51**	**1.50**	**-27.44**
Free volume = 2.3 ccm	4.33	-72.63	1.86	-17.70
Free volume = 3.3 ccm	2.94	-81.42	1.33	-41.15

Tab. 49 – IFA-597, rod 11, sensitivity analysis on free volume, results and relative errors.

8 Conclusions

The aim of this activity is to assess the capabilities of TRANSURANUS code version 2012 in simulating MOX fuel rods subjected normal operation and power ramp with particular focus on the FGR phenomenon. The datasets adopted for the calculation consist of rod BD8 from the PRIMO MOX Experimental Program and IFA-597. These databases are included in the IFPE database and have been released by the OECD-NEA in the framework of MOX fuel performance benchmarking activities.

In the following, separated conclusions are reported for each database distinguishing between the reference calculation and the sensitivity analysis. The reference calculations model the gas intra-granular diffusion coefficient according to Matzke for the thermal part and to a constant for the a-thermal part. The inter-granular behavior is modeled according to the modified Koo model specifically developed for fast power ramps.

PRIMO Experiment rod BD8
The experiment consists of a base irradiation in the BR-3 reactor up to 30 MWd/kgHM with average linear power of 19 kW/m and a power ramp test in the OSIRIS reactor characterized by ramp rate of 460 kW/m-h and ramp terminal level at axial peak of 39.5 kW/m.

The reference analysis brings to the following conclusions:

- Burn-up analysis: the simulations highlight excellent agreement with the experimental trends: no significant error is observed. It suggests that power-history and power axial shape are correctly modeled.
- FGR analysis: the simulation can be divided in base irradiation and power ramp phases.
  - During the base irradiation the FGR remains low and the final value is in good agreement with respect to the experimental data. This suggests that the fuel temperature is correctly estimated even if the fuel temperature during the experiment was not measured (rod BD8 was not instrumented).
  - The ramp phase is characterized by high fuel temperatures (in the order of 2000°C) and considerable FGR is expected to occur. High temperature enhances gas diffusion inside grains and the fast power increase at the beginning of the ramp test can cause micro-cracking that also favors FGR. The reference simulation predicts 7.65% that is 30% under-estimated compared to the PIE measurement (11.23%). Nevertheless, this result is well within the acceptability lower band (-50%).
- Grain size analysis: only the radius at which the grain growth phenomenon is observed and the mean grain size in that region are given in the database. The simulations qualitatively fit the experimental trends.
- Deformation analysis: cladding and fuel column length change and cladding diameter creep down were measured after base irradiation. TU code over-predicts the fuel shortening and slightly underestimates the cladding elongation. Nevertheless, these measured quantities are affected by large uncertainties. The cladding creep down is in good agreement with the experiment.

Extensive sensitivity analysis has been conducted to assess the code capabilities, the main results can be summarized as follows:

- If the standard and the temperature dependent inter-granular models are applied (assuming the reference intra-granular model), the FGR is further underestimated. This is connected to the fact that no "step" release is possible with those models.
- The intra-granular thermal diffusion according to Matzke and a-thermal diffusion according to White and Tucker generally predicts higher FGR. Nevertheless, it remains under-predicted if the standard and the temperature dependent inter-granular models are applied and it becomes over-predicted if the Koo model is selected.
- The intra-granular thermal diffusion according to Turnbull has two distinct effects. It tends to reduce the FGR if the standard and the temperature dependent inter-granular models are applied (because of the huge grain boundaries capacity respect to other models) and it becomes largely over-predicted if the Koo model is selected (if ramp conditions are met, all the gas stored in grain boundaries is released).
- Fuel conductivity correlations affect the FGR. Among the correlations available for MOX fuel, the reference correlation according to ITU fitted to experimental data by Duriez at al. causes FGR under-prediction. The same correlation in its conservative form provides FGR in excellent accordance to measured value.
- Swelling and relocation models mainly affect gap width and doesn't have strong influence on FGR because most of the release occurs during the power ramp when the gap between fuel pellets and cladding is closed.
- The MATPRO densification model impacts on FGR because it affects both the gap size and fuel porosity. High fuel porosity causes a decrease in fuel conductivity and cause higher fuel temperature and gas release. The MATPRO model predicts higher porosity at the end of the base irradiation; it enhances fuel temperature during the power ramp increasing the FGR.
- Fuel fabrication porosity and gap size (modeled according their design tolerances), impact on FGR mainly in the base irradiation and has a minor in the influence during the power ramp.
- Grain size analysis revealed slight influence on FGR of this parameter within ±25% its average value: FGR increase is observed with small grains and vice versa.

IFA-597

This dataset consists of two rods, labeled rod 10 (equipped mainly with solid pellets), and rod 11 (equipped with hollow pellets only). The experiment consists of four cycles of irradiation named IFA-597.4, .5 , 6, 7. They took place in the Halden HBWR. The linear power was in the range 15 – 35 kW/m. The final burn-up was about 35 MWd/kgMOX. The power histories are given only for the first three power cycles.

The reference analysis brings to the following conclusions:

- <u>Burn-up analysis</u>: the simulations highlight excellent agreement with the experimental trends: no significant error is observed. It suggests that rods' geometry, power-history and power axial shape are correctly modeled.
- <u>Fuel temperature analysis</u>: the fuel temperature was measured during the experiment by means of thermocouples inserted in the pellets hole at the top of both rods.
    - o <u>Rod 10</u>: fuel temperature is correctly predicted by the code until the end of IFA-597.5. During IFA-597.6, the experimental data suggest that gap closure occurred while the code predicts open gap. The fuel temperature is therefore overestimated.
    - o <u>Rod 11</u>: fuel temperature is underestimated during the first cycle IFA-597.4 of about 50°C. During IFA-597.5 the code prediction is in good accordance with the measurements while in the last cycle IFA-597.6 it is overestimated of about 150°C due to the same reason reported for rod 10.

- Inner rod pressure analysis: rods' internal pressure was measured by means of bellow type pressure transducers. They were accommodated in the lower plenum of both the rods and provided pressure measurements during the whole irradiation time.
  - Rod 10: pin pressure is well captured during IFA-597.4 and slightly underestimated during IFA-597.5. Because of the 50% under-prediction of the FGR, pressure is underestimated during the last cycle. The under-estimation is mainly due to the pressure burst that occurred at 12000 hrs caused by a large gas release; the code doesn't predicts a so large burst even if the modified Koo model is selected.
  - Rod 11: rod inner pressure is overestimated at the beginning of the simulation. It suggests that the initial free volume is not exactly consistent with the real design. The measurements show fission gas pressurization of the pin since the end of IFA-597.4 while the simulation doesn't predict any significant release until the beginning of IFA-597.6. The pressure burst is observed similarly to rod 10 and underestimated.
- FGR analysis: the fractional gas release is computed based on pressure measurements in combination with free volume estimation during the experiment. The final values of FGR are obtained correcting the estimation on the basis on PIE.
  - Rod 10: TU code underestimates the FGR of about 50%. The estimated FGR is 21 % while the simulation provides 9.9%.
  - Rod 11: The simulation predicts FGR in the order of 4% while the estimated FGR is four times greater.

Extensive sensitivity analysis has been conducted to assess the code capabilities, the main results can be summarized as follows:

- If the standard and the temperature dependent inter-granular models are applied (assuming the reference intra-granular model), no main difference is observed in the fuel temperature behavior. FGR and pin pressure are similar to the reference simulations for both rods.
- The intra-granular thermal diffusion according to Matzke and a-thermal diffusion according to White and Tucker predicts slightly higher FGR than the reference model.
- The intra-granular thermal diffusion according to Turnbull underestimates the FGR.
- Fuel conductivity correlations affect the fuel temperature. Among the correlations available for MOX fuel, the reference correlation according to ITU fitted to experimental data by Duriez at al. predicts the fuel temperature correctly except in the last part of the simulation and cause FGR under-prediction. The same correlation in its conservative form provides higher FGR, but, on the other hand, it over-predicts fuel temperature. Other correlations tested are consistent with the reference one.
- Swelling and relocation models mainly affect gap width. Only rod 10 is sensitive to the selection of fuel swelling and relocation models. Models that predicts larger gaps, provide higher fuel temperature, FGR and pin pressurization and vice versa.
- The MATPRO densification model impacts on fuel temperature and FGR because it affects mainly the gap size. It predicts smaller gap and therefore, lower fuel temperature and FGR respect to the reference simulations.
- Helium release models have no influence on fuel temperature, pin pressure and FGR in the simulations, this is due to code limits.
- Fuel fabrication porosity impacts on FGR because it affects fuel temperature through increasing or decreasing the conductivity. Higher porosity causes a significant temperature increase and vice-versa. FGR varies accordingly.
- The gap initial size influences the thermal resistance of the gap. Its increase causes temperature increase and vice-versa. Fuel temperature has a feedback effect on FGR and therefore on pin

internal pressure. Larger gap simulations provide results on FGR that are in good agreement with experimental evidence; however they cause fuel temperature overestimation in both rods.

- Grain size analysis is based on the design uncertainty on this parameter. It revealed that smaller grains retain less fission gas than bigger ones. It is reflected on the simulations where good agreement with the experimental data is observed in both rods, if smaller grains are assumed. However, the FGR thermal feedback leads to fuel temperatures overestimation.

In conclusion, the TRANSURANUS code version 2012 highlights good capability to simulate rod BD8 from the PRIMO Experiment. The FGR phenomenon, its connected processes and phenomena and the dimensional change are captured well within their acceptability margin.

The simulation of rod 10 from the IFA-597 Experiment is considered sufficiently satisfactory since the code captures the fuel temperature trend for the main part of the irradiation and under predicts the FGR with an error that matches the acceptability lower band (-50%). The code has limited capability to simulate the hollow pellet rod 11: the fuel temperature is well captured excepts in the last phase of the experiment while, the FGR and consequently the pressurization, are largely underestimated. Should be mentioned that IFA-597 was planned to irradiate the two rods up to around 60 MWd/kgMOX but, due of excessive inner pressure build-up caused by high un-expected FGR, it was interrupted at 33 MWd/kgMOX.

REFERENCES

[1]   *OECD NEA/CSNI/R,* **Fuel Safety Criteria in Member Countries: Compilation of Responses Received from NEA Member Countries**. Paris, July 2003.

[2]   *P. Van Uffelen,* **Contribution to the Modeling of Fission Gas Release in Light Water Reactor Fuel**. PhD Thesis, Nuclear engineering, University of Liege, 2002.

[3]   *IAEA* **Status and Advances in MOX Fuel Technology**. technical report number 415, Vienna 2003.

[4]   *Carbajo, J.J., Yoder, et al*. **A review of thermo-physical properties of MOX and UO₂ fuel**. Oak Ridge National Laboratory, ORNL/TM/351, 2000.

[5]   *Massih, Ali R*. **Models for MOX fuel behavior, a selective review**. SKI Report 2006,10, January 2006.

[6]   *Lassmann K.*, **TRANSURANUS: a fuel rod analysis code ready for use**, Journal of Nuclear Material 188 (1992) 295-302.

[7]   *Van Uffelen P.*, **Modeling of Nuclear Fuel Behavior**, **Publications Office,** JRC Publications, Report EUR 22321 EN, European Commission, 2006.

[8]   *Lassmann K., A. Schubert, P. Van Uffelen, Cs. Gyory, J. van de Laar*, **Transuranus Handbook Version "v1m1j06"**, EC, JRC, ITU, July 2012.

[9]   *OECD/NEA*, **The Public Domain Database on Nuclear Fuel Performance Experiments for the Purpose of Code Development and Validation, International Fuel Performance Experiments (IFPE)**. http://www.nea.fr/html/science/fuel/ifpelst.html.

[10]   *L.J. Ott*, **Mixed-oxide (MOX) fuel performance benchmark** - summary of the results for the PRIMO MOX rod BD8, OECD, 2009.

[11]   *Tolonen, P., Pihlatie, M., Fujii, H*. **The MOX fuel behavior test IFA597-4/5/6;Thermal and gas release data to a burn-up of 25 MWd/kgMOX**. HWR-652, OECD Halden Reactor Project, February 2001.

[12]   *Tverberg, T*. **Mixed-oxide (MOX) Fuel Performance Benchmark, Summary of the Results for the HRP MOX rods.** OECD Halden Reactor Project.

[13]   *World Nuclear Association* **Mixed Oxide (MOX) Fuel.** http://www.world-nuclear.org

[14]   *Provost, J.L., Schrader, M., Nomura, S*. **MOX fuel fabrication and utilization in LWRs worldwide**. ibid., pp. 29–37.

[15]   *Adamson, M.G., Aitken, E.A., Caputi, R.W*. **Experimental and thermodynamic evaluation of the melting behavior of irradiated oxide fuels**. Journal of Nuclear Materials, Vol.130, 1985.

[16]   *Lippens M., et al*. **Comparative thermal behavior of MOX and UO2 fuels**. Thermal Performance of High Burn-up LWR Fuel (Proc. Sem. Cadarache, 1998), OECD, Paris (1998).

[17]   *Duriez, C., Alessandri, J.P., Servais, T., Philipponneau, Y*. **Thermal conductivity of hypostoichiometric low Pu content (U, Pu)O2–x mixed oxide**. J. Nucl. Mater. Vol. 277 (2000) pp. 143–158.

[18]   *Krebs, W.D., Goll, W*. **Operational performance of MOX fuel in light water reactors**. paper presented at ANS Winter Mtg, Albuquerque, 1997.

[19]   *Rossiter, G.D., Cook, P.M.A., Weston, R.* **Isotopic modelling using the ENIGMA-B fuel performance code**. ibid., pp. 227–238.

[20]   *Lippens, M., Maldague, T., Basselier, J., Boulanger, D., Mertens, L.* **Highlights on R&D work related to the achievement of high burnup with MOX fuel in commercial reactors**. MOX Fuel Cycle Technologies for Medium and Long Term Deployment (Proc. Symp. Vienna, 1999), C&S Papers Series No. 3/P, IAEA, Vienna (2000) 220–232.

[21]   *Bernard, L.C., Blanpain, P.* **Overall models and experimental database for UO2 and MOX fuel increasing performance**. ibid., pp. 291–304.

[22]   *Caillot, L., Delette, G., Piron, J.P., Lemaignan, C.* **Analytical studies of the behaviour of MOX fuel,.** Light Water Reactor Fuel Performance (Proc. ANS Int. Top. Mtg Portland, 1997), American Nuclear Society, La Grange Park, IL (1997) 62–69.

[23]   *Wiesenack, W., Mcgrath, M.* **Performance of MOX fuel: an overview of the experimental programme of the OECD Halden Reactor Project and review of selected results**. MOX Fuel Cycle Technologies for Medium and Long Term Deployment (Proc. Symp. Vienna, 1999), C&S Papers Series No. 3/P, IAEA, Vienna (2000) 253–262

[24]   *Freshley, M.D., Brite, D.W., Daniel, J.L., Hart, P.E.* **Irradiation-induced densification of UO$_2$ pellet fuel**. Journal of Nuclear Materials, 62, pp 138-166, 1976.

[25]   *Freshley, M.D., Brite, D.W., Daniel, J.L, Hart, P.E.* **Irradiation-induced densification and PuO$_2$ particle behavior in mixed-oxide fuel**. Journal of Nuclear Materials, 81, pp 63-92, 1979.

[26]   *Schubert, A., Györi, C., Elenkov, D., Lassmann, K., van de Laar*, *J.* **Analysis of Fuel Centre Temperatures with the TRANSURANUS Code.** International Conference on Nuclear Fuel for Today and Tomorrow – Experiences and Outlook, Würzburg (Germany), 16-19 March 2003.

[27]   *Weston, R., Palmer, I.D., Wright, G.M., Rossiter, G.D., Corcoran, R.C., Gilmour, T.C., Walker, C.T., Bremier*, *S.* **Progress on SBR MOX Fuel Development**. ENS International Topical Meeting - Nuclear Fuel: Development to Meet the Challenge of a Changing Market, Stockholm, 27-30 May, 2001.

[28]   *Wiesenack*, *W.* **Assessment of UO$_2$ Conductivity Degradation Based on In-pile Temperature Data**. Proceedings of the 1997 International Topical Meeting on LWR Fuel Performance, Portland, Oregon, March 2-6 (1997), p. 507.

[29]   *Stratton, R.W.* **Closing statement**. MOX Fuel Cycle Technologies for Medium and Long Term Deployment (Proc. Symp. Vienna, 1999), C&S Papers Series No. 3/P, IAEA, Vienna (2000) 531–534.

[30]   *White*, *R.J.* **Fission gas release**. HWR-632, OECD Halden reactor Project, 2000.

[31]   *Wiesenack, W. McGrath*, *M.* **Performance of MOX fuel: an overview of the experimental programme of the OECD Halden Reactor Project and review of selected results.** IAEA-SM-358/18, Symposium on MOX fuel cycle technologies for medium and long term deployment, Vienna, Austria, 1999, CSP-3/P, pp. 253-262.

[32]   *Kamimura, K., Kobayashi, Y., Nomata, T.* **Helium generation and release in MOX fuels**. MOX Fuel Cycle Technologies for Medium and Long Term Deployment (Proc. Symp. Vienna, 1999), C&S Papers Series No. 3/P, IAEA, Vienna (2000) 263–270.

[33]   *S. Djurle, et al.,* **The Super-Ramp Project, Final report of the Super-Ramp project**, STIR-32, Studsvik AB Atomenergi, Studsvik, Sweden, 1984.

[34] CEA, **Material Testing Reactors / The OSIRIS Reactor** *http://www.emtr.eu/osiris.html*

[35] *Nuclear Energy Directorate*, **OSIRIS nuclear reactors and service department**, Division for Nuclear Activities Saclay.

[36] *Takayki Nakano*, **The MOX fuel behavior test IFA-597.4.5.6.7**. Thermal and Gas Release Data, OECD HRP, June 2002.

[37] *IFE, OECD-HRP* **Halden Boiling Water Reactor**. Institutt for energiteknikk, Halden January 2003.

[38] *Turnbull, J.A.* **Fuel Behavior Data Available from IFE-OCDE Halden Project for Development and Validation of Computer Codes**. Review of Nuclear Fuel Experimental Data. OECD-NEA, 1995.

[39] *Mertens L., Lippens M., Alvis J.,* **The FIGARO programme: the behavior of irradiated MOX fuel tested in IFA-606 experiment**. description of the results and comparison with COMETHE calculation, Paper presented in EHPG meeting, Lillehammer, Norway, HPR-349, paper 30, March 2008.

[40] *Cayet, N.* **Investigation of Delayed Fission Gas Release**. HWR-488, May 1996.

[41] *P.T. Elton, K. Lassmann,* **Calculational methods for diffusional gas**. J. Nucl. Mater. 101 (1987) 259-265.

[42] *Hj. Matzke,* **Gas release mechanisms in UO$_2$-a critical overview**. Radiation Effects, 1980, Vol. 53, pp. 219-242.

[43] *D.M. Dowling, R.J. White and M.O. Tucker,* **The effect of irradiation-induced resolution on fission gas release**. J. Nucl. Mater. 110 (1982) 37-46.

[44] *P. Van Uffelen, A. Schubert, J. van de Laar, C. Győri,* **Development of a transient fission gas release model for TRANSURANUS**. Water Reactor Fuel Performance Meeting, October 19-23, Seoul, Korea, 2008.

[45] *D. R. Olander,* **Fundamental Aspects of Nuclear Reactors Fuel Elements**. Department of Nuclear Engineering University of California, Berkeley, 1976.

[46] *H. Bailly, D. Menessier, C. Prunier,* **The Nuclear Fuel of Pressurized Water Reactors and Fast Neutron Reactors**. Collection du Commissariat a l'Energie Atomique, Lavoisier Pub., Intercept, Paris, Andover, 1999.

[47] *R. J. White,* **The reduction of fission gas swelling through irradiation induced resolution**. OECD/NEA, pellet clad interaction in water reactor fuels, Seminar Proc., Aix-en-Provence, France, 2004.

[48] *OECD/NEA,* **Scientific Issues in Fuel Behavior**. Nuclear Science Committee, 1995.

[49] *A.H. Booth,* **A Method of Calculating Fission Gas Diffusion from UO$_2$ Fuel and its Application to the X-2-f Loop Test**. CRDC-721 (1957).

[50] *M.V. Speight,* **A calculation on the migration of fission gas in material exhibiting precipitation and resolution of gas atoms under irradiation**. Nucl. Science and Engineering 37 (1969) 180-185.

[51] *K. Forsberg, A.R. Massih,* **Diffusion theory of fission gas migration in irradiated nuclear fuel**. J. Nucl. Mater. 135 (1985)140-148.

[52] *R.J. White,* **A new mechanistic model for the calculation of fission gas release**. Proceedings of the 1994 International Topical Meeting on Light Water Reactor Fuel Performance, West Palm Beach, Florida (1994) 196-202.

[53] *J.A. Turnbull et al.,* **The diffusion coefficients of gaseous and volatile species during the irradiation of uranium dioxide**. J. Nucl. Mater. 107 (1982) 168-184.

[54] *R. Manzel, F. Sontheimer, H. Stehle,* **Fission gas release of PWR fuel under steady and transient conditions up to high burn-ups**. Light Water Reactor Fuel Performance, Orlando, Florida (1985), DOE/NE/34130-1, Volume 2, p. 4-33.

[55] *J.A. Turnbull,* **Presentation at the IAEA Research Coordination Meeting on Fuel Modeling at Extended Burn-up (FUMEX)**. 1-5 April 1996, Bombay, India.

[56] *C. Duriez, J. P. Alessandri, T. Gervais, Y. Philipponneau*, **Thermal conductivity of hypostoichio-metric low Pu content (U,Pu)O$_{2-x}$ mixed oxide**, Journal of Nuclear Materials 277 (2000) 143-158.

[57] *C. Ronchi*, **Annual Report of the European Institute for Transuranium Elements** Commission of the European Communities EUR 18715 EN (1998) .

[58] *J.J. Carbajo, G.L. Yoder, S.G. Popov, V.K. Ivanov*, **A review of the thermophysical properties of MOX and UO2 fuels**, Journal of Nuclear Materials 299 (2001) 181-198.

[59] *D.D. Lanning, C.E. Beyer*, **Proposed FRAPCON-3 MOX fuel thermal conductivity model compared to Halden fuel temperature data**, Enlarged Halden Programme Group Meeting on High Burn-up Fuel Performance, Safety and Reliability, StorefjellResort Hotel, Gol, Norway, 8-13 September 2002.

[60] *P.G. Lucuta et al*., Journal of Nuclear Materials 232 (1996) 166-180.

[61] *W. Wiesenack*, **Assessment of UO$_2$ Conductivity Degradation Based on In-pile Temperature Data**, Proceedings of the 1997 International Topical Meeting on LWR Fuel Performance, Portland, Oregon, March 2-6 (1997), p. 507.

[62] *W. Wiesenack, M. McGrath*, **Performance of MOX fuel: an overview of the experimental programme of the OECD Halden Reactor Project and review of selected results** (IAEA-SM-358/18), Symposium on MOX fuel cycle technologies for medium and long term deployment, Vienna, Austria, 1999, CSP-3/P, pp. 253-262.

[63] *Lassmann, H Blank,* **Modeling of fuel rod behavior and recent advances of TU code,** Nuclear Engineering and design 106(1988) 291-313 North-Holland, Amsterdam.

[64] *W. Dienst, I. Müller-Lyda, H. Zimmermann*, **Swelling, Densification and Creep of Oxide and Carbide Fuels under Irradiation**, Proc. Int. Conf. on Fast Breeder Reactor Fuel Performance, Monterey, California, March 5-8 (1979) 166.

[65] *R.Pesl et al.*, **SATURN-S: Ein Programmsystem zur Beschreibung des thermomechanischen Verhaltens von Kernreaktorbrennstäben unter Bestrahlung**, Kernforschungszentrum Karlsruhe, KfK 4272 (1987) 58.

[66] *H. Zimmermann*, **Investigations on Swelling and Fission Gas Behavior in Uranium Dioxide** Journal of Nuclear Materials 75 (1978) 154-161.

[67] *H. Assmann, H. Stehle*, **Thermal and In-reactor Densification of UO2: Mechanisms and Experimental Results**, Nucl. Eng. Des., 48 (1978), 49-67

[68] *Federici, E., Courcelle, A., Blanpain, P., Cognon, H.* **Helium production and behavior in nuclear fuelsduring irrdiation in LWR**. International LWR Fuel Performance Meeting, San Francisco, California, USA, September 30 - October 3 2007.

[69] *Ronchi, C., Hiernaut, J. P.* **Helium Diffusion in Uranium and Plutonium Oxides**. Journal of Nuclear Materials, Vol. 325, pp. 1-12, 2004.

[70] *K. Lassmann, C. O'Carroll, J. van de Laar, C.T. Walker,* **The radial distribution of plutonium in high burn-up UO$_2$ fuels**. J. Nucl. Mater. 208 (1994) p. 223.

[71] *D. G. Cacuci*, **Handbook of Nuclear Engineering**, Vol. 3

[72] *K. Lassmann, A. Moreno* **The Light-Water-Reactor Version of the URANUS Integral Fuel –Rod Code**; Atomkernenergie (ATKE) Bd. 30 (1977) p. 207-215.

[73] *Rozzia D., M. Adorni, A. Del Nevo, F. D'. Auria,* **Capabilities of TRANSURANUS Code in Simulating Power Ramp Tests from the IFPE Database,** Nucl. Eng. and Des. Issue, Vol. 241 pp. 1078–1086, 2011. Expanded paper from Int. Conf. of Nuclear Energy for New Europe (NENE) 2009.

[74] *Rozzia D., A. Del Nevo, M. Adorni, F. D'. Auria,* **Modeling of BWR Inter-Ramp Project Experiments by means of TRANSURANUS Code,** Annals of Nuclear Energy (2012) - Vol. 50 (2012) pp. 238–250.

[75] *Rozzia D., A. Del Nevo, M. Adorni, F. D'. Auria,* **Assessment of FGR in LWR Fuels Subjected to Power Ramps by TRANSURANUS Code, From the IFPE Database,** Proceeding of Int. Conf. of NENE 2011, September, 12-15, 2011, Bovec, Slovenia. Paper n°-903.

[76] *MATPRO-Version 11 (Revision 2)*, **A Handbook of Material Properties for Use in the Analysis of Light Water Reactor Fuel Rod Behavior**, NUREG/CR-0497 TREE-1280, Rev. 2, 1981.

[77] *Lee, B., et al.,* **Improvement of Fuel Performance Code COSMOS with Recent In-pile Data for MOX and UO2 Fuels**, Nuclear Technology, Vol. 157, pp. 53-64, 2007.

[78] *Mikityuk, K., A. Shestopalov and P. Fomichenko*, **Calculational Model for Fuel Rod Behavior Under Accident Conditions,** Preprint IAE-6144/5, Moscow, 1999.

[79] *White, R., et al.*, **Capabilities and Validation of the ENIGMA Fuel Performance Code**, International Topical Meeting on LWR Fuel Performance, Avignon, France, Vol. 2, p. 919, 1991.

[80] *Lanning, D., C. Beyer and C. Painter*, **FRAPCON-3: Modifications to Fuel Rod Material Properties and Performance Models for High-burn-up Application**, NUREG/CR-6534, October 1997.

[81] *Rashid, Y., R. Dunham and R. Montgomery*, **FALCON MOD01: Fuel Analysis and Licensing Code, Volume 1: Theoretical and Numerical Bases**, ANA-04-0666 Report, EPRI, Palto Alto, CA, and ANATECH Corp., San Diego, CA, 2004.

[82] *Suzuki, M.*, **Light Water Reactor Fuel Analysis Code FEMAXI-V (ver. 1)**, JAERI-Data/Code 2000.

[83] *Medvedev, A., S. Bogatyr and V. Kuznetsov*, **Code START-3: Initial Results of Blind Prediction of MOX Fuel Performance on Data Provided by the Halden Project**, Task Force on Reactor-based Plutonium Disposition, OECD/NEA, Paris, France, 2001.

APPENDIX A: PRIMO, Sensitivity analyses

A.1 Assessment of the impact of FGR models on FGR (runs M1)

Fig. A. 1 - PRIMO Program, rod BD8, sensitivity analysis on FGR models, FGRMOD4, BI
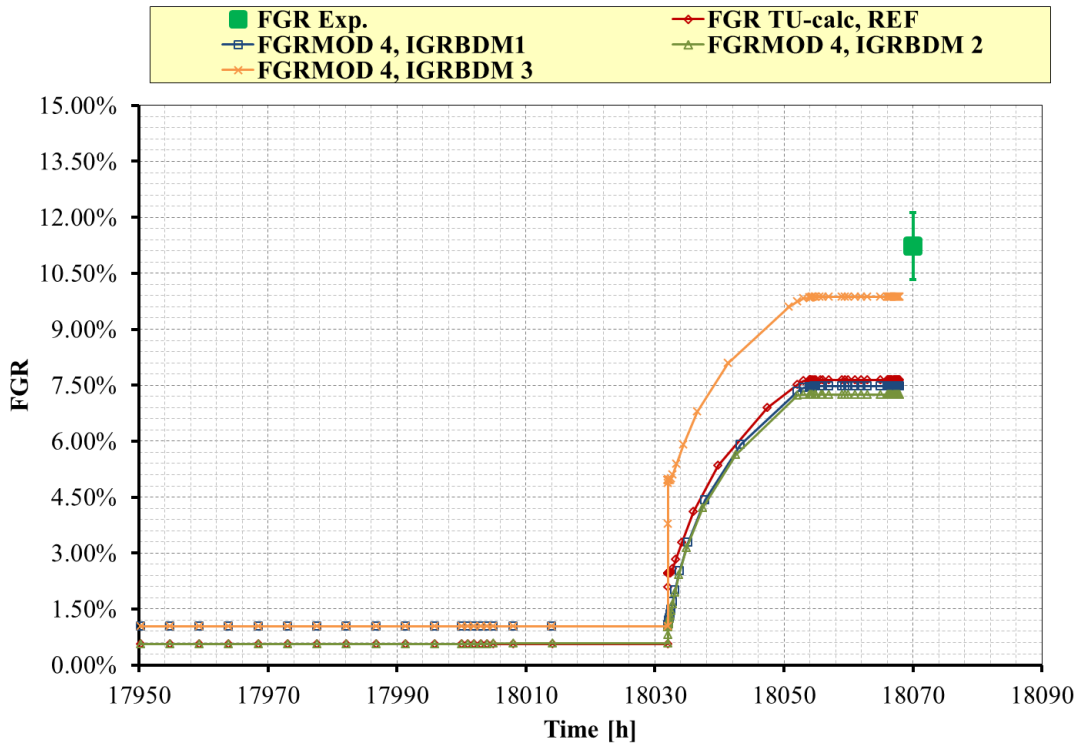
Fig. A. 2 - PRIMO Program, rod BD8, sensitivity analysis on FGR models, FGRMOD4, PR.
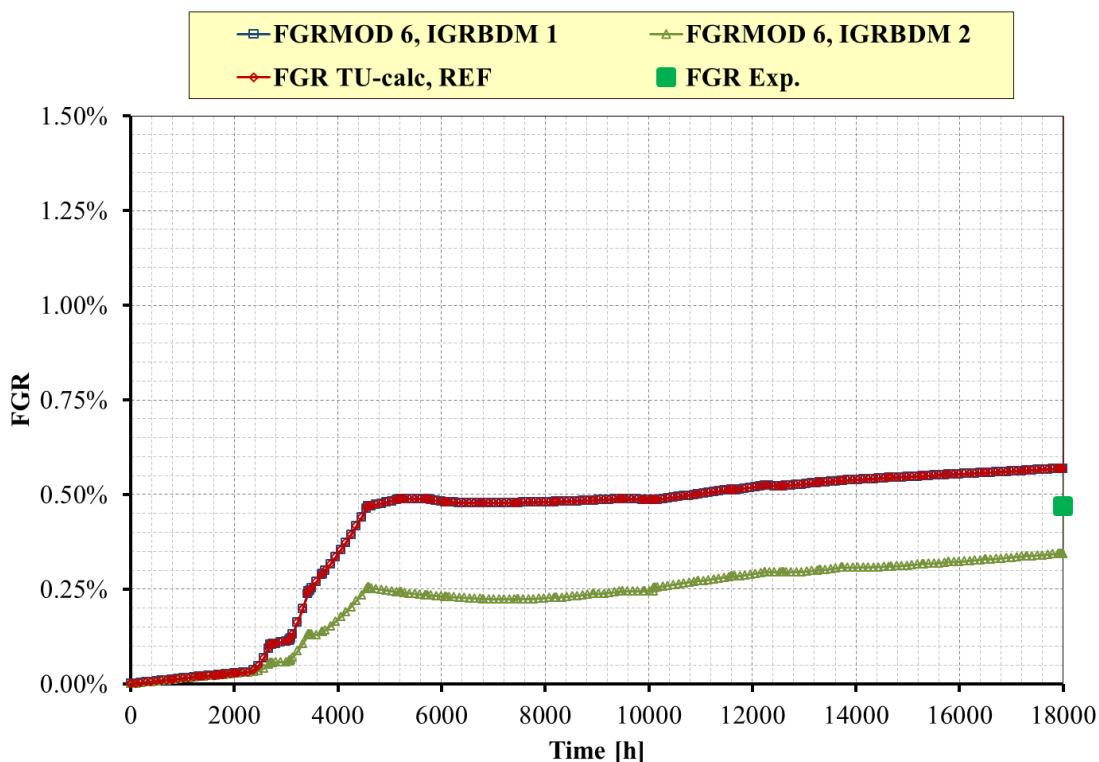
Fig. A. 3 - PRIMO Program, rod BD8, sensitivity analysis on FGR models, FGRMOD6, BI.
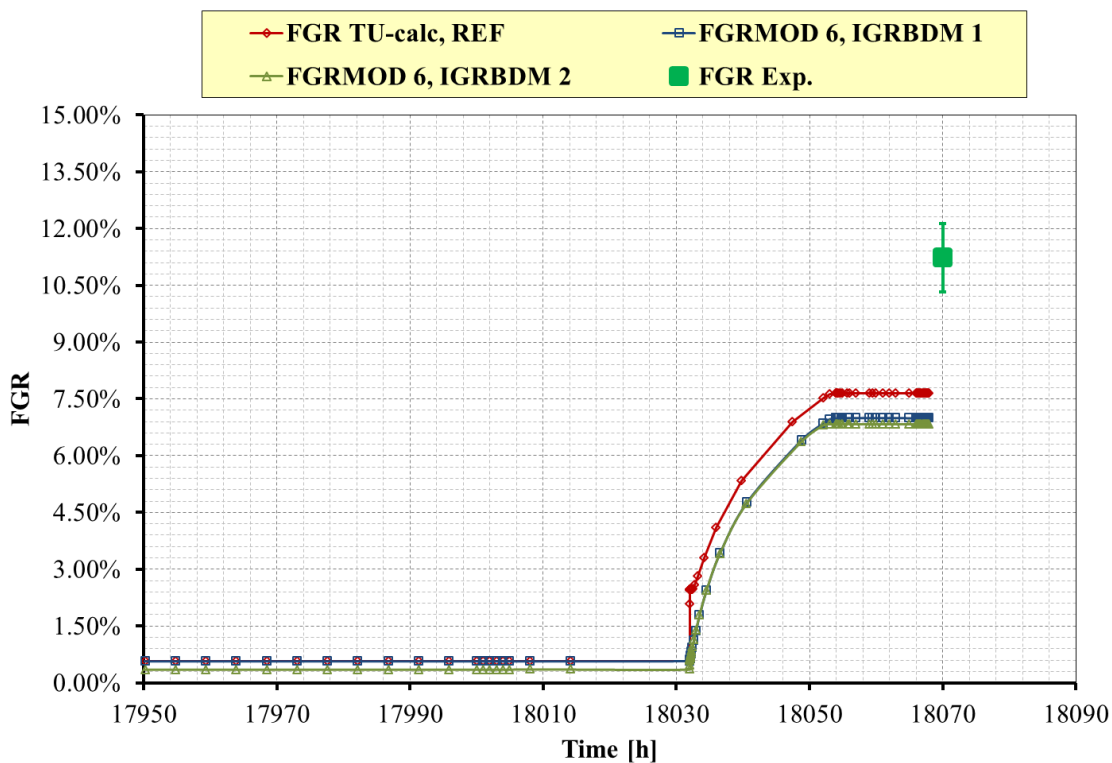
Fig. A. 4 - PRIMO Program, rod BD8, sensitivity analysis on FGR models, FGRMOD6, PR.
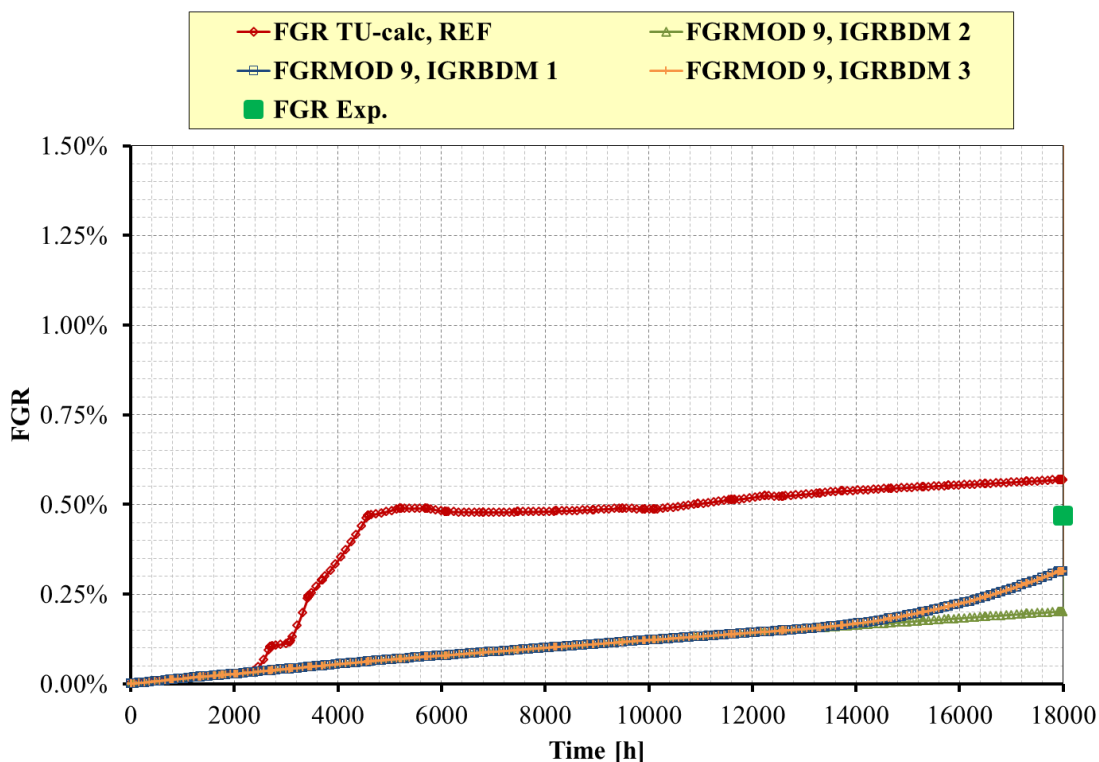
Fig. A. 5 - PRIMO Program, rod BD8, sensitivity analysis on FGR models, FGRMOD9, BI.
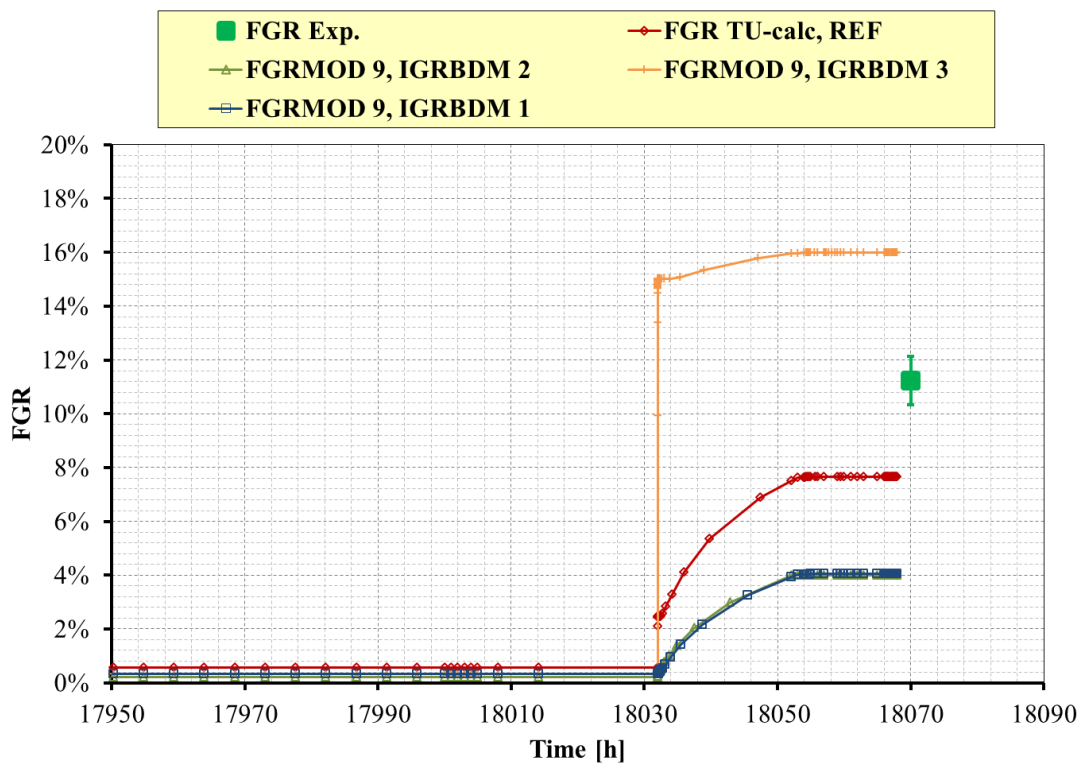
Fig. A. 6 - PRIMO Program, rod BD8, sensitivity analysis on FGR models, FGRMOD9, PR.

A.2 Assessment of the impact of fuel conductivity on FGR (runs C1)
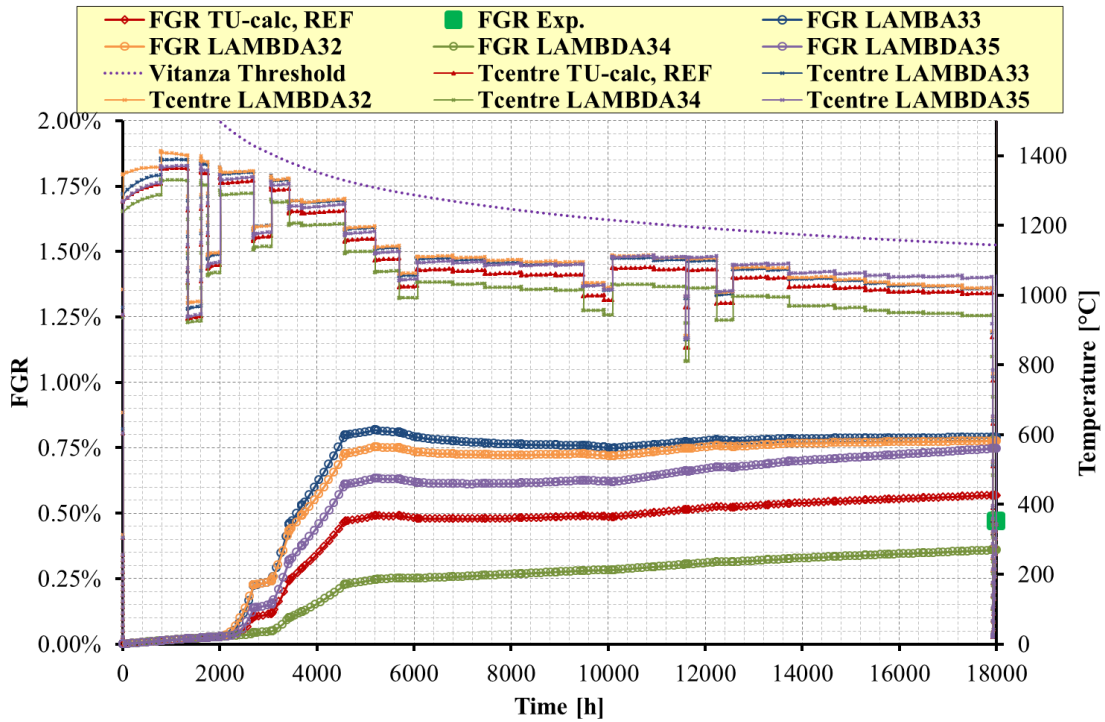
Fig. A. 7 - PRIMO Program, rod BD8, sensitivity analysis on fuel conductivity, rod centerline temperature in peak axial position and FGR, base irradiation.
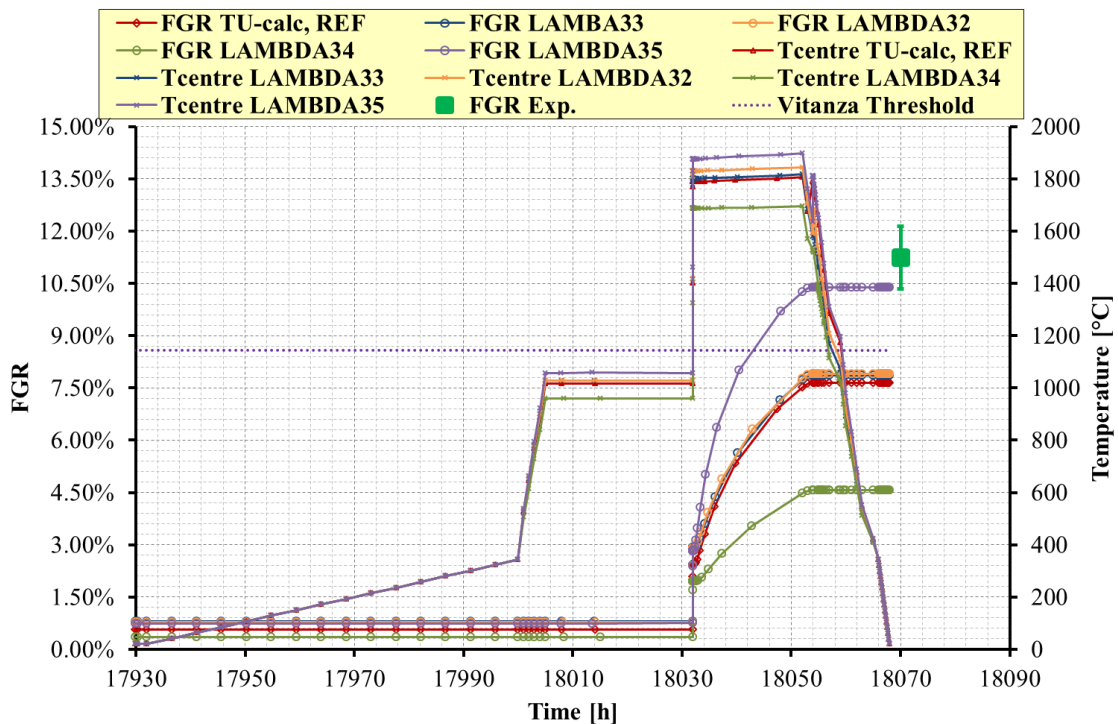
Fig. A. 8 - PRIMO Program, rod BD8, sensitivity analysis on fuel conductivity, rod centerline temperature in peak axial position and FGR, power ramp.

A.3 Assessment of the impact of fuel relocation on FGR (runs M2)
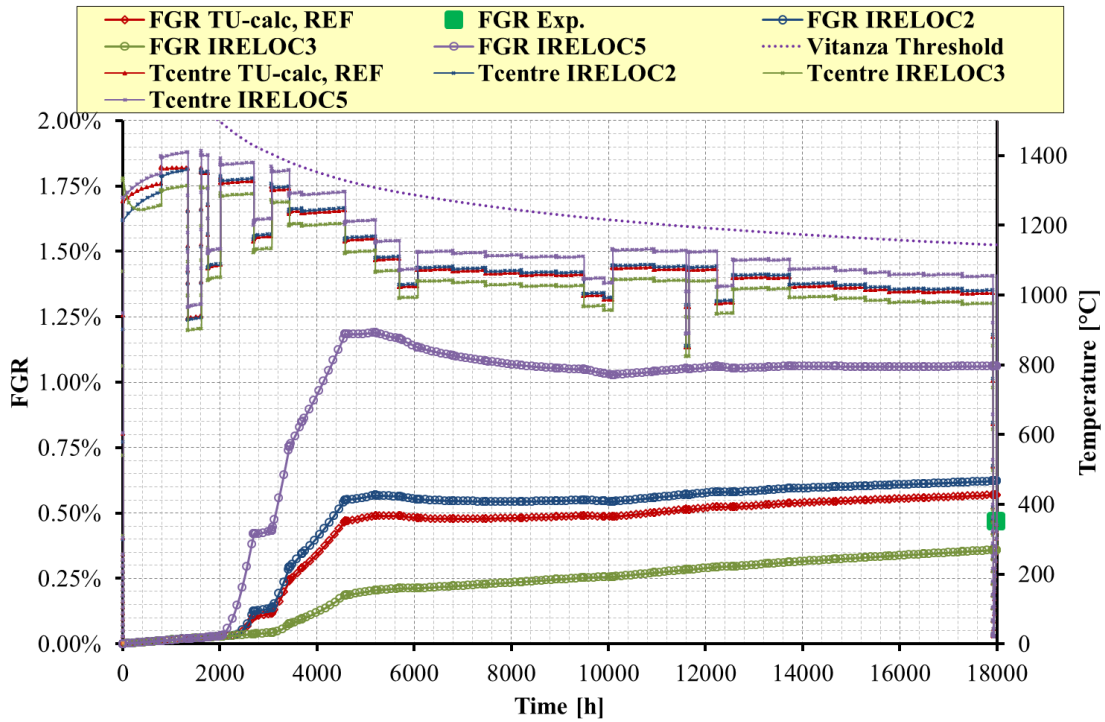
Fig. A. 9 - PRIMO Program, rod BD8, sensitivity analysis on fuel relocation models, FGR and fuel temperature in peak axial position, base irradiation.
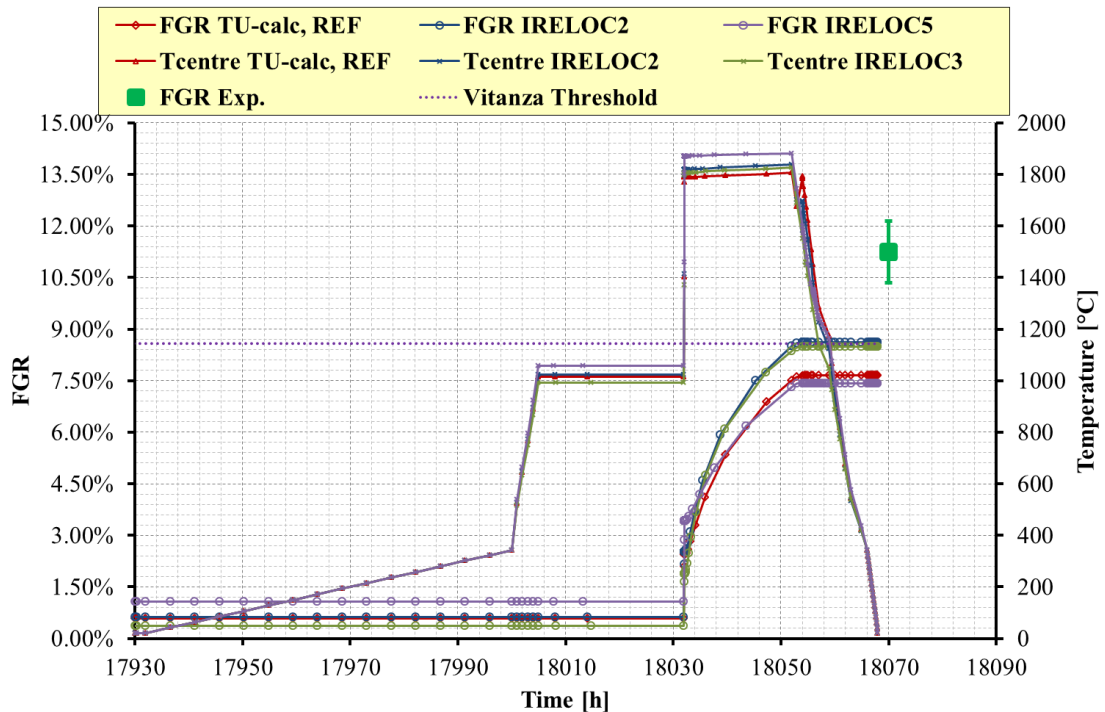
Fig. A. 10 - PRIMO Program, rod BD8, sensitivity analysis on fuel relocation models, FGR and fuel temperature in peak axial position, power ramp.

A.4 Assessment of the impact of fuel swelling correlations on FGR (runs C2)
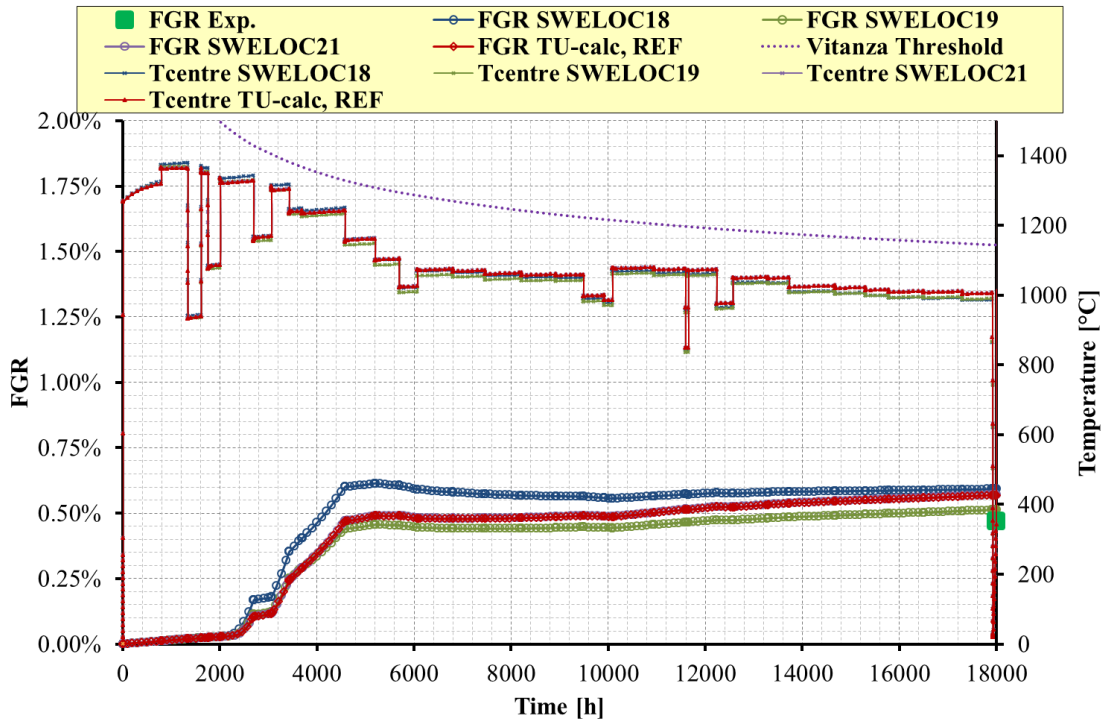
Fig. A. 11 - PRIMO Program, rod BD8, sensitivity analysis on fuel swelling correlations, FGR and fuel temperature in peak axial position, base irradiation.
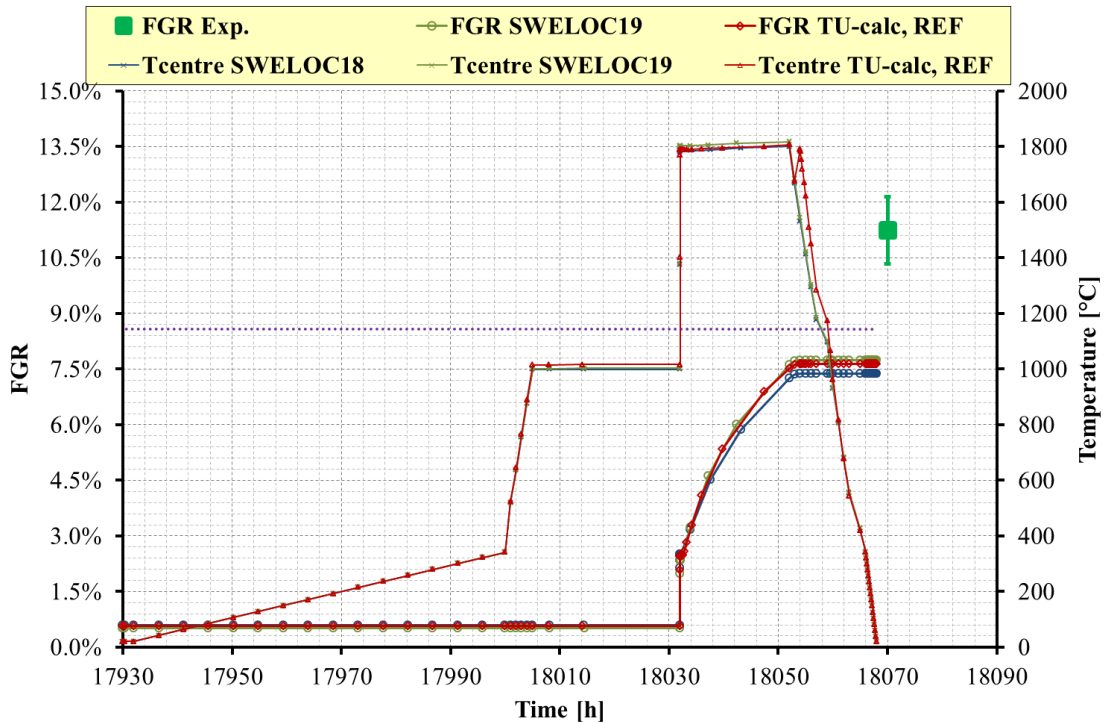
Fig. A. 12 - PRIMO Program, rod BD8, sensitivity analysis on fuel swelling correlations, FGR and fuel temperature in peak axial position, power ramp.

A.5 Assessment of the impact of fuel densification models on FGR (runs M3)
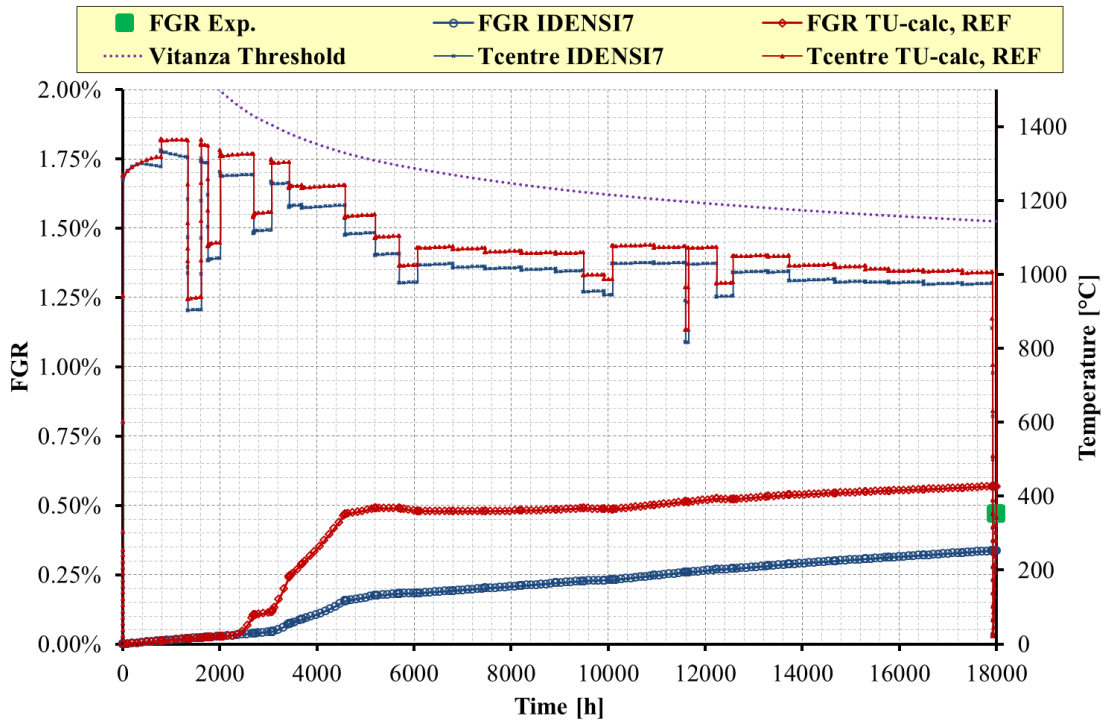
Fig. A. 13 - PRIMO Program, rod BD8, sensitivity analysis on densification models, FGR and fuel temperature in peak axial position, base irradiation.
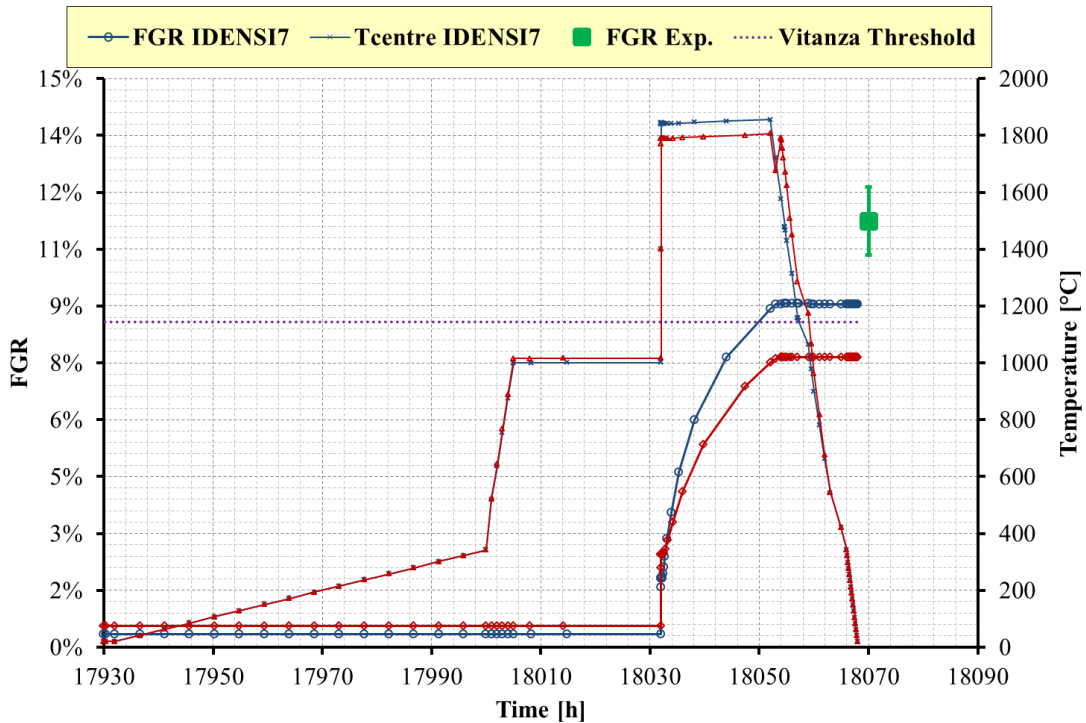
Fig. A. 14 - PRIMO Program, rod BD8, sensitivity analysis on densification models, FGR and fuel temperature in peak axial position, power ramp.

A.6 Assessment of the impact of fuel density on FGR (runs D1)
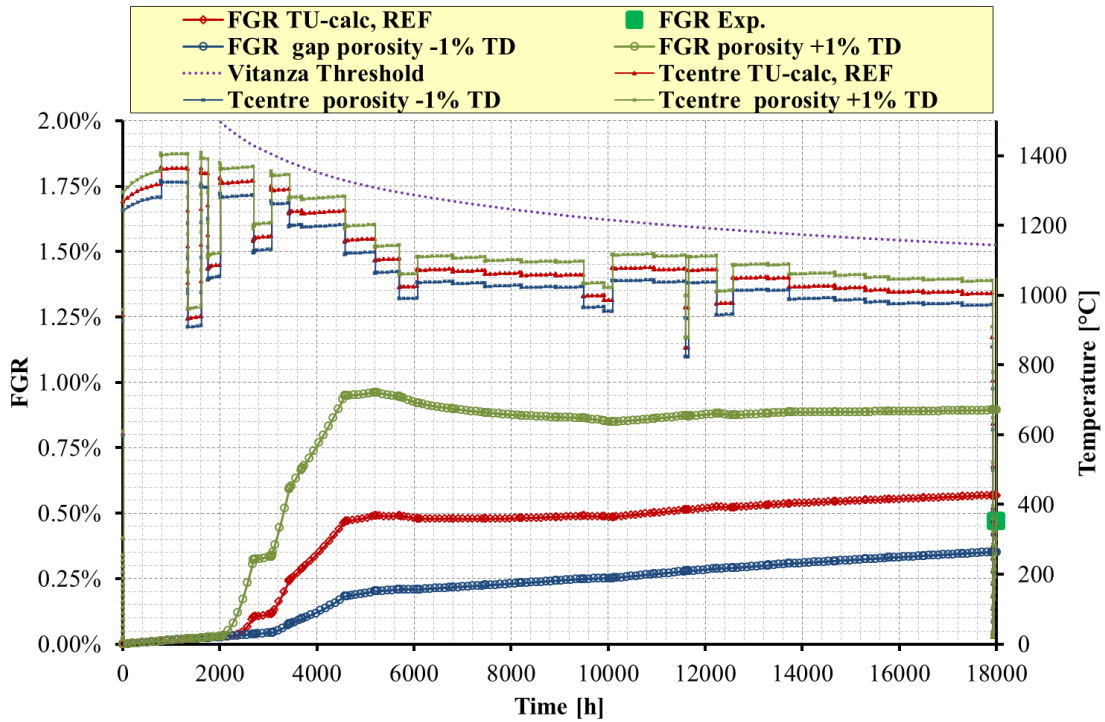
Fig. A. 15 - PRIMO Program, rod BD8, sensitivity analysis on fuel density, FGR and fuel temperature in peak axial position, base irradiation.
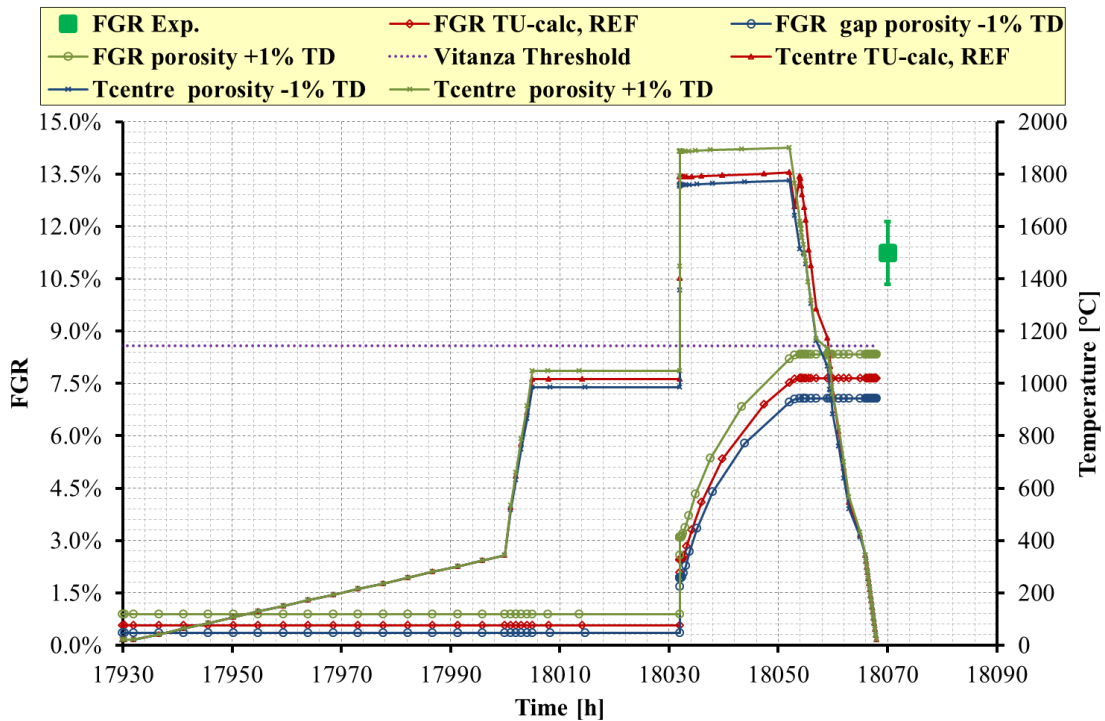
Fig. A. 16 - PRIMO Program, rod BD8, sensitivity analysis on fuel density, FGR and fuel temperature in peak axial position, power ramp.

A.7 Assessment of the impact of fuel average grain size on FGR (runs D2)
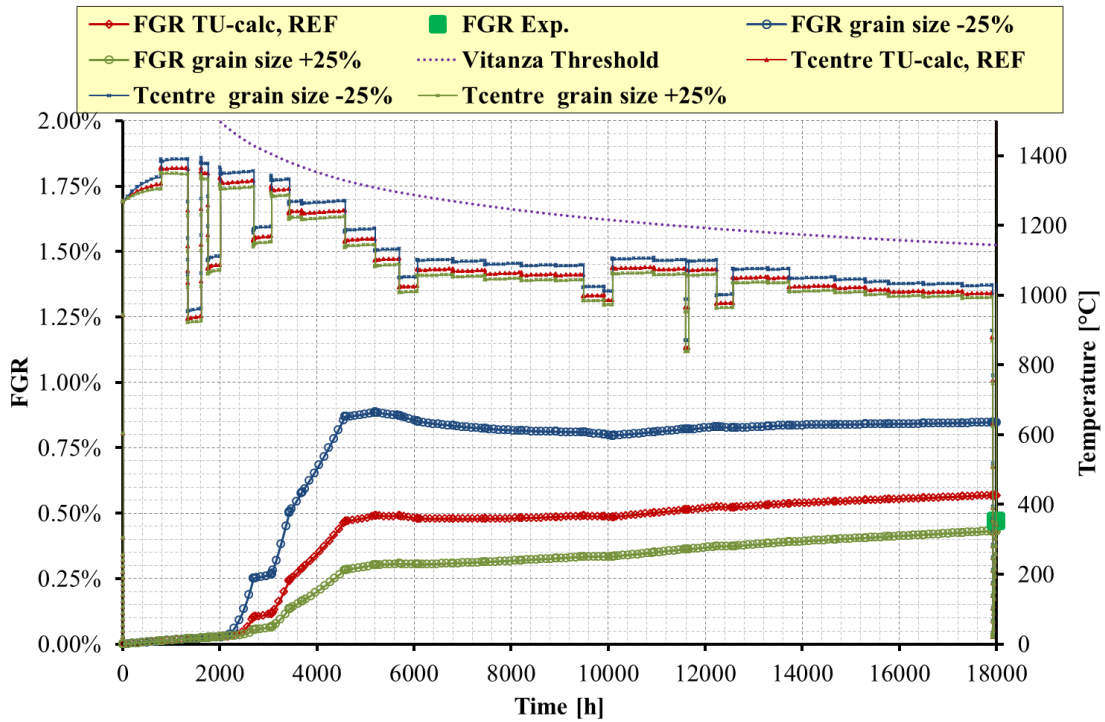
Fig. A. 17 - PRIMO Program, rod BD8, sensitivity analysis on fuel average grain size, FGR and fuel temperature in peak axial position, base irradiation.
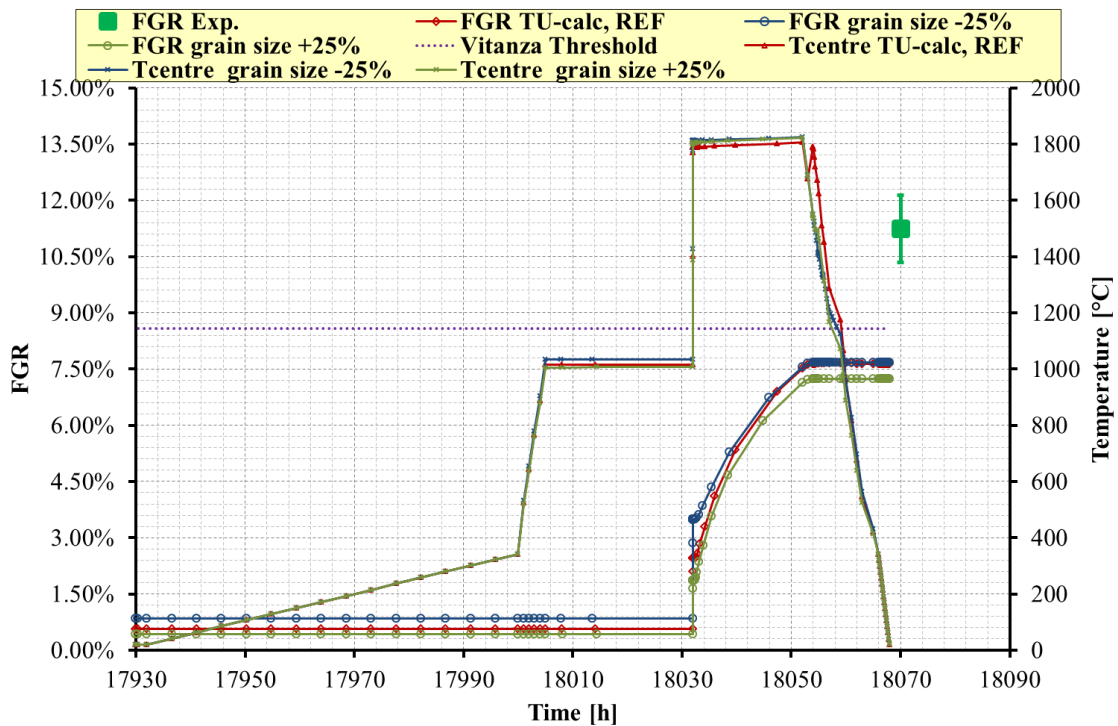
Fig. A. 18 - PRIMO Program, rod BD8, sensitivity analysis on fuel average grain size, FGR and fuel temperature in peak axial position, power ramp.

A.8 Assessment of the impact of initial gap size on FGR (runs D3)
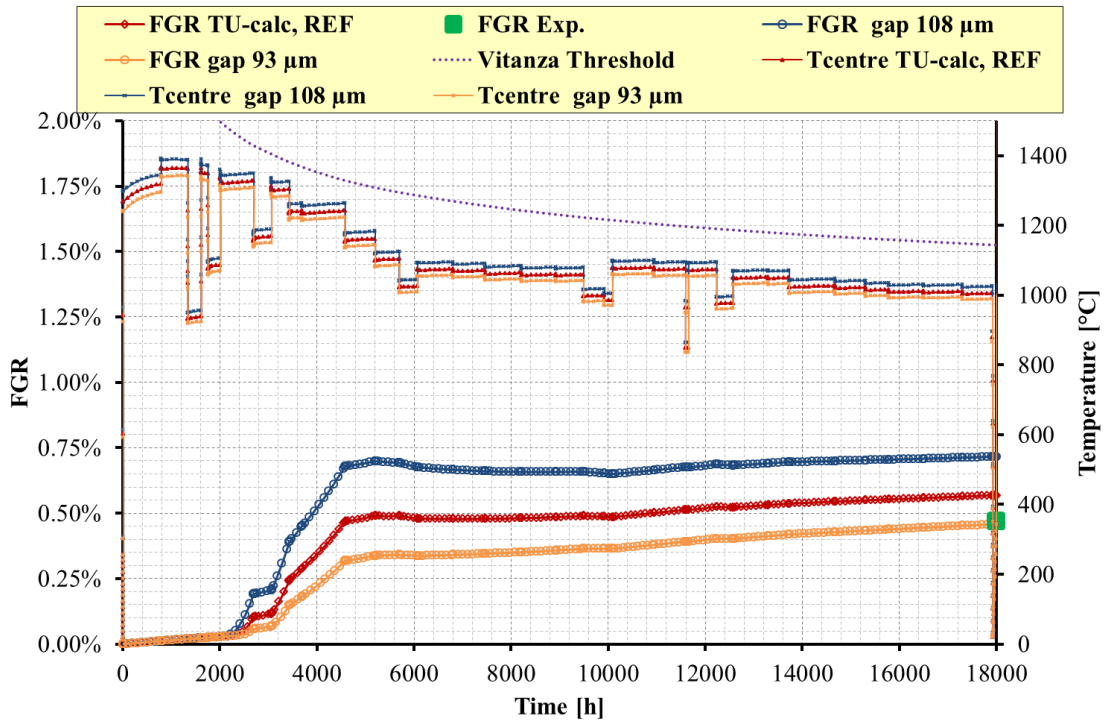
Fig. A. 19 - PRIMO Program, rod BD8, sensitivity analysis on fuel gap initial size, FGR and fuel temperature in peak axial position, base irradiation.

Fig. A. 20 - PRIMO Program, rod BD8, sensitivity analysis on fuel gap initial size, FGR and fuel temperature in peak axial position, power ramp.

APPENDIX B: IFA-597, Sensitivity analyses

B.1 Assessment of the impact of FGR models on FGR (runs M1)

(a) Rod 10, FGR
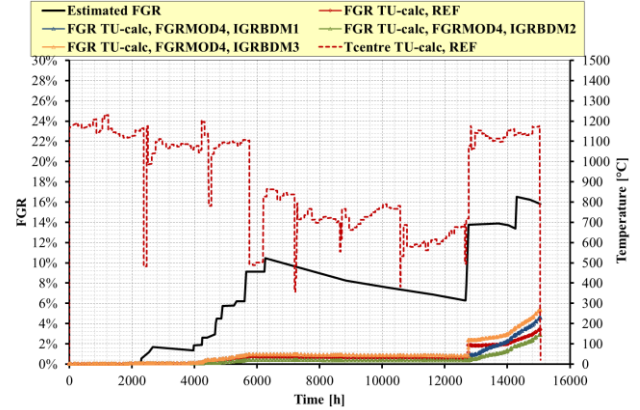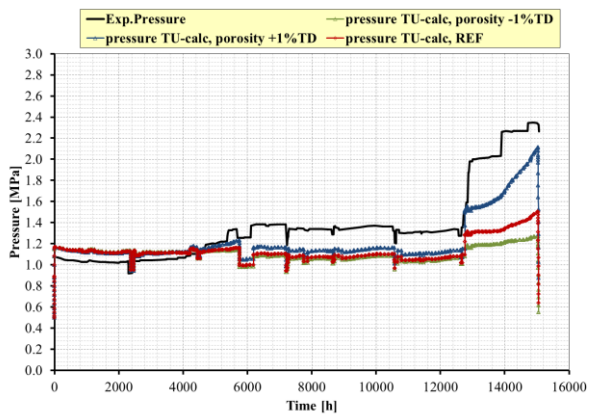

(b) Rod 11, FGR
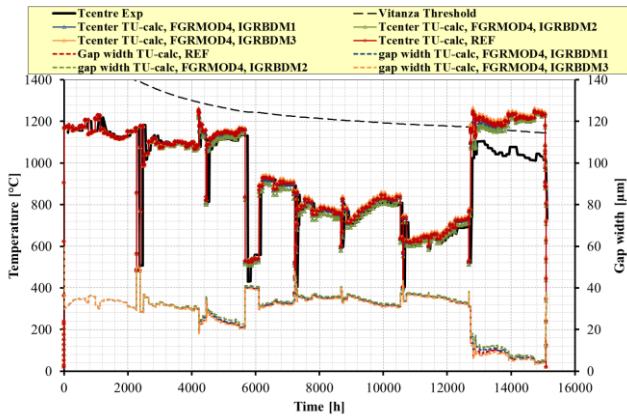
(c) Rod 10, temperature
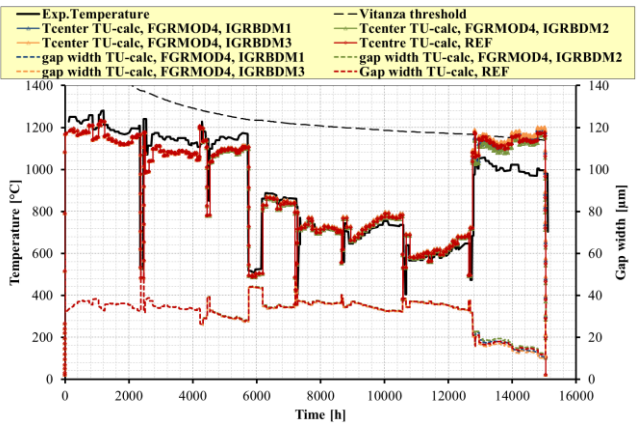
(d) Rod 11, temperature
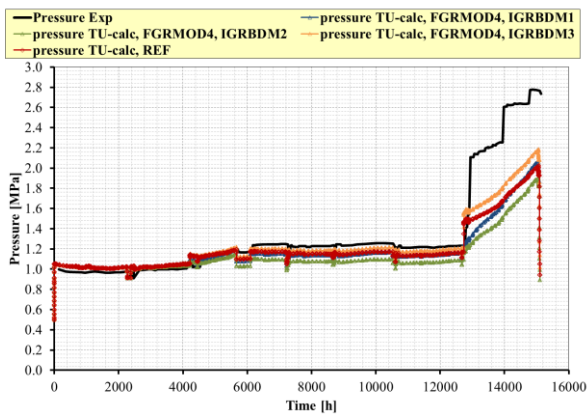
(e) Rod 10, pin pressure
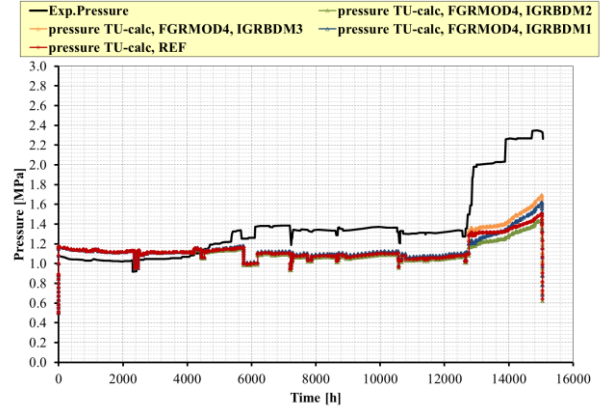
(f) Rod 11, pin pressure

Fig. B. 1 - IFA-597, rod 10 and rod 11, sensitivity analysis on FGR models, FGRMOD4.
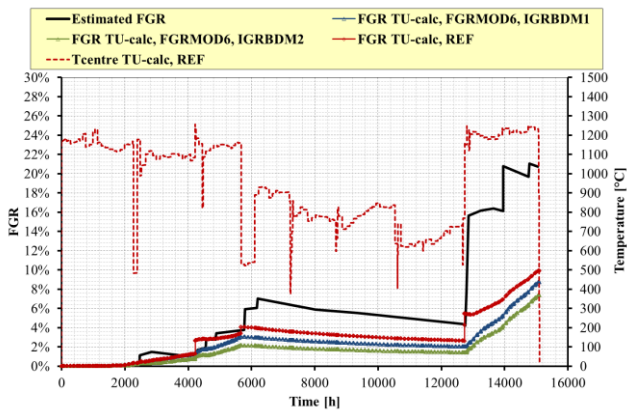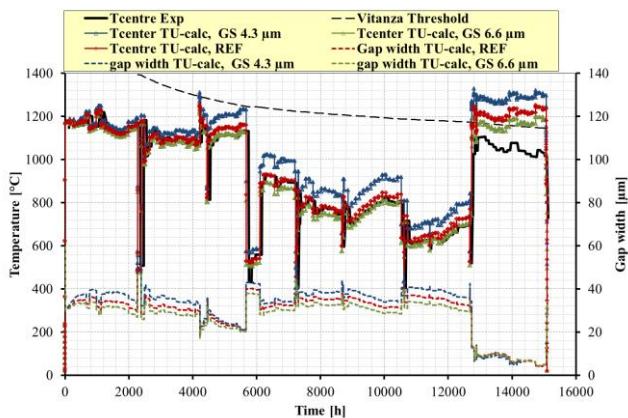
(a) Rod 10, FGR
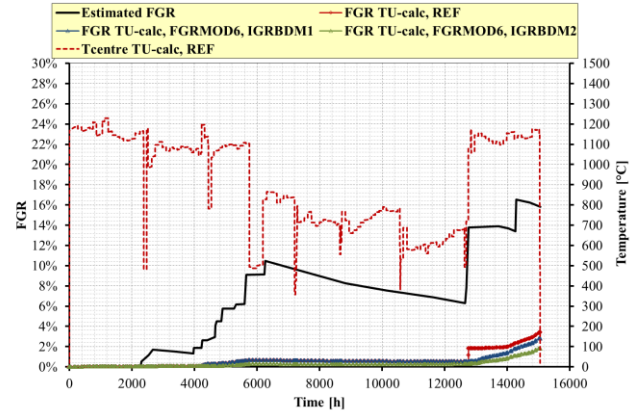
(b) Rod 11, FGR
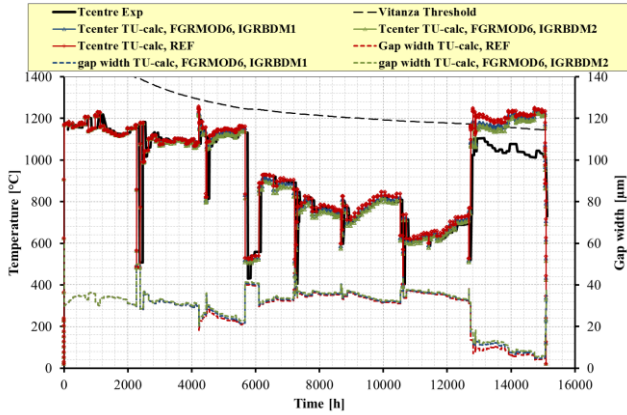
(c) Rod 10, temperature
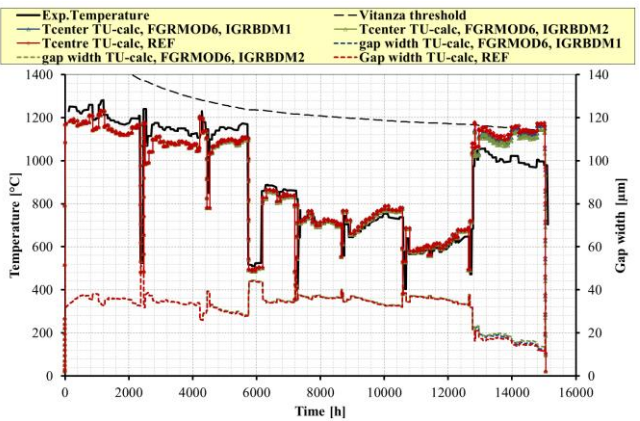
(d) Rod 11, temperature
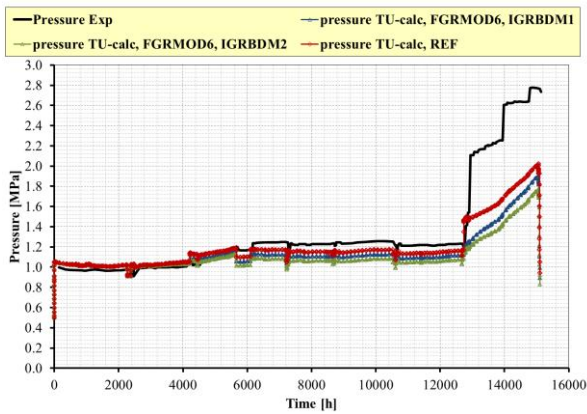
(e) Rod 10, pin pressure
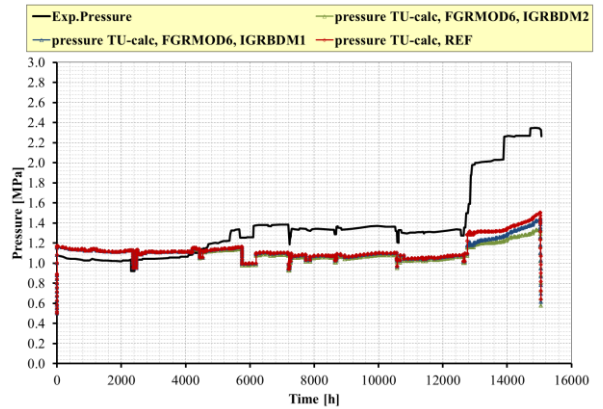
(f) Rod 11, pin pressure

Fig. B. 2 - IFA-597,rod 10 and rod 11, sensitivity analysis on FGR models, FGRMOD6.
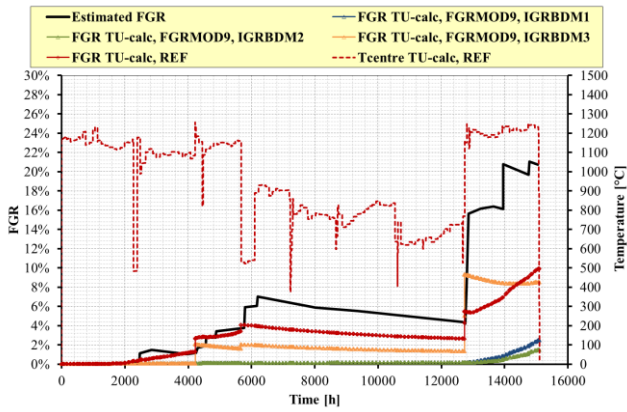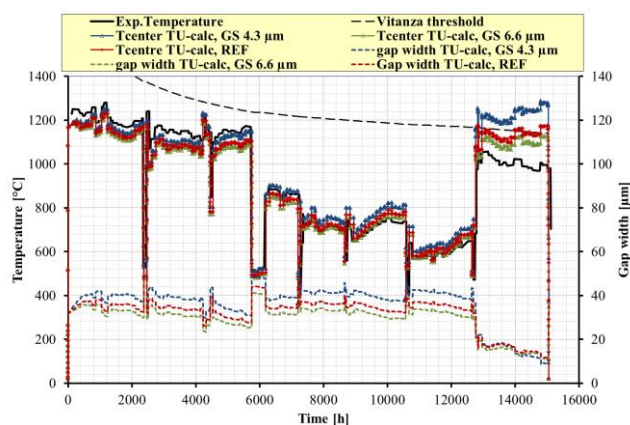
(a) Rod 10, FGR
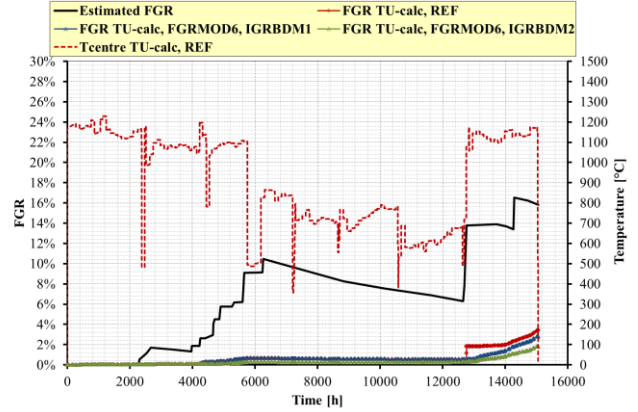
(b) Rod 11, FGR
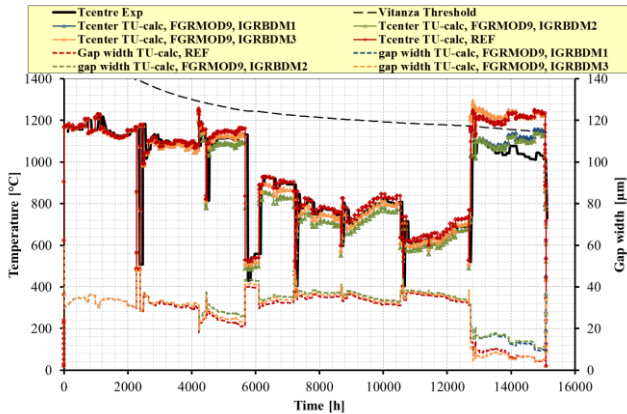
(c) Rod 10, temperature
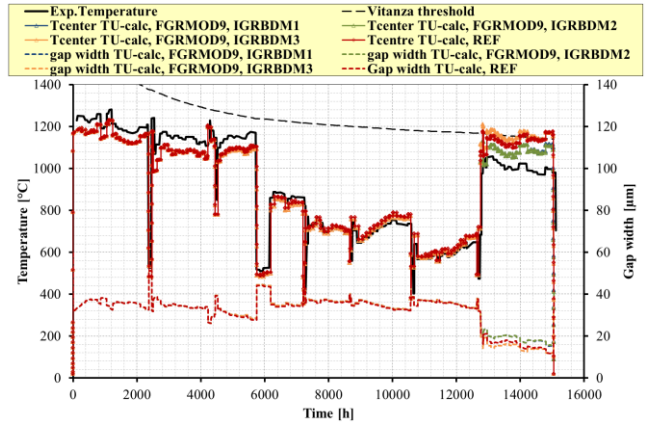
(d) Rod 11, temperature
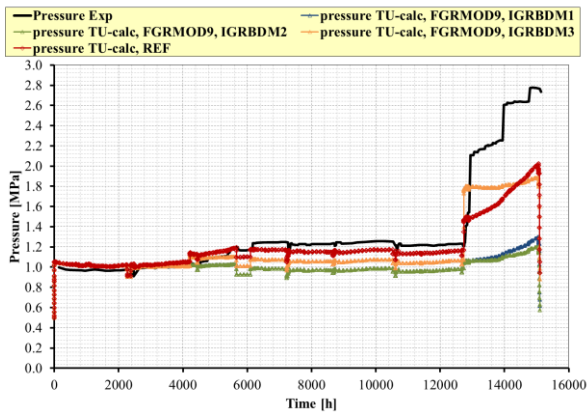
(e) Rod 10, pin pressure
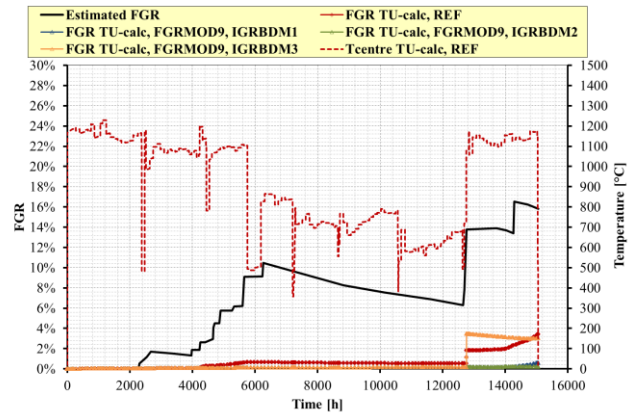
(f) Rod 11, pin pressure

Fig. B. 3 - IFA-597, rod 10 and rod 11, sensitivity analysis on FGR models, FGRMOD9.

B.2 Assessment of the impact of fuel conductivity correlation (runs C1)
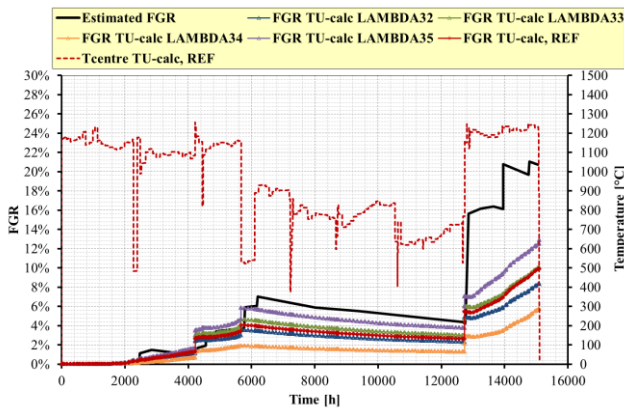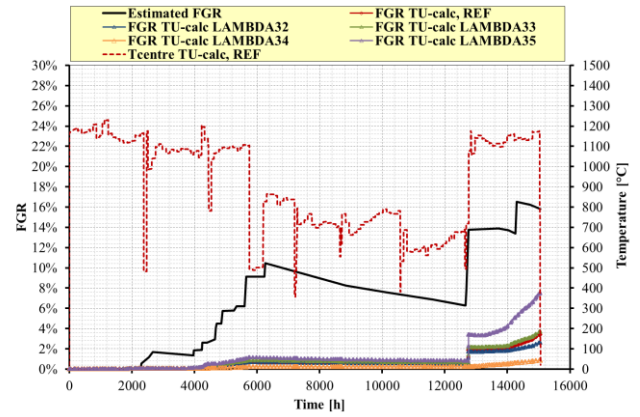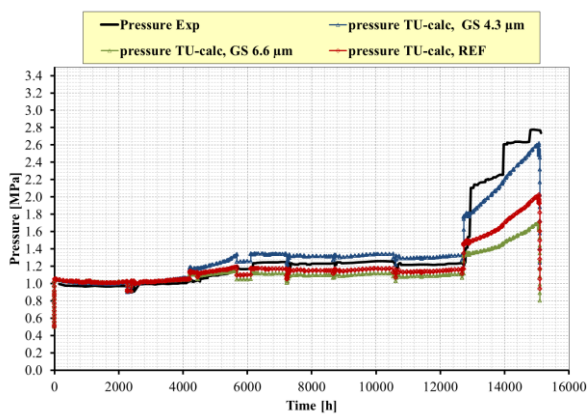

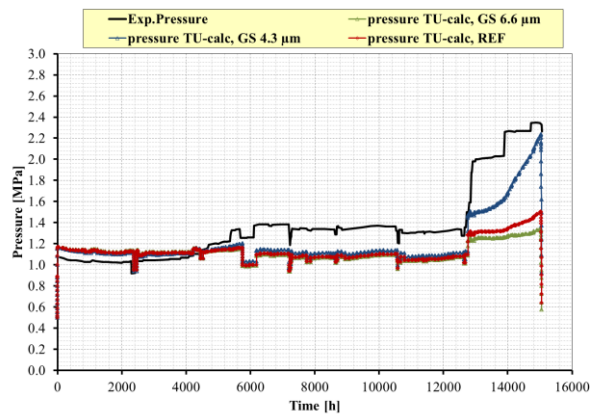(a) Rod 10, FGR

(b) Rod 11, FGR
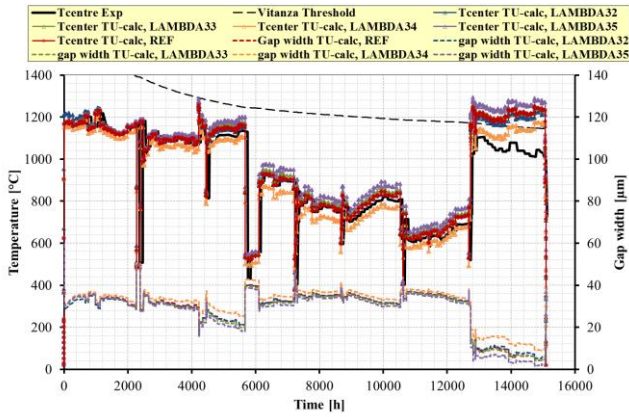
(c) Rod 10, temperature
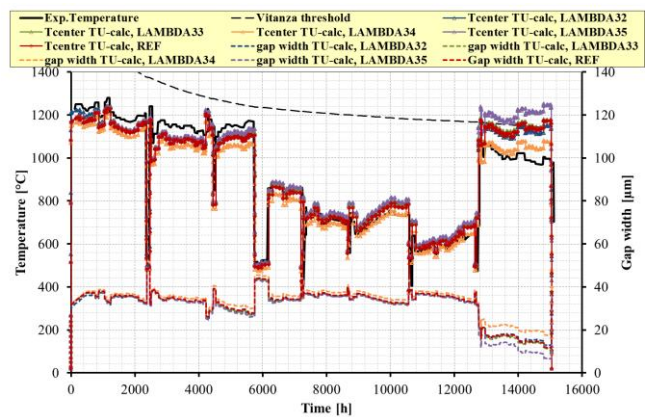
(d) Rod 11, temperature
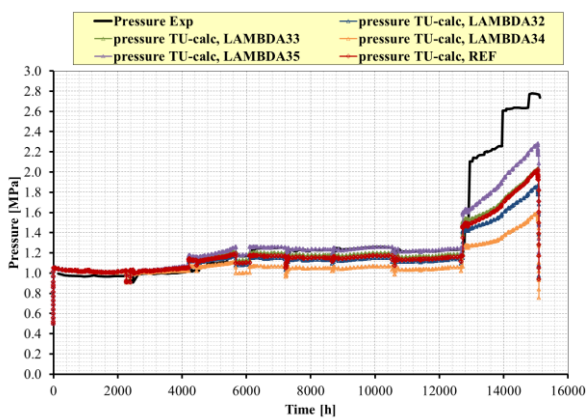
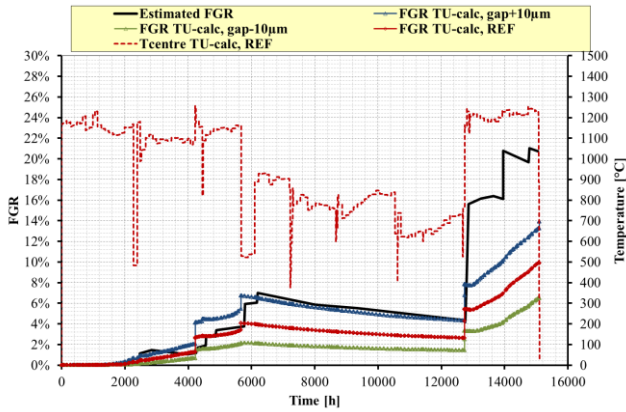(e) Rod 10, pin pressure
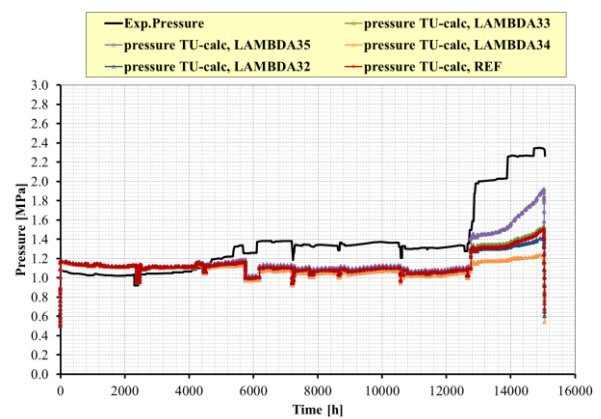
(f) Rod 11, pin pressure

Fig. B. 4 - IFA-597, rod 10 and rod 11, sensitivity analysis on fuel conductivity correlations.

B.3 Assessment of the impact of fuel relocation model (runs M2)
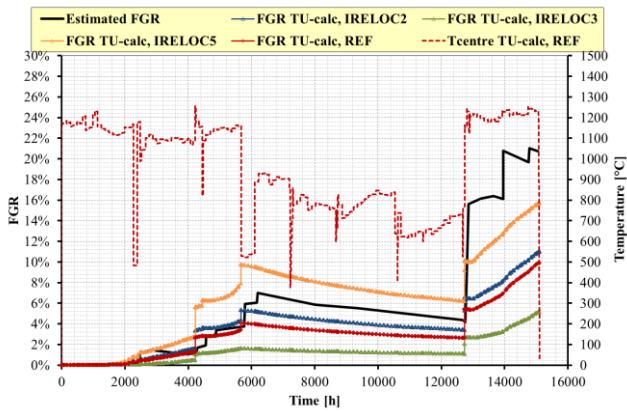
(a) Rod 10, FGR
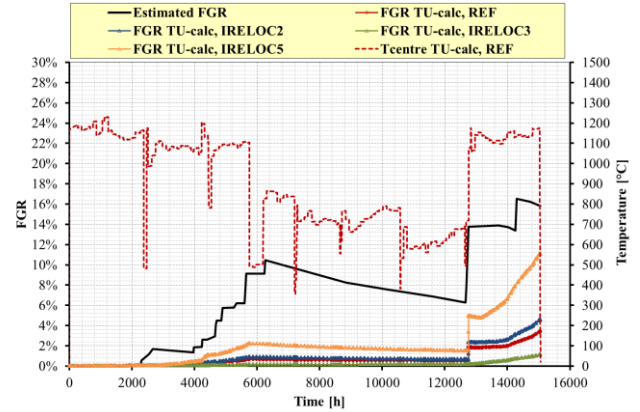
(b) Rod 11, FGR
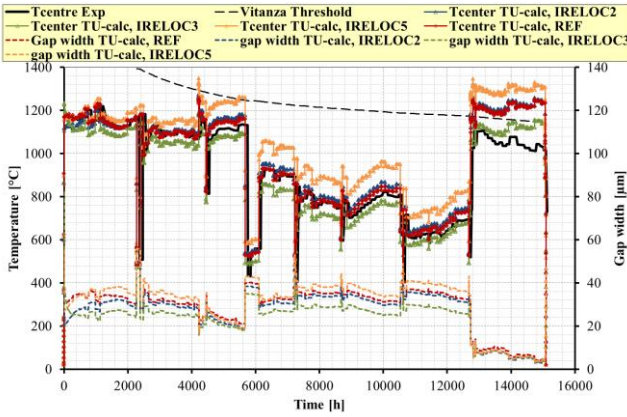
(c) Rod 10, temperature
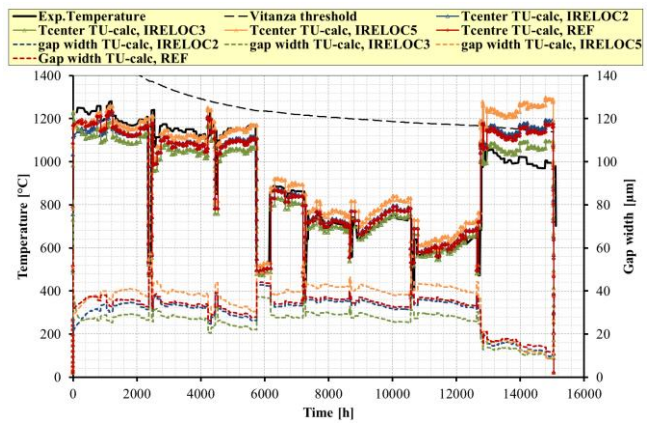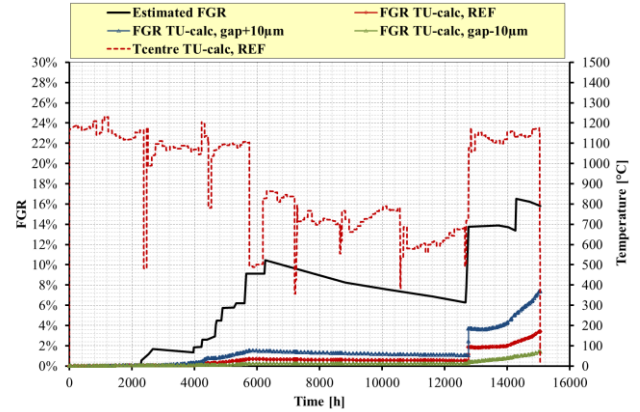
(d) Rod 11, temperature
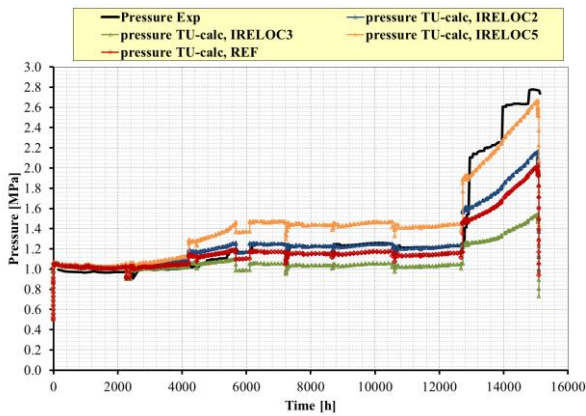
(e) Rod 10, pin pressure
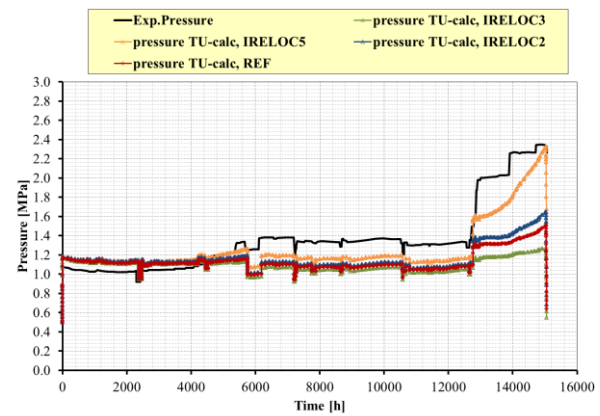
(f) Rod 11, pin pressure

Fig. B. 5 - IFA-597, rod 10 and rod 11, sensitivity analysis fuel relocation models.

B.4 Assessment of the impact of fuel swelling correlation (runs C1)
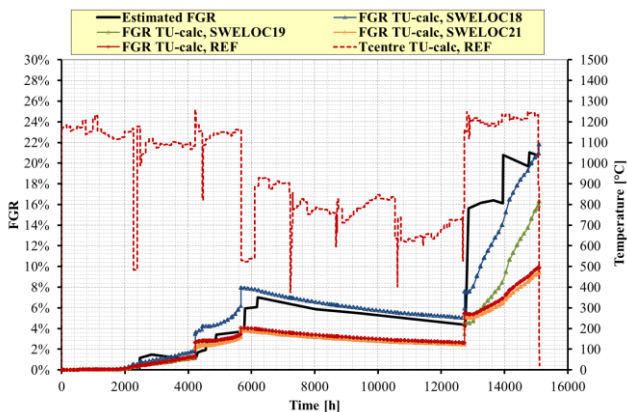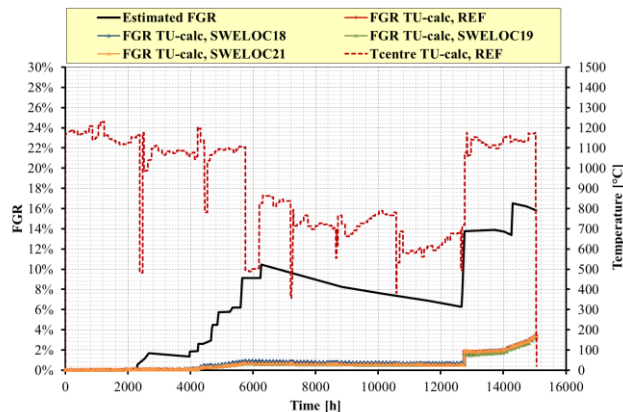
(a) Rod 10, FGR

(b) Rod 11, FGR
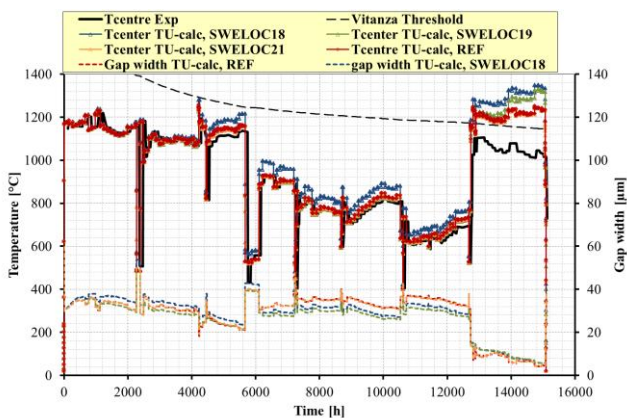
(c) Rod 10, temperature
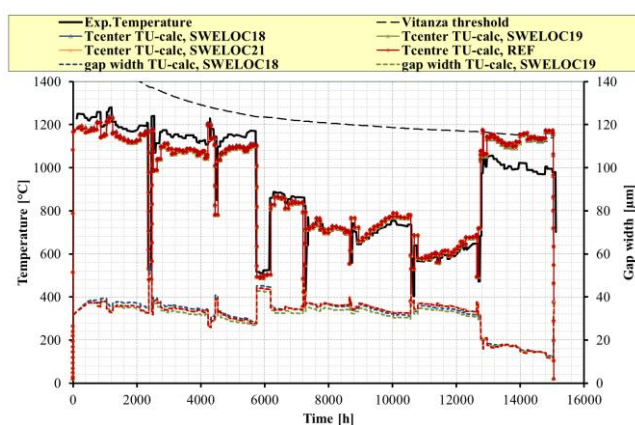
(d) Rod 11, temperature
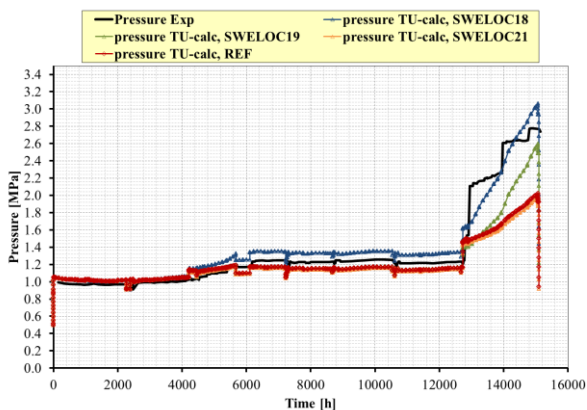
(e) Rod 10, pin pressure
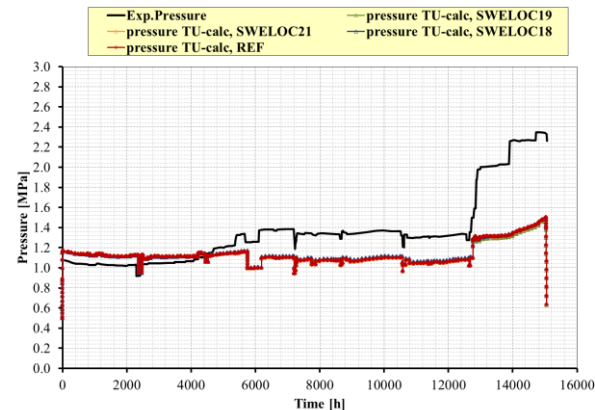
(f) Rod 11, pin pressure

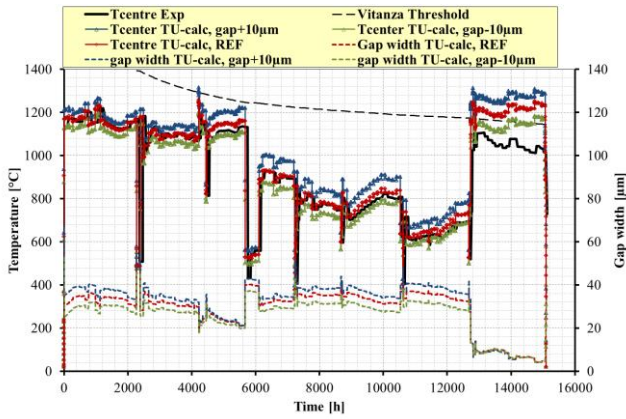*Fig. B. 6 - IFA-597, rod 10 and rod 11, sensitivity analysis on fuel swelling correlations.*

B.5 Assessment of the impact of fuel densification model (runs C1)
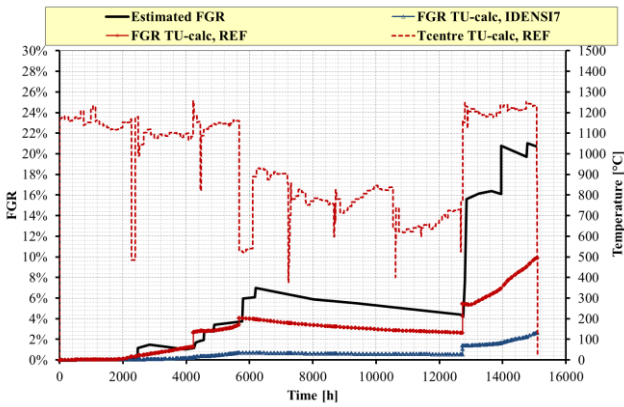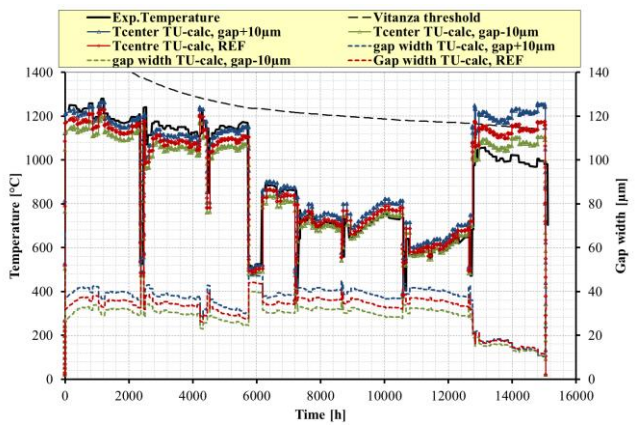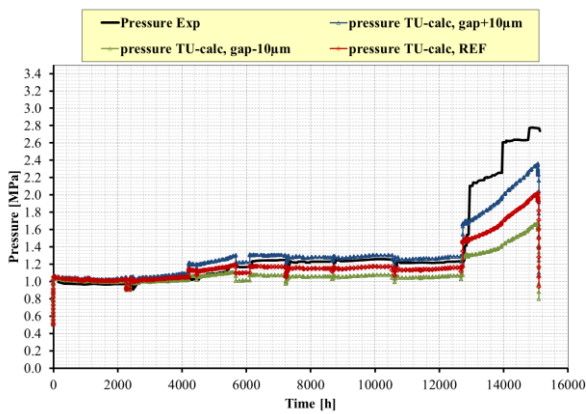

(a) Rod 10, FGR
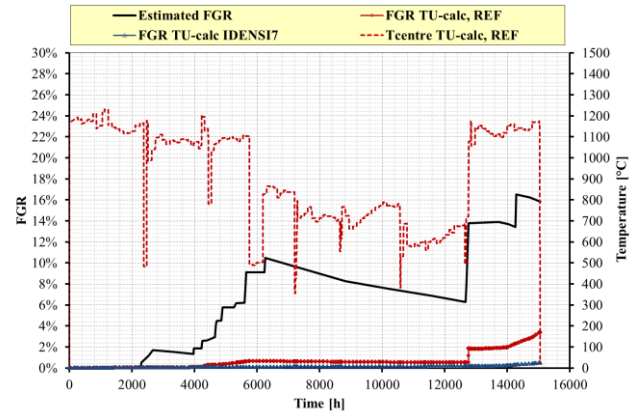
(b) Rod 11, FGR
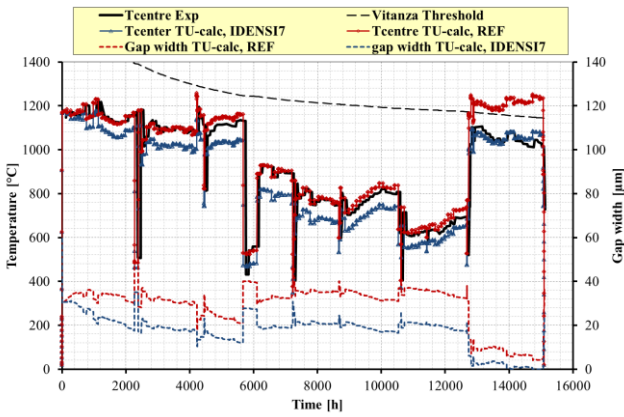
(c) Rod 10, temperature
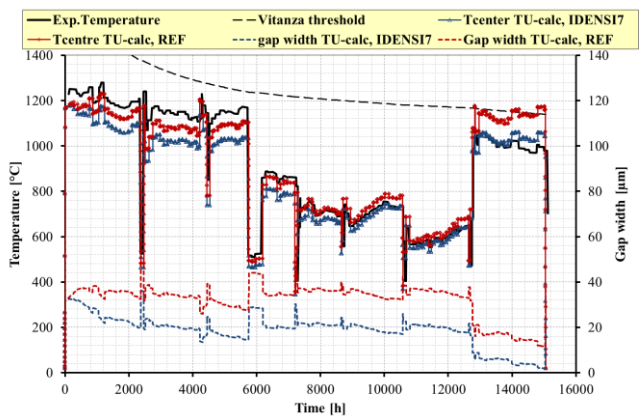
(d) Rod 11, temperature
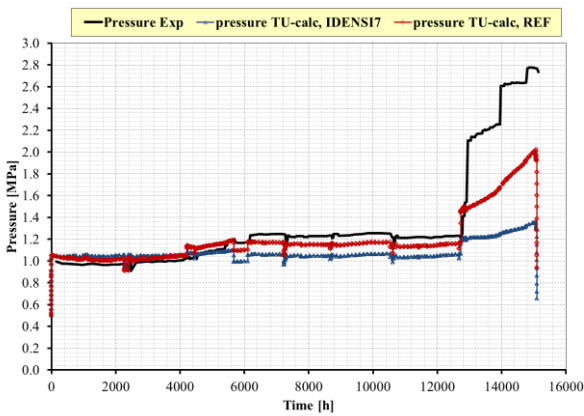
(e) Rod 10, pin pressure
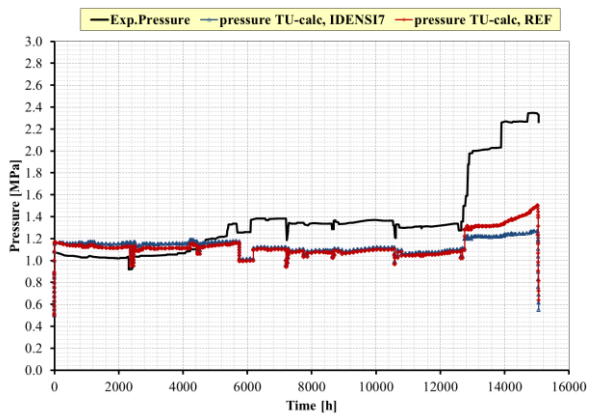
(f) Rod 11, pin pressure

Fig. B. 7 - IFA-597, rod 10 and rod 11, sensitivity analysis on fuel densification models.

B.6 Assessment of the impact of Helium release model (runs M2)
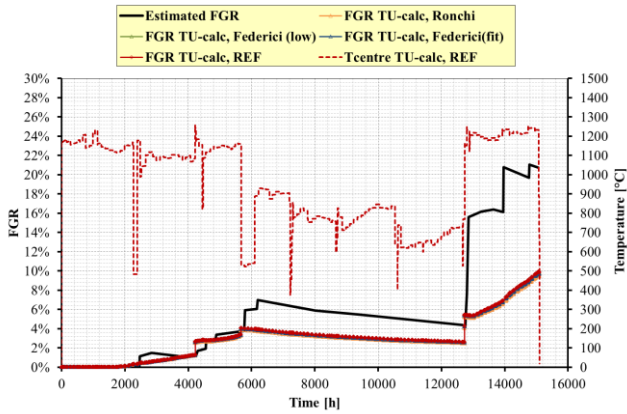
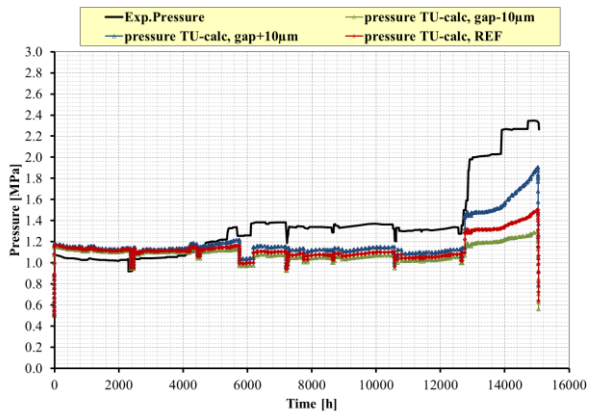

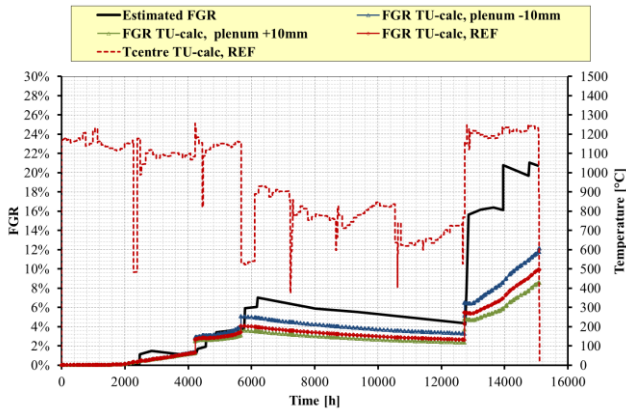(a) Rod 10, FGR
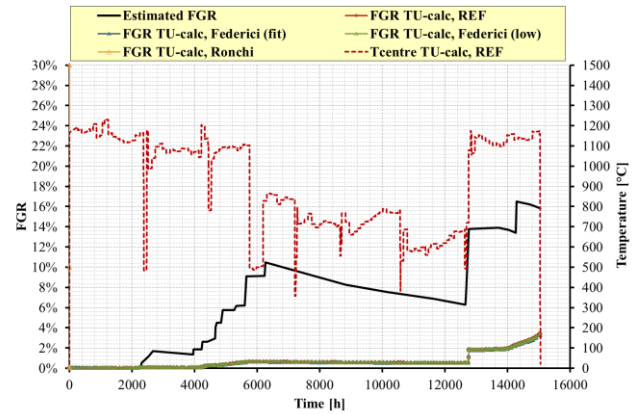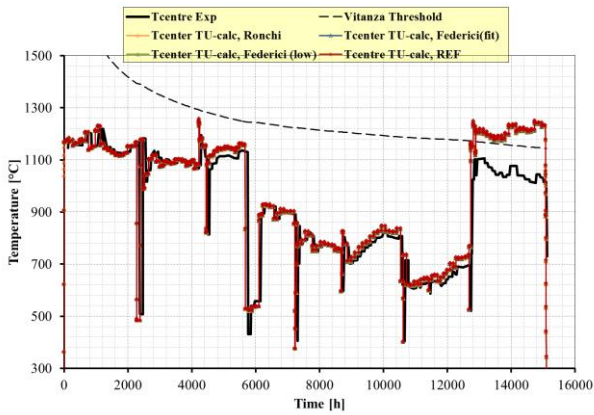
(b) Rod 11, FGR

(c) Rod 10, temperature
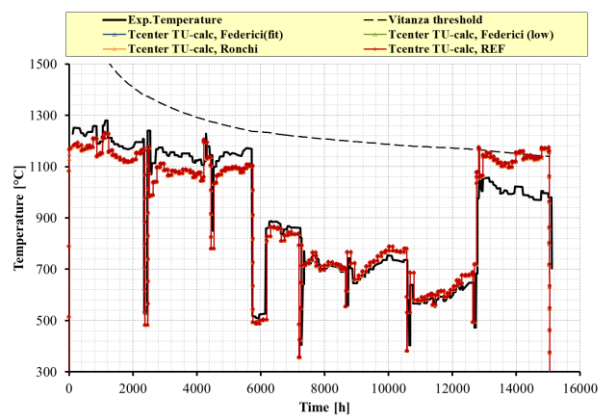
(d) Rod 11, temperature
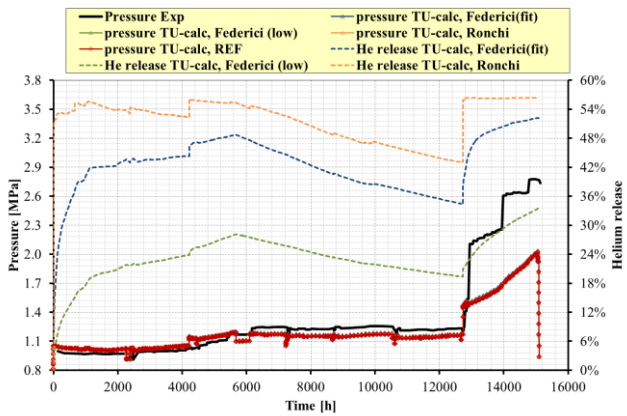
(e) Rod 10, pin pressure
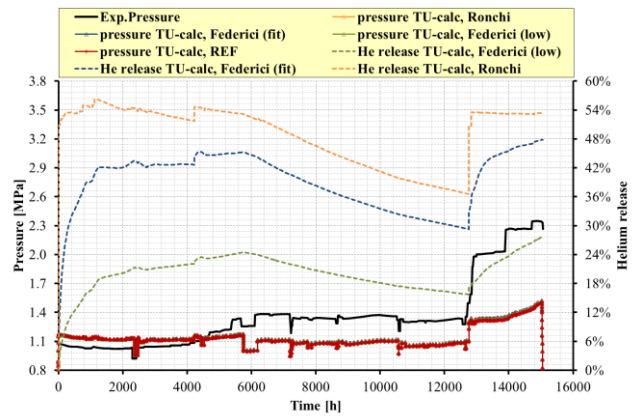
(f) Rod 11, pin pressure

Fig. B. 8 - IFA-597, rod 10 and rod 11, sensitivity analysis on Helium release models.

B.7 Assessment of the impact of fuel density (runs D1)
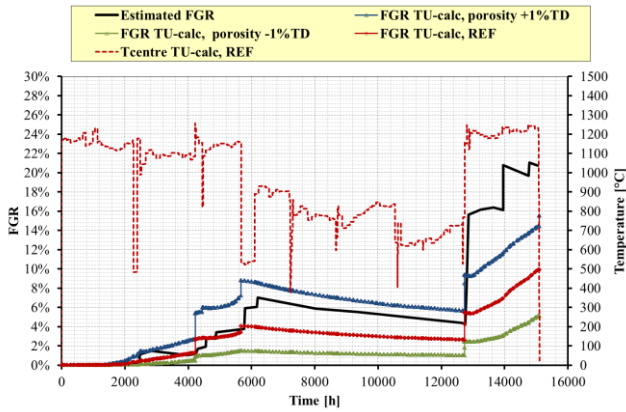
(a) Rod 10, FGR
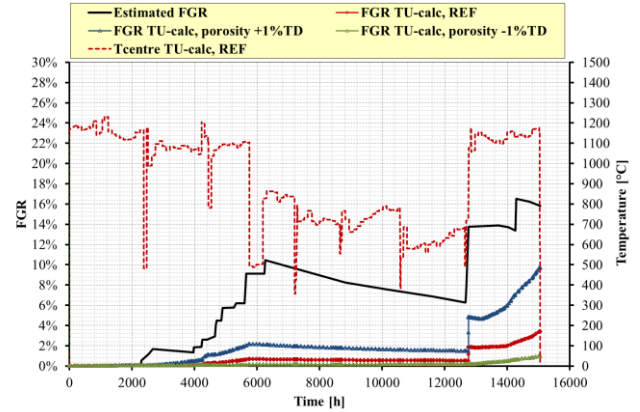
(b) Rod 11, FGR
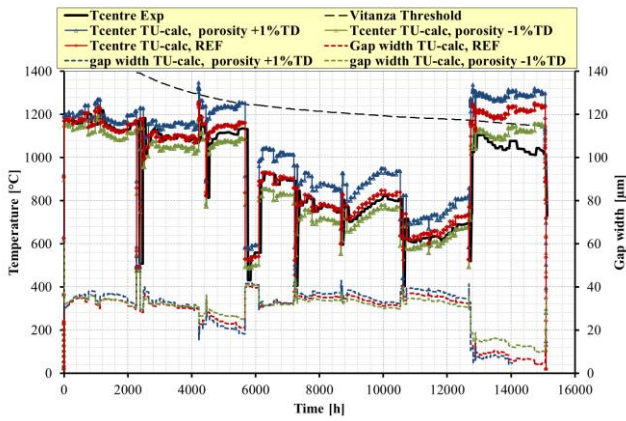
(c) Rod 10, temperature
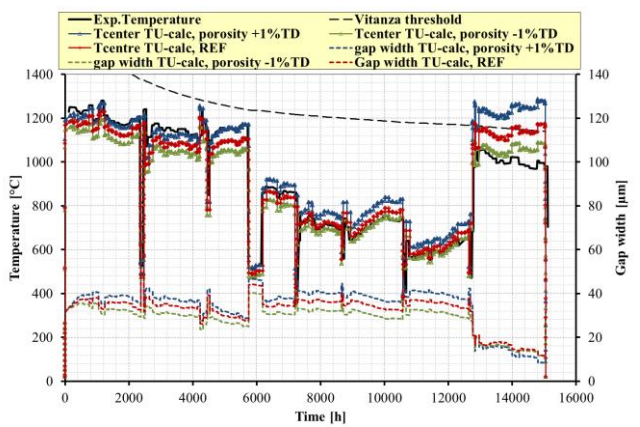
(d) Rod 11, temperature
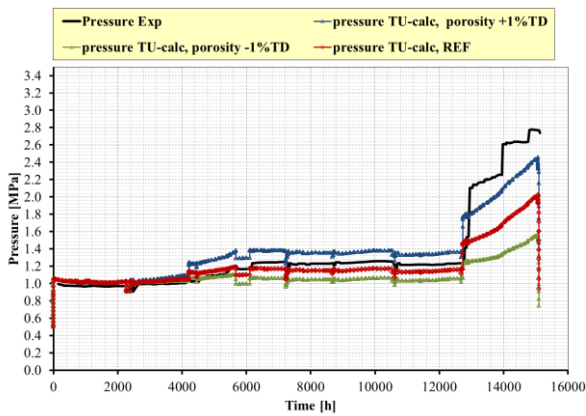
(e) Rod 10, pin pressure

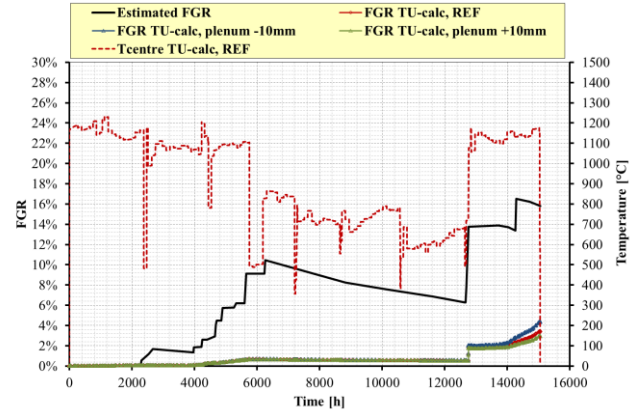(f) Rod 11, pin pressure

Fig. B. 9 - IFA-597, rod 10 and rod 11, sensitivity analysis fuel initial density.

B.8 Assessment of the impact of grain size(runs D2)
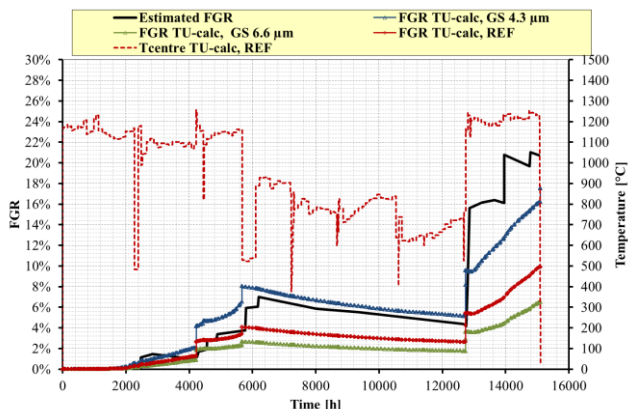
(a) Rod 10, FGR
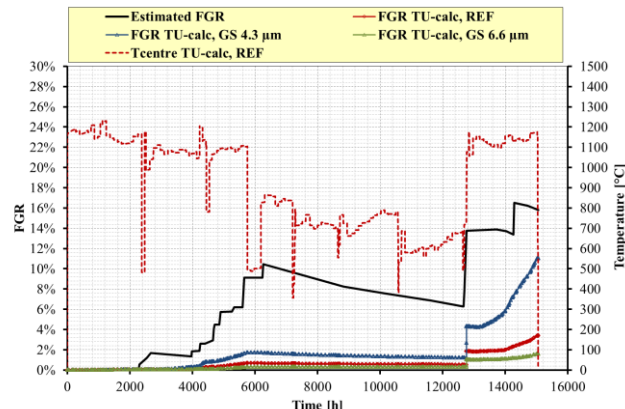
(b) Rod 11, FGR

(c) Rod 10, temperature

(d) Rod 11, temperature

(e) Rod 10, pin pressure

(f) Rod 11, pin pressure

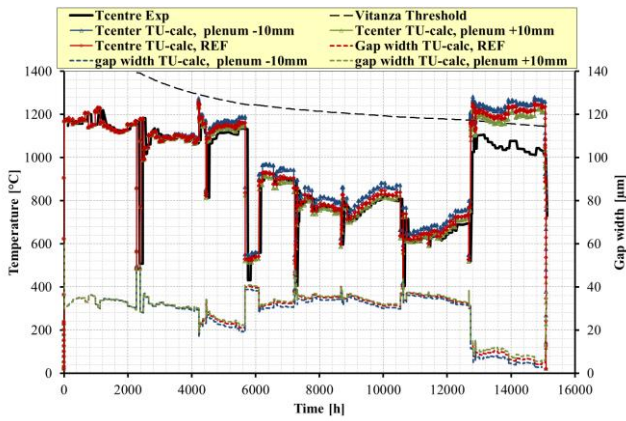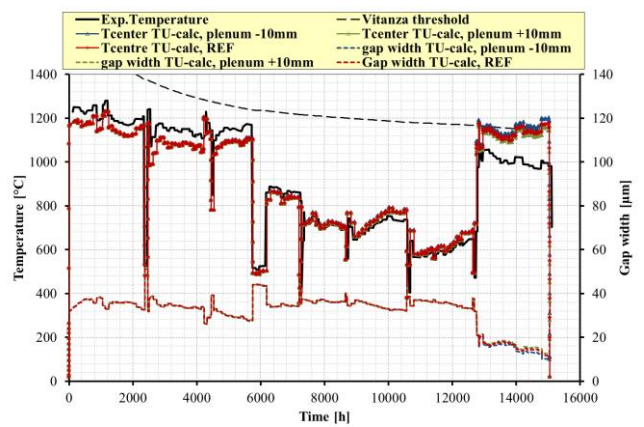*Fig. B. 10 - IFA-597, rod 10 and rod 11, sensitivity analysis on fuel grain size.*

B.9 Assessment of the impact of gap width (runs D3)
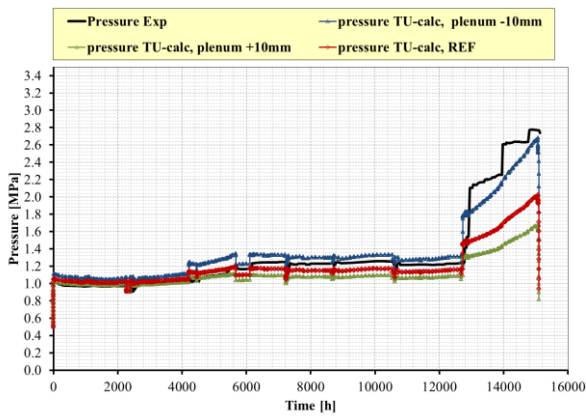

(a) Rod 10, FGR

(b) Rod 11, FGR

(c) Rod 10, temperature

(d) Rod 11, temperature

(e) Rod 10, pin pressure

(f) Rod 11, pin pressure

Fig. B. 11 - IFA-597, rod 10 and rod 11, sensitivity analysis on initial gap width.

B.10 Assessment of the impact of plenum length (runs D4)
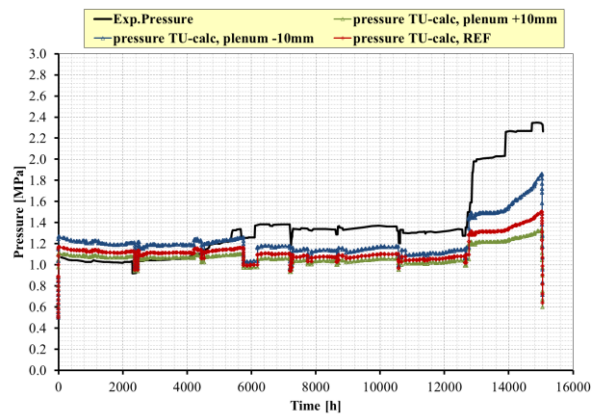

(a) Rod 10, FGR

(b) Rod 11, FGR

(c) Rod 10, temperature

(d) Rod 11, temperature

(e) Rod 10, pin pressure

(f) Rod 11, pin pressure

Fig. B. 12 - IFA-597, rod 10 and rod 11, sensitivity analysis on plenum length.